BEAM PHYSICS DEVELOPMENTS FOR A RARE ISOTOPE ACCELERATOR

By

Mauricio Portillo

A DISSERTATION

Submitted to
Michigan State University
in partial fulfillment of the requirements
for the degree of

DOCTOR OF PHILOSOPHY

Physics and Astronomy Department

2002

ABSTRACT

BEAM PHYSICS DEVELOPMENTS FOR THE RARE ISOTOPE ACCELERATOR

By

Mauricio Portillo

In support of a proposal for a Rare Isotope Accelerator facility, this thesis provides a preliminary analysis of a number of related subsystems. An overview of the requirements for the driver accelerator, production stations, and beam purification systems is presented. Some minor developments in the theory of beam transport and acceleration are presented in order to discuss a technique for isobar separation and multiple charge state selection. Changes to the COSY INFINITY code for carrying out map-based calculations are described. The results obtained by simulation are presented in detail for an isobar separator and a multiple charge state selection system. The concept of beam stripping is discussed in order to characterize the components of the multiple charge state beams. The production of rare isotopes via spallation of heavy targets using fast protons is discussed. Results obtained from experiments at an ISOL facility with direct and two-step target geometries are presented. Implications of the results to the design of future targets for rare isotope production are included. Some developments in beam diagnostic techniques are discussed along with the experimental results obtained from them.

To all my family and friends who have listened to my ideas and cared for my well-being…

ACKNOWLEDGMENTS

This work was supported by the U.S. Department of Energy, Nuclear Physics Division, under Contract W-31-109-ENG-38 and by Physics & Astronomy Department, Michigan State University. Special thanks go to my committee members: Jerry Nolen, Martin Berz, Brad Sherrill , Wayne Repko, Vladimir Zelevinsky, Norman Birge.

Thanks go out to the following friends, colleagues, and relatives for their care and support: Leslie Buck, Renee Irwin and Jan, Petr Ostroumov, Robert Janssens, Ben Zeidman, Vladislav Aseev, Declan Mulhall, Teresa Barlow, Maria Grah, Wei-Qi Shen, Art Ruthenberg, Frank Nelson, Simanta 'Chintu' Das, Naomi Leach, Todd Brown, as well as many others not mentioned.

To my relatives who believed in me and accepted me for the person that I am and the choices I made. Most importantly, I thank my mother, father, and brother for giving me their support and strength to overcome many obstacles.

TABLE OF CONTENTS

LIST OF TABLES

LIST OF FIGURES

Chapter 1

INTRODUCTION

1.1 The need for beams of rare isotopes

The concept of constructing a facility for carrying out advanced studies using energetic beams of rare isotopes has been of interest for at least a decade [ISL92]. Interest has largely been aimed at developing a method that would provide beams of short-lived nuclei having sufficient energy to break the Coulomb barrier. The beams could be directed at thin targets to induce Coulomb excitation (testing collective properties) and transfer reactions (testing single-particle aspects) of nuclei that have otherwise been too difficult to handle because of their short half-lives.

An ideal secondary beam would be one having a normalized transverse emittance $\leq$0.3 mm-mr and a longitudinal emittance of $\leq$5 keV/u-ns at energies ranging from 0.1 to 10 MeV/u. These types of conditions make it possible to obtain very short pulses of beam with low transverse momentum spread to allow for adequate time-of-flight and rigidity resolutions in nuclear studies. Current heavy ion accelerators are capable of providing these types of beams by extracting the rare isotopes as ions from a standing source. In recent years, however, there have been a number of facilities that have extended the method to beams of rare isotopes [Nolen02a]. For the most part, such efforts have been rather limited to a limited number of relatively light rare isotopes. There is still much room left for improvement in terms of the yield, number of available species, and efficiency of transport and acceleration.

Another technique that has been used to provide rare isotope beams is the in-flight method [Sherrill92]. It requires that very fast nuclei passing through a thin target get broken up by nuclear interactions at grazing incidence with light target nuclei. The products essentially keep going with the same velocity as the incoming projectile and are then directed to a secondary target. This requires that the secondary beam be purified from the primary beam and other unwanted products by way of rigidity selection through a fragment separator. One major advantage is that the secondary beam does not need any further acceleration as it is delivered to the second target. The main drawback, however, is that the secondary beam has a lot of transverse and longitudinal momentum spread from the reaction at the primary target. To make the process efficient the fragment separator must have a very large momentum acceptance and extra characterization of the projectile before it reacts with the secondary target.

In recent years there have been on-going efforts to slow down the secondary beams with a degrader after rigidity selection. The degrader is made of solid material and should remove enough momentum from the beam such that it can later be stopped with a gas filled trap [Savard99]. The trap, sometimes referred to as a gas (filled) catcher, actually transports the ions with a DC field across a region that has confining RFQ fields. During this transport process, the interacting with the gas cools them as ions until very little momentum spread is left in the products. To keep the products ionized, the gas should be filled with a very pure noble gas, such as helium. The cooled products are then extracted at the other end of the trap for use in experiments.

Such a process is to be extended to providing cooled beams of rare isotopes for subsequent acceleration in the RIA post accelerator. It is a very attractive approach since

the release times are expected to be down to as low as a few milliseconds and the process is largely independent of the chemical properties of the products [Savard02]. Ion species of refractory elements, such as tungsten and rhenium, should become accessible through this technique.

The RIA facility will be based on the idea that the same driver accelerator that is used to provide beams for fragmentation can also be used to produce rare isotopes from within a stationary target [Savard01]. For the in-flight technique the beams usually consist of the heaviest projectiles ($Z_p \geq 18$) to collide with targets of the lightest possible species ($Z_t \leq 18$). The target thicknesses must be relatively thin, such that nuclei traversing the medium without reacting (primary beam) will loose smaller percentage of momentum than the reaction products. For incident energies of 400 – 500 MeV/u the range of thickness is expected to lie in the range of 1-10 g/cm^2 [Jiang02]. The reactions that yield most of the products can be grouped in a number of categories and are as follows:

- Fission reactions occur when the collision induces enough excitation energy on the projectile nucleus to cause it to de-excite by spontaneous fission. Particles as light as a proton or deuteron at the target can induce these type of reactions.
- Spallation occurs when a very direct impact between target and projectile occurs. The high level of excitation can produce a wide array of products that are usually not accessible through fission.
- Fragmentation reaction occurs when two nuclei collides at low impact parameter with the target nucleus. One usually describes it as having the target nucleus scrape off nuclear matter from the projectile as it passes.

The fragmentation process may be regarded as lying between the two extremes, spallation and fission. At the extremes it is possible to distinguish the spallation and fission processes through their respective mass distribution of the products. This point is explained in more detail in Chapter 4. The important thing to keep in mind is that fragmentation reactions are orchestrated through the combination of target and projectile used in the reaction to obtain favorable kinematics from the reaction.

A critical component of the RIA facility will be the fragment separator. The momentum acceptance of the device must be about ±9% to deliver products at the gas catcher and about ±3% to deliver the products to secondary targets at the focal plane. The optics requires that a beam, such as of uranium, be delivered at a 1 mm diameter to the thin target. The power density in the foil is expected to get as high as 1 MW/cm^3 and has prompted the special development of windowless liquid lithium targets [Nolen02b].

Other techniques that are incorporated into the RIA plan will require production at thick targets. This can be though of as a kinematically reversed situation of the in-flight method since the beam will consist of light targets ($Z_p \leq 18$) impinging on heavier ones ($Z_t \geq 52$). The typical thickness of the target is expected to lie between 10 to 100 g/cm^2, such that the products are generated within the target matrix. The energy of the primary beam per nucleon is usually higher since they are lighter species. The expected energies lie between 500 to 1000 MeV/u. Most of the energy of the primary beam will be dumped in the material, except for the last ~50 MeV/u, which produce a very small fraction of the entire yield. The large fraction of energy that does react can produce a large flux of neutrons from spallation reactions. A significant fraction of the neutrons have energies in the few MeV range and will cause fission reactions on heavy nuclei, such as 238U.

Although fragmentation reactions occur, they are generally not mentioned in applications with heavy targets since the products do not contribute beneficially as much as they for do in the in-flight method.

The thick target must be kept at high temperatures (~2000ºC) in order to enhance the diffusion of the products out of the material. Target materials used must be refractory and able to release products rapidly to minimize losses by decay. The exit port is strategically positioned at the container to minimize the path length to the ionization and extraction region. The diagram in Fig. 1.1 depicts the transport process from the target matrix to the extraction region.

Notice that the figure indicates that the ionized products are extracted to a mass separator. The process of purifying the products right after production has come to be referred to as Isotope Separation On-Line, since the production and mass separation occur continuously. The ions from the gas catcher are also expected to be purified with the mass separator system. In that case, however, there will be no need for an ionizer since the products remain ionized in the gas. Both processes are expected to be complements of each other in the ISOL arrangement of the RIA facility as shown by the diagram in Fig. 1.2. Both of these systems are to be able to provide beams of relatively low momentum spread. Notice that the diagram indicates that the products from the in-flight process are to be diverted to a direct experiment. This pertains to the secondary target scenario where products of high momentum can react with a secondary target, as mentioned earlier. Thus there are three techniques that are to become available with beams from the RIA driver accelerator, which should give it a wide range of flexibility for experiments with rare isotopes.

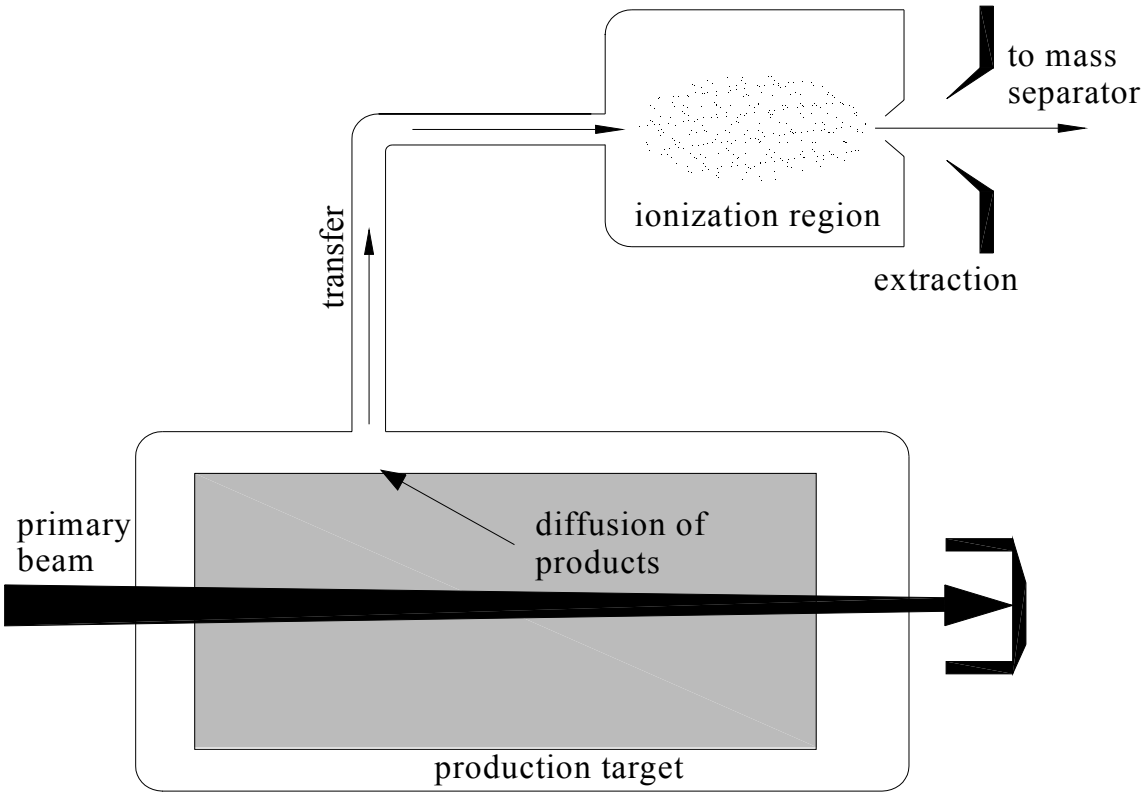

Figure 1.1 Diagram illustrating the production and transfer method in the on-line mass separation technique.

Here, we shall only directly address the ISOL method through the production in thick targets; hence, the ISOL method will always refer to the thick target scheme, unless otherwise specified.

1.2 Technological aspect of the RIA driver accelerator

The productions that are necessary to sustain the RIA facility are at a level that demands a high level of performance from the driver accelerator. The present design of the driver requires that there be a total of 1.3 GV of effective RF acceleration available for acceleration.

The beam power necessary is expected to be ~100 kW for the in-flight targets (high Z_p) and ~400 kW to the thick targets (low Z_p). The accelerator is designed to be a linac

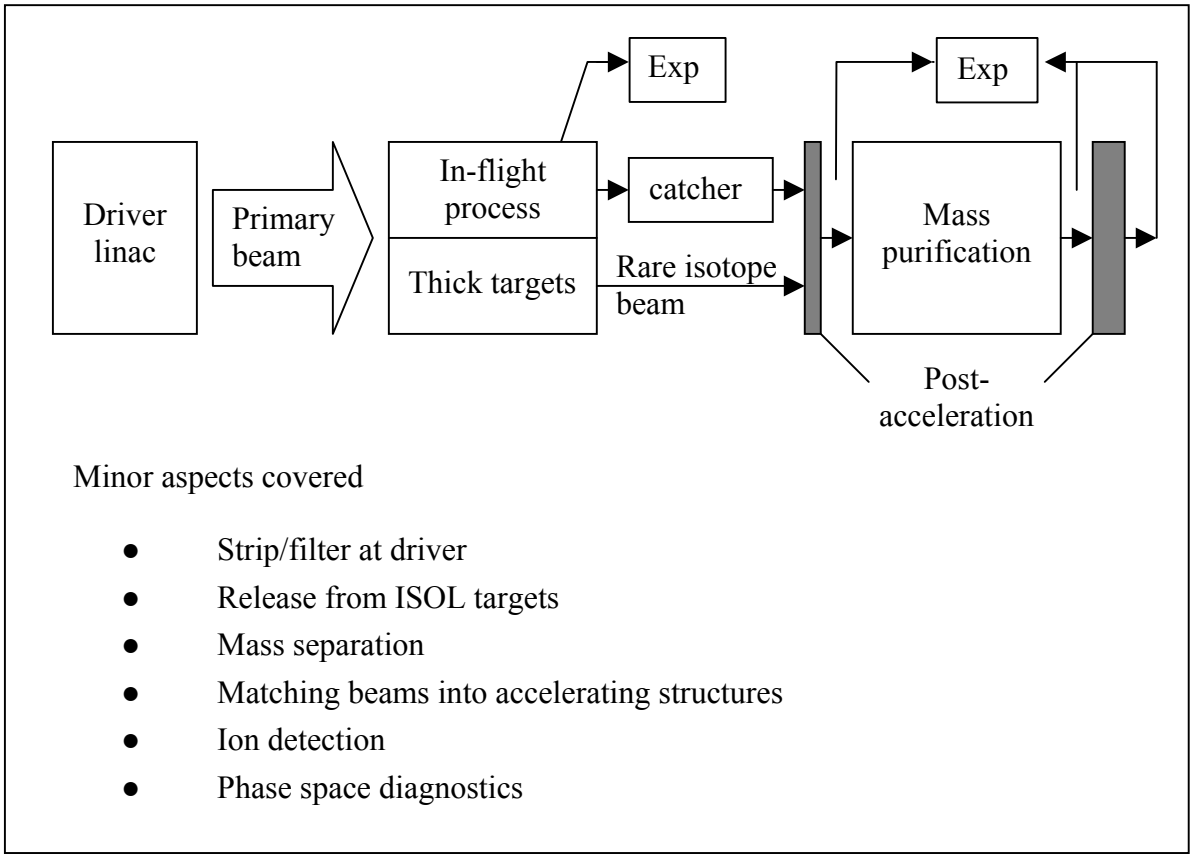

Figure 1.2 Scheme for the Rare Isotope Accelerator system at Argonne. The regions labeled with Exp represent points at which certain experiments can make use of the products.

that relies almost exclusively on superconducting cavity structures [Shepard99]. To maximize the energy of the ions over the entire spectrum of elements ($1 \leq Zp \leq 92$) all cavities must be independently phased. In the case of protons the expected final energy is about 800 MeV at an output of 400 kW, where the limiting factor is expected to be the amount of available RF power. At the other end of the spectrum, it is expected that up to ~100 kW of 400 MeV/u uranium ions can be delivered to in-flight targets. The limiting factor here is the efficiency of charge stripping of uranium ions at the source and at least two stripper foils. This problem has been addressed by implementing multiple charge state acceleration as described in Chapter 3.

1.3 Overview of contents

This thesis addresses some of the concepts needed for the RIA facility. The pictorial representation of the concepts in Fig. 1.2 should be seen as a macroscopic view of only a handful of many challenging aspects of the facility. There are a number of ways to approach the problem and studies continue to find which solutions are viable in terms of cost and technological requirements. As seen by the diagram, a large part of the effort requires beam development; hence, a lot of the topics covered will deal with beams. Some knowledge related to topics in numerical simulation by ray tracing and mapping are helpful to the reader, and there are a variety of books and other manuscripts that may be used for reference. Inevitably, there are some details that need some closer attention; therefore, a brief introduction related to beam theory is provided in the following sections of this chapter. It serves as a reference for much of the notation and terminology that is to be used for the remainder of this dissertation.

The chapter that follows will begin by demonstrating that an implementation to the COSY INFINITY code system can allow for the simulation of beams that are accelerated by electrostatic potentials. Under such conditions the energy of all the particles with equivalent charge may change by the same amount, and the effects on the transverse phase space must be simulated. It will be shown that it is possible to use higher order maps to design a mass separator for the purification at the isobar mass level. The separator is necessary for mass purification at the post-accelerator.

A chapter will also be devoted to the simulation of time-varying fields on beams with realistic radio frequency bunch structure. The COSY INFINITY code system has been modified to permit simulation of radio frequency cavities using higher order maps. A method of transport maps will be applied by applying some further modifications to the

COSY INFINITY code system. It will be demonstrated that a bunched beam of multiple charge states can be transported through a system of magnets and RF devices in order to match the beam between sections of the driver linac.

The fourth chapter will be devoted to topics related to the production and release of rare isotopes using a conceptual target set up at an ISOL facility. Although, the focus was initially intended for comparing the production of neutron rich isotopes by using either fast neutrons or relativistic protons, it is important to shed light on the aspects of release time, ionization efficiency, and detection. It will be shown that all such topics play a vital role of optimizing ISOL targets for facilities such as RIA.

The remaining chapters will be devoted reporting results that were found in these studies that are relevant to the RIA facility. A number of beam tests from a surface ionization source were carried out at a mass separator set up constructed at the Dynamitron facility at Argonne National Laboratory. We report the emittance measurements and production rates that were observed and make recommendations for future studies. Some focus will also be shed on instrumentation that has been designed for RIA applications, and has either been constructed and tested for the RIA facility or are still under development. One of these instruments is used to image low intensity beams using multichannel-plate technology.

1.4 Beam transport concepts and notation

In the study of beam transport, or beam optics, it is necessary to develop an approach for determining the orbit of charged particles in the presence of electromagnetic fields. It is necessary to derive the equations of motion that take into account any interaction that will have a significant effect on the trajectory motion. There are a number of approaches

that may be adopted in deriving the equations of motion under electromagnetic interactions. For example, the Lagrangian or Hamiltonian techniques may offer a more direct window into the conservation laws by knowledge of the electromagnetic potential. There is also the more common approach in which the concept of a force is applied in deriving the equations of motion. The Lorentz equation in vector form states that the electromagnetic force on a charged particle is given by

$$\boldsymbol{F} = qe\left(\boldsymbol{E} + \mathbf{v} \times \boldsymbol{B}\right), \tag{1.1}$$

where q is the charge number and sign, while e is the unit of charge in SI units. The particle moves with velocity, $\mathbf{v}$, in the rest frame of a magnetic field, $\boldsymbol{B}$, and electric field $\boldsymbol{E}$. Choosing a Cartesian frame of reference the form of the equations of motion can be expressed in relativistic from as follows:

$$\frac{d\boldsymbol{P}}{dt} = \boldsymbol{F}, \qquad \frac{d\boldsymbol{R}}{dt} = \mathbf{v} = \frac{\boldsymbol{P}/m}{\sqrt{1+(P/mc)^2}} \tag{1.2}$$

Here, m is the rest mass of the particle and $\boldsymbol{P}$ is its momentum. Depending on the form of the electric and magnetic fields, much effort may be devoted to finding analytical forms of the solution or writing algorithms to solve the differential equations numerically, or a combination of both. On the other hand, a large part of the effort may also go into determining the form of the electric and magnetic fields. One needs to consider the amount of accuracy that is necessary for the application and detail about the geometry of the elements that induce the fields. In some applications it is even necessary to account for the self-interaction of particles in the beam, which is sometimes referred to as the space charge effect. Evaluating the field distribution becomes even more complex when considering the effects of time-varying fields. The effect of time-varying fields is left to

the Chapter 3, and here we only consider beams transported through electrostatic and magnetostatic elements.

1.4.1 The reference particle

Most structures used for optical elements in beam optics have very well characterized properties and are designed with the intent of having some type of symmetry about the motion of an ideal particle trajectory. This ideal particle, commonly referred to as the reference particle, follows a particular trajectory path that is known from the properties of the fields. For example, a homogeneous dipole is designed such that the reference particle enters at a certain point, follows a circular path, and exits at a predestined location.

In actuality, beams consist of particles that have trajectories close to those of the reference particle but deviate within some proximity. Sources of charged particles are designed to produce particles with properties very close to those of the reference particle, but are limited to producing ensembles of particles whose coordinates are those of the ideal reference particle only on the average. The deviation from this average is usually quantified as the emittance in phase space, which in effect specifies the amount of volume occupied by the ensemble of particles. The design of any beam transport system should be tailored such that some specified acceptance is obtained and that the extent of any deleterious effects on the emittance by the applied fields is kept to a minimum. Since the cost of an optical system tends to go up with the amount of acceptance, it is advantageous to select a particle source that produces beams of minimum emittance at the amount of particle flux that is necessary. More on the beam phase space will be discussed later.

The path and instantaneous momentum of the reference particle must be determined for any beam optics problem. For most optical elements the path is well known. Otherwise, the path needs to be determined by solving equations (1.1) and (1.2) analytically or by numerical ray tracing methods within a stationary frame of reference.

1.4.2 Equations of motion in relative particle coordinates

In a stationary reference frame, the location of any arbitrary particle in the beam can be specified in Cartesian coordinates as

$$\boldsymbol{R} = \left(X, p_x, Y, p_y, Z, p_z\right), \tag{1.3}$$

in which each variable is a function of time. If the position of the reference particle,

$$\boldsymbol{R_0} = \left(X_0, p_{0x}, Y_0, p_{0y}, Z_0, p_{0z}\right), \tag{1.4}$$

is known at any time, then we can define a relative coordinate system in which the position of an arbitrary particle may be expressed by the position vector

$$\boldsymbol{r} = \boldsymbol{R} - \boldsymbol{R}_0 \tag{1.5}$$

In this moving frame of reference, the direction of the *z*-axis is parallel to the momentum vector of the reference particle. These set of relative coordinates form a set of canonical conjugate pairs. By canonical transformations a more convenient set of coordinates can be derived that can be used to describe the motion of beam particles. The following set of canonically conjugate pairs is convenient to use in describing ensembles of particles [Berz90a]:

$$\begin{aligned} r_1 &= x = (X - X_0) & r_2 &= a = (p_x - p_{0x})/p_0 \\ r_3 &= y = (Y - Y_0) & r_4 &= b = (p_y - p_{0y})/p_0 \\ r_5 &= l = -(t - t_0)\mu_0 & r_6 &= \delta_K = (K - K_0)/K_0 \end{aligned} \tag{1.6}$$

Notice that the momentum variables in the transverse plane are now divided by the magnitude of the momentum of the reference particle, p_0, to obtain the variables a and b in units of radians. The relative position variables x and y have units of meters. The variable l is proportional to the difference in the time-of-flight between the particle of interest and the reference particle by the time-position factor, $\mu_0 = \mathrm{v}_0\gamma/(1+\gamma)$. γ is the total energy of the particle divided by mc^2 and v_0 is the velocity of the reference particle. From now on we treat m as the rest mass of any particle and m_0 as the rest mass of the reference particle.

In Appendix A it is shown how the canonical transformation can be used to obtain s as the independent variable in place of the time, t. Here, s is the position along the optic axis in the stationary frame. The reference frame moves with the reference particle and is allowed to rotate such that the momentary direction of the s component points in the direction of motion of the momentum of the reference particle, $\boldsymbol{p}_0$. The last variable has been replaced by δ_K, which is the fractional difference in kinetic energy relative to the reference particle and is a unitless quantity. At times it is necessary to describe the motion of particles that have mass or charge that varies from that of the reference particle. It is convenient to use the two variables,

$$r_7 = \delta_m = (m - m_0)/m_0 \qquad\qquad r_8 = \delta_q = (q - q_0)/q_0 \ ,$$

to describe the fractional mass and charge difference, respectively. In the context of beam optics, the system of coordinate system described above is sometimes referred to as *particle optical coordinates* and we shall use them in chapters to follow.

1.4.3 The transfer map and characteristic symmetries

The method of calculating the final coordinates of a particle that propagates through some region of space with a function acting on the initial coordinates is sometimes called the mapping method. When working within the concept of maps it is more natural to use the position of the reference particle along the optic axis, s, as the independent variable instead of time. The method is based on the concept of finding some function, $\mathcal{M}(s_0,s)$, that will act on the components of the initial position vector of some particle, $\boldsymbol{r}_0 = \boldsymbol{r}(s_0)$, to yield the vector components of the particle at a later point along s. We can express this action on the vector as,

$$\boldsymbol{r}(s) = \mathcal{M}(s_0, s)\big(\boldsymbol{r}(s_0)\big), \tag{1.7}$$

This function is sometimes called the transfer function, or transfer map, and its action on the initial position vector is governed by the forces that the particle experiences relative to the reference particle while being transported from s_0 to s. A map can also act on another to yield the overall map of back-to-back transport systems. If the particle encounters two regions whose map is known for s_0 to s_1 and s_1 to s_f, then the map of the system from s_0 to s_f is give by

$$\mathcal{M}(s_0, s_f) = \mathcal{M}(s_1, s_f) \circ \mathcal{M}(s_0, s_1). \tag{1.8}$$

As long as the map is a continuous function along the region of s that is of interest, we can expand the action of the map as a power series about the reference particle position. This allows us to express the component, i, of the final position vector as,

$$r_{f,i} = \sum_{k=1}^{8} r_{0,k}\left\{(r_i, r_k) + \frac{1}{2}\sum_{l=1}^{8} r_{0,l}\left\{(r_i, r_k r_l) + \frac{1}{3}\sum_{m=1}^{8} r_{0,m}\{(r_i, r_k r_l r_m) + \cdots\}\right\}\right\}, \tag{1.9a}$$

where the values of the map coefficients (r_i,r_k), $(r_i,r_k r_l)$, $(r_i,r_k r_l r_m)$, $\cdots$ are generally functions of the independent variable s, but are evaluated at s_f here. The coefficients are

related to the initial and final coordinates by partial differentiation as in a Taylor expansion where

$$(r_i, r_j) = \left(\frac{\partial r_{f,i}}{\partial r_{0,j}} \right)_{r_{0,j}=0} \qquad (r_i, r_j r_k) = \left(\frac{\partial^2 r_{f,i}}{\partial r_{0,j} \partial r_{0,k}} \right)_{r_{0,j}=r_{0,k}=0} \qquad \cdots . \tag{1.9b}$$

Since the system refers to an optical system, we can regard the linear terms (r_i,r_k) as the first order effect. All higher order effects are aberrations, and we refer to (r_i,$r_k r_l$) terms as second order aberrations, (r_i,$r_k r_l r_m$) as third order aberrations, and so on. The terms in Eq. (1.9a) may collected in groups that share the same order to obtain the form,

$$r_{f,i} = \sum_{k=1}^{8} r_{0,k}(r_i, r_k) + \frac{1}{2}\sum_{l=1}^{8}\sum_{k=1}^{8} r_{0,l} r_{0,k}(r_i, r_l r_k) + \frac{1}{3}\sum_{m=1}^{8}\sum_{l=1}^{8}\sum_{k=1}^{8} r_{0,m} r_{0,l} r_{0,k}(r_i, r_m r_l r_k) + \cdots .$$

Each term is may be referred to as a sum of monomial terms with aberrations of the same order. In a realistic computation, expansion must be truncated at some order, N_m, and all higher terms neglected. Eq. (1.9) may then be expressed in the more simplified form,

$$r_{f,i} \;=_{N_m}\; r_i^{(1)} + r_i^{(2)} + r_i^{(3)} + \cdots + r_i^{(N_m)} . \tag{1.10}$$

Depending on the complexity of the fields that lead to the solution of the map, the accuracy of the solution improves as the order, N_m, of the expansion is increased. The subscript notation after the equal sign will hereby be neglected any time N_m=1, except when necessary.

In applying the map formalism one must be careful about the range in phase space in for which the series converges. This is particularly important for higher N_m values where the forces need to be evaluated with higher precision.

When one considers only the linear terms of the expansion, the map may be represented in the form of a linear matrix. For now, we will consider only the first six

components of the position vector. In such a case, the action of the map on the vector can the be written as the matrix equation,

$$\boldsymbol{r}_f = \begin{bmatrix} x_f \\ a_f \\ y_f \\ b_f \\ l_f \\ \delta_f \end{bmatrix} = \mathbf{A}\,\boldsymbol{r}_0 = \begin{bmatrix} (x,x) & (x,a) & (x,y) & (x,b) & (x,l) & (x,\delta) \\ (a,x) & (a,a) & (a,y) & (a,b) & (a,l) & (a,\delta) \\ (y,x) & (y,a) & (y,y) & (y,b) & (y,l) & (y,\delta) \\ (b,x) & (b,a) & (b,y) & (b,b) & (b,l) & (b,\delta) \\ (l,x) & (l,a) & (l,y) & (l,b) & (l,l) & (l,\delta) \\ (\delta,x) & (\delta,a) & (\delta,y) & (\delta,b) & (\delta,l) & (\delta,\delta) \end{bmatrix} \begin{bmatrix} x_0 \\ a_0 \\ y_0 \\ b_0 \\ l_0 \\ \delta_0 \end{bmatrix}, \tag{1.11}$$

where the matrix $\mathbf{A}$ represents the map. The subscript for variable having the fractional kinetic energy has been left out, so that δ must be understood to represent δ_K. If all three variables had been included such that there is an 8 dimensional position vector, then $\mathbf{A}$ would simply be an 8×8 matrix.

For any system made up of one or more optical elements, the first order map is of primary importance since it is used to identify the most critical optical qualities of the system. The matrix also reflects upon many of the symmetries of the motion. The most notable of them is referred to as horizontal midplane symmetry and it is a result of having only electromagnetic fields that are symmetric about the y=0 plane. As a consequence, all cross terms between the horizontal and vertical plane will vanish such that the matrix in Eq. (1.11) becomes [Berz85]

$$\mathbf{A} = \begin{bmatrix} (x,x) & (x,a) & 0 & 0 & (x,l) & (x,\delta) \\ (a,x) & (a,a) & 0 & 0 & (a,l) & (a,\delta) \\ 0 & 0 & (y,y) & (y,b) & 0 & 0 \\ 0 & 0 & (b,y) & (b,b) & 0 & 0 \\ (l,x) & (l,a) & 0 & 0 & (l,l) & (l,\delta) \\ (\delta,x) & (\delta,a) & 0 & 0 & (\delta,l) & (\delta,\delta) \end{bmatrix}. \tag{1.12}$$

Maps of devices, such as quadrupoles, higher order multipoles, and electromagnetic sectors where the motion of the reference particle is restricted to the y=0 plane, all fall into this category.

If there is no bending of the reference trajectory at all, i.e. no dipole fields, then a double midplane symmetry is obtained. The result is that the terms located at the bottom-left and top-right 4×4 sub-matrices of Eq. (1.12) vanish as well. Since there is then no cross term relation between the x—a, y—b and l—δ phase space planes, then three remaining subspaces,

$$\mathbf{A}_x = \begin{bmatrix} (x,x) & (x,a) \\ (a,x) & (a,a) \end{bmatrix}, \quad \mathbf{A}_y = \begin{bmatrix} (y,y) & (y,b) \\ (b,y) & (b,b) \end{bmatrix}, \text{ and } \quad \mathbf{A}_l = \begin{bmatrix} (l,l) & (l,\delta) \\ (\delta,l) & (\delta,\delta) \end{bmatrix} \tag{1.13}$$

may be treated separately.

Another common symmetry that occurs in optical systems is that of rotational, or axial, symmetry. Unlike double midplane symmetry in which the two planes of symmetry, x—z and y—z, are offset by an angle, ϕ=90°, rotation about the z-axis, axially symmetric systems have symmetry about any arbitrary angle. In this case, all the same terms vanish as in the double midplane symmetry, but additionally, all corresponding terms in the x—a and y—b subspaces will be equivalent.

Maps of devices having no time-varying fields will have terms that in turn have no explicit dependence on time. Hence, any terms in Eq. (1.9) with partial differentiation with respect to the time variable, l, will, therefore, vanish so that $(l,\cdots)=0$ except for (l,l).

Finally, there is the condition in which either there is no change in the energy of all particles in the beam or there is and equivalent change for all particles. This assumes that all particles have the same charge as the reference particle, ($q_0 e$). An example of such a

system would be a DC accelerating column in which a potential drop between the entrance and exit changes the energy of every particle by $\Delta K=-q_0 e(V_f-V_0)$. For this case, any terms in Eq. (1.9) with partial differentiation with respect to the energy variable, δ, will vanish such that $(\delta,\cdots)=0$ except for (δ,δ).

If midplane symmetry about y=0 is imposed, along with explicit time-independence and energy constancy, then the resulting form of the transfer matrix is

$$\mathbf{A}=\begin{bmatrix} (x,x) & (x,a) & 0 & 0 & 0 & (x,\delta) \\ (a,x) & (a,a) & 0 & 0 & 0 & (a,\delta) \\ 0 & 0 & (y,y) & (y,b) & 0 & 0 \\ 0 & 0 & (b,y) & (b,b) & 0 & 0 \\ (l,x) & (l,a) & 0 & 0 & (l,l) & (l,\delta) \\ 0 & 0 & 0 & 0 & 0 & (\delta,\delta) \end{bmatrix}. \tag{1.14}$$

Since all six variables are canonical conjugates, then the symplectic condition applies as pointed out in Appendix A. If we apply the symplectic condition to Eq. (1.14) we obtain the following relations between the first order map elements:

$$(x,x)(a,a)-(x,a)(a,x)=p_{0,0}/p_{0,f} \tag{1.15a}$$

$$(y,y)(b,b)-(y,b)(b,y)=p_{0,0}/p_{0,f} \tag{1.15b}$$

$$(l,l)=\mu_{0,f}/\mu_{0,0} \tag{1.15c}$$

$$(\delta,\delta)=K_{0,0}/K_{0,f} \tag{1.15d}$$

$$(x,x)(l,a)-(x,a)(l,x)=\frac{p_{0,0}\mu_{0,0}}{K_{0,0}}(x,\delta) \tag{1.15e}$$

$$(a,x)(l,a)-(a,a)(l,x)=\frac{p_{0,0}\mu_{0,0}}{K_{0,0}}(a,\delta) \tag{1.15f}$$

$$(a,x)(x,\delta)-(x,x)(a,\delta)=\frac{K_{0,0}}{K_{0,f}}(l,x) \tag{1.15g}$$

$$(a,a)(x,\delta)-(x,a)(a,\delta)=\frac{K_{0,0}}{K_{0,f}}(l,a) \tag{1.15h}$$

Here, $p_{0,0}$, $K_{0,0}$, and $\mu_{0,0}$ are, respectively, the momentum, kinetic energy, and time-factor of the reference particle at the initial position, while the subscript *f* denotes the final position. It is assumed that the change in energy, $(K_{0,f}-K_{0,0})$, is the same for any particle that is transported by the system. This can happen when all the particles are accelerated over some common change in electrostatic potential. Since the fields are static in time, we refer to this as DC acceleration. Here, a deceleration is understood in the sense that the acceleration is negative, hence any change in energy is herby called acceleration regardless of its sign.

When there is no change in energy, Eqs. (1.15a) through (1.15d) will all go to unity. We note that this is a direct consequence of the invariance of phase space volume under canonical transformations, as stated by Liouville's theorem [Landau76b]. It implies that as long as the total energy of the system is a constant of the motion, then the action of the map is effectively a canonical transformation on the ensemble of particles.

1.4.4 Focusing properties as determined from the first order map elements

Special focusing conditions are identifiable from vanishing terms in the map. Furthermore, other map elements may become meaningful when one or more particular elements vanish. Some examples are introduced now for the case in which the system has particles that all have the same mass, charge and energy, and the electromagnetic fields are time-invariant and symmetric at least about the *y*=0 plane.

Consider the path of the trajectories as seen from a side profile of the beam along the x—z plane. We are interested in the values of the first order subspace matrix $\mathbf{A}_x$ of a system with special optical qualities. For example, if the rays enter the system parallel to each other and exit such that all rays cross at the same x—position then we have what is called a parallel-to-point condition, and the (x,x) term will vanish. The diagram in Fig. 1.3(a) illustrates a schematic representation of this condition. This condition indicates that the exit plane, $z=z_f$, is a focal plane. If instead the focal plane is at $z=z_0$, then we must have that $(a,a)=0$, and there exist a point-to-parallel focus as shown by Fig. 1.3(b).

Vanishing of the two off-diagonal terms in the x—a phase space are also of special importance. The vanishing of the (x,a) term signifies that there is a point-to-point focusing condition as depicted in Fig. 1.3(c). This gives an object-image relation between the entrance and exit plane of the transport system. Any imaging device is characterized by a spatial magnification factor, M_x, which in this case has a value that is equivalent to the term (x,x). The term (a,x) vanishes whenever the rays undergo a parallel-to-parallel focus, as shown in Figure 1.3(d). In this case, there is an angular magnification, N_x, in which the ratio of the exit to entrance angle of the rays is given by the term (a,a). An optical system of this type is considered a telescope focused at infinity.

According to Eq. (1.15a), the determinant of $\mathbf{A}_x$ must be equivalent to the ratio of the incoming to outgoing momentum of the reference particle. This means that only the first or second term of the equation is allowed to vanish simultaneously and restricts the combinations allowed between the four focusing conditions already discussed. There are only two combinations allowed. The combination in which $(a,x)=(x,a)=0$ is recognized

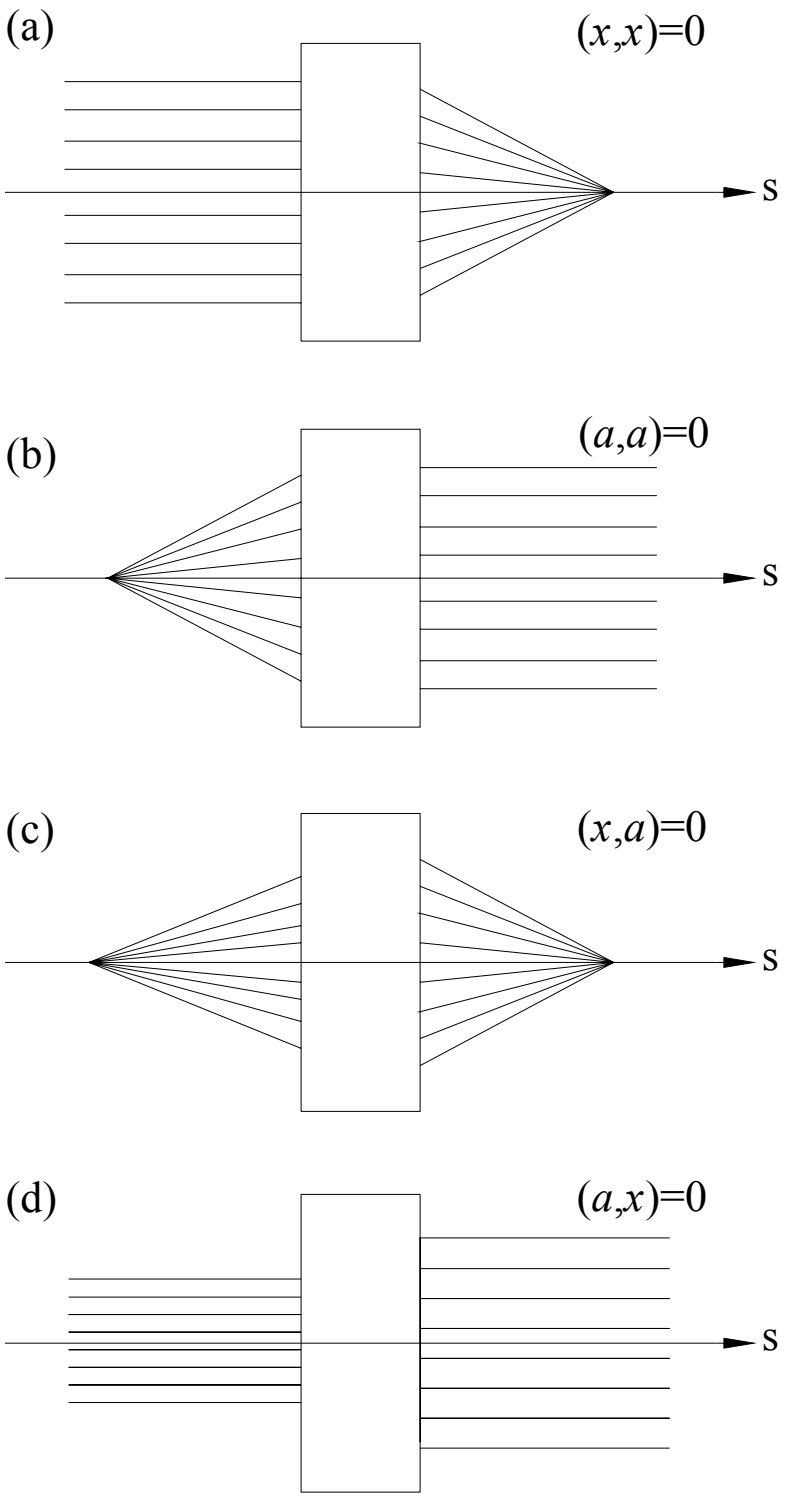

Figure 1.3 Schematic representation of several focusing conditions in which elements of the map may vanish. (a) Represents parallel-to-point focus in which $(x,x)=0$. (b) Represents point-to-parallel focus in which $(a,a)=0$. (c) Represents point-to-point focus in which $(x,a)=0$. (d) Represents parallel-to-parallel focus in which $(a,x)=0$.

as one with telescopic focus and having both spatial and angular magnifications, M_x and

N_x, respectively. The $(x,x)=(a,a)=0$ combination simply implies that the $z=z_0$ and $z=z_f$ are both focal planes. The complexity that would arise from not having at least midplane symmetry is the terms (x,y), (x,b), (a,y), and (a,b) would also be required to vanish to obtain the focus conditions described above. Otherwise, these same arguments apply to elements of the $\mathbf{A}_y$ subspace matrix if considering a beam profile along the y—z plane.

The (x,δ) term characterizes the separation along the horizontal plane of particles that differ in δ, whether its δ_K, δ_m, or δ_q. Devices that impose a bend along the horizontal plane can cause the values of (x,δ) and (a,δ) to deviate from zero. If the system is imaging, then we refer to the (x,δ) term as the dispersion. More discussion on the meaning of these terms will be provided when sections related to sector-field spectrometers are encountered.

It should also be noted that the above conditions could also be extended to higher order aberrations by considering the higher order derivatives of Eq. (1.9). This discussion is left to other sections where the concept of the phase space ellipse is introduced.

1.5 Numerical approach to computing rays

Some of the beam optical systems to be presented later have been studied with by either ray trace computation or mapping. In some cases a comparison is made between the results found by using both methods, thus a brief description of the numerical approach used by each is suitable.

1.5.1 Ray trace method of computation

In the ray trace method the trajectory for every particle must be computed by numerical integration of the equations of motion. This is usually carried out in a

Cartesian frame of reference with the set of six ordinary differential equations (ODEs) obtained from the components of [Reiser94a]

$$\frac{d\boldsymbol{R}}{dt} = \mathbf{v} \tag{1.16a}$$

and

$$\frac{d\mathbf{v}}{dt} = \frac{\boldsymbol{F} - \mathbf{v}(\mathbf{v}\cdot\boldsymbol{F})/c^2}{\gamma m} = \frac{qe\left(\boldsymbol{E} + \mathbf{v}\times\boldsymbol{B} - \mathbf{v}(\mathbf{v}\cdot\boldsymbol{E})/c^2\right)}{\gamma m}. \tag{1.16b}$$

These are simply a rewritten form of Eq. (1.2) in which the electromagnetic force, $\boldsymbol{F}$, is replaced with Eq. (1.1). Notice that the last term in the numerator becomes negligible compared to the terms in $\boldsymbol{F}$ for the non-relativistic limit, $\gamma = (1 - \mathrm{v}^2/c^2)^{-1/2} \approx 1$.

The commercially available code system, SIMION 7, was utilized in some of the calculations. It has the ability to determine electric and magnetic potentials along a 3D grid representing the region of space [Simion7]. The user enters the electrode and pole boundary conditions, which the code uses to apply a finite difference technique to solve Laplace's equation, $\nabla^2\Phi=0$. Since there are no expansions involved in describing the fields or trajectories, these computations are not truncated to a specific order as in the map-based approach. SIMION solves trajectories by integration of the non-relativistic form of Eq. (1.16) by iteratively computing

$$\Delta\boldsymbol{R} = \int_{t_0}^{t_f} \mathbf{v}\,dt \tag{1.17a}$$

and

$$\Delta\mathbf{v} = \frac{1}{m}\int_{t_0}^{t_f} \boldsymbol{F}\,dt\,. \tag{1.17b}$$

It uses a fourth order Runge-Kutta numerical integrator with adaptive control over its own progress. Adaptive control allows frequent changes in the integration step to minimize computational effort while keeping some predetermined accuracy [Press92].

One advantage of solving by ray tracing is that it is straightforward to apply the electromagnetic fields directly to the equations of motion without the need for expansions. This is especially advantageous when applying finite difference algorithms to determine the fields, which has made it possible to extend the technique for effectively solving Vlasov equations [Birdsall85]. The fields can also vary with time as the trajectories are being computed. Overall, this technique allows more flexibility in treating the properties of the fields. There are set backs to using this method, however.

The most notable difficulty with ray tracing is the large amount of computation that is necessary when there is a large number of elements over a long path and large number of ensembles. Sector magnets, which are more suited for computer-based optimization, can be physically large and more tedious to handle with ray tracing. Ensembles must be limited in size, which makes it difficult to obtain accuracy. On the other hand, with mapping once the elements of the map are determined, calculating final positions of rays is simply a matter of evaluating polynomials. One major advantage lies in the fact that the lower order coefficients tend to be of primary importance. Thus, it is advantageous to optimize an optical problem by successive evaluations and including more accuracy each time by increasing, as well as increasing the level of electromagnetic field complexity if necessary.

1.5.2 Computation of maps

There have been a number of computer codes with algorithms for determining the coefficients of the Taylor expanded form of the map. A well known example is the beam optics code TRANSPORT, which started off as being a second order code [Brown64] and was later extended to third order [Carey92]. While TRANSPORT was evolving to third order capability other codes, such as TRIO [Matsuo76] and GIOS [Wollnik87], also become available with third-order capabilities. All these codes, however, relied on the development of an analytical representation of formulas for the coefficients and were based on a select list of elements with known field characteristics. With the advent of specially made custom formula manipulators, the code COSY 5.0 was even able to push the envelope even further by evaluating up to fifth-order terms [Berz87a]. These methods, however, become prohibitively complicated at higher orders.

The advent of differential algebraic (DA) techniques has made it possible to extend algorithms to higher orders and to more types of elements. The DA approach stems from the transformation of crucial function space operations of addition, multiplication, and differentiation, to a suitable set of equivalence classes [Berz90b][Berz99a]. The implementation of these operations into the optics code, COSY INFINITY, allows calculation of maps to arbitrary order [Berz90a]. From here on we refer to this code simply as COSY, since it is used extensively in these studies.

To gain understanding of how COSY goes about evaluating elements of the map, we should revert back to Eq. (1.9). Taking the derivative with respect to the independent variable, s, to obtain component i of a set of expanded first order differential equations (ODEs) given by,

$$\frac{dr_i}{ds} = r_i' = \sum_{k=1}^{8} r_k (r_i, r_k)' + r_k (r_i, r_k)' + \frac{1}{2} \sum_{k[2]=1}^{8} \sum_{k[1]=1}^{8} r_{k[2]} r_{k[1]} (r_i, r_{k[2]} r_{k[1]})' + \cdots$$
$$+ \frac{1}{N_m} \sum_{k[N_m]=1}^{8} \cdots \sum_{k[1]=1}^{8} r_{k[N_m]} \cdots r_{k[1]} (r_i, r_{k[N_m]} \cdots r_{k[1]})' \quad . \quad (1.18)$$

If the equation is written in unexpanded form then we obtain that

$$\frac{dr_i}{ds} = f_i (r_1, r_2, r_3, r_4, r_5, r_6, r_7, r_8, s) = f_i (x, a, y, b, l, \delta_K, \delta_m, \delta_q, s) , \quad (1.19)$$

where the coordinates of the function *f* may depend on *s*. We restrict ourselves to the case in which δ_m and δ_q are independent of *s*, i.e. $\delta_m' = \delta_q' = 0$. We want to show that the set of ODEs implied by Eq. (1.19) are related to the time dependent Hamiltonian, which are in turn obtained from the equations of motion.

To make this relation realizable we must carry out a Legendre of the type discussed in Appendix A to switch the independent variable from *s* to *t*. In fact, the transformation would essentially be the reverse of the one in the appendix in which the equations were transformed from *t* to *s* dependence. This type of transformation should yield a new set of ODEs,

$$\frac{dr_i}{dt} = h_i (x, p_x, y, p_y, s, p_s, t) . \quad (1.20)$$

where the coordinates are also regarded as functions of time. We can compare the h_i components with the system of Hamiltonian equations,

$$\begin{aligned} \dot{x} &= \partial H / \partial p_x & \dot{p}_x &= -\partial H / \partial x \\ \dot{y} &= \partial H / \partial p_y & \dot{p}_y &= -\partial H / \partial y , \\ \dot{s} &= \partial H / \partial p_s & \dot{p}_s &= -\partial H / \partial s \end{aligned} \quad (1.21)$$

where the dot notation stands for *d/dt* and the former independent variable, *s*, and its corresponding momentum, p_s, have now been transformed into variables. Although we

worked about it backwards, it has been shown that the Hamiltonian of the system can be transformed to give the ODEs of Eq. (1.19), which in turn may be expanded to the form of Eq. (1.18). Integrating each term in Eq. (1.18) yields the corresponding terms in Eq. (1.9), and in effect, solves the expanded form of the equations of motion in map form.

The form of the Hamiltonian in (x,a,y,b,l,δ_K,s) space and the corresponding equations of motion have been worked out by Makino and Berz in full 3D curvilinear coordinates [Kyoko98][Berz99b]. The equations are more involved in full curvilinear form, hence, we do not elaborate on them here. For these studies, we restrict the discussion to the form of the equations of motion under midplane symmetry conditions about the *y*=0 plane. The motion of the reference particle is restricted to this plane, and the instantaneous curvature of the motion is given by, *h(s)*=1/ρ*(s)*, where ρ is the radius of curvature. Under these condition the equations of motion are given by

$$x' = a(1+hx)p_0 / p_z \tag{1.22a}$$

$$y' = b(1+hx)p_0 / p_z \tag{1.22b}$$

$$l' = (1+\delta_m)(1+hx)\frac{1+\eta}{1+\eta_0}\frac{p_0}{p_z} \tag{1.22c}$$

$$a' = \left((1+\delta_m)\frac{1+\eta}{1+\eta_0}\frac{p_0}{p_z}\frac{E_x}{\chi_{E0}} - \frac{B_y}{\chi_{M0}} + b\frac{p_0}{p_z}\frac{B_z}{\chi_{M0}}\right)(1+hx)(1+\delta_q) + h\frac{p_z}{p_0} \tag{1.22d}$$

$$b' = \left((1+\delta_m)\frac{1+\eta}{1+\eta_0}\frac{p_0}{p_z}\frac{E_y}{\chi_{E0}} + \frac{B_x}{\chi_{M0}} - a\frac{p_0}{p_z}\frac{B_z}{\chi_{M0}}\right)(1+hx)(1+\delta_q) \tag{1.22e}$$

$$\delta_K' = 0, \tag{1.22f}$$

where the prime still represents the derivative with respect to s and all parameters with subscript 0 are of the reference particle. The quantity η is a measure of relativity as given by,

$$\eta = \frac{K}{mc^2} = \frac{K_0(1+\delta_K) + \Delta K(x,y,s,t)}{m_0 c^2 (1+\delta_m)}. \tag{1.23}$$

The quantities,

$$\chi_{E0} = \frac{p_0 \mathrm{v}_0}{q_0 e} \qquad \text{and} \qquad \chi_{M0} = \frac{p_0}{q_0 e} \tag{1.24}$$

are the electric and magnetic rigidity, respectively, of the reference particle. We can evaluate the momentum ratio that appears in each of Eqs. (1.22) by

$$\frac{p_0}{p_z} = \sqrt{(1+\delta_m)^2 \frac{\eta(2+\eta)}{\eta_0(2+\eta_0)} - a^2 - b^2}\,. \tag{1.25}$$

Equation (1.22f) vanishes since we have assumed that there are no fields with explicit time dependence in the system. This does not necessary mean that the kinetic energy of a particle cannot vary along the motion. Indeed, if a particle enters a region in which the electric potential varies in space (not time), then it will experience a change in kinetic energy, ΔK. This is reflected by the form of η in (1.23) where ΔK. Suppose we assume initially that there is explicit time dependence, then the change in kinetic energy will vary as,

$$\Delta K\big(\boldsymbol{R}(t),t\big) = q\int_{t_0}^{t} \boldsymbol{E}\big(\boldsymbol{R}(\tau),\tau\big)\cdot \mathbf{v}(\tau)\; d\tau\,. \tag{1.26}$$

If we turn off the time dependence, then $\boldsymbol{E} = -\nabla V$ and ΔK can be evaluated from

$$\Delta K(x,y,s) = -qe(1+\delta_q)V(x,y,s)\,. \tag{1.27}$$

This assumes that the potential has been expressed in the curvilinear coordinates and that the potential is specified relative to the entrance position such that $V(x,y,0)=0$.

At this point we can compare Eqs. (1.22) and (1.18) and observe that by expanding the components of the electric and magnetic fields on the right side of each equation in (1.22), one can form a relation between the s derivatives of the map elements and the equations of motion. The code COSY uses a numerical ODE integrator and DA functions to determine each element of the map as described by Berz and Wollnik [Berz87b]. At its core this ODE integrator utilizes an eighth-order Runge-Kutta algorithm with adaptive control over its own progress, making frequent changes in its step size, similar to the fourth order integrator of SIMION.

The code has integrated features that allow it to algebraically determine elements of the map without numerical integration. This can substantially reduce computational time; especially in the first stages of a problem where not a lot of accuracy is needed. The method is based on an analytical solution in which it is assumed that the particle experiences no forces along its direction of the velocity and that the curvature remains constant along the motion. This is true of a number of situations; the most obvious one being that of a drift along a field free region. Another is the case in which fringing fields at the boundaries of a homogeneous magnet are ignored. In this case the magnetic field is always parallel to the y—axis and the field changes abruptly at the dipole boundaries. This is very similar to the case of a light ray entering a glass medium with constant index of refraction, except there the curvature is h=0 and the velocity changes abruptly at the boundary. Indeed, COSY also has features that calculate the maps of glass optical

systems [Berz99c]. For both glass optics and magnetic dipoles the exact shape of the boundary must be specified.

In any electromagnetic device there is always some level of fringing, and in fact, may depend exclusively on fringing for its focusing strength. Any optical elements with fields varying along the optic axis require numerical integration of the ODEs along the *s*-axis .

Devices such as dipoles and multipoles tend to have extensive regions along the optic axis over which there is little variation along the *s*—axis. This region depends on the size of the gap and any shunts, or clamps, that may be applied in the region just outside of the pole region [Wollnik87a][Hübner70]. The regions in which fringing is negligible are calculated using the efficient DA methods and the fringing regions may be treated in a number of ways. For computational efficiency one may use a symplectic scaling option, and for accuracy and flexibility one may specify the coefficients of an Enge function to describe the field dependence on *s* [Höffstatter96]. The equation for this function is given by,

$$F(s) = \frac{1}{1 + \exp\left(a_1 + a_2(s/G) + \cdots + a_6(s/G)^6\right)}, \tag{1.28}$$

where G is the gap width of the dipole, or diameter if it is a multipole. The constants a_1 thru a_6 are the Enge coefficients. We use the available default values that derive from measurements taken of a family of unclamped multipoles at the PEP facility [Brown81] and plot the corresponding Enge function in Figure 1.4.

Before going on to the next section, a few things should be mentioned about the other possible beam interactions. The effects of energy loss by emission of synchrotron radiation are not accounted for in the equations of motion in COSY, nor are the self-interaction forces due to space charge. These effects will not be important for our

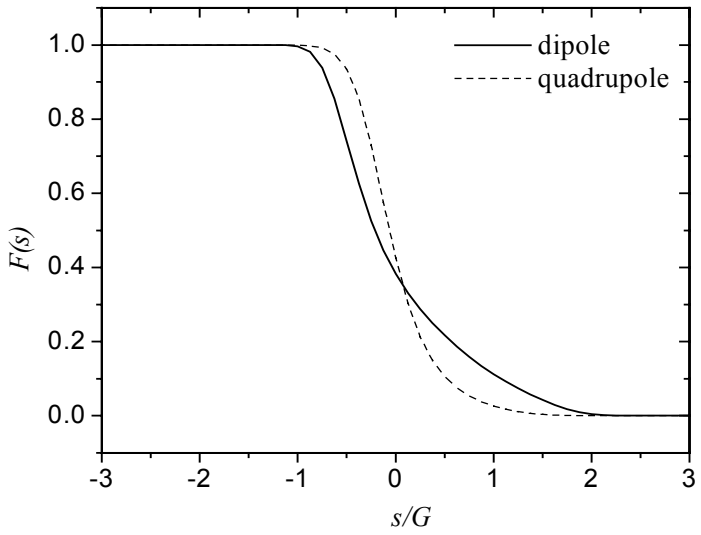

Figure 1.4 Enge functions for dipole and quadrupole elements as a function of position over gap width, *G*. The Enge coefficients used were derived from measurements as cited in the text.

applications, but can in principle be formulated into the equations [Vorobiev01] [Berz90a]. COSY currently accounts for the forces from electromagnetic field interaction with a particle's spin, but is a negligible effect here; therefore, it is left as a reference [Berz99d][Makino99].

Generally, the COSY code system offers a variety of options that makes it advantageous to use over other applications with maps. For one, the user interface is written as a high level language to let the user write custom programs. One can readily create custom optical elements in this way. There are also a variety of algorithms for optimization of optical system. They allow one to specify any objective function that is to be minimized [Berz97].

1.6 The phase space of beams

If we neglect the rotational degrees of freedom, then the motion of any particle may be specified by its vector position and momentum. In the case where there exists a large group of particles it is useful to apply the concept of phase space volume. In this macroscopic description one specifies the phase space volume that an ensemble of

particles occupies. The phase space can be fully described by some six-dimensional volume with the coordinate variables X, P_X, Y, P_Y, Z, and P_Z. It is useful to apply other coordinate systems from beams, and it has already been demonstrated that by a canonical transformation the system may also be described by the variables x, a, y, b, l, and δ_K. From now on, these variables will be used to describe phase space, unless otherwise specified.

It is customary to describe the phase space by the amount of area that the beam occupies in each of the three subspaces, x—a, y—b, and l—δ_K. The first of these two subspaces are said to lie along the transverse planes since the direction of motion in this plane is perpendicular to that of the reference particle's. The units are usually in m-rad, or mm-mr. The direction lying tangent to the orbit of the reference particle is referred to the longitudinal direction and the phase space area along the l—δ_K plane is usually referred to as the longitudinal phase space. The units are given in meters with an understood fractional quantity. To obtain units of energy and time one needs to multiply quantity by the energy of the reference particle, K_0, and divide by the factor, μ_0. The units commonly used are keV for energy and ns for time.

1.6.1 The concept of the phase space ellipse

Since beams tend to exhibit bell shaped distributions along any of the phase space variables, contour plots along any subspace will generally exhibit a family of ellipse-shaped boundaries. The contour lines indicate the level of beam intensity and the integrated intensity as one goes to a lower and lower intensity level is sometimes used as a figure of merit in beam applications. Further discussion about this topic is left to another section below.

We restrict the following discussion to the *x*—*a* subspace noting that it also applies to the other two subspaces in the same manner as treated here. The equation of the ellipse representing the phase space boundary may be expressed by the equation,

$$\gamma_x x^2 + 2\alpha_x xa + \beta_x a^2 = \varepsilon_x , \tag{1.29a}$$

or in matrix form,

$$\begin{bmatrix} x & a \end{bmatrix} \cdot \begin{bmatrix} \gamma_x & \alpha_x \\ \alpha_x & \beta_x \end{bmatrix} \cdot \begin{bmatrix} x \\ a \end{bmatrix} = (\boldsymbol{r})^{\mathrm{T}} \cdot \boldsymbol{\sigma} \cdot \boldsymbol{r} = \varepsilon_x . \tag{1.29b}$$

Here, $\gamma_x, \alpha_x,$ and β_x are known as the Twiss, or Courant-Snyder, parameters and in order to have only one unique solution for some given ε_x we demand that the determinant of the sigma matrix, $\boldsymbol{\sigma}$, be unity; i.e.

$$\beta_x \gamma_x - \alpha_x^{\,2} = 1 . \tag{1.30}$$

The area bounded by the ellipse will be referred to here as the *emittance area* and is given by $\pi\varepsilon_x$, where ε_x will simply be called the *emittance*. One should be aware that other references might refer to the area as the emittance.

It is useful to solve for *a* and *x* from (1.29a) to obtain the two quadratic solutions,

$$a = \frac{-\alpha_x x \pm \sqrt{\beta_x \varepsilon_x - x^2}}{\beta_x} \qquad \text{and} \qquad x = \frac{-\alpha_x a \pm \sqrt{\gamma_x \varepsilon_x - a^2}}{\gamma_x} . \tag{1.31}$$

The factors inside the square root must remain positive to be within the region bounded by the points of extremum at x_m and a_m as illustrated by the Fig. 1.5. The extrema are solved for by setting the quadratic terms to zero and applying condition (1.30) to obtain,

$$x_m = \sqrt{\beta_x \varepsilon_x} \qquad \text{and} \qquad a_m = \sqrt{\gamma_x \varepsilon_x} . \tag{1.32}$$

By inserting each of these into equation (1.29a) we obtain the other two terms shown in the same figure,

$$a_e = -\alpha_x \sqrt{\varepsilon_x / \beta_x} \qquad \text{and} \qquad x_e = -\alpha_x \sqrt{\varepsilon_x / \gamma_x} \,. \tag{1.33}$$

Hence, the width along the x— and a—axes of the ellipse are determined by the parameters β_x and γ_x, respectively. The parameter α_x quantifies the tilt of the ellipse in the sense that the ellipse in Figure 1.5 has a value $\alpha_x<0$.

1.6.2 The normalized emittance

Take the situation where we have an ensemble particles forming an upright ellipse at $s=s_0$ in the x—a phase space with emittance, $\varepsilon_{x,0} = x_{m,0} a_{m,0}$, and reference particle momentum, $p_{0,0}$. The ensemble is transported through a telescopic focusing system that applies DC acceleration to obtain the final momentum, $p_{0,f}$, as it exits at $s=s_f$. As long as there exists at least midplane symmetry, then equation (1.15a) applies and we must have that $(x,x)(a,a) = p_{0,0} / p_{0,f}$. Since (x,x) and (a,a) are the magnification along the x— and a—axes, respectively, we must have that

$$\varepsilon_{x,f} = x_{m,f} a_{m,f} = (x,x) x_{m,0} \cdot (a,a) a_{m,0} = \varepsilon_{x,0} \frac{p_{0,0}}{p_{0,f}} \,. \tag{1.35}$$

This result implies that the emittance changes by a factor proportional to the ratio of the initial to final momentum. If there is a positive acceleration then the emittance will be

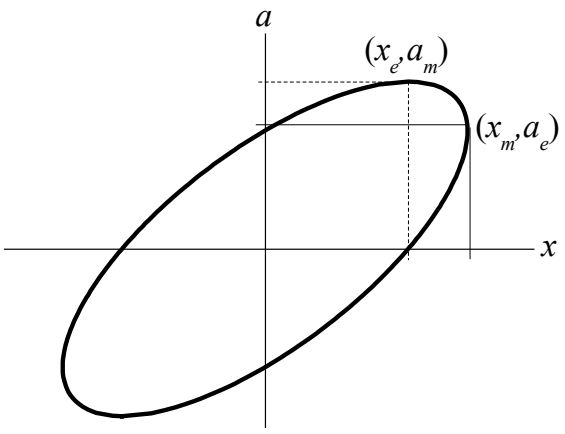

Figure 1.5 Diagram illustrating the points of extremum in the phase space ellipse along the x—a plane. The tilt is such that $\alpha_x<0$.

reduced by this factor, and vice-a-versa for negative acceleration, or deceleration. Note that we assumed a telescopic system with upright ellipses for simplicity. This result, however, applies to any system of time-independent fields.

There is an invariant quantity that becomes apparent if both sides of Eq. (1.35) are multiplied by the final momentum. We define this invariant quantity, $\varepsilon_{x,n}$, as the normalized emittance such that,

$$\varepsilon_{xn} mc = \varepsilon_{x,f} p_{0,f} = x_{m,0} a_{m,0}, \tag{1.36}$$

where the constant *mc* may be divided out to obtain the same units as the standard emittance. Since there is invariance along *s*, then the subscript for position may be dropped and we can simply write the normalized emittance as

$$\varepsilon_{xn} = \varepsilon_x \gamma_0 \beta_0 . \tag{1.37}$$

The normalized emittance is essentially the phase space occupied by the beam in the rest frame of the reference particle. As long as there are only conservative forces acting on the system of particles and there is no self-interaction or interaction with any other external medium, then this quantity will remain constant. Non-conservative interactions can be caused by a number of things. For example, there are collisions with walls, foils, or residual gas particles that generally tend to cause an increase in the normalized emittance. The emanation of synchrotron radiation will generally cause a decrease, although negligible in most cases. It is most prominent in the case of highly relativistic light particles, such as electrons. Finally, external forces that originate from time-varying potentials will generally cause some increase in the normalized emittance.

1.6.3 The transformation of the sigma matrix

The concept of the phase space ellipse is used to describe the effects caused by of optical elements on the beam's phase space. It is mainly restricted to first order transformations since higher order effects will distort the boundary to shapes that deviate from the equation of an ellipse. A number of examples of this effect will be given later, but for now we accept the restriction in order to discuss the effect on the sigma matrix under such linear transformations.

As follows from (1.29b), the equation of the ellipse for any subspace at some initial $s=s_0$ can be written in terms of its respective sigma matrix, $\boldsymbol{\sigma}_0$, by the equation

$$(\boldsymbol{r}_0)^{\mathrm{T}}\boldsymbol{\sigma}_0\boldsymbol{r}_0 = \varepsilon_0 . \tag{1.38}$$

We suppose that in going from s_0 to s_f the particles in the beam experiences DC acceleration and that map of the system is given by $\mathbf{A}$ such that,

$$\mathbf{A}\,\boldsymbol{r}_0 = \boldsymbol{r}_f , \tag{1.39a}$$

and its inverse defined in the sense that,

$$\mathbf{A}^{-1}\boldsymbol{r}_f = \boldsymbol{r}_0 . \tag{1.39b}$$

If we assume midplane symmetry and restrict our attention to only the x—a subspace, then as suggested from (1.13),

$$\mathbf{A} = \begin{bmatrix} (x,x) & (x,a) \\ (a,x) & (a,a) \end{bmatrix} \tag{1.40}$$

We should like to determine the inverse of $\mathbf{A}$ such that $\mathbf{A}^{-1}\mathbf{A}=\mathbf{I}$, where $\mathbf{I}$ is the unity matrix. First, note that

$$\begin{bmatrix} (a,a) & -(x,a) \\ -(a,x) & (x,x) \end{bmatrix} \cdot \begin{bmatrix} (x,x) & (x,a) \\ (a,x) & (a,a) \end{bmatrix} = \frac{p_{0,0}}{p_{0,f}} \cdot \mathbf{I} , \tag{1.41}$$

where the ratio of the initial and final momentum outside of the unity matrix results from Eq. (1.15a). The matrix on the left is similar to the inverse matrix if we divide it by this factor to obtain,

$$\mathbf{A}^{-1} = \frac{p_{0,f}}{p_{0,0}} \begin{bmatrix} (a,a) & -(x,a) \\ -(a,x) & (x,x) \end{bmatrix}. \tag{1.42}$$

The equation of the ellipse at s_f may be expressed by,

$$(\boldsymbol{r}_f)^{\mathrm{T}} \boldsymbol{\sigma}_f \boldsymbol{r}_f = \varepsilon_f = \frac{p_{0,0}}{p_{0,f}} \varepsilon_0, \tag{1.43}$$

where the results from Eq. (1.35) has been applied. If we use (1.39b) to express Eq. (1.38) as,

$$(\boldsymbol{r}_f)^{\mathrm{T}} \left(\left(\mathbf{A}^{-1} \right)^{\mathrm{T}} \boldsymbol{\sigma}_0 \mathbf{A}^{-1} \right) \boldsymbol{r}_f = \varepsilon_0, \tag{1.44}$$

then a direct comparison with (1.43) implies that sigma matrix at s_f may be evaluated from the initial sigma matrix through the transformation,

$$\boldsymbol{\sigma}_f = \frac{p_{0,0}}{p_{0,f}} \left(\mathbf{A}^{-1} \right)^{\mathrm{T}} \boldsymbol{\sigma}_0 \mathbf{A}^{-1}. \tag{1.45}$$

Writing this equation out explicitly for the *x*—*a* subspace, we obtain that

$$\begin{bmatrix} \gamma_{x,f} & \alpha_{x,f} \\ \alpha_{x,f} & \beta_{x,f} \end{bmatrix} = \frac{p_{0,0}}{p_{0,f}} \cdot \frac{p_{0,f}}{p_{0,0}} \begin{bmatrix} (a,a) & -(x,a) \\ -(a,x) & (x,x) \end{bmatrix} \cdot \begin{bmatrix} \gamma_{x,0} & \alpha_{x,0} \\ \alpha_{x,0} & \beta_{x,0} \end{bmatrix} \cdot \frac{p_{0,f}}{p_{0,0}} \begin{bmatrix} (x,x) & (x,a) \\ (a,x) & (a,a) \end{bmatrix}. \tag{1.46}$$

Carrying out the matrix multiplication to obtain the elements of the final sigma matrix in terms of the elements of the map, we obtain the following set of equations:

$$\gamma_{x,f} = \frac{p_{0,f}}{p_{0,0}} \left[\gamma_{x,0} (a,a)^2 - 2\alpha_{x,0} (a,x)(a,a) + \beta_{x,0} (a,x)^2 \right] \tag{1.47a}$$

$$\alpha_{x,f} = \frac{p_{0,f}}{p_{0,0}}\left[-\gamma_{x,0}(x,a)(a,a) + \alpha_{x,0}\left((x,x)(a,a) + (x,a)(a,x)\right) - \beta_{x,0}(x,x)(a,x)\right] \tag{1.47b}$$

$$\beta_{x,f} = \frac{p_{0,f}}{p_{0,0}}\left[\gamma_{x,0}(x,a)^2 - 2\alpha_{x,0}(x,a)(x,x) + \beta_{x,0}(x,x)^2\right] \tag{1.47c}$$

The simplest example of an evolving ellipse under transformations is that of a system where there are no fields, i.e. a drift. If the reference particle undergoes a shift along the optic axis of length, L_0, then the map is simply given by,

$$\mathbf{A}(L_0) = \begin{bmatrix} 1 & L_0 \\ 0 & 1 \end{bmatrix}. \tag{1.48}$$

The spatial envelope within which the beam is bounded is given by x_m. As a function of the drift length, and according to Eq. (1.32) it must take the form

$$x_m(L_0) = \sqrt{\varepsilon_{x,0}\left(\gamma_{x,0}(L_0)^2 - 2\alpha_{x,0}(L_0) + \beta_{x,0}\right)}. \tag{1.49}$$

Also, inserting the matrix values into Eq. (1.47a) will show that the term, $\gamma_{x,f}$, remains constant. An example of this is depicted in Fig. 1.6 where an initially upright ellipse propagates through two drifts of the same length. Notice that the ellipse expands along the x but remains constant along a.

To illustrate the effects that focusing and defocusing elements have on the phase space ellipse a rather complex system of electric quadrupoles is depicted in Fig. 1.7. The optical system extends over a total length, L, and has mirror symmetry about the center

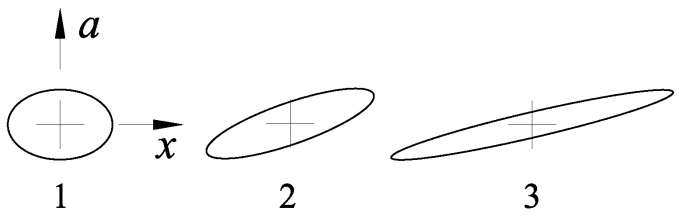

Figure 1.6 The evolution of the x—a phase ellipse through two equivalent drifts.

position, $s=L/2$. Each triplet is also symmetric about its center position, and the fringe field effect for each quad has been accounted for in calculating the maps with COSY.

The beam is assumed to be made of ions of 100 keV with charge state $q=+1$. The

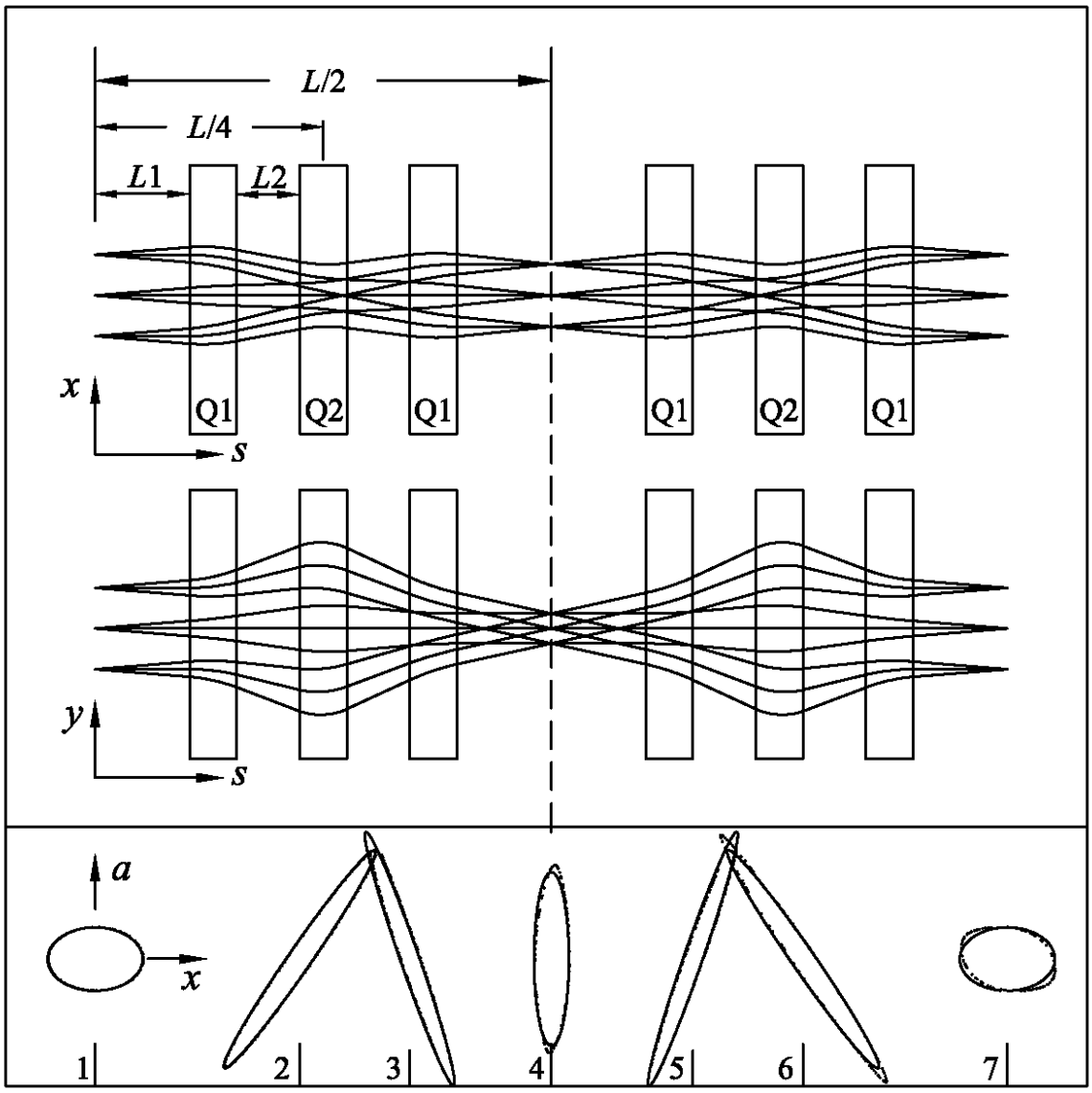

Figure 1.7 Sextet system of total length L made up of electric quadrupoles as described in the text. Plots of the ray trajectories along the x—s and y—s planes are shown in the top two plots, while snap shots of the x—a phase space ellipse are shown for both a first order (line) and a fifth order calculation (dots). Other setting are as follows: quad apertures radius = 2.5 cm, quad length = 15 cm, $L1$ = 30 cm, $L2$ = 20 cm.

trajectory path of the ions along the *x*—*s* and *y*—*s* planes are shown in the top two plots of the figure for quad strengths Q1=–0.74 kV and Q2=1.3 kV, where positive polarity implies a focus along the *x*—plane. A fitting algorithm had been used to find Q1 and Q2 such that the sextet has telescopic focusing in both the *x*—*a* and *y*—*b* planes at the exit. This can be seen by the way each ray coming in parallel at the entrance comes out parallel again at the exit where (*a,x*)=0. Also, rays that are diverting at the entrance converge at the exit, since (*x,a*) also vanishes there.

Only the phase space ellipse of the *x*—*a* plane has been illustrated in the bottom plot. Snap shots of the *x*—*a* phase space ellipse are shown for both a first order (line) and a fifth order calculation (dots) at positions labeled 1 through 7. At *s*=0 the particles all lie along the boundary of the upright ellipse with x_m=4 mm and a_m=2.5 mr. The higher order aberrations cause projections of filaments to form as the particles diverge away from the boundary of first order. This is seen more clearly at positions 4 and 7 in the form of an asymmetric filamentation. This is caused by third and fifth order geometric aberrations, such as (*x,xxx*), (*x,aaa*), (*x,xxxxx*), and so on, which as expected results from elements focusing with electric fields [Wollnik87b]. The effects of the aberrations have been exaggerated by a factor of 20 for illustration purposes.

Some last details in the first order ellipse that are important to notice are the focusing and defocusing effects. The elongation of the ellipse in going from point 2 to point 3 is caused by defocusing of the first quad. The second quad focuses in such a way that the ellipse is "flipped" and the particles are converging afterward. The combination of defocusing and focusing causes the ellipse to become upright at the midpoint of the system (point 4). The final ellipses show some distortion at the extremes. At times

there is some confusion as to whether these types of geometric distortions also cause the bounded phase space area to change. The answer is no, since according to Liouville's theorem the volume of phase space remains constant even though the shape generally will not [Reiser94ab]. Hence, the boundaries of both the first and fifth order calculations remain constant since $p_{0,0}/p_{0,f}=1$, which is a consequence of Liouville's theorem that was pointed out in Appendix A.

1.6.4 The rms emittace and higher order effects

Beam calculations based on phase space dynamics must be carried out using particle ensembles of finite size. An ensemble of particles represents a sample taken from the volume occupied in phase space. To analyze a sample it is necessary to use statistical methods for evaluating the effects from fields. A simple statistical method for evaluating first order properties of the ellipse from rms values is introduced in this section. It is based on the concept of evaluating the rms emittance, $\tilde{\varepsilon}$. Here, it shall be applied only to the x—a subspace, $\tilde{\varepsilon}_x$, but it is easily extendable to the y—b and l—δ subspaces.

The first step in evaluating the properties of the rms emittance is to calculate the following rms values given that there are N particles in the ensemble:

$$< x^2 >= \frac{1}{N}\sum_{i=1}^{N}\left(x_i - < x >\right)^2 \tag{1.50a}$$

$$< a^2 >= \frac{1}{N}\sum_{i=1}^{N}\left(a_i - < a >\right)^2 \tag{1.50b}$$

$$< xa >= \frac{1}{N}\sum_{i=1}^{N}\left(x_i - < x >\right)\left(a_i - < a >\right) \tag{1.50c}$$

The three quantities are considered to be the second moments, while <x> and <a> are the average values, or the first moments along the x— and a—axes, respectively. The corresponding rms emittance is related to the second moments by,

$$\tilde{\varepsilon}_x^{\,2} = < x^2 >< a^2 > - < xa >^2 . \qquad (1.51)$$

This quantity is invariant under linear transformations where there is no acceleration. In cases where there is DC acceleration but the transformation is still linear, the final rms emittance is proportional to the initial by the factor, $p_{0,0} / p_{0,f}$. This is similar to the case of the initial and final emittance as shown by (1.35). In fact, the emittance and the rms emittance are linearly proportional to each other and remain so as long as there are only linear transformations acting on the particles.

The constant of proportionality between $\tilde{\varepsilon}_x$ and ε_x depends on the type of density distribution in phase space that is assumed. To demonstrate how the rms emittance varies with the type of distribution three plots have been generated with differing density distributions and illustrated in Fig. 1.8. Each distribution has an equivalent rms emittance, and an ellipse whose emittance is equivalent to the value of the rms emittance has been drawn for each of the three.

The leftmost distribution is called a boundary type since the particles are randomly distributed along the boundary of an ellipse. It may be generated using the method of spheres in 2 dimensions [Muller59]. The rms emittance value turns out to be one half of the emittance of the ellipse whose boundary is being populated. This is shown by the ellipse, labeled $\varepsilon_x = 2\tilde{\varepsilon}_x$, in the first plot. A waterbag-type distribution, generated by using the method of spheres [Lewis75], is shown at center and has only about 22% within the ellipse of rms emittance, while the Gaussian-type, on the right, has 68%. Both

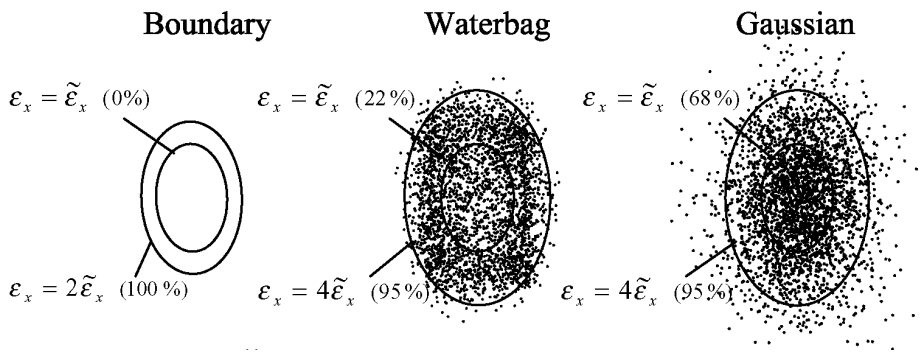

Figure 1.8 Plots of three differing phase space distributions with equivalent rms emittance. The type of distribution is labeled above each plot and at the left side of each plot is the percentage of particles lying within the corresponding ellipse of emittance ε_x.

waterbag and Gaussian distributions contain 95% of the particles within an ellipse of $\varepsilon_x = 4\tilde{\varepsilon}_x$.

The boundary-type distribution is useful for looking closely at higher order effects since it samples the extremities of the phase space. Such use was demonstrated above with the *x*—*a* phase space plots at the bottom of Fig. 1.7. The waterbag-type distribution, which is just an extension of the method of spheres to 6D, is an almost uniform distribution. Although, it does tend to form a low-density pocket towards the center of the ellipse, the ease in generating the waterbag distribution makes it an attractive option for many applications. The Gaussian-type distribution is one that best describes many experimentally observed beams and is ideal to use for more precise calculations. A method prescribed by Box is used to generate the random distribution of this type [Box58].

Once the rms emittance has been evaluated, the rms emittance may be divided out of each of the values in (1.50) to evaluate the Twiss parameters by the following:

$$\beta_x = \frac{< x^2 >}{\widetilde{\varepsilon}_x} \tag{1.52a}$$

$$\gamma_x = \frac{< a^2 >}{\widetilde{\varepsilon}_x} \tag{1.52b}$$

$$\alpha_x = -\frac{< xa >}{\widetilde{\varepsilon}_x} \tag{1.52c}$$

Solving for $<x^2>$, $< a^2>$ and $< xa>$ from the above equations and inserting the results into (1.51) proves that this results is true. The negative sign in (1.52c) keeps the tilt orientation consistent with Fig. 1.5.

Something that that should be kept in mind when applying higher order effects is that the rms emittance may grow even though the actual emittance remains constant. This is due to the fact that the rms values are very sensitive to particles that may form outside the first order ellipse boundary. This can become especially troublesome for repetitive systems, such as storage rings, where very low-density halos may form around a high density region. Despite this fact, the rms method remains an invaluable tool for evaluating beam systems. It offers reliable first order knowledge of the ellipse orientation, which is useful in matching one optical system to another.

Chapter 2

DESIGN OF AN ISOBAR SEPARATOR USING AXIALLY SYMMETRIC ELEMENTS WITH ACCELERATION

In this chapter we describe the design of a high resolution mass separator that uses accelerating axially symmetric elements so that the system is an achromat. The RIA facility will need exceptionally high mass resolution to separate masses at the level of isobar mass differences. A brief description of other types of mass separators will be given along with reasons for choosing a spectrometer with a decelerating column, which we call a dual-potential spectrometer. Much of the chapter will be devoted to details of this spectrometer along with the factors that affect its performance.

2.1 Isobaric purity and mass separators

Much of the success of future rare isotope facilities depends not only on the intensity of the isobar of interest, but also on the purity of the beam. Isobars have very small mass differences, and beams coming from ISOL targets will be susceptible to cross contamination by other ions of similar mass to charge ratio or ions of some energy that may cause a contaminant to cross over into the region of others. Furthermore, for isobars far from the line of stability there will be tails from other more intense ion species that will also cross over. To make matters more complicated, the mass window will have to be large enough such that transmission of the wanted ions species is maximized. Under these stringent conditions one is many times forced to speak of mass separator devices in terms of the level of purification from contaminants, as we shall do so in a later section.

We shall explore the feasibility of high mass resolution separators with high transmission for the RIA facility. High transmission with a resolution of $m/\Delta m$=20,000 is the base line goal for the present study. This resolution corresponds to a mass excess difference of 5 MeV at mass A=100.

Other methods exist as possible alternatives to the scheme that will be presented in the next section and a brief discussion should be devoted to them. For many chemical elements for which the ionization potential is low enough, there is the possibility of using laser resonance ionization techniques to obtain high chemical selectivity [Alkhazov89] [Koester02]. This is an ideal way to suppress isobars that have differing chemical properties from the species of interest. The efficiency is usually between 1 and 7% and is mostly limited to elements with of ionization potentials <7 eV. Alternatively, using surface ionization can be almost 100% efficient for ionization potentials of less than ~5eV. This method is limited to about one tenth of the entire spectrum of elements [HagebØ92]. A combination of these techniques and other more general ionization techniques having less selective ionization have to be employed to extend the amount of available beams. Consequently, it is helpful to shift the mass selectivity to devices lying beyond the ionization region.

Magnetic sectors provide spatial separation between masses and have been the heart of most isotope separators for several decades [Smythe34]. One limitation stems from increasing higher order aberration effects in going to larger acceptance sector magnets. Other limitations stem from the fact that all ion sources impose some level of energy spread on the beam and also from instabilities of the power supplies. The effects, which appear as smearing and chaotic shifts of the spectrum, will be magnified along with the

resolution. The most fundamental problems, however, are still the energy dispersion and geometric aberrations. Reducing geometric aberrations will require strategic superposition of multipole fields, and energy dispersion must be eliminated designing a spectrometer that is achromatic.

Cyclotrons carry some degree of achromicity by using RF electric fields and have been used for mass selection. By extending the number of turns before extraction, they have been known to give a mass resolution of as high as ~10^4 [Huyse95] [Chartier97]. One of the drawbacks is that the transmission efficiencies turn out to be rather low (3 to 5%). Furthermore, the output energy range of cyclotrons is limited and some experiments may require that ions arrive at the slowest velocities possible, such some in nuclear astrophysics.

Another type of RF device that offers a similar type of mass dispersion but without the longitudinal acceleration is the quadrupole mass separator (QMS). They are especially appealing since they do not require magnetostatic fields, which allows over all system dimensions relatively minute in comparison. Unfortunately, some of the best QMS designs to date have been know to achieve resolutions of no better than about 300 under DC beam operation. Studies that focus on improving QMS performance seem to indicate that the distorted fringing fields at from the ends of the rods introduce aberrations that effectively increase both the transverse and longitudinal emittance of the beam [Takebe95]. Such effects also cause the overall acceptance and transmission to suffer. Some of these distortions may be eliminated by refining the rod design and alignment; however, a recent study shows that the rod design requires at least a 1 μm position accuracy to approach a mass resolution of ~2000 [Yoshinari95]. Despite such

improvements much work still remains to improve the acceptance, thus such devices remain impractical for isobar separation.

Considering such technical dilemmas with the other types of devices, the use of single-pass magnetic bends remains the best alternative. By coupling magnetic dipole systems with DC electric field devices, it is possible to compensate for energy spread effects. There will still exist a multitude of technical barriers to eliminate in going with magnetic sectors. For example, the uniformity of the fields has to be maintained to a high level. We shall explore this problem with the use of a Poisson solver to determine the fields that should be expected from some of the sector designs. Issues concerning control and stability must also be addressed, since the object and image sizes are necessarily small.

The design goal of the isobar separator described below are a mass resolving power of at least 20,000 given a transverse emittance of 10π mm-mr for ions at 100 keV/250 amu (1 mm entrance slit width and ±20 mr maximum divergence) and a ±10 eV energy spread.

2.2 Achromatic mass separators

As mentioned in the previous section, when considering mass separators at the level of isobar mass differences it is necessary to include the effect of the beam energy spread from the ion source. It is possible to obtain some energy spread due to the ripple of the ion source power supplies; however, the voltage ripple from modern power supplies can be suppressed to about the 10^{-5} level. Instabilities of the source platform potential have been known to be caused by the driver beam as it is injected in the form of intense pulses into the target, but this should not be a problem with the RIA driver since it functions

essentially in continuous wave (cw) mode. The most probable cause of energy spread is the thermal energy spread associated with plasma type ion sources. Many low charge state plasma sources can impose energy spreads that are on the order of ~10 eV. Thus, considering a spread in the energy at the 10^{-4} level will be necessary. Magnetic sectors disperse the ions according to magnetic rigidity, $\chi_M=p/qe$, thus the mass and energy dispersion are equivalent; i.e.

$$(x,\delta_m)=(x,\delta_K) \tag{2.1}$$

Because of this additional dispersion in energy the resolution of the spectrometer will suffer unless the (x,δ_K) can be eliminated.

The principle of an achromatic mass separator can be understood in terms of the first order transport map in matrix form. Consider the position variable in the horizontal plane, x and a, in a subspace that also includes the mass and energy variables, δ_m and δ_K, respectively. If we consider the position vector (x,a,δ_m,δ_K), then the transfer map can be expressed as,

$$\mathbf{A}=\begin{bmatrix} (x,x) & (x,a) & (x,\delta_K) & (x,\delta_m) \\ (a,x) & (a,a) & (a,\delta_K) & (a,\delta_m) \\ (\delta_K,x) & (\delta_K,a) & (\delta_K,\delta_K) & (\delta_K,\delta_m) \\ (\delta_m,x) & (\delta_m,a) & (\delta_m,\delta_K) & (\delta_m,\delta_m) \end{bmatrix} \tag{2.2}$$

which yields the final position vector when we take its product with the initial position vector. This subspace is sufficient to consider as long as mid-plane symmetry is preserved. Formally, an achromatic system should have no energy effects whatsoever; however, here we are only considering a first order achromat in which (x,δ_K) vanishes. Higher order achromats require that higher order aberrations with δ_K dependence also vanish. Also, note that if the term (a,δ_K) does not vanish, then particles gain angular

divergence from the energy differences. This is not acceptable if the particles are to continue on through further beam system, such as the post accelerator. A *fully achromatic* system must have both terms vanishing.

2.2.1 Double-focusing spectrometer

We look first at the properties of a double-focusing mass separator [Yavor97a] like the one illustrated in Fig. 2.1. Note that there are other ways to arrange the magnetic and electric fields to obtain the similar properties of this system [Nolen84]; however, we use this particular one for its simplicity. With this system we can evaluate the map of the magnetic and electric fields, $\mathbf{A}_B$ and $\mathbf{A}_E$, respectively, in separate form. The product of the two,

$$\mathbf{A} = \mathbf{A}_E \cdot \mathbf{A}_B, \tag{2.3}$$

yields the map of the total system. Imposing point-to-point horizontal focusing at B and C results in the energy dispersion term

$$(x, \delta_K) = (x, x)_E (x, \delta_K)_B + (x, \delta_K)_E \tag{2.4}.$$

Requiring that this term vanish implies that rays of different energy will get refocused at C as illustrated by the figure.

Note that for the system shown in the figure the term (a, δ_K) does not vanish, and rays of different energy are converging as they approach the focal plane and will diverge right

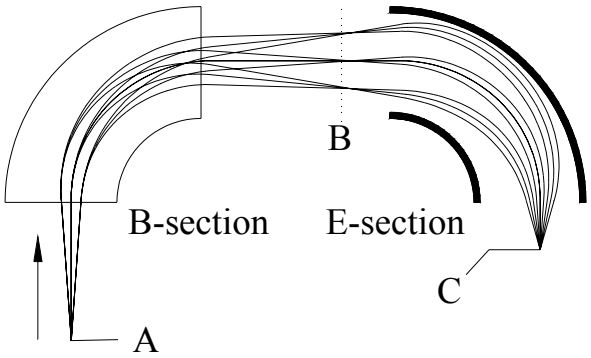

Figure 2.1 Double-focusing spectrometer with rays of multiple divergence as well as multiple energies. Rays are focused in the horizontal plane but split by varying energy at point B.

after. This is only a simple illustration of an achromat, but there actually exist solutions in which systems with magnetic and electric sectors in tandem form a fully achromatic mass separator. One such design has been previously introduced for the RIA system as a possible candidate for an isobar separator [Davids94]. Studies of the performance of previously constructed designs using large dipoles but at lower resolution has been discussed elsewhere [Davids89] [Davids92].

Although such designs are conceptually sound, there are some technical difficulties with very large electric sectors. Small mutual vertical inclinations along the surfaces of any pair of electrodes tend to misalign the beam from the mid-plane and will give so called "parallelogram-type" defocusing [Yavor97b]. This effect has been known to cause severe losses in the resolving power [Matsuda77]. In principle, small corrections can be made on the electrodes to obtain a more uniform field without misalignments; however, there are inherent technical difficulties when working with electrodes at high potential.

2.2.2 Dual-potential spectrometer

To avoid the effects of electrostatic condensers another method of energy focusing was devised which uses at least two stages of magnetic separation at different potentials [Ciavola97]. So-called dual-potential spectrometers have been used in the past for the purpose of eliminating unwanted scattered particles, but they were not achromatic [Wollnik95]. The present design is a dual–potential achromat with a layout illustrated in Fig. 2.2.

The system is broken down into four sections. The beam enters section H (points A-C) at K_H=100 keV and thereafter is decelerated through an immersion lens system at section I (from C to D). The third stage (points D-F) lies at a 90 kV potential on an

isolated platform so that the beam drops in energy to K_L=10 keV. The potential may vary as long as the ratio of the initial to final kinetic energies remains constant at K_H/K_L=10. The radius of the magnetic sectors in section H (labeled DH) are R_H=2.5 m, while those of section L (labeled DL) are just $R_H/\sqrt{10}$. This scales with the rigidity to keep all the pole tip field strengths at the same value. All sectors bend through an angle of 60º. The DH sectors have positive entrance and exit edge angles of 24º. Those of the DL sectors are slightly lower at 23º for both entrance and exit. Finally, the last section is simply the reverse of section I and accelerates the beam back to K_H as the beam exits the isolated platform.

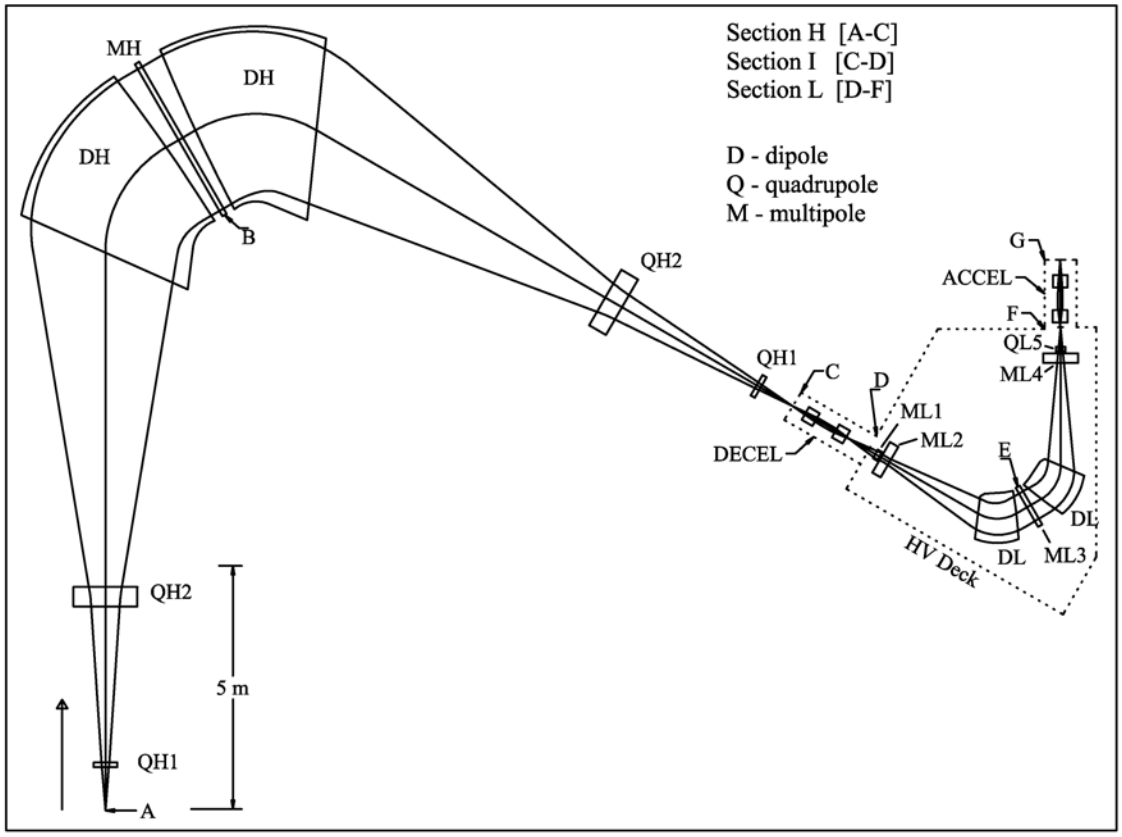

Figure 2.2. Layout of dual-potential spectrometer. The spectrometer is broken down into 4 sections as described in the text [Portillo01a]. Overall footprint is 20m x 30 m.

Magnetic multipole fields are imposed at the midpoint of both sections H and L (MH and ML3, respectively). The multipole MH provides quadrupole, hexapole, octupole, decapole, and duodecapole fields for correcting geometric and fringing field induced aberrations at section H to 5th order. Multipole ML3 also contains up to duodecapole fields in order to correct the aberrations of section L, as well as the aberrations imposed by the immersion lenses. The remaining multipoles at section L (ML1, ML2, and ML4) are imposed for correcting higher order chromatic aberrations up to 5th order. The effects of the higher order multipoles are explained in the next section.

First order calculations of the map were used to obtain telescopic focusing at points C, D, F, and G.. Thus, the terms (x,a), (a,x), (y,b), and (b,y) all vanish simultaneously for the map at these points. Fringe field effects are always accounted for since they have an effect on the value of these terms.

The first order transfer maps for the first three sections can be evaluated and their matrix product,

$$\mathbf{A} = \mathbf{A}_L \cdot \mathbf{A}_I \cdot \mathbf{A}_H, \tag{2.5}$$

gives the transfer map from point A to point F. The resulting energy and mass dispersion terms are then

$$(x,\delta_K) = (x,\delta_K)_L(\delta_K,\delta_K)_I - (x,x)_I(x,\delta_K)_H \tag{2.6}$$

and

$$(x,\delta_m) = (x,\delta_m)_L - (x,x)_I(x,\delta_m)_H, \tag{2.7}$$

respectively. In arriving at these results we have used $(x,x)_H = (x,x)_L = -1$ for the magnification of the mirror symmetric bend sections. The first-order result of the layout gives the net energy dispersion $(x,\delta_K)=0$. After optimization the symmetry and telescopic focus of both Section H and L causes (a,δ_K) to vanish at each, and therefore, in the entire

system to obtain a full achromat. The telescopic focus tends to make the envelope sizes very insensitive to the detail of the initial beam ellipse.

The rest of the optics may be understood if Eq. (2.1) is applied to Eq. (2.6) to obtain that

$$\frac{K_L}{K_H} = 1/(\delta_K, \delta_K)_I = \frac{(x, \delta_m)_L}{(x, \delta_m)_H (x, x)_I}. \tag{2.8}$$

Combining this with Eq. (2.7) we can obtain a value for the expected ratio between the separation at point C to that of point F,

$$\frac{(x, \delta_m)_H (x, x)}{(x, \delta_m)(x, x)_H} = 1 - \frac{K_L}{K_H}. \tag{2.9}$$

This factor implies that there is a loss in separation as K_L becomes approaches K_H. If K_L=K_H then there is no net separation due to mass at the exit of the spectrometer. In principal as long as K_L is much smaller than K_H, then only a small amount of mass separation is actually lost.

As shown by Eq. (1.35), the emittance will grow as K_L is lowered which sets limits on the acceptance of section L. Also, there are limits on how high a potential can be imposed on the ion source platform, thus limiting the kinetic energy, K_H. The parameters adopted for this system imply that we should expect about a 10% loss in mass separation. This loss, however, is outweighed by the gain in resolution that results from getting rid of the energy spread effect. Fig. 2.3 illustrates this point, where a series of *x*—*a* phase space distribution plots is shown. Three sets of ensembles with masses m-Δm, m, and m+Δm enter the spectrometer with the same boundary-types phase space distributions. The respective masses in terms of the relative particle coordinate, δ_m, are –Δ, 0, and +Δ, where Δ =1/20,700. We have assumed that the beam enters the spectrometer with an

aspect ratio of y_m/x_m=8 so that the beam has a 1 mm full width along the x—axis and divergence lying between the limits of a_m=±20 mr. In the y—phase space the initial beam has ±4 mm by ±2.5 mr. Such beams are obtainable by the use of quadrupole multiplets prior to the object slits as described in the literature [Wollnik91].

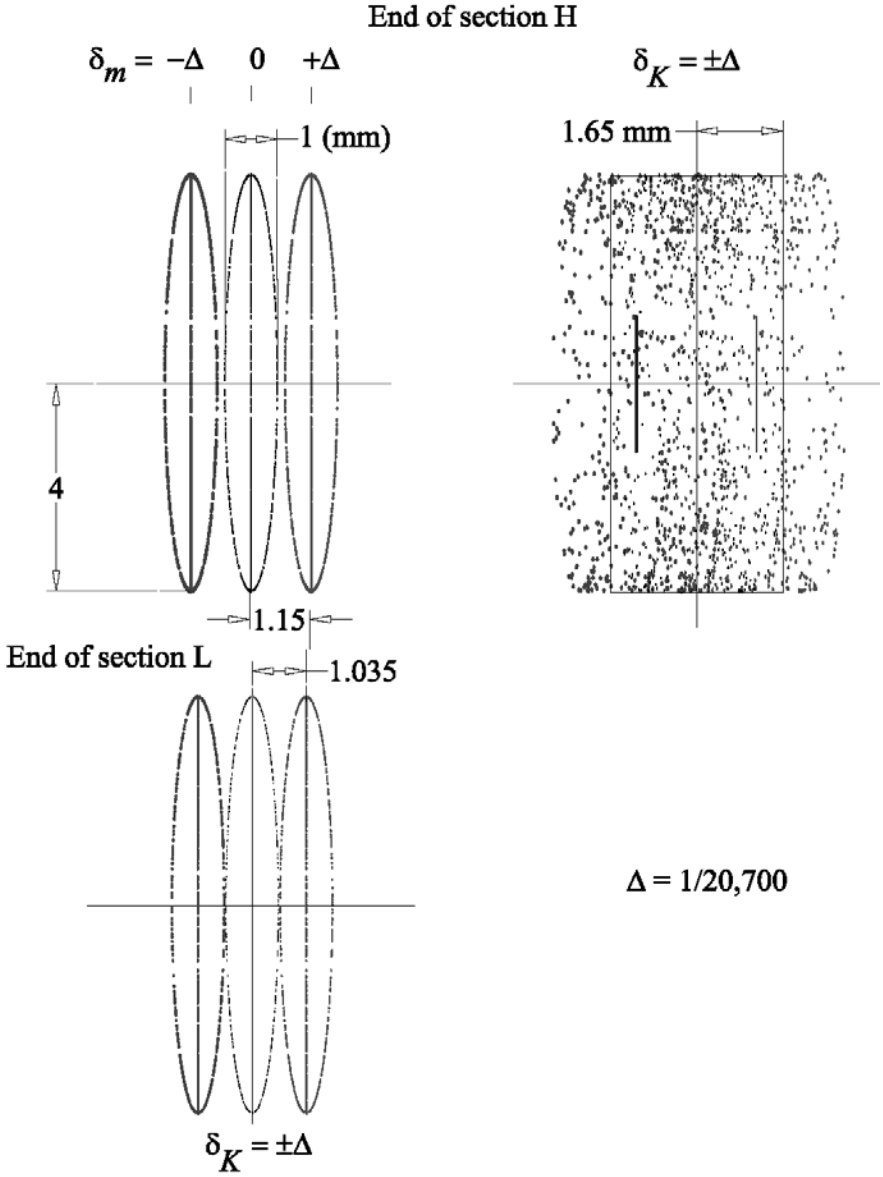

Figure 2.3 Mass spectra in x—a phase space for three masses of similar boundary-type initial distributions. Going from the top-left to top-right plot shows the effect on the mass spectrum at the end of section H when adding a random energy spread that lies between δ_K=-Δ and +Δ. The dual-potential separation results in the spectrum taken at the end of section L, which shows the effect of the achromatic correction.

The two adjacent plots at the top of Fig. 2.3 are snap shots of the phase space at the exit of section H. In the top-left plot all particles have the same energy; i.e. δ_K=0 for each particle. In the top-right plot there has been a random distribution of energies imposed on all particles, such that energies lie between δ_K=-Δ and +Δ. The mass and energy dispersion at the end of section H are $(x,\delta_K)_H$=$(x,\delta_m)_H$=23,000 mm, and it is obvious that the energy distribution of the particles has a destructive effect on the resolution. The particles of one mass will overlap the adjacent one by a maximum of 0.65 mm.

The plot at the bottom-left is a snap shot of the distribution at the exit of section L. The particles still have the energy distribution imposed; however, the achromatic condition that results by the dual-potential scheme has eliminated the energy dispersion. Comparing this plot with the plot right above it, we see that the separation is smaller by 10%, such that the resulting mass resolution is $m/\Delta m$=20,700.

To determine the size of the apertures for all the elements along the beam transport line it is helpful to plot the beam envelope, or the maximum extent of the beam along the transverse plane. A series of these plots are illustrated in Fig. 2.4 in which the *s*-axis is projected as a straight line. Fig. 2.4(a) is a plot of the rays along the *s*—*y* plane. The rays are defined such that their initial positions start from the limits of the *y*—*b* phase space. This is also done for rays along the *s*—*x* plane in Fig. 2.4(b); however, for this plot it seems that there are only rays of divergence from a point source. This is because the rays that extend over position cannot be seen on the scale of the huge beam projections along *x* resulting from the divergence of the beam. The elements are represented by the size of the aperture of the corresponding elements. In the case of the sector magnets the ends represent the gap between the pole tips.

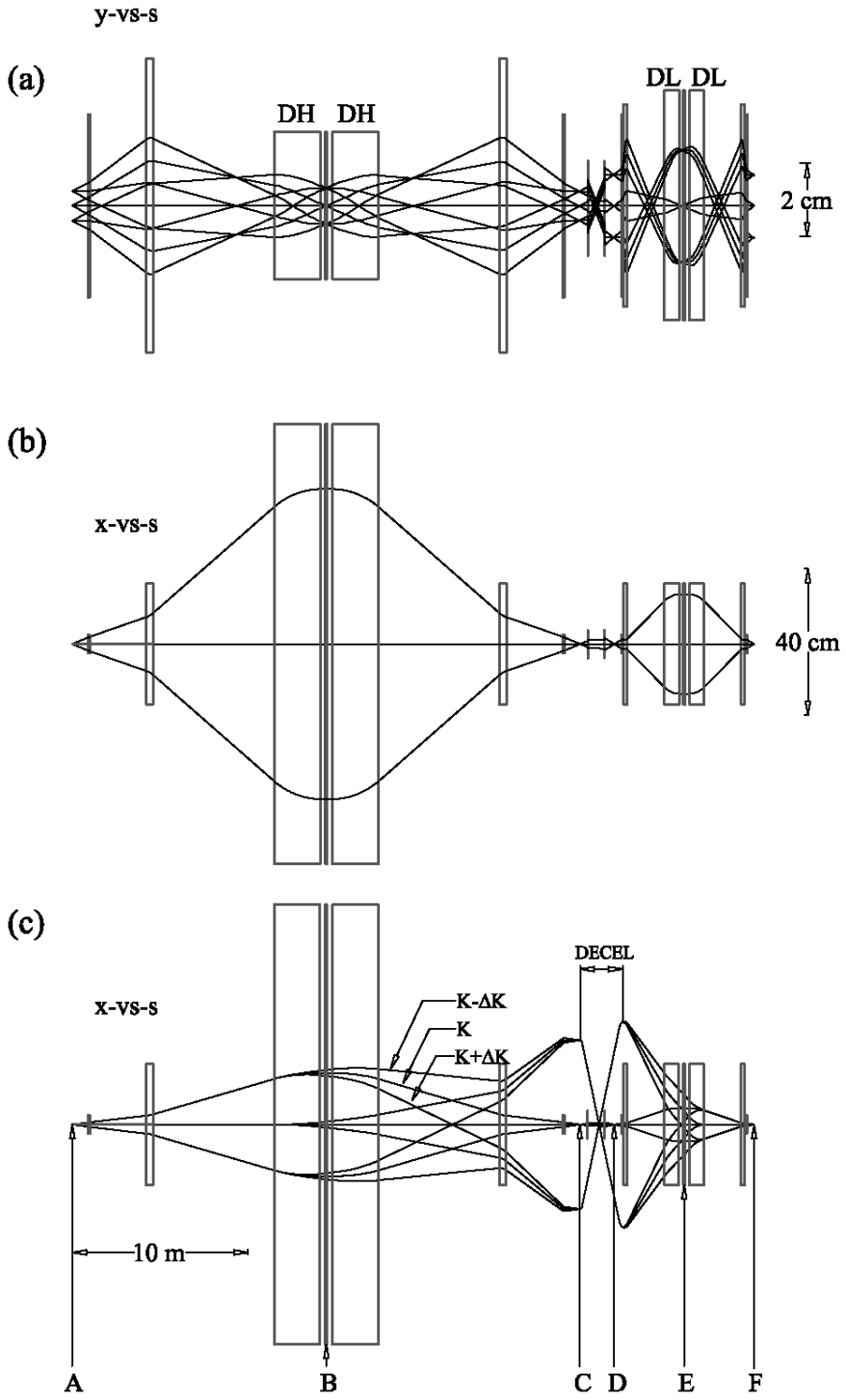

Figure 2.4. Beam envelopes for the dual-potential spectrometer in the horizontal and vertical planes. Plots are illustrated for the *s*—*y* (a) and *s*—*x* (b) planes for the effects of the transverse phase space on the rays. The last plot illustrates the effect of energy dispersion along *x*.

There are some features with special significance that should be pointed out. The

integrated area under the x versus s curve within the dipole region is proportional to the mass resolution [Wollnik71]; hence, the x envelope is maximized in the dipole regions.

The y envelope has been kept to a minimum throughout, which is the reason for choosing an initial beam aspect ratio of y_m/x_m=8. Part of the reason for having this is to minimize the gap each dipoles to a minimum. Also, the cross term aberrations between the x—a and y—b planes at the multipole regions are reduced by a factor proportional to the ratio between of x over y. These terms will cause a correction in one plane to cause a distortion in the other [Yavor97a], thus it is critical that this ratio be sufficiently large. The ratio has been kept at x_m/y_m=86 between at multiple MH and is 9.2 at multipole ML3. A combination of an increase in emittance in section L and the smaller x envelope is what cause this ratio at ML3 to be almost an order of magnitude lower than at MH.

The plot in Fig. 2.4(c) represents the energy dispersion. Both divergence and dispersion along the s—x plane are plotted for rays of varying divergence and energies starting from a point source at A. Notice that the rays of different energies converge back to the same position and direction as they exit the second dipole DL, showing that the overall system is fully achromatic. From this plot we can estimate the maximum extent of each ray of energy varying from that of the reference particle. The energy differences are actually exaggerated by a factor of 10 for illustration purposes.

2.3 Correcting higher order aberrations

A considerable amount of effort has gone into determining higher order aberrations and suppressing them with multipole fields. For determining the effects of higher order aberrations the COSY INFINITY code system was employed to calculate maps of up to 5th order.

The fact that one can evaluate maps to arbitrary order is only one of the reasons for choosing COSY. The code also allows the user to implement custom algorithms that simulate other optical elements that are not in its own library. For this study it was necessary to implement algorithms that calculate maps of some axially symmetric structures that impose DC acceleration, such as those of immersion lenses. In the case of an immersion lens, we simulate the potential for a simple gap lying between two tubes of equal radii and of differing potentials [Geraci02]. Going to arbitrary order is particularly important in the case of axially symmetric lenses, since their focusing strength comes solely from fringing fields and, in the case of immersion lenses, the emittance can change according to (1.35). The effects of higher order aberrations are potentially high and having access to arbitrary order evaluations is useful in obtaining an accurate analysis of a spectrometer that requires exceptional detail. Using map-based optics enables more rapid system optimization

2.3.1 Aberrations at magnetic sector sections

Any optical system has geometric aberrations even when fringe field effects are not considered [Wollnik87c]. For a magnetic sector of large radius and large beam entrance

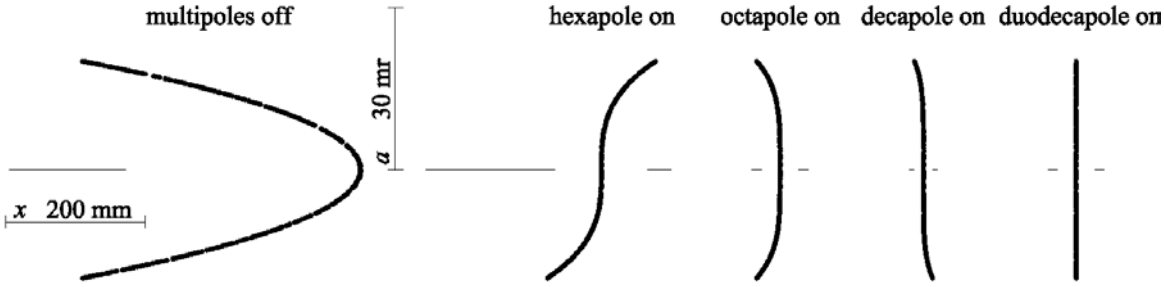

Figure 2.5 Effect of applying each successive multipole field on the x—a phase space plot calculated to 5th order at the end of section H. The effects from the y—phase space are included.

angle of inclination aberrations can be especially large if not corrected. The plot of the *x*—*a* phase space at the very left of Fig. 2.5, illustrates this. The snap shots for all the plots in the figure are taken at the end of section H under successive application of magnetic multipole fields at MH (see Fig. 2.2). These are all 5th order calculations.

The second order aberration clearly dominates before it is suppressed by a magnetic hexapole field, as is done for the plot labeled as hexapole from above. For each successive *n*th multipole that is turned on, the (*n*+1) order aberration appears to dominate and requires that the next order multipole field be applied.

The field strength used for each multipole is approximately proportional to the maximum extent of the distortion along the *x*—axis, starting with a 10 G/cm field strength for the hexapole. We have assumed that the field comes from a circular multipole having an aperture with 60 cm radius. In practice, a rectangular multipole that more closely matches the beam envelope at position B will be used.

Besides the use of discrete multipoles, it is also possible to correct higher order aberrations by shaping the edges of the dipole magnet. We have already imposed an edge angle for first order focusing, but in addition the edges could be rounded relative to this edge as is shown for the sector illustrated in Fig. 2.6. The first shape to notice is the sector with no edge angles or curvature, labeled as simple sector. Then equivalent positive edge angles are imposed at both the entrance and exit sides. Finally, a circular curved shape is carved out from the exit side relative to the tilted edge. The rounded edge should be at the side where the beam is largest in the horizontal plane. According to Fig. 2.2 this has to be at the inside edges of the mirror symmetric dipole pairs. In order to correct the second order geometric aberration of (x,aa)=-134 m/rad^2 at section H requires

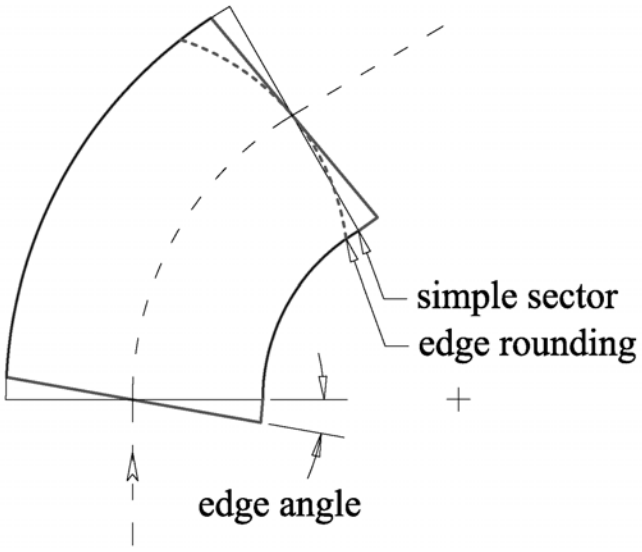

Figure 2.6 Top view of a magnetic sector in which positive edge angles have been imposed at both entrance and exit positions. In addition, a round curvature shape (small dashes) has been cut out at the exit to correct the second order aberration. The simple sector (thin line) is that of the sector before edge angles and curved edges are imposed.

a round curvature with radius of 37 m. This curvature is barely visible from Fig. 2.2. On the other hand, Section L requires one with a radius of 9.6 m to correct its second order aberration.

The rounding of the edges tends to also correct other higher order terms. COSY allows the user to specify any edge shape. In principle, this option can be used to search for a shape that will suppress all higher order aberrations; however, the effects due to fringing at the edges should probably be looked at in more detail before assuming that this scheme will work in the real situation. This is because the effects on field uniformity due to magnetic saturation may cause additional aberration effects for such a wide pole tip. This topic is addressed in the next subsection.

Before going on, we should make some mention of the effect of the multipole fields on other aberration terms. The on and off condition that the correcting hexapole field has on the *y*—*b* phase space is shown by the two plots in Fig. 2.7. The smearing seen at the boundaries is caused by the cross term (*y,ab*), which is suppressed by the hexapole field.

On the other hand, the cross term (*x,bb*) actually by about 0.3% aberration, which is not very noticeable from the plots. Compared to the (*x,aa*), (*x,aaa*), and (*x,aaaa*) aberrations most other aberrations are negligible in comparison and the corrective action on the resolution of such terms evidently outweighs any growth of other terms. In the section that follows, however, we will show that the combination of all aberrations set a limit on how fine the resolution can actually become.

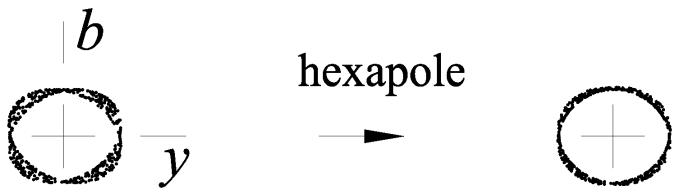

Figure 2.7 Effect of turning on the hexapole field correction on the *y—b* phase space at the end of section H.

2.3.2 Obtaining homogeneous sector fields

Up until now we have assumed that the fields of any dipole are perfectly homogeneous. This would seem to be somewhat of a reasonable assumption considering that the required flux density at the pole tip at each sector magnet is only 3 kGauss; however, perfectly homogeneous fields cannot be achieved in practice. Preliminary magnet design calculations have been done to illustrate the sensitivity of the resolving power to the field shapes. We have chosen to use the POISSON code system to determine the field distribution along the *x—y* plane based on a multipole harmonic analysis [Warren87]. An algorithm in COSY that allows the user to specify the field distribution then calculated the map.

A preliminary cross section of the DH dipoles is assumed. Results of the 2D calculations using POISSON are shown in Fig 2.8 in the form of field distributions. The figure contains a diagram of the first quadrant of two H-type magnets along with the

fields predicted by the calculation. The permeability tables used are those that are listed in the code for a type 1010 steel. A fit was used to determine the amount of current necessary to obtain 3 kGauss at the center point. It is based on the assumption of a uniform electrical current flowing through cross section of the coil region. The area occupied by the coil is constant for all simulations as its horizontal width is decreased and the height is increased. The pole half-gap stays constant at 5 cm, but the groove in which the coil is set into varies in depth from 0 (Fig. 2.8(a)) to 4 cm (Fig. 2.8(a)). The thickness in steel between the top of the coil and the top of the magnet is kept constant to keep flux in that region constant. Hence, any depth in the coil groove will require a thickening of the top portion of the magnet, which increases the total weight of the sector. For example, for zero depth the 60º sector will require 7900 kilograms of steel, while at a

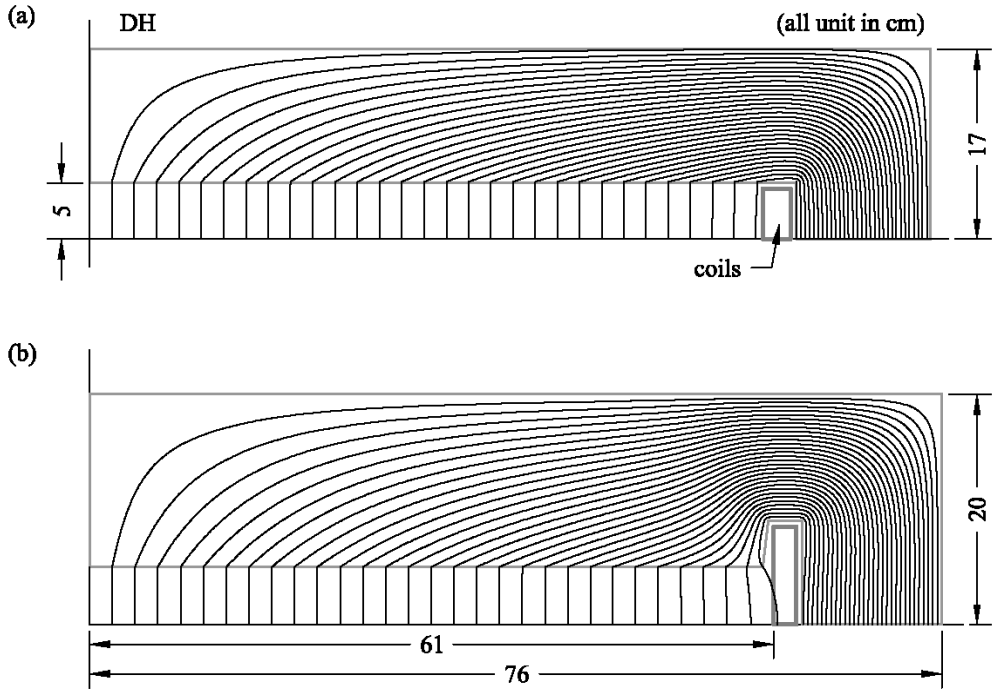

Figure 2.8 Diagram showing the lines of magnetic flux for the design of the DH sector of section H. The beam occupies a region that extends up to 43 cm in the horizontal.

4 cm depth the amount of steel gets up to 10,100 kilograms at 4 cm.

The purpose of this exercise is to attempt to reduce the increase in field strength as we reach the region of the coil. Fig. 2.9 illustrates this point where we have plotted the field strength of the *y*-component of the B-field as a function of the distance from the center of the dipole. For the dipole with no groove we observe that the field rises continuously until we reach the coil. As we make the groove deeper we see that the field is suppressed sooner as we go out in *x*. This operation will also reduce the maximum field strength to a value that is about 2% larger than at the center where x_m=48 cm. According to Fig. 2.4 the beam is only expected to reach as far as x_m=43 cm. At that position there is comparatively little improvement by making any kind of adjustment at the coil.

The next step is to determine the effects on the aberrations resulting at the map if we

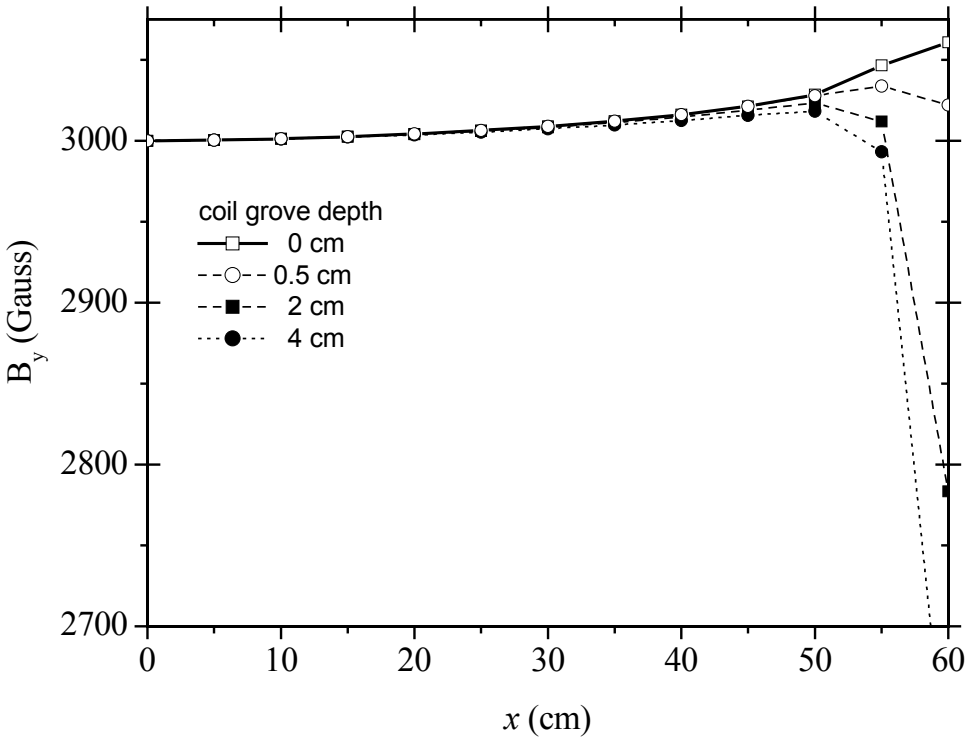

Figure 2.9 Plots of the *y*—component of the B-field versus the *x*—position from the center of the DH sector. The shape H-magnet is varied in depth in an attempt to make the distribution more uniform.

apply the distribution for the dipole having the 4 cm groove. With all multipoles at MH turned off, we calculate the map to 5th order at the exit of section H and evaluate the phase space. The results may be compared against those of the homogeneous dipole by observing the plot of the *x—a* phase space in Fig. 2.10. The inhomogeneous sector ends up having all aberrations being almost 4 times stronger than those of the homogeneous sector. This implies that even very small deviations from a homogeneous condition will cause larger higher order effects. Henceforth, will be necessary to apply field corrections by surface coils along the top and bottom poles. These types of corrections have been used for various applications in the past with and show promising results [Wollnik72] [Wollnik87e]. Since correction coils are more effective at imposing uniformity, there is no need to go with the 4 cm groove H-magnet. This also serves to reduce the cost of the magnets according to the scheme used above.

What is important at this point is that at least we have an idea of what type of field distribution to expect and the effects on the mass resolution. The challenge will be in providing a field that will have an integral uniformity with deviations in the field of

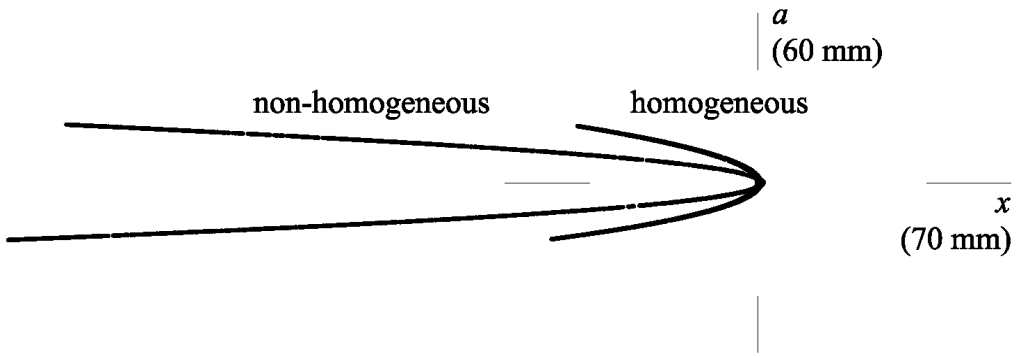

Figure 2.10 Plot of the *x—a* for a 5th order calculation of a magnetic sector with homogeneous field distribution and another with the field distribution predicted by POISSON.

$\Delta B/B \leq 10^{-5}$. Also, it may be very useful to use types of steel that have higher permeability in the range of field strengths needed for more uniformity. The quality of the steel must be high to minimize fine structure in the field as well as the global effects discussed above.

The design of the DL sectors has been considered as well. In Fig. 2.11 we show the cross section of a dipole having a 6 cm gap and a horizontal region that extends between +/-50 cm for the beam. The beam extends a maximum of about 16 cm in the horizontal and less than 3 cm in vertically. There are non-uniformities visible by the lines of flux in the region close to the coils. Imposing a greater degree of uniformity will require the application of surface coils as in the case of the DH sectors.

Before going on, it should be mentioned that there are other methods used to obtain wide homogeneous fields. For example, the so-called Purcell filter [Purcell55] requires a separation between a pole tip and the magnet yoke obtain more uniformity. Another

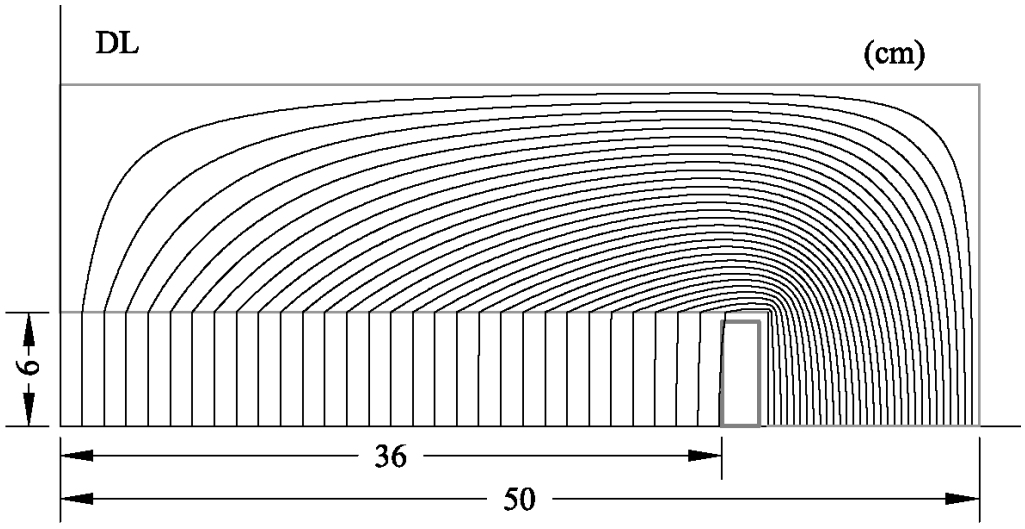

Figure 2.11 Diagram showing the lines of magnetic flux for the design of the DL sector of section L. The beam is expected to occupy a region that extends up to about 16 cm in the horizontal.

method suggested by Halback is to introduce vertical slots in the steel to improve the field uniformity [Nolen87]. Although these other methods may be used, surface coils may still be implemented to permit fine tuning. Furthermore, surface coils can make up for field strength dependent effects that other methods lack in.

2.3.3 The deceleration column

Some of the dynamics that are predicted by the calculations for the deceleration column in Section I are explained here. For the map it is essential to determine terms such as (δ_K, δ_K) and $(x,x)_I$ in Eqs. (2.6) and (2.7). The derivation of those equations relies on the assumption that $(x,a)_I = 0$, and must be a condition that is imposed in the optimization of the parameters. For good beam stability we also require telescopic focusing of this section, such that $(a,x)_I$ vanishes simultaneously. Since potentially large sources of higher order geometric aberrations may actually derive from the deceleration column, then we examine the magnitude of the higher order terms.

It will be shown that it is possible to determine some aberration terms from the results of ray tracing. This will be done from the initial and final positions given by the ray trance result. We do this for the purpose of comparing the ray trance and map results with some amount of detail, keeping in mind that it is more efficient to determining the aberrations from the map-based approach. Modifications to the COSY code have been implemented in order to calculate the map elements of single or multiple gap structures of axial symmetry. COSY uses the potential, V(r,s), to determine the matrix elements via integration of the equations of motions as described in Chapter 1.

Two methods exist for determining the potential. The first method relies on the fact that a system with axial symmetry allows the potential distribution, V(r,s), to be

determined from the derivatives of the potential distribution along the *s*—axis (*r*=0) [Reiser94b]. An analytical form of on-axis potential may be obtained from models based on measurements as described in the literature [Hsi-men86]. One disadvantage is that the analytical expression of V(0,*s*) is usually an approximation whose errors become amplified as one evaluates higher and higher derivatives. Hence, one has to be extra careful in calculating the higher order aberrations from approximate on-axis functions. Another problem is that the parameters that can be specified with approximations are limited in number and range of validity. This is true of gap models, such as the IMMCAV1 subroutine in Appendix B, where only the gap width and tube radius may be specified as geometrical parameters.

The second method that is used to determine the potential off-axis is a more physical model that approximates the system by representing the electrodes as a sum of discrete charged rings. A Poisson solver determines the charge on each ring that is necessary to satisfy the equivalent boundary conditions, usually the electric potential of the electrodes [Geraci02]. Since the method is more accurate in determining the potential even close to the walls of the structure, evaluating off-axis fields are more immune to errors at the higher derivatives. Also, the method permits a realistic representation of the electrodes by including effects such as the edge curvature of the tubes (see Appendix B). Once the electric fields are expressed as the sum of the fields of charged rings, the field or potential on-axis is represented as a sum of analytic functions. DA methods can then be used in COSY to evaluate off axis fields to arbitrary order.

As an example, we start with the model for a single gap structure, or immersion lens, as shown in Fig. 2.12. Ion trajectories come in parallel from left to right as they pass

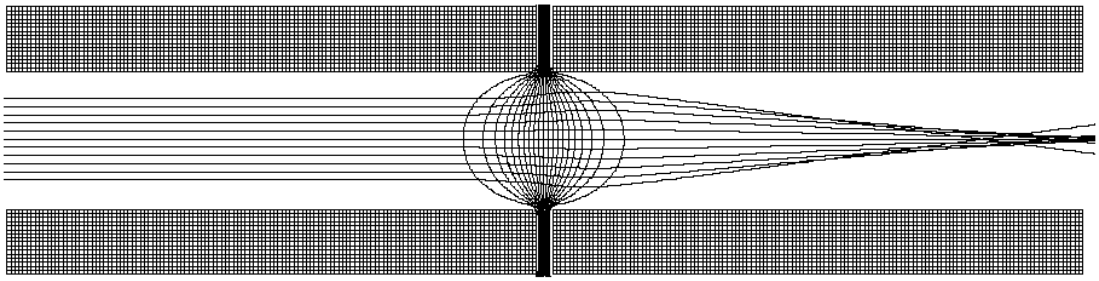

Figure 2.12 Immersion lens structure with ions coming in with parallel trajectories from left to right. The lines of potential along the center illustrate the fringing obtained in the gap region.

through the fringing fields at the region of the gap shown by the lines of equipotential. Notice that right as the beam passes the gap region, its envelope grows in size even as the rays are getting diverted from the optic axis. This occurs because the first half of the gap is diverging, while the second half is converging.

The results in Fig. 2.12 are obtained from a simulation using Simion 7. The values of the initial and final radial positions, r_f and r_i, respectively, are plotted in Fig. 2.13. From them we can extract the value of the aberrations by applying a 5th order polynomial fit. A comparison is made with the results obtained for the equivalent structure implemented in COSY. We have used the immersion lens structure called ONEGAP in COSY, which uses the method of charged rings to determine the potentials. The aberration coefficients are listed in Table 2.1 in columns two and three, for COSY and Simion, respectively. Notice that the amount of error in the coefficient gets larger for higher and higher order terms. Notice, that if we apply r_i=0.5 mm the accumulated error at r_f between the two is actually only 5.6%. The errors are mostly attributed to the fact that the curvature of the tube at the gap regions is specified with an accuracy limited by the use of 5 mesh points. The results, however, agree reasonably well in order to apply them to the map of the spectrometer.

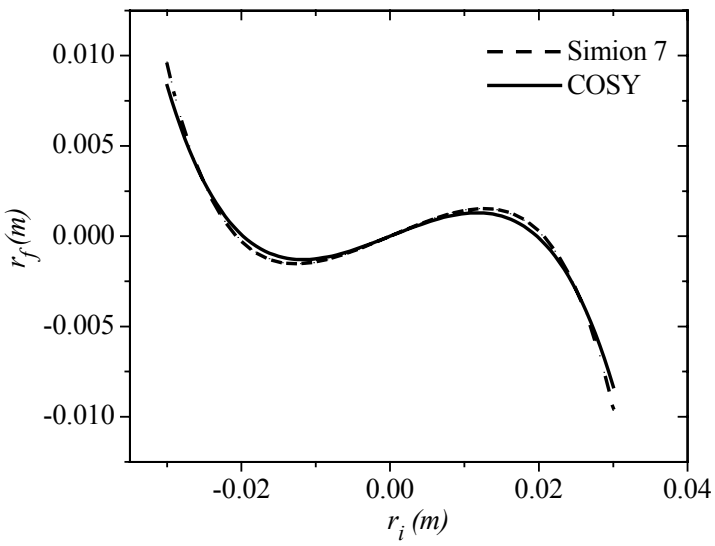

Figure 2.13 Plot of the final versus initial radial positions, r_f and r_i, respectively, of the simulation in Figure 2.12. A 5th order polynomial fit is used to extract the aberration coefficients from Simion 7 results. The curve obtained from applying the aberrations according to COSY are plotted for comparison. The coefficients are listed in Table 2.1.

Table 2.1 List of coefficients determined by numerical simulations.

order of coefficient [units]	COSY coefficients	SIMION 7 fit coefficients	error [%]
1 (x,x) [m/m]	0.1663	0.1736	5.9
3 (x,xxx) [m/m^3]	-364.4	-281.9	23
5 $(x,xxxxx)$ [m/m^5]	-139900	-293100	110

Before going on, we should make note of the fact that these structures can be arranged back-to-back to simulate multi-gap acceleration columns. There are some restrictions, however, since the fields of separate structures are not allowed to overlap if they are to be evaluated as individual maps. If two gaps of equivalent potential difference are moved close to each other the superposition of the fringing fields will effectively weaken the focusing power of the combined system. This effect will not be reflected in the map if calculated under similar conditions. As a general rule of thumb, the gaps should be separated by at least three tube radii in order to avoid an overlap between the fields of each gap. Otherwise, the boundary conditions need to be redefined to avoid errors.

The boundary conditions for multi-gap acceleration columns can actually be specified with two of the subroutines added to COSY as part of this study. The subroutines CUSCOL1 and STDCOL1 allow the user to specify the boundary conditions for multiple column structures in conjunction with the subroutine ACCELCOL1, which calculates the map. The use of these structures is described in more detail in Appendix B. These accelerating columns are commonly used for boosting the energy of ions after extraction from a region of ionization. They are also common to Tandem, Van DeGraff, and other similar DC acceleration devices.

The accelerating column of the dual-potential spectrometer did not require overlapping gap structures. Consequently, its map is calculated using two immersion lenses of the type shown in Fig. 2.12. The simulation was also done with Simion 7, not only for comparison, but also to obtain the beam envelope. Some development efforts are still needed to make such graphical representations available in the COSY code system.

The diagram of section I is shown in Fig. 2.14 as a cross section along the *x*—*s* plane. The gaps are 1 cm in width and the radius along the column is kept constant at 5 cm. The beam enters from the left at 100 keV and is decelerated to 29.9 keV in the first gap. The map of the first gap is generated in COSY from the entrance of section I to the dotted line, where it has parallel-to-point focus.

The map of the second gap goes from the dotted line on to the end of section I to obtain point-to-parallel focus. The full map of this system gives telescopic focus with a magnification of $(x,x)_I$=-2.135, and at (δ_K, δ_K)=10 as the beam exits at 10 keV. A 1% value of δ_K before deceleration becomes 10% after. By symmetry the column also

imposes telescopic focusing in the *y*—*s* plane. The beam envelopes along both *x* and *y* are plotted under the same scale in Fig. 2.15.

Finally, we compare the results of the phase space distributions obtained from Simion

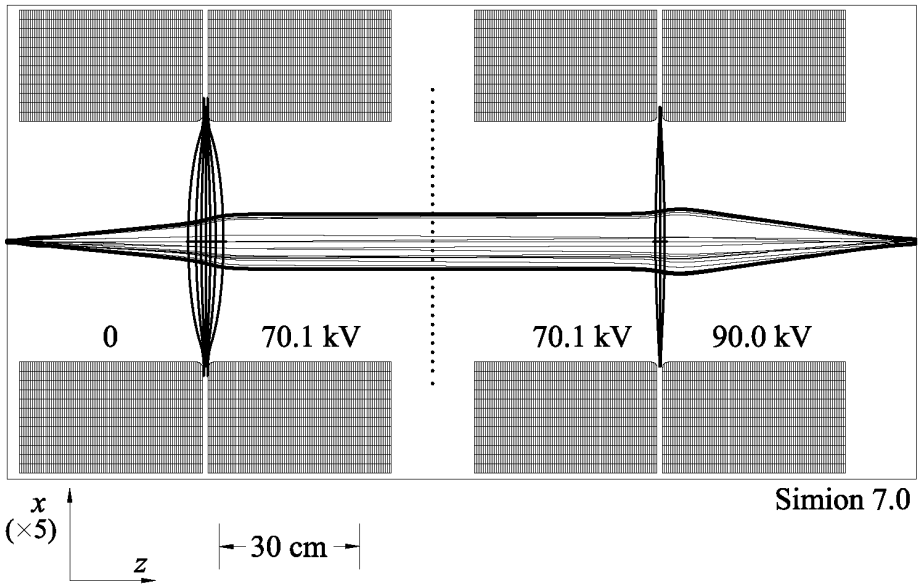

Figure 2.14 Cross section of the deceleration column along the *x*—*s* plane of section I. The beam comes in from the left at 100 keV then gets decelerated to 29.9 keV in the first gap and to 10 keV in the second.

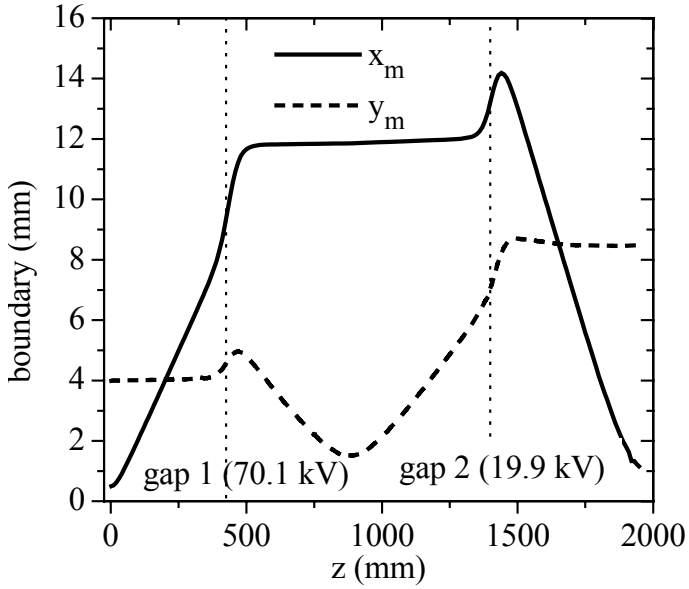

Figure 2.15 Plot of beam envelopes along *x* and *y*. The dotted line represents the center position of the gap for the labeled amount of deceleration.

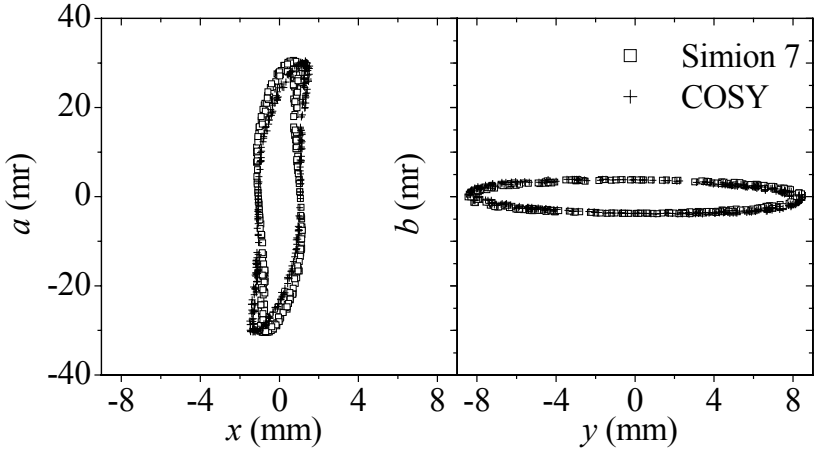

Figure 2.16 Phase space distributions in the *x*—*a* and *y*—*b* phase space given by Simion and COSY.

7 and COSY in Fig. 2.16. At least in the *x*—*a* phase space plot, the effects of the 3rd and 5th order aberrations are very clearly seen from the boundary-type distributions. The distorted ellipse given by COSY has a more pronounced "S-shape" due to the stronger 3rd order aberration from that of Simion. It also may seem that there is an effect from extra drift in the COSY ellipse orientation; however, this is actually a result from the difference between the calculated first order terms.

2.4 Purity according to the enhancement factor

In an earlier section we characterized the spectrometer based on its first order spectrum and demonstrated its effectiveness at separating isobars at a mass resolution of 20,700, the results of which are presented in Fig. 2.3. Now we should like to characterize the spectrometer in more detail by using a recommended standard.

We shall now introduce some concepts that are useful in characterizing the performance of a spectrometer and apply it to the one calculated earlier. First the following terms must be defined:

w - denotes wanted particles of mass m

u - denotes unwanted particles of mass $m+\Delta m$

i - denotes beam before the separator

f - denotes beam after the separator

N - number of particles w or u particles accepted

C - concentration of accepted w or u particles

We assume that only unwanted species of mass $m+\Delta m$ make up the impurity. The initial and final purity ratios are defined by,

$$r_i = N_{wi} / N_{ui} \tag{2.10a}$$

and

$$r_f = N_{wf} / N_{uf} \ . \tag{2.10b}$$

Usually one is interested in the concentration of wanted species after mass separation defined by

$$C_{wf} = \frac{N_{wf}}{N_{wf} + N_{uf}} = (1+1/r_f)^{-1} . \tag{2.11}$$

But, r_f is a function of r_i and the mass resolution and may be determined from,

$$EF = r_f / r_i . \tag{2.12}$$

where EF is the enhancement factor [Camplan81], which is a function of the mass resolution, $R_m=m/\Delta m$. This enhancement factor varies with the emittance of the beam and the shape of the distribution. If we know this enhancement factor then we can always determine the concentration, C_{wf}, for some r_i. We will adopt the Gaussian

distribution as the one which best describes the phase space density and define the emittance such that 95% of the particles lie within 4 times the rms width (see Fig. 1.8) under the phase space parameters defined at the end of Section 2.1.

The first thing that we shall like to determine is the maximum order that is necessary in determining the effects on the performance. Again, one must be careful that errors are not being amplified and making it seem as if we need more accuracy. In Fig. 2.17 we plot the results of the transmission and *EF* as a function of the order of the calculation. We have assumed that vertically aligned slits have been set at the exit of section L to suppress unwanted beam, *w*. Notice that the transmission tends to level out after applying higher than 3rd order aberrations. The effects caused by the aberrations that are left after applying the multipole fields seem to have negligible effects after this point. It seems that the best transmission expected for R_m=20,000 will be about 93%.

The enhancement factor improves as higher order terms are corrected. The enhancement tends to level out to a point where further improvements become minute

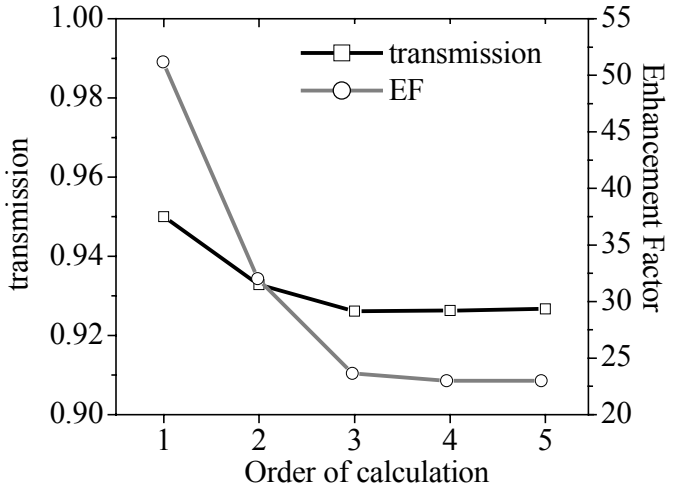

Figure 2.17 The transmission and enhancement factor as resolution of R_m=20,000 as a function of the order of the calculation.

after 3rd order. The effects of aberrations past 5th order seem to have little effect on the spectrum and further corrections offer no improvement. The simulations are therefore sufficient accurate at 5th order.

We also need to vary the separation between two masses in order to determine the dependence of *EF* on R_m. Note that we take R_m as being $1/\delta_m$ here. Again, this result is dependent on the initial density distribution, which we have assumed to be Gaussian. The results are illustrated in the two plots in Fig. 2.18. Plot (a) is that of the final wanted and unwanted concentrations as a function of R_m assuming that the initial concentrations, C_{wi} and C_{ui}, are equivalent. Plot (b) is the enhancement factor as a function of R_m. Two inset plots have been included to show the mass separations corresponding to both R_m= 2,000 and 50,000.

By applying a phase space of zero width in the horizontal we are able to test the contribution of aberrations to the final line width. Evidently, the resolution calculated here seems to be very close to some fundamental limit. Right after turning on the 2nd order aberrations the "line" spectrum looks no different that those with finite emittance of the Gaussians distributions. The only conceivable way to go beyond this limit is to further reduce the cross terms that arise from correcting the *x*—*a* phase space aberrations.

One dominant cross term that limits any further enhancement is the $(x,a\delta_K)$ aberration. It grows with the 2nd order correction imposed by the hexapoles at MH and ML3. Whenever the energy spread gets beyond ±25 eV, the enhancement factor suffers significantly due to this term. There were attempts to suppress this type of chromatic aberration by applying multipole fields at ML1, ML2, and ML4 and fitting on the reduction of the second moment along horizontal, $\langle x^2 \rangle$. Although there was a slight

reduction to the second moment, a negligible improvement was seen on the part of the enhancement factor. The only way to gain in the enhancement may be to reduce δ_K from the source. This is one of the advantages of using the ion cooling system that follows the

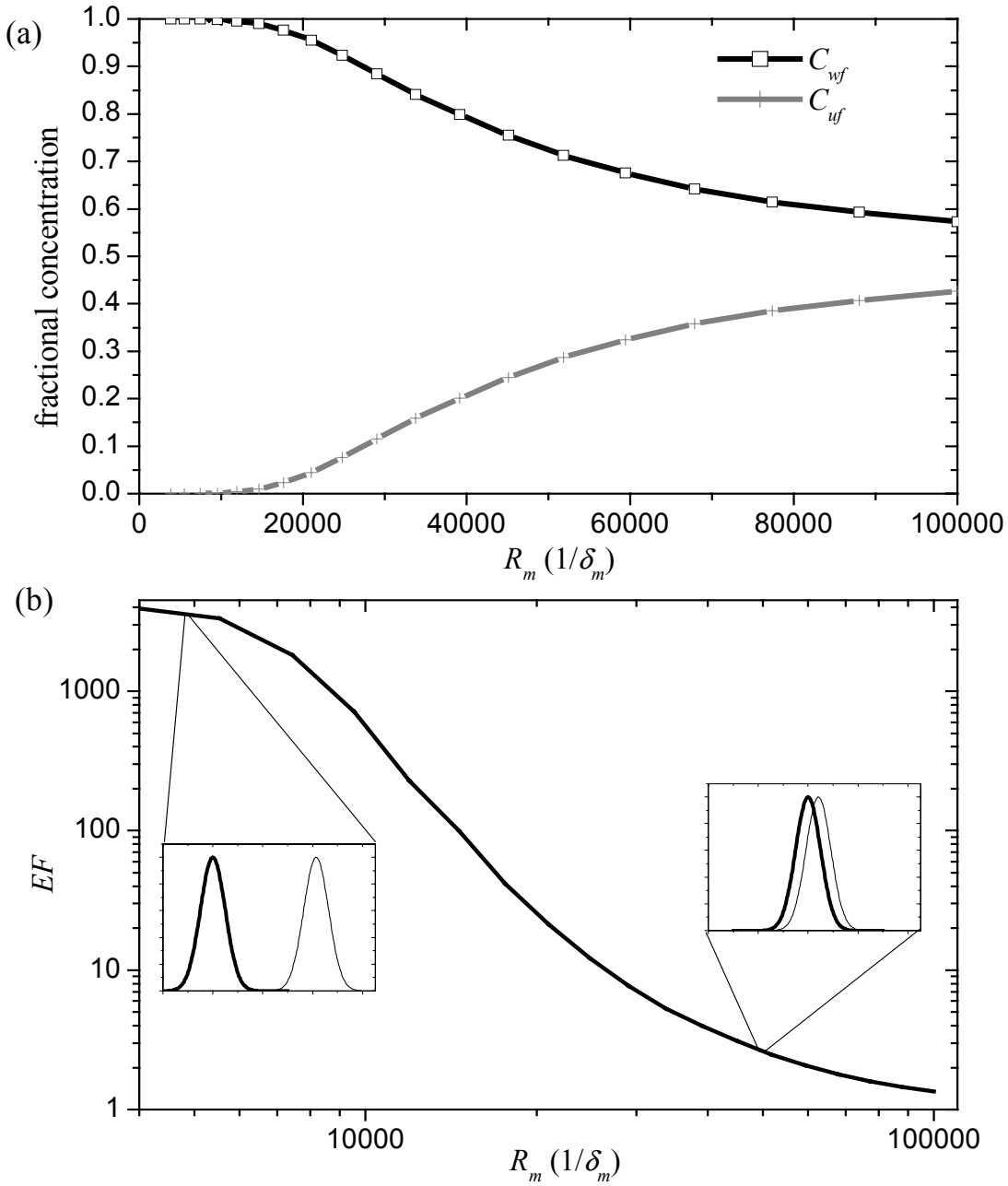

Figure 2.18 (a) Concentrations of wanted and unwanted species after separation as a function of resolving power. (b) *EF* as a function of resolving power. Inset plot shows the separation of two masses according to R_m.

gas catcher described in Chapter 1. We do not quote any numbers here for the improvements that are expected, since gas catchers are a relatively new development and are still under much research.

We summarize this section with a set of plots which show the expected mass lines of the spectrometer system after all the corrections have been optimized for suppression of hither order terms. The full emittance in the *x*— and *y*—planes are imposed to obtain the mass spectra from lines of $m/\Delta m$=20,000 as shown in Fig. 2.19. Plot (c) is that of a snap shot at the end of Section L. We can compare this plot with two plots above this one taken for Section H. In plot (a) we have removed the energy spread in the beam, while in plot (b) we have imposed the energy spread to show the effect of the energy dispersion from Section H. Without the energy spread imposed on the Gaussian distributions we get very close to what is expected from the 1st order calculation. The achromat condition after Section L clearly improves the resolution of the system significantly.

Unfortunately, this may not be the end of the story when it comes to factors that affect the mass resolution. We have not accounted for the possibility of formation of tails that result from beam scattering with residual gases. This effect causes the formation of tails that will also cause the enhancement factor to drop [Menat42]. The tails usually drop off slowly as exponential as a function of momentum and can migrate far across the spectrum. The dual-potential spectrometer, however, eliminates much of this effect already. Since the effect grow in proportion to the vacuum of the system, it may also be important to go with ultra-high vacuum systems. Also, it may be necessary to make some studies on the effect of misalignments of any of the components. At this point we have only seen the properties of an ideal spectrometer where everything is perfectly aligned.

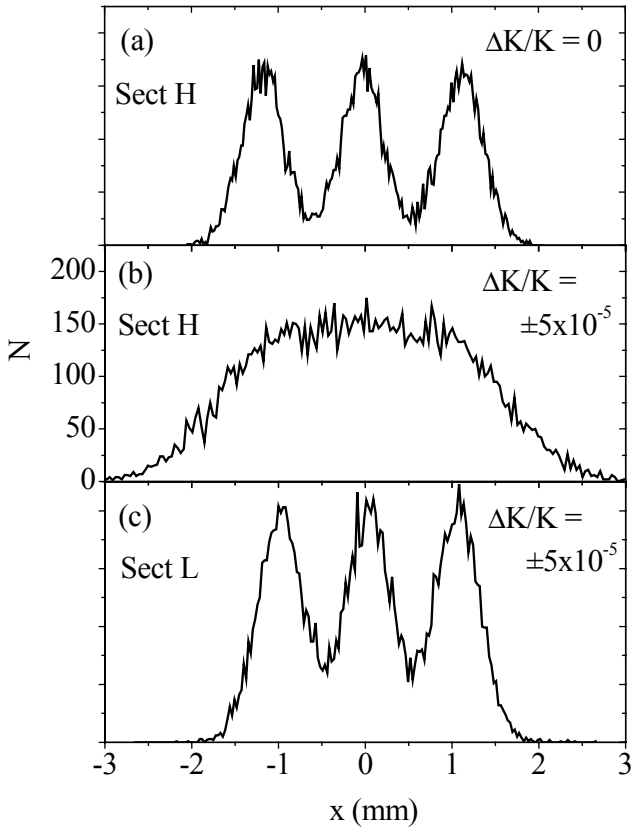

Figure 2.19 Mass spectra at two sections of the mass separator for $m/\Delta m$=20,000. The top most figure (a) illustrates the spectrum for a beam with no energy spread at the focal plane of the first section of the separation. The next plot (b) shows what a Gaussian distribution in energy with 95% of particles having energy between $\Delta K/K$=±5x10^{-5} (±5 eV at 100 keV). The last plot (c) demonstrates how the achromatic character added by the section after deceleration can improve the resolution.

Furthermore, one also has to keep in mind that ripples and other power supply instabilities will be magnified by a factor proportional to R_m and providing feedbacks systems for stability will be an important part of the overall system design.

2.5 Issues related to beam matching and the pre-separator

This chapter shall end with a discussion related to sections of the rare isotope accelerator that lie before and after the isobar separator. This is relevant since those sections affect some aspects in the design of the separator. We shall also point out how possible alternatives to the pre- and post-separator sections will affect the design.

2.5.1 Obtaining the required aspect ratio

Mass separator performance will always trace back to the beam characteristics of the emitting ion source. We have assumed that the extraction has axial symmetry and that the *x—a* and *y—b* emittance are equivalent. A beam of 10π mm-mr emittance area for a 100 keV/250 amu implies that there is a 0.0093 mm-mr normalized emittance. Although this is a reasonable assumption for most common ISOL ion sources, beams extracted from electron cyclotron resonance (ECR) type sources must be considered as a possible option. Such sources are good for providing higher charge state; however, they tend to have emittances that are higher by at least a factor of 3. Since the separator is designed to accept a maximum divergence of a_m=±20 mr, the beam aspect ratio would have to shifted to y_m/x_m=8/3 for a beam width of 3 mm in *x*. Consequently, the mass resolution would suffer by at least factor of 3 if the transmission were to be conserved. In order to obtain different aspect ratios, however, there will be the need to design a beam optical system that can vary the output y_m/x_m. Beam matching with the separator will require that it also yields upright ellipses (α_x= α_y=0), β_y=1.6, and a value of β_x that varies from 0.025 to 0.075.

One possible design solution is shown in Fig. 2.20. This sextet system is reminiscent of the one in Fig. 1.7. It has the same overall length, but the triplets have been shifted away from the center by 11.5 cm. This sextet is different in that it has magnifications of M_x=-1/$\sqrt{8}$ and M_y=-1. The plots of the initial and final ellipse show the effect on the x— and y—phase space. We have assumed that the beam is circular at the entrance with β_x=β_y=1.6 and α_x= α_y=0, and its telescopic properties insure that the ellipses will be upright at the exit. This system has had to lose the symmetry in the excitation of the

quads compared to those of the sextet in Fig. 1.7; however, the values of the excitation differ by less than 20% from the symmetric case. We have listed the excitation values in Table 2.2 for direct comparison. We should note that it is possible to shorten the outside quads and lengthen the middle quad a bit for each triplet value is similar in magnitude.

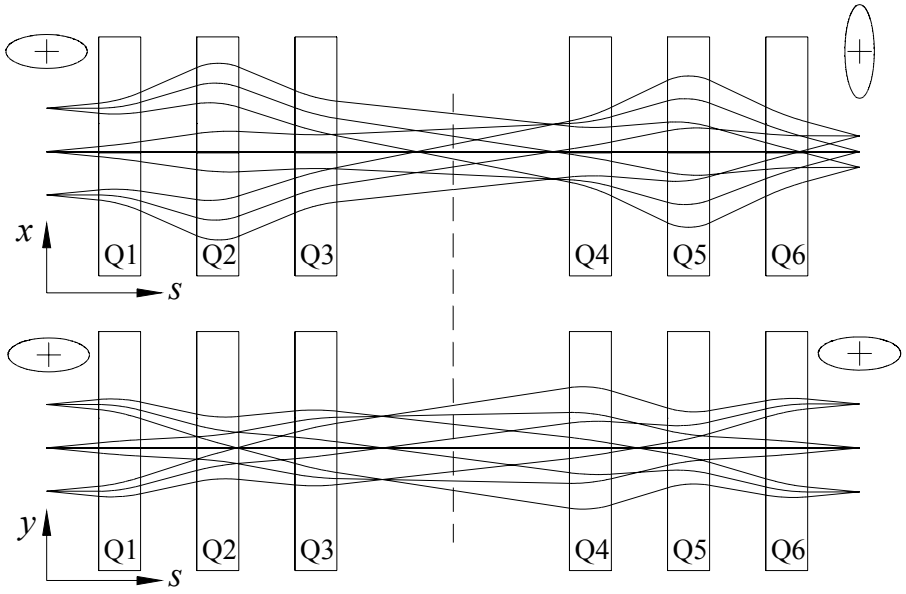

Figure 2.20 Sextet with magnifications of M_x =-1/$\sqrt{8}$ and M_y=-1. Dimensions are similar to those of the sextet in Fig. 1.7, except that the triplets have been shifted outwards from center by 11.5 cm.

Table 2.2 List of electric quad excitation voltage values in kilovolts.

quad	Fig. 1.7	Fig. 2.20
Q1	-0.7415	-0.7576
Q2	1.309	1.152
Q3	-0.7415	-0.6578
Q4	-0.7415	-0.8918
Q5	1.309	1.502
Q6	-0.7415	-0.6484

In order to obtain an aspect ratio of y_m/x_m=8 it necessary to use two similar optical systems in tandem to obtain M_x=(-1/$\sqrt{8}$)(-1/$\sqrt{8}$)=1/8 and M_y= (-1) (-1)=1. Finding the solution of a single sextet that obtains M_x=-1/8 has not been possible using the dimensions of the quads shown; however, further studies might yield such a solution. The advantage of using a tandem system is that it allows some manipulation of the aspect ratio while still retaining telescopic focusing. This ultimately gives the system more options in tuning the system in order to match the beam to the separator.

One other important thing to keep in mind is that after the mass separation, it will be necessary to bring the beam back to an aspect ratio of y_m/x_m=1 under upright ellipse focus. Otherwise, the rest of the rare isotope accelerator must be designed to accept aspect ratios different from unity, which may not be very practical. The ideal thing to do is to place a similar matching system but in reverse right after re-acceleration to 100 keV.

2.5.2 Choosing the scheme of separation

The solution for the dual-potential spectrometer as introduced above depends on a deceleration from 100 keV to 10 keV between the two magnetic separations. The system, however, can just as well be operated in reverse, in which case the beam must come in at 10 keV from the side of the source, be separated in momentum by section L, and then be accelerated to 100 keV for the energy correction from section H (see Fig. 2.2). The diagram in Fig. 2.21(b) depicts this situation. The diagram in Fig. 2.21(a) depicts the current design scheme. A third situation is depicted in Fig. 2.21(c) in which the beam comes in at 10 keV, is accelerated to 100 keV to go through the same system in (a) followed by a deceleration back to 10 keV. The differences lie in how other essential sections are floated at high voltage (HV) on top of an isolated platform, or HV Deck.

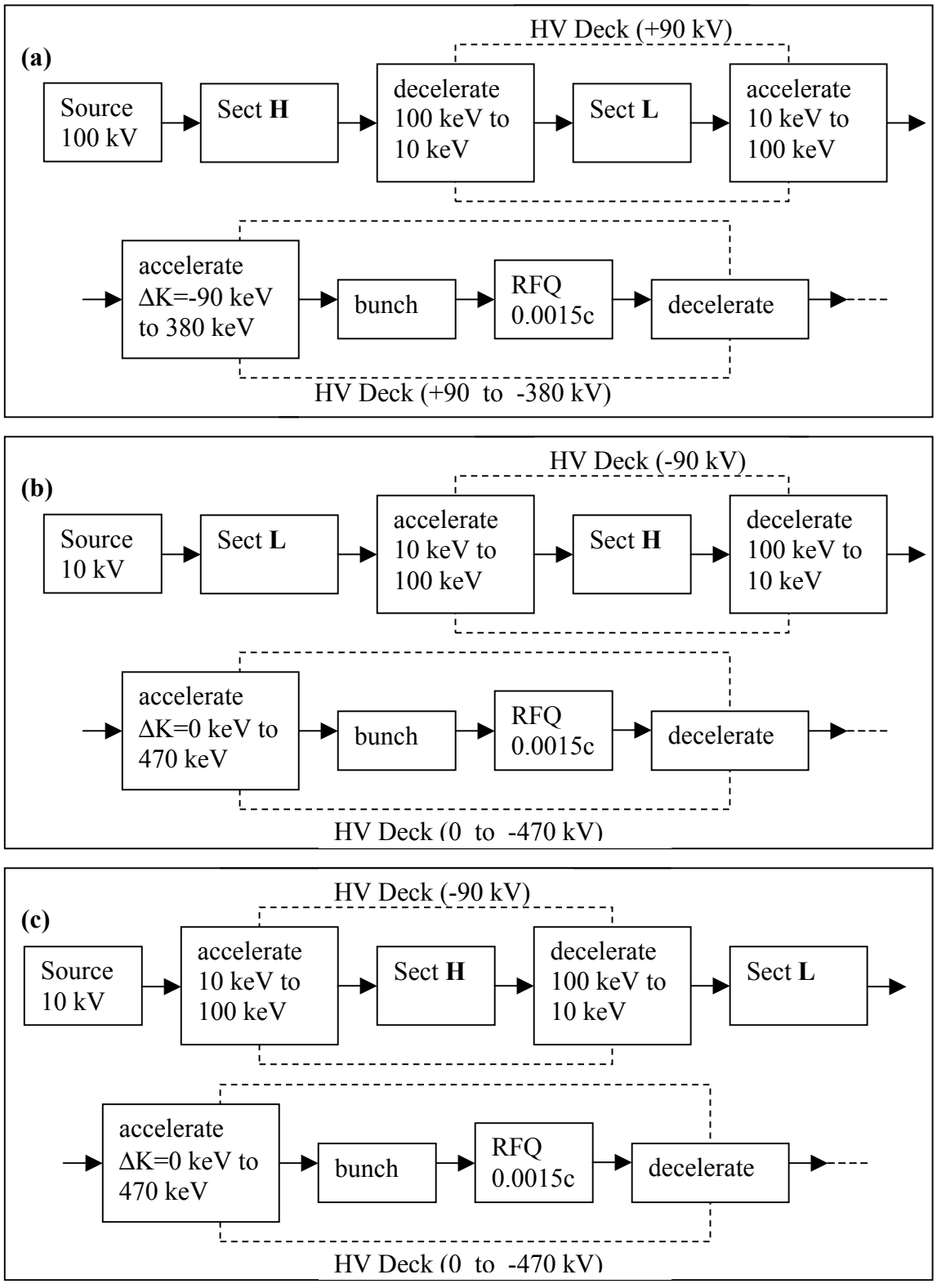

Figure 2.21 Various schemes of source extraction, separation, and post-acceleration. Preseparation and beam matching have been left out for simplicity.

Every section that requires isolation has been labeled and encompassed by a dashed line. It is assumed that there exists a DC acceleration column at each boundary where the beam crosses the dashed line. For simplicity, we do not show the beam matching systems discussed in the previous subsection.

It is also necessary to consider the first stage of RF acceleration that follows right after the mass separator. That section will consist of a buncher and a radio frequency quadrupole (RFQ) accelerator that accepts beams of velocity 0.0015*c*. Since ions of different mass will have different velocities coming off of the separator, it will be necessary to apply DC acceleration before the ions enter the RF accelerator. This requires that the RF accelerator system be isolated at high voltage. Below the boundary that depicts the HV deck of the RF accelerator we show the necessary range for the potential on the platform considering a mass range between 6 to 240 amu.

A preliminary evaluation has been made to assess which scheme is the most practical. For each scheme we factor in some of the technical difficulties and cost. The following factors favor the use of scheme (a) in Fig. 2.21:

1. Sect L is physically smaller, (see Fig. 2.2). More floor space is available if section L is isolated instead of Sect H.
2. An additional 90 kV would be necessary if using scheme (b) or (c) to match the accepted RFQ velocity. Considering that the RFQ system may require power levels on the order of 50 kW favors using lower isolated potentials.
3. The distance between source and separator is expected to be at least 20 meters long, which makes it necessary to consider effects during transport. The cross

section for scattering with residual gases is proportional to the inverse of the velocity, making such events at least 3 times less probable with 100 keV ions. Also, the higher emittance at 10 keV would make the beam more susceptible to aberrations from focusing elements.

4. Fluctuations of the voltage at the ion source on top of 100 kV are less noticeable than at 10 kV. This can be important if there is any energy resolving devices. For example, to resolve a ±5 eV energy spread at 10 keV requires 10 times less resolving power that for a 100 keV beam.

Whatever scheme is ultimately adopted will affect the isolation of both the source and RF acceleration. There are still some development efforts that may go into the final determination.

2.5.3 Considering some aspects of the pre-separator

Before concluding this chapter we should consider some minor aspects of the pre-separator. The current layout of the RIA facility has the production targets several meters below ground level [Savard01]. The isobar separator will be at ground level along with the rest of the post accelerator system. This requires that the beam be bent upward and then horizontally again as shown by the scheme in Fig. 2.22. This section makes up what is called the preseparator system.

The scheme shown in the figure assumes that there will be no horizontal bends imposing momentum dispersion. This entails using electrostatic deflection plates as the one shown for the bend that sends the beam up towards ground level. This bend may be used to limit the maximum energy spread of the beam. This will be important in eliminating energy tails that form at the extraction region of the source where vacuum

tends to be poor [Camplan81]. An energy resolution of $K/\Delta K$>1000 would suffice the best here (i.e. accepting a ±50 eV energy window).

The first dipole magnet should bring the beam back to the horizontal plane. It will allow the option of sending of beams containing other isotopes of interest to alternate channels where they may be directly studied or collected for medical and other applications. A resolution of about R_m=1000 may be sufficient for this purpose. The bend should avoid adding any dispersion that will interfere with that of the isobar separator. This separator should only impose (y, δ_m) and (y, δ_K) dispersions to the beam

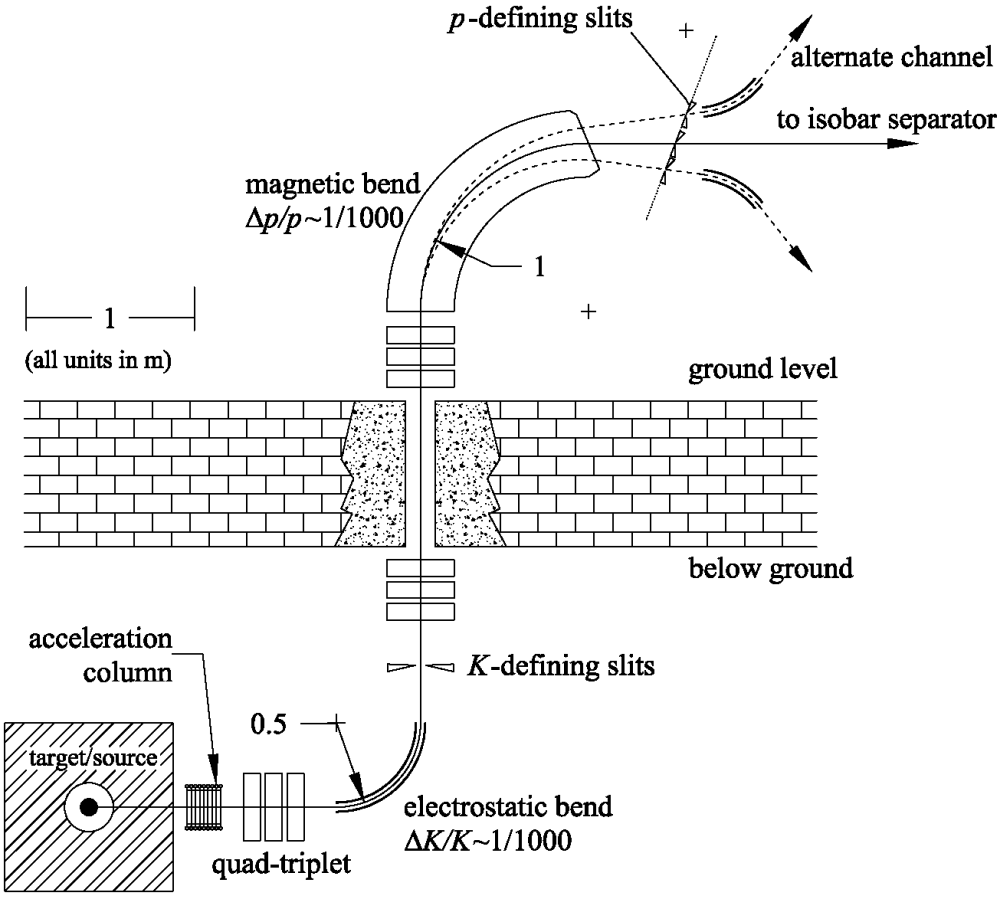

Figure 2.22 Conceptual design of preseparator for the RIA facility. The beam must be transported from below ground level to the isobar separator and rare isotope accelerator above ground.

and avoid any dispersion in the *x*—plane. This will avoid any chromatic interference with the isobar separator and allow the beam to keep a more definite structure in the horizontal plane. The rest of the beam transport in the horizontal plane should either be electrostatic or achromatic.

Chapter 3

APPLICATIONS WITH ACCELERATING RF DEVICES OF AXIAL SYMMETRY

In this chapter we shall focus on aspects related to the RIA driver accelerator, although some are applicable to the rare isotope post-accelerator as well. The first section of this chapter will discuss the implementation of axially symmetric electrostatic devices with time-varying fields into the COSY code system. Such devices are necessary not only for acceleration, but also for preserving longitudinal properties of beams with bunch structure. Some numerical examples are provided that may serve as a reference for calculating maps of such structures. The next section will discuss the application that requires the optimization tools and higher order capability of COSY for the design and simulation of multiple charge state beam transport systems in the RIA driver. It will also cover some background about the design of the driver system and reasoning behind the use of multiple charge state beams. Finally, we shall give an overview of the charge stripping calculations, since they provide the basis for the design.

3.1 Axially symmetric devices with time-varying fields

Electrostatic devices having axial symmetry play a vital role in acceleration systems. In fact, axial symmetry is used almost exclusively in all accelerating structures. There are some exceptions, such as in the case of RFQ accelerators, which have midplane symmetry. This type of accelerator, however, is mainly applicable at low β (approximately β=0.001 to 0.05) where the electrostatic quadrupole strength is most effective for very heavy ions of large mass to charge ratio, m/q. On the other hand,

structures with axial symmetry having static or time-varying fields are used throughout the spectrum of velocities.

The previous chapter covered axially symmetric structures with DC acceleration and demonstrated that maps of such structures could be calculated to arbitrary order with COSY. This chapter will discuss how the same can be done with structures having time-varying fields. The power of using map optics for optimizing the design of a system will be demonstrated with a particular application at the driver linac system. We shall use the term RF structure or device at times since the velocity of heavy ions and the practical dimensions of accelerating structures demand that the fields vary at RF frequencies (approximately between 1 MHz and 1 GHz).

3.1.1 Time-varying fields in COSY

The algorithms in COSY are very well suited for applications in beam dynamics in which energy conservation applies. This is especially useful in repetitive systems, such as in storage rings. As pointed out through (1.22f), however, much of this capability stems from the assumption that the variable, δ_K, is a constant of the motion, which tends to limit the way maps for RF structures are evaluated. The only known subroutine that calculates maps of structures with time-varying fields in COSY is one called 'RF', for RF cavity. It allows the approximation of a cavity by applying a kick in the electromagnetic potential over some infinitesimal section of s. It also allows the kick to be variable along the x—y plane. Unfortunately, it is not straightforward with such a model to make a correlation between the simulation and the geometry of a realistic RF device. To go beyond this limitation the program needs to be able to evaluate systems that take up a finite amount of space along s and account for the geometrical dimensions of the

structure in some detail. In particular, one should have the option to specify the time-dependent field distribution of the system. This requires that the equations of motion have an s dependent form of δ_K' as was demonstrated by Geraci and others by the derivation of the equation [Geraci02],

$$\delta_K^{'} = 2K_{rel}\left[aa'+bb'+\frac{E_s p_s l'}{\chi_{E0} p_0}\right] \tag{3.1a}$$

where the quantity,

$$K_{rel} = \frac{p_0 c}{2K_0}\frac{1}{\sqrt{a^2+b^2+(p_s/p_0)^2+(mc/p_0)^2}}, \tag{3.1b}$$

is the so-called relativistic factor. Here, p_s is the longitudinal component of the momentum vector, **p**=(p_x, p_y, p_s), for any arbitrary particles in phase space. K_0 and p_0 are the reference particle momentary kinetic energy and magnitude of the momentum, respectively. The rest of the constants and variables are the same as those defined in section 1.5. Eq. (3.1) is incorporated into a modified version of COSY such that it replaces Eq. (1.22f). It is important to keep in mind that in deriving Eq. (3.1) only the time dependent interaction of the electric field is accounted for and time-varying magnetic fields are neglected. This is generally a reasonable assumption, considering that axially symmetric induced magnetic fields are very weak in comparison to those of the electric. In realistic situations there are some stray electric and magnetic fields that are induced. Some of them stem from the electrical flow through the supports inside the structure [Ostroumov01]. Current RIA based studies have demonstrated that some of these fields carry a dipole component that steer the beam, especially for quarter-wave resonators at frequencies as low as 115 MHz. Such effects are, however, mainly perturbative in comparison to the effect of the axially symmetric fields. They are beyond

the scope of these studies, and shall be neglected here so that we may concentrate more on the details that are of primary importance in the dynamics of the beam.

The added capabilities in COSY allow the user to simulate effects from axially symmetric one-, two-, three-, and four-gap structures, as described in Appendix B. A sinusoidal time dependence on the field has been assumed for any structure, although the user can program other functions if necessary. The one-gap model is conceptually just an immersion lens with the potential drop between the tubes varying sinusoidally. The field distribution for calculating the map of this structure may be evaluated through either the method of evaluating derivatives of the approximate on-axis potentials [Reiser94b] or by using the more accurate method of charged rings [Geraci02]. This also applies for the two-gap structure. For all other structures only the method of charged rings is applicable. Aside from being able to specify the maximum potential and phase of the accelerating tubes, it is also possible to specify other parameters. Some of these parameters include the gap widths, spacing between gaps, radii of apertures, and dimensions of outer cavity walls. The parameters may be varied to optimize beam properties along the x—a, y—b, and l—δ_K subspaces as will be discussed next.

3.1.2 Properties of the longitudinal phase space

A brief overview of is given here of the expected values for the longitudinal subspace map. Also included is a review of some of the relevant quantities that are useful and any units of conversion that apply to the longitudinal phase space. Since the effects of the longitudinal phase space on its respective ellipse are slightly different than those of the transverse phase space, it is helpful to start with some discussion of the Twiss parameters.

It is usually more common to find longitudinal phase space expressed in terms of time and energy difference, relative to the reference particle. In COSY the choice of units are those of l and δ_K, which are proportional to time and energy spread as pointed out in (1.6). With the use of these coordinates one still needs to define some ellipse shaped boundary that is based on the beam distribution in longitudinal phase space. The Twiss parameters of this ellipse are related by the relation,

$$\beta_l \gamma_l - \alpha_l^{\,2} = 1, \tag{3.2}$$

and the maximum extent of the boundary along the l—δ_K plane (see Fig. 1.5) are given by,

$$l_m = \sqrt{\beta_l \varepsilon_l} \qquad \text{and} \qquad \delta_{K\,m} = \sqrt{\gamma_l \varepsilon_l}\ . \tag{3.3}$$

Here, ε_l is the longitudinal emittance in the l—δ_K plane and has units of meters. In these units one often refers to the total bunch width as the quantity $2l_m$ and the total energy spread as $2\delta_{Km}$. A quick review of some useful conversions to obtain these results in different units is now in order.

All quantities are specified relative to those of the reference particle, such that Δt is the difference in time-of-flight, Δs is the difference in length along the optic axis, $\Delta\beta$ is the difference in velocity over c, Δp is the difference in momentum, and ΔK is the difference in energy between some particle and the reference particle. According to the definition of the canonical variable, l, in Eqs. (1.6) the relation,

$$\Delta l = -\Delta t \cdot \mu_0 = \Delta s \frac{\gamma_0}{(1+\gamma_0)}. \tag{3.4}$$

may be used to convert between units of the first coordinate in the plane. For the other coordinate we can use the relativistic forms of momentum and kinetic energy to arrive at the relation,

$$\frac{\Delta\beta}{\beta_0} = \frac{1}{\gamma_0(\gamma_0+1)}\frac{\Delta K}{K_0} = \frac{1}{\gamma_0^{\,2}}\frac{\Delta p}{p_0}. \tag{3.5}$$

Thus for example, to convert ε_l into units of time-of-flight and energy one needs to multiply by the factor K_0/μ_0. A typical longitudinal emittance is expressed in ns-keV/u which would further require that this quantity be divided by the unit mass, A.

Instead of using units of time, one can also use units that correspond to the RF phase shift, $\Delta\varphi$, for some frequency, ν. This phase shift can be calculated by $\Delta\varphi = \omega \cdot \Delta t$, where $\omega = 2\pi\nu$ is the angular frequency in units of radians. The bunch width may then be specified as $2l_m$, $2\Delta t_m$, $2\Delta s_m$, or $2\Delta\varphi_m$, while the relation in (3.5) can be used to obtain velocity, energy, or momentum spread in the other variable. With this bit of useful knowledge we return the discussion to the longitudinal subspace.

One distinct feature that is different from the transverse plane derives from the transformation of the sigma matrix. Since the longitudinal phase space is not dependent on the energy of the reference particle, the inverse transformation no longer requires the application of some scaling factor, such as $p_{0,0}/p_{0,f}$ in the transverse subspace. The final Twiss parameters are evaluated from the initial ones by the following equations resulting from the transformation of the sigma matrix of the type shown in Section 1.6:

$$\gamma_{l,f} = \gamma_{l,0}(\delta_K,\delta_K)^2 - 2\alpha_{l,0}(\delta_K,l)(\delta_K,\delta_K) + \beta_{l,0}(\delta_K,l)^2 \tag{3.6a}$$

$$\alpha_{l,f} = -\gamma_{l,0}(l,\delta_K)(\delta_K,\delta_K) + \alpha_{l,0}\big((l,l)(\delta_K,\delta_K) + (l,\delta_K)(\delta_K,l)\big) - \beta_{l,0}(l,l)(\delta_K,l) \tag{3.6b}$$

$$\beta_{l,f} = \gamma_{l,0}(l,\delta_K)^2 - 2\alpha_{l,0}(l,\delta_K)(l,l) + \beta_{l,0}(l,l)^2 \tag{3.6c}$$

We shall now like to consider the first order matrix elements under the action of a drift of length, L_0. To begin with, a particle will not experience any change in energy so that $(\delta_K,\delta_K)=1$, $(l,l)=1$ and $(\delta_K,l)=0$. The relative shift depends solely on the velocity of the particle relative to that of the reference particle by,

$$\Delta l = -(t - t_0)\beta c \frac{\gamma_0}{(1+\gamma_0)} = -L_0\left(\frac{1}{\beta} - \frac{1}{\beta_0}\right)\beta \frac{\gamma_0}{(1+\gamma_0)} = L_0 \frac{\Delta\beta}{\beta_0}\frac{\gamma_0}{(1+\gamma_0)}, \qquad (3.7a)$$

and with the use of (3.5) yields the form,

$$\Delta l = L_0 \frac{1}{(\gamma_0 + 1)^2}\delta_K = (l, \delta_K)\delta_K . \qquad (3.7b)$$

Hence, the longitudinal submatrix for the drift simplifies to,

$$\mathbf{A}_l(L_0) = \begin{bmatrix} (l,l) & (l,\delta_K) \\ (\delta_K, l) & (\delta_K, \delta_K) \end{bmatrix} = \begin{bmatrix} 1 & \dfrac{L_0}{(\gamma_0+1)^2} \\ 0 & 1 \end{bmatrix}. \qquad (3.8)$$

The values of the matrix can then be substituted into (3.6c) and we obtain from the first equation in (3.3) that the half-bunch width varies with the initial twiss parameters according to the relation,

$$l_m(L_0) = \sqrt{\varepsilon_l\left(\frac{\gamma_{l,0}}{(\gamma_0+1)^4}(L_0)^2 - \frac{2\alpha_{l,0}}{(\gamma_0+1)^2}(L_0) + \beta_{l,0}\right)}. \qquad (3.9)$$

This function defines the envelope within which the bunch resides in throughout propagation along the drift. The equation inside the square root is that of a parabola which opens upward. The minimum is always greater than zero and occurs at $L_0 = \alpha_{l,0}(\gamma_0^{\,2}+1)/\gamma_{l,0}$ to give $l_m = \sqrt{\varepsilon_l/\gamma_{l,0}}$. The minimum may occur at a positive or negative value of L_0 depending on the sign of $\alpha_{l,0}$.

It should be noted that for the subspace in the longitudinal plane a drift does not imply that there is a field free region. It only means that there is no time dependent fields and that the Eqs. derived in (1.15) under the arguments of symplecticity still apply. As far as the topic of map elements under time-varying fields is concerned, we shall only study those having axially symmetric properties. Monomials containing l or δ_K will not necessarily vanish; therefore, the transformation of the type described in Appendix A

would no longer give the same symplectic relations. Although we do not go into the details of the canonical transformation, it is important to mention that such relations can be useful in checking the validity of some map elements. Although one can use the symplectic approach to check accuray, there is little hope that it will lead to better performance in evaluating all the coefficients of the map.

3.1.3 Map calculations with RF devices

This section will illustrate the numerical results from a simple model with time-dependent fields. The model consists of only one two-gap structure that is set at the center of two equivalent drifts at either side. Between the starting point and the midpoint of the first encountered gap is a distance, L. As shown in Fig. 3.1, the system is symmetric about the center point of the tube that has a potential varying as,

$$V = V_0 \cos(\omega t + \varphi) \tag{3.10}$$

where V_0 is the maximum potential. The tube is centered inside a grounded cavity structure that also has axial symmetry. The voltage characteristics and dimensions of the system are specified through the input parameters of a subroutine, called TWOGAP described in Appendix B. The parameters used in this example are listed in Table 3.1, where the parameters V_0, φ, and L are vary.

The gap-to-gap distance has been evaluated based on the velocity of the reference

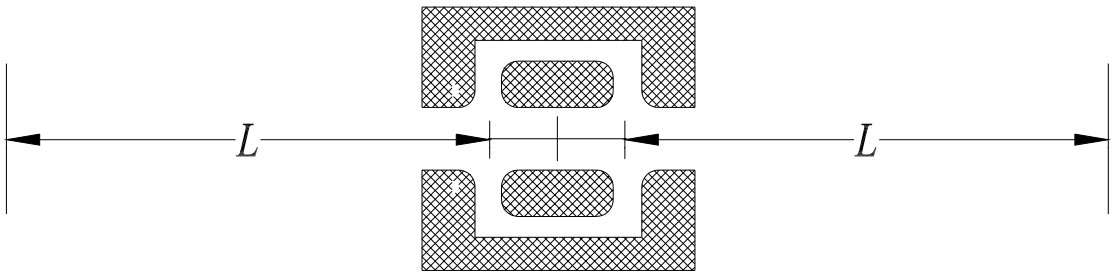

Figure 3.1 Two-gap structure system symmetric about the center.

Table 3.1 Parameters used for TWOGAP cavity in Fig. 3.1.

Frequency (ν)	350 MHz
V_0	(varies)
φ	(varies)
Gap-to-gap distance	17.1 cm
Width of both gaps	2.1 cm
Inner radius of tube (RI)	2.5 cm
Outer tube radius (RO)	5.0 cm
Aperture radii (RI)	2.5 cm
Radii of curvature (RE=RD)	0.5 cm
Cavity radius (RRES)	7.1 cm

particle and the frequency of the cavity. For this application we need the particle to experience the same polarity and magnitude of the field at both gaps. This implies that the cavity must undergo a $(n+1/2)\pi$ shift in φ as the particle travels from one gap to the other, where n is an integer. If we assume that the velocity does not vary appreciably after the first gap then the gap-to-gap distance is simply given approximately by,

$$\beta_0\lambda(n+1/2) \tag{3.11}$$

where $\lambda\nu=c$. The gap width has been taken to be one eighth of this distance.

The parameters assumed for the incoming beam are listed in Table 3.2. These are required of the application to be discussed in a later section. Notice that we have assumed that the longitudinal ellipse is initially upright; thus, according to (3.9) the bunch is expanding with s as it approaches the cavity. Since the transverse phase space effects will be neglected for now, we assume that $\varepsilon_x=\varepsilon_y\sim0$ for these calculations.

Table 3.2 Properties of the incoming beam for the model described by Fig. 3.1.

reference particle energy/A	85.3 MeV/u
unit mass (A)	238
charge state (q_0)	+90
ε_l	14.7 μm (20 keV-ns/u)
α_l	0
$2l_m$ or $2\Delta\varphi_m$	4 mm 8º

The effects that the oscillating field will have on the bunch are heavily dependent on the phase of the cavity. To show this dependence we take the case of L=13.2 m and V_0=2.2 MeV being constant as the phase varies from –180º to 180º. The plots in Fig. 3.2 show four different quantities as the phase is varied relative to the phase $\varphi = \varphi_b$. The phase φ_b is defined as the point where a minimum in (δ_K,l) occurs, which is at –53.4º shown by the upper plot. Notice in the same plot that (l,δ_K) also goes through a minimum at this phase. This is characteristic of system with symmetry along s.

The bottom plot shows the fractional energy gain of the reference particle. The maximum energy gain occurs at $\Delta\varphi$=90º, and signifies that at this phase the tube takes on the maximum negative potential as the particle is in the region of the first gap. Conversely, maximum energy loss occurs at $\Delta\varphi$=–90º. Although not obvious by the plots, what is happening between $\Delta\varphi$=–90º and 90º is that the particles at the front of the bunch are losing energy relative to the ones at back. This is referred to as bunching in the sense that particles in the front had a higher energy than the reference particle, and therefore, arrived earlier. The rate of expansion of the bunch is either decreased, or if V_0 is high enough, the bunch will actually begin to contract. Going from expansion to contraction is equivalent to stating that α_l changes sign from negative to positive.

Outside of this phase region the opposite effect occurs and we call it debunching. Note that (δ_K,l) remains negative at the bunching region of the phase. Since this is a general property, it is useful to impose the conditions $(\delta_K,l)<0$ and $(K_{0,f}-K_{0,0})/\ K_{0,0}=0$ when searching for φ_b. It should be also be pointed out that the "bunching strength" of the system is actually proportional to this quantity, and we shall refer to $-(\delta_K,l)$ as the "bunching strength" of the cavity.

One interesting aspect of axially symmetric devices in DC mode is that they always yield a positive refractive power, $1/f$, regardless of the polarity of the field [Reiser94c]. This property, however, does not translate over for the case of oscillating fields. As seen by the second plot in Fig. 3.2, the refractive power actually varies with the phase of the cavity. What we actually get is a refractive power that is proportional to (δ_K,l), and consequently, there is maximum defocus at maximum debunching. This is an unfortunate quality, since a transport system requires bunching throughout in order to preserve beam stability in longitudinal phase space. The ideal situation is to get both focusing and bunching, simultaneously, as in the case of a well tuned RFQ. From the plots we can conclude that for a linac with axial structures it is more ideal to approach $\Delta\varphi$=90º from $\Delta\varphi$=0 without losing too much bunching strength. Unfortunately, there is a trade off and one must settle for something in between that preserves the beam stability. Furthermore, there will be a need for refocusing structures to offset the defocusing effect. Applications related to beam stability of more complex systems, such as extended sections of linear accelerators, would be ideal for this type of implementation in COSY. Instead, we shall redirect the discussion to aspects that are related to higher order effects with cavities.

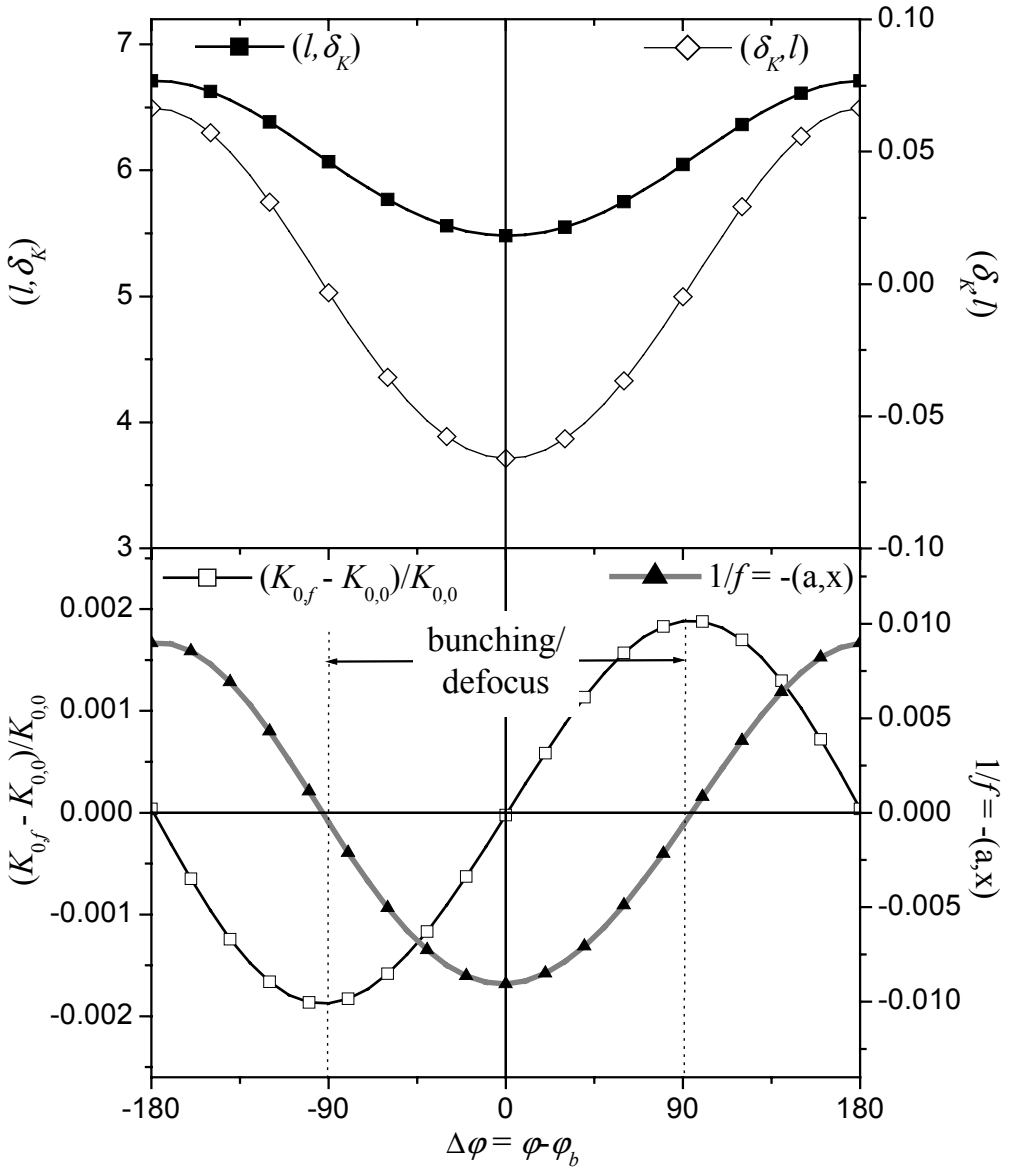

Figure 3.2 Relative phase dependence of the quantities (l, δ_K), (δ_K, l), $1/f$, and $(K_{0,f} - K_{0,0})/ K_{0,0}$.

The most straightforward method of showing higher order effects in longitudinal phase space is to extend the bunch throughout the RF cycle. We shall define the length, $\Delta l(2\pi)$, as the distance that the full bunch occupies throughout one period of the RF cycle, which is given approximately by

$$\Delta l(2\pi) \approx \frac{c\beta_0 \delta_{Km}}{v(1+\gamma_0)^2}\left(1+\frac{\gamma_0(1+\gamma_0)}{\delta_{Km}}\right). \tag{3.13}$$

This assumes that we initially have an upright ellipse, and that after a sufficient interval of time $l_m \approx l_e$. Here,

$$l_e = -\alpha_l \sqrt{\varepsilon_l / \gamma_l} \tag{3.14}$$

in analogy with the subscript convention used for the *x*—*a* phase space in Fig. 1.5. This approximation applies well within a few percent for the ellipse defined in Table 3.2, and we adopt those parameters for our initial conditions in this example.

It is also helpful to have an idea of how far the bunch can propagate before the full bunch width becomes the size of $\Delta l(2\pi)$. Applying Eq. (3.7) this distance is found to be

$$L(2\pi) = \frac{(1+\gamma_0)^2}{\delta_{Km}} \frac{\Delta l(2\pi)}{2}. \tag{3.15}$$

Furthermore, we define the ratio,

$$r_l = 2l_m / \Delta l(2\pi), \tag{3.12}$$

which gives the fraction of the RF cycle occupied by the bunch width. For the ellipse here we find that $L(2\pi)$ is 53 meters for $r_l \approx 0.5$.

The symmetry of the system in Fig. 3.1 makes it possible to reorient the phase space ellipse with the cavity so that it makes a complete flip by the time the bunch reaches the exit of the system. It requires that the relative phase be set at $\Delta\varphi = 0^\circ$ in order to bunch without any gain in energy by the reference particle, and that the value of V_0 be set so that the energy and time variable magnifications, (δ_K, δ_K) and (l, l), respectively, yield a value of -1. This rebunching action is synonymous with telescopic focusing in transverse phase space as it has that $(\delta_K, l) = (l, \delta_K) = 0$. We solve for the value of V_0 for a series of L values and plot the results in Fig. 3.3. Notice that as the size of the incident bunch at the

cavity grows, while the amount of cavity potential necessary for rebunching goes down exponentially. Clearly there is much to gain in terms of reducing the required RF power for rebunching. On the down side, we see from Fig. 3.4 that the there is a price to pay for allowing the bunch to increase. The phase space plots in this figure have been evaluated to fifth order from the values in Fig. 3.3. Notice that the aberration effects grow with bunch width. The aberrations effectively increase the longitudinal phase space and may ultimately result in halo formation as the filamented phase space propagates.

Clearly, there are a number of trade-off factors to be considered in rebunching and acceleration. The distortions in the phase space ellipse, whether transverse or longitudinal, translate into emittance growth. At this point we have not even considered the effects of changing geometrical factors of the cavity or the linearity of the time-dependence of the field. Such factors are restricted by certain technical aspects of constructing RF devices and are beyond the scope of this study. Instead, the discussion

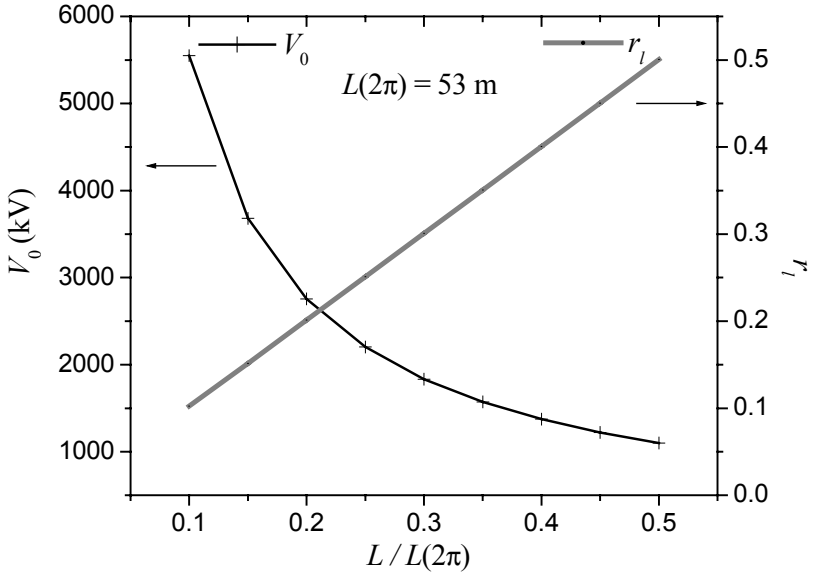

Figure 3.3 Cavity potential V_0 necessary to obtain upright ellipse at exit of system given length L before the first gap.

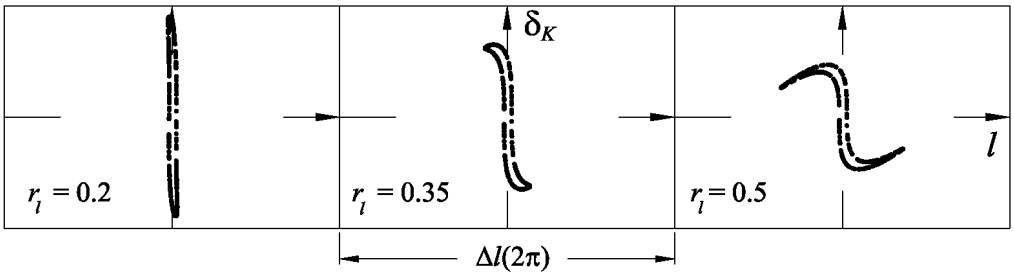

Figure 3.4 Resulting phase space plots for each corresponding r_l as evaluated to 5th order by COSY.

below concentrates on a particular application in which cavities are used for bunching a beam of multiple charge states.

3.2 Applications with multi-*q* beams

The RIA driver linac is to be designed with the capability of delivering high power beams of ions from the complete spectrum of masses from the periodic table. Except for a few room temperature RFQ accelerators at the low energy section, the entire linac is based on current state-of-the-art superconducting (SC) elements. With over 400 independently phased SC cavities ranging in frequency from 58 MHz to 800 MHz, the driver is expected to deliver up to 1.3 GV of RF potential [Shepard99]. This translates into ~900 MeV protons and ~400 MeV/u uranium ions, when considering independent phasing for variation of the velocity profile at each mass. The maximum energy per nucleon becomes limited at lower values for elements of higher *Z* due to the increasing difficulty in stripping electrons away. A diagram illustrating a simplified diagram of the driver is shown in Fig. 3.5 for the acceleration scheme for uranium.

A number of factors affect the decision to use SC technology, most of which stem from the high power requirement of the linac. The ultimate goal is to deliver up to ~400 kW in CW to multiple targets. SC cavities are ideal for CW operation, and their

relatively short, high-gradient designs provide very strong longitudinal focus and high transverse acceptance. This will ultimately lead to reduction in halo formation from higher order aberration effects. Furthermore, CW beam minimizes transient effects in the target that would otherwise occur when using pulsed beams, such as from synchrotron based schemes or room temperature linacs in pulse mode.

Probably the most unique feature of the linac is that it will accelerate multiple charge states (multi-*q*) beams. This feature allows charge states that would otherwise be diverted to a beam dump, to be accepted by the linac for acceleration. It also reduces unwanted radiation at parts of the facility that would otherwise require a considerable amount of shielding. It is estimated that the losses from not accepting multi-*q* beams would have to be made up by requiring a factor of 16 or more output from either ECR or other sources that produce high charge states. To date the best known performance has been from the AECR-U source, which can produce about 0.8 pμA of *q*=30 uranium [Lyneis98] [Lyneis02]. Since the present linac design requires two stages of stripping for

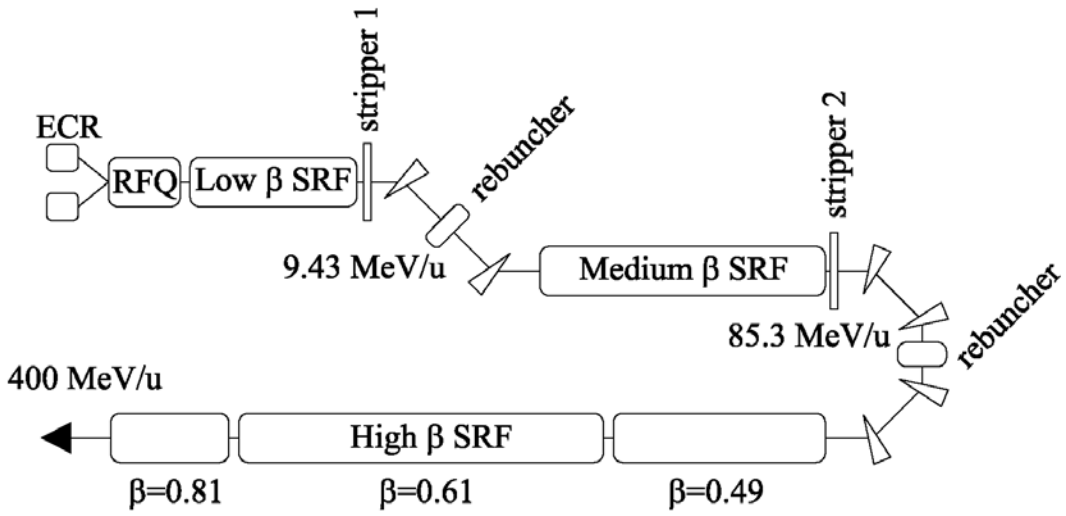

Figure 3.5 Simplified layout of RIA driver linac under the acceleration scheme of uranium. SRF signifies array of superconducting cavity structures.

uranium, only a few kilowatts of power would result from this type of source if only one charge state is kept from the ECR or after any stripper.

The entire linac is designed for transporting multi-q beams throughout, beginning with extraction from the ECR source. We shall not go into detail related to aspects of the acceleration of multi-q beams, but instead cite the following references in which relevant details are covered:

- Bunching of a two-charge state (q=28 and 29) DC beam of uranium emitted from an ECR source followed by multi-q acceleration through an RFQ and low β SRF linac [Ostroumov00a].
- Acceleration of a five-charge state beam (q=73 to 77) of uranium through a medium β SRF linac after stripping at ~10 MeV/u [Ostroumov00b].
- Acceleration of a four-charge state beam (q=88 to 91) of uranium through a high β SRF linac after stripping at 85.3 MeV/u [Ostroumov99][Ostroumov00b].

The work on the topics listed above is ongoing and these references are not necessarily the most recent. They do, however, offer a good overview of the overall plan for the RIA driver linac.

The focus here will be on the aspects related to filtering out the unwanted charge states and matching of multi-q beams to accelerating structures. These occur at the bends shown in the diagram in Fig. 3.5. Since the beam has bunch structure after each of the two foil strippers, there will be a requirement for rebunching and matching the longitudinal phase space back into the next linac section. The bend sections must incorporate achromat and isopath optical qualities in which the matrix approach is valuable to the design. Since the higher order effects of the full system are of special

interest, it is necessary to apply higher order map calculations for the bunching and focusing. Applying the newly developed COSY RF structures is useful for these systems, and we shall show some examples of this.

The filtering of DC multi-q beams from the ECR does not require bunch structure enhancements until after q-state filtering. As we shall show later, the filtering requires a simplified version of the systems required at the stripping sections and RF calculations are not necessary. We shall focus on the required systems for filtering and rebunching beams after the stripping stages and end the chapter with some detail about the stripping process itself.

3.2.1 The conditions for an isopath

The term isopath is interpreted here as meaning equal path lengths for particles that start at the same point but can vary in rigidity. According to (1.24) particles that differ in rigidity from the reference particle must have one or more of either δ_K, δ_q, or δ_m differing from zero. At first we shall only regard the δ_K variable and then explain why it should extend to the other two variables. We shall only consider reference particle motion in the horizontal plane here, although the theory can be extended to motion beyond midplane symmetry.

To develop an understanding of an isopath in terms of the transfer map, we should first quantify the path difference. Suppose the reference particle travels from s_i to s_f sot that it travels a distance, L_0, while some other particle of $\delta_K \neq 0$ travel the distance, L, over the same time interval of the motion. As long as each of their respective velocities remain constant throughout then the path difference may be obtained from,

$$\Delta L = L - L_0 = c(\beta t - \beta_0 t_0) = -\frac{(1+\gamma_0)}{\gamma_0} l + \delta_K \frac{L_0}{\gamma_0(1+\gamma_0)}\left(1 + \frac{l}{L_0}\frac{(1+\gamma_0)}{\gamma_0}\right), \tag{3.13}$$

where we have applied Eq. (3.5) and the definition of l from Eq. (1.6). Since we shall only consider the approximation in which $l << L_0$, then we can drop the second term in the large parenthesis and treat the results as exact. If we now substitute the relation for l in terms of the initial position vector,

$$l = (l,x)x_i + (l,a)a_i + (l,\delta_K)\delta_K, \tag{3.14}$$

then the final form of (3.13) can be expressed as,

$$\Delta L = -\frac{(1+\gamma_0)}{\gamma_0}\left\{(l,x)x_i + (l,a)a_i + \left[(l,\delta_K) - \frac{L_0}{\gamma_0(1+\gamma_0)}\right]\delta_K\right\}. \tag{3.15}$$

From this relation we see that in order to obtain an isopath (l,x) and (l,a) must vanish, and that

$$(l,\delta_K) = \frac{L_0}{\gamma_0(1+\gamma_0)} \tag{3.16}$$

must also be satisfied. According to the symplectic relations (1.15g) and (1.15h), if (l,x) and (l,a) vanish then (x,δ_K) and (a,δ_K) must vanish as well. Notice that the relations (1.15e) and (1.15f) also imply the same conditions. We infer that under these conditions, having a system that is an isopath in δ_K must imply that the system is also fully achromatic.

The diagram in Fig. 3.6 sums up the situation discussed up to now. Notice that two particles starting at the same position and direction will exit at the same point and direction if the system is fully achromatic. In addition, if the system is also an isopath then both particles would have traveled the same distance, $L=L_0$. We now consider the x displacement away from the reference orbit,

$$x(s) = (x, \delta_K)\delta_K \,, \tag{3.17}$$

anywhere along s. To first order the momentary radius is given by $R(1+hx)$, where the variable $h(s)=1/R(s)$ as defined in Chapter 1, and the derivative of the length, L, is given by,

$$\frac{dL}{ds} = (1 + hx) \,. \tag{3.18}$$

Furthermore, since for the reference particle $x=0$ over all s, the derivative of the path difference must simplify to the relation,

$$\frac{d}{ds}(L - L_0) = \frac{d}{ds}\Delta L = hx \,. \tag{3.19}$$

Finally, if we integrate (3.19) over the entire path and substitute $x(s)$ from (3.17) into this equation, then we obtain the integral relation,

$$\Delta L = \delta_K \int_{S_i}^{S_f} h(s)(x, \delta_K)ds \,. \tag{3.20}$$

To obtain an isopath system over the motion this integral must vanish. It should be noted at this point that, since we have assumed that there is no change allowed in the velocity in obtaining (3.13), then there can be no acceleration in the direction of motion. Bending or accelerating with electrostatic fields will not allow this condition to be satisfied; therefore, the system should consist of only magnetic fields.

We can make some inferences about the type of magnetic field arrangement that will

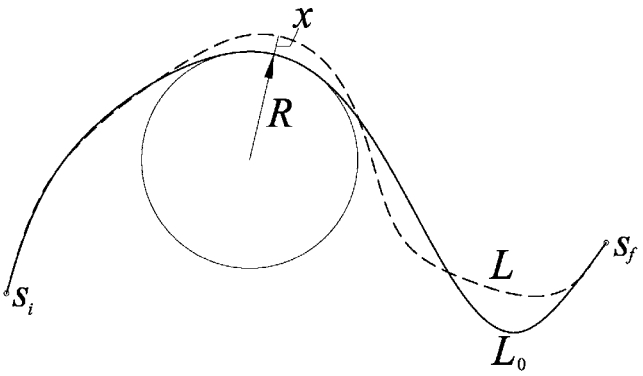

Figure 3.6 Path of the reference particle and some arbitrary particle of length L_0 and L, respectively.

allow the integral in Eq. (3.20) to vanish and yield and an isopath. It is helpful to look at the sets of paired plots in Fig. 3.7. They show two of the simplest schemes for obtaining an achromat. The first achromat, shown by the diagram in Fig. 3.7 (a1), consists of a mirror-symmetric dipole pair with an *x*-focus quadrupole at the center. The plot of its dispersion function in Fig. 3.7 (a2) demonstrates how there is no way to make the integral in Eq. (3.20) vanish. In this case because both the dispersion and *h* cannot chage sign throughout.

The other type of achromat is shown in Fig. 3.7 (b1) and is constructed of four dipoles, in which $h>0$ for the two outside ones and $h<0$ for the inner ones. Four dipole systems have the possibility of having the integral vanish given the right combination of

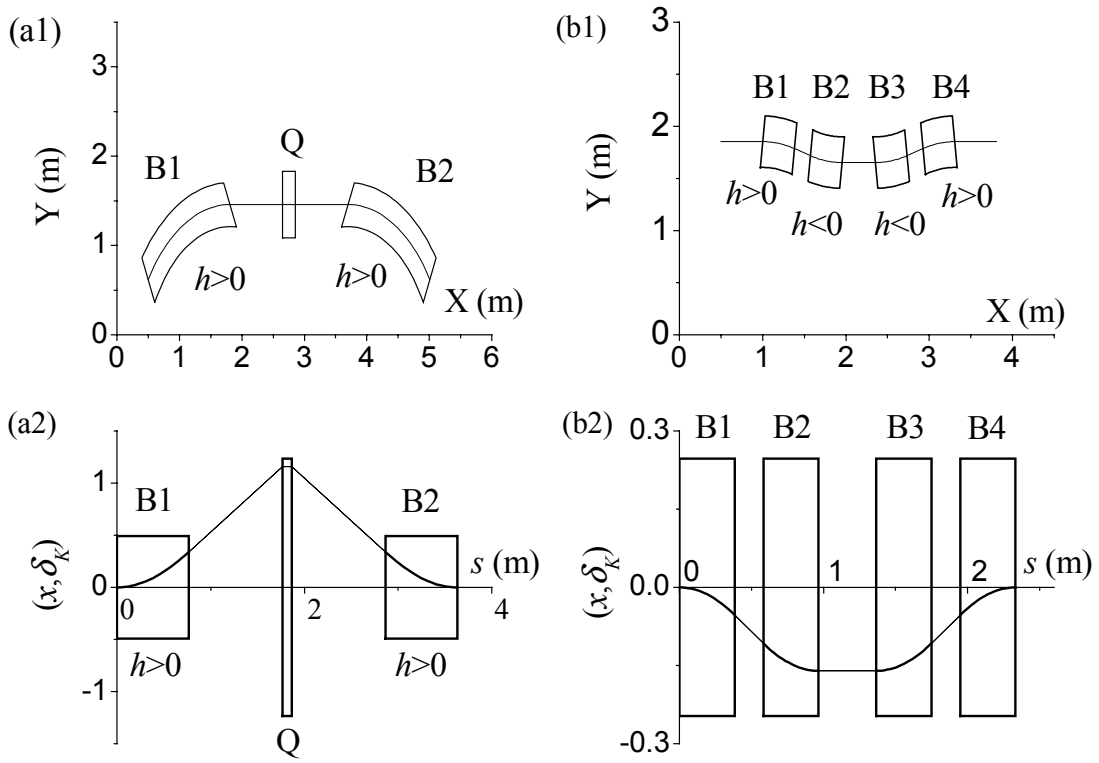

Figure 3.7 Simplest possible pure magnetic achromatic systems. The possibility of obtaining an isopath by the mirror symmetric system (a1) and four dipole system (b1) is determinable from their respective dispersion functions, (a2) and (b2), as described in the text.

bends. For simplicity we show the reference trajectory as coming in and exiting along the same line; however, the actual arrangement would require an overall bend and/or shift as we shall show later on.

As pointed in Chapter 2 the achromat feature is certainly necessary to avoid horizontal dispersion from the beam energy spread. Since the achromat feature depends only on rigidity, then an achromat in δ_K is also achromatic in δ_q, and δ_m; hence, (x,δ_K), (x,δ_m), and (x,δ_q) vanish simultaneously. The same arguments that have been outlined for δ_K here also extend over to systems that are isopath with respect to variables δ_q and δ_m. Isopaths with respect to these two paramters have other unique features that may be understood from the diagram in Fig. 3.6. Suppose that the two particles have the same velocity but different charge. If the path lengths are equivalent, then so will the time of arrival. This implies that the isopath condition with respect δ_q will occur whenever (l,δ_q) vanishes. The same applies when particles vary in mass, where an isopath exist for (l,δ_m)=0. Keep in mind that systems having (l,δ_K)=0 are often referred to as being isochronous in the sense that the particles are not relativistic (β<<1). This condition does not imply equal path length unless $\beta \approx 1$.

All three filtering sections of the RIA driver will certainly require that they be fully achromatic. The first one, which filters DC beams from the ECR, need only be of the mirror-symmetric type in Fig. 3.7 (a1), since there is no need for bunch preservation. The filter systems following the two strippers; however, will require rebunching and longitudinal phase space matching for the sections of linac that follow them. Only systems that have the isopath property, such as the system in Fig. 3.7 (b1), are appropriate for this.

3.2.2 Transporting and filtering of multiple q-charge state beams

As shown by Fig. 3.5 the RIA driver accelerator system requires two stages of charge stripping and filtering of unwanted *q*-states for ions of 238U. The details about the stripping and the effects that it has on the beam are left for the next section. In this section we shall only focus on the design of systems that provide filtering as they match and transport the accepted *q*-states to the section of linac that follows. The minimum requirements of such a system are as follows:

- The system provides dispersion region(s) for expunging unwanted *q*-states and allows the accepted *q*-states to be transported with minimal emitttance growth.
- It must rebunch the beam such that the longitudinal phase space characteristics match with the next linac with for maximum acceptance.
- At least at the rebuncher and exit regions, the system should also retain achromatic character for minimum horizontal dispersion.
- Maintains isopath characteristics at the rebunching and exit regions.

The last requirement is presently the subject of some controversy. It is obvious that there is the need for some control over the arrival time of bunches with different *q*; however, it is not clear whether there may be some advantage gained at the proceeding linac by manipulating the arrival time at the rebuncher. The study of the dynamics of multi-*q* state beams along each section of the linac remains a topic that is open to exploring other techniques. Such techniques may increase the acceptance when applying a shift in energy and/or arrival time between *q*-states before the beam that enters the next linac [Ostroumov00b]. In this study, we shall assume that the conditions required by the next linac are such that each bunch arrives at the same time and energy. Thus, the phase of the

rebuncher shall be set such that $\Delta\varphi$=0º according to Fig. 3.2 so that there is no shift in time or energy between each *q*-state bunch.

To begin with, a detailed analysis of a 180º bend rebunching *q*-state filter at 85.3 MeV/u will be given, and then a description of a simpler alternative follows. After this there will be a description of the solution for the bunching *q*-state filter after the 9.43 MeV/u stripper. That one will consist of a shift that leaves the linac sections offset, i.e. a "dog-leg" illustrated in the diagram in Fig. 3.7.

3.2.2.1 The 180º bend rebunching q-state filter

The beam conditions for the system at 85.3 MeV/u have changed since initial stages of the study. The filter has remained an 180º bend system since that allows the overall length of the accelerator system to be shortened; however, it was initially intended to be a system that accepts *q*-states 89, 90, and 91 of 238U. Since then there has been some speculation as to whether stripping at this energy will actually yield maximum *q*-states distribution at *q*=90 and whether the foil thickness predicted by the codes are accurate (see next section). We shall stick with the initial predictions here, which state that the beam shall have the longitudinal phase space parameters specified in Table 3.2 after going through the stripper. The transverse phase space emittance has an area of 1.5π mm-mr in both the *x*— and *y*—planes. The bounding ellipses have an upright position and the beam has a circular shape with a diameter of 4 mm. The entire transport system should deliver the beam to the entrance of the next linac with the same parameters and having as few higher order effects as possible. Any changes in the design are expected to be relatively small with little or no change in the dynamics of the system.

The initial design had assumed that a 350 MHz linac preceded the stripper section and that the beam should be matched to a 700 MHz linac after the rebunching *q*-state filter.

Since a 350 MHz structure offers more acceptance with fewer longitudinal aberrations, it is chosen for the rebunching cavities located at the midpoint of the system. We assumed that there are two side-by-side two-gap structures located symmetrically about this midpoint, which is labeled as 5 on the diagram shown in Fig. 3.8. The two-gap structures have the parameters that are listed in Table 3.1. The parameters used for the elements shown in the diagram of Fig. 3.8 are listed in Table 3.3. The dynamics that take place can be broken down by the discussion that follows.

Without the RF cavities, the section between points 3 and 5 is that of a mirror-symmetric dipole-pair achromat having 45º bends. The focus is telescopic from entrance to exit in both the *x*— and *y*—planes. The horizontal focus is shown by the solid lines representing rays of varying divergence. An *x*—focusing quad (Q5) sits at either side of point 4 with enough room left between the two to allow the selection of dispersed charge states with $88 \le q \le 92$. Two trajectories of particles having q lower and higher than the reference particle are shown by the dotted line. The largest separation between them exists at point 4, where there is a charge dispersion of (x,δ_q)=-0.53 cm/%q. With this dispersion the maximum separation between beams varying by one charge unit is ~6 mm as shown by the *x*—*y* plot in Fig. 3.9. In the figure we have assumed Gaussian distributions that will encompass 95.5% of the beam that lies within these phase space boundaries. In this case, the boundaries will be circular with 3 mm radius and yields a charge resolving power of $R_q \approx 200$.

Since the higher q-states have a smaller radius at the dipoles, they end up traveling a shorter path. The arrival time difference can be evaluated from $(-\Delta t,\delta_q)$, which is evaluated by dividing (l,δ_q) by μ_0 to obtain units of time. A value of 4.68 ps/%q is

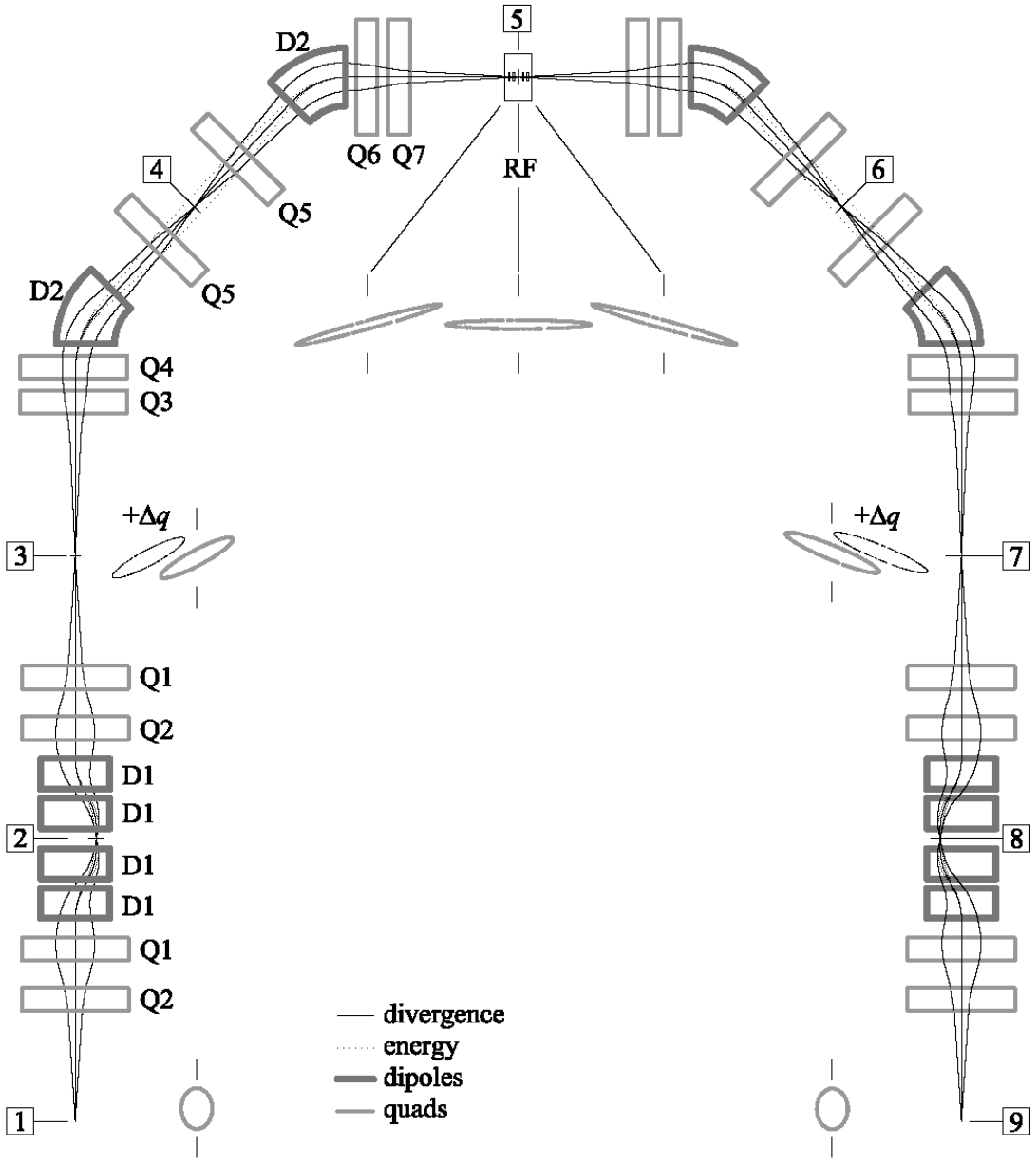

Figure 3.8 Diagram illustrating the 180º bend rebunching q-state filter. The system is mirror symmetric about point 7. The first order longitudinal phase space ellipses are shown for two q-states, one of which has charge q_0 and the other $q_0+\Delta q$. The details of the beam dynamics are described in the text.

obtained this way and yields that a q=91 ion arrives 5.2 ps faster ($\Delta\varphi$=0.7º in terms of the RF cycle) than a q=90 at the end of the mirror symmetric system. In order to offset this effect, a chicane is placed before the 90º bend. Notice that the reference trajector enters

Table 3.3 Parameters used for the elements in Fig. 3.8.

Dipole	Bend radius (cm)	Bend angle (°)	strength (T)
D1	80.3	21.9	4.47
D2	71.8	45	5.0

Quad	Strenght (T/m)
Q1	-24.09
Q2	24.09
Q3	18.70
Q4	-18.70
Q5	17.08
Q6	-17.49
Q7	17.83

Cavity parameters		(see Appendix B)	
frequency	350 MHz	$\Delta\varphi$	0º
Max. Potential	949.2 kV		
RI	2 cm	RLRES	21.43 cm
RO	4 cm	RRES	8.29 cm
RLDT1	12.86 cm	RE	0.5 cm
RD	0.5 cm	Cavity Length	20.72 cm

- 3 cm aperture radius for all quadrupoles.
- Effective length of all quadrupoles is 30 cm.
- All dipole pole gaps are taken to be 5 cm.

and exits along the same line, similar to the four dipole system depicted in Fig. 3.7 (b1). By tuning this system such that the four D1 dipoles are at 4.47 T we can cancel out the arrival time difference right after the second D2 dipole. The first order ellipses in the longitudinal phase space are shown along the inner part of the diagram of Fig. 3.8 at each point labeled from 1 through 9. Notice that the chicane causes the higher charge state ($+\Delta q$) to arrive at position 3 later, in such a way that the bunches of varying q all arrive at the RF cavities at the same time. We also estimate that since $(-\Delta t,\delta_K)$=0.58 ns/%K, a ±5% fluctuation in the phase of the cavity can impose a time spread of about 1.4 ps. This type

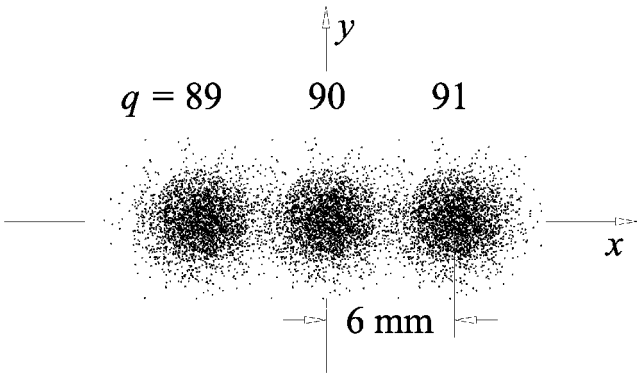

Figure 3.9 Plot of beam distribution for position 5 in Fig. 3.8.

of information is useful when considering the level of phase and frequency stability needed at the RF structures.

We make note of the fact that the chicane is also a mirror symmetric achromat about its center position (point 2). To first order, the multi-q beam is telescopically focused from point 1 to 3 with magnifications of M_x=M_y=1; therefore, the transverse phase space should remain the same as it started at point 1. The orientation of the longitudinal phase space evolves as shown by the phase space plots. Notice that the orientation of the longitudinal is the same as it started at point 1 due to the symmetry of the system about point 5. In the second half of the sytem, the dynamics of the transverse plane evolve in a similar way as in the first but in reverse.

3.2.2.2 Phase space calculations

The higher order effects on the multi-q beam are of major importance. Here, we will demonstrate the effects of 2nd and 3rd aberrations from elements in the transport. It is intuitively clear that particles of higher charge state will obtain stronger focusing in both the transverse planes and the longitudinal plane (see next section). However, such effects are not apparent until one goes to at least 2nd order as expected from magnetic fields of mid-plane or double mid-plane symmetry [Wollnik87f]. Here, the focus will be

exclusively on the effects that are expected from systems having only dipoles, quadrupoles, and axially symmetric RF cavities.

The initial phase space distributions considered here are of the ellipse boundary-type described in the first chapter. There are three boundary distributions of charge states q=89, 90, and 91 that overlap each other initially. A similar approach was shown earlier by Fig. 3.8 by a two q-state system in longitudinal phase space; however, only first order effects were considered there. Here, we demonstrate the higher order effects on the phase space, starting with the transverse phase space plots in Fig. 3.10. We show the phase space that results right after the chicane at point 3 of Fig. 3.8. Only the results of the 2nd order calculation are plotted since the 3rd order results are exactly the same for both x— and y—phase space planes. First order results will show all ellipses overlapping with that of the first order result for the δ_q=0 phase space. Effects from 1st or 3rd order aberrations are not evident, since there are now axially symmetric devices. For the x—a plot on the left the chromatic dispersion along the boundary for ellipses of different q is attributed to the (x,$x\delta_K$), (x,$a\delta_K$), (a,$x\delta_K$), and (a,$a\delta_K$) terms. The aspect ratio between

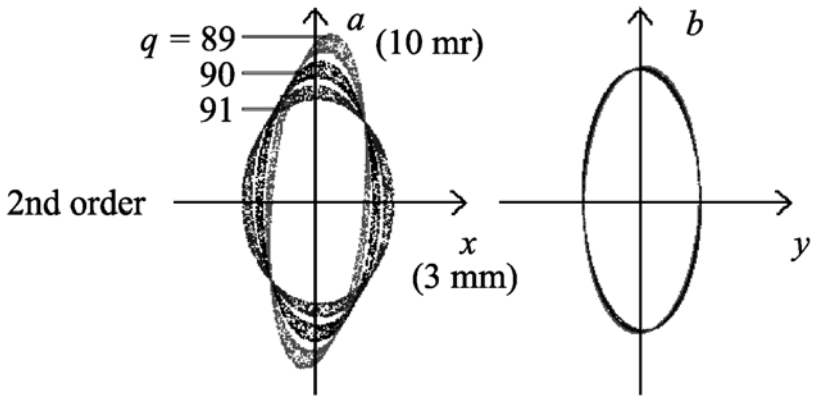

Figure 3.10 Transverse phase space plots at point 3 in Fig. 3.8. Calculated with COSY to 2nd order.

each q-ellipse also vary due the $(x,\delta_K\delta_K)$ and $(a,\delta_K\delta_K)$ terms. Similar effects are present in the y—b phase space from the $(y,y\delta_K)$, $(y,b\delta_K)$, $(b,y\delta_K)$, $(b,b\delta_K)$, $(y,\delta_K\delta_K)$ and $(b,\delta_K\delta_K)$ terms. As shown by the y—b plot at right, these effects are not nearly as strong as they are in the x—a plane. There is somewhat of a different situation once the 90º bend sections are included.

The plots in Fig. 3.11 are calculated for position 9, where the effects of the entire system are included for the 2nd order (top pair of plots) and 3rd order (bottom pair of plots) phase space calculations. From the y—b phase space plots it is evident that there are now much stronger $(y,\delta_K\delta_K)$ and $(b,\delta_K\delta_K)$ effects present. These are attributed mostly to the two 90º bend sections, and some minor contributions from each section of chicane.

The effects at 3rd order are attributed to achromatic focusing effects by the RF cavity. Terms such as $(y,yy\delta_K)$ and $(x,xx\delta_K)$ contribute to the blurring of the boundaries at each

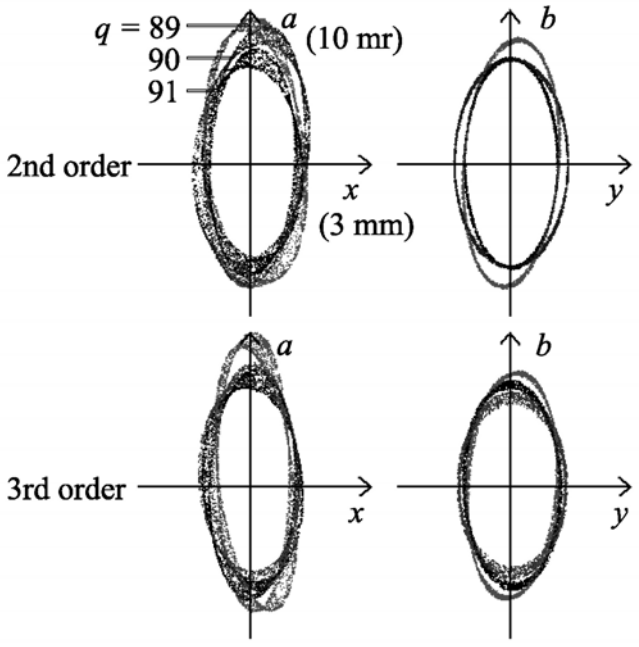

Figure 3.11 Transverse phase space plots at point 3 in Fig. 3.8. Calculated with COSY to 2nd order (top pair) and 3rd order (bottom pair).

respective phase space plane. An estimate is made of the emittance growth in the 3rd order plots based on the amount of extra space that the particles occupy outside of the boundary for the q=90 ellipse. There is ~50% growth in emittance in the x—a phase space, while the y—b plane grows by ~30%. Most of the contributions to the emittance growth in the x—a plane result from the elongation of the q=89 ellipse.

Finally, we show the effects on the longitudinal phase space plot in Fig. 3.12 as calculated at the exit of the system at point 9 of Fig. 3.8. We have used the variable $-\Delta t$ instead of l for the horizontal axis. The maximum extent of the horizontal axis is also shown in units of degrees of the RF phase and is 19º, which is equivalent to 150 ps in terms of the period. Very weak achromatic effects are evident, and for the most part the q-ellipses overlap with little relative shift at their boundaries. What does seem to be a rather large effect is the 3rd order aberration, $(l,\delta_K\delta_K\delta_K)$, of the buncher. The effect is due to the large amount of drift space that is imposed by adding the chicane system on either side. In order to reduce this effect we would need to switch to a lower harmonic

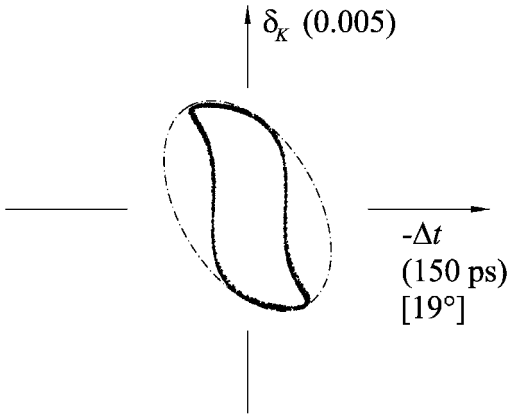

Figure 3.12 Longitudinal phase space ellipse at exit of 180º bend system. Calculated to 3rd order with COSY. Boundary of all q-states overlap. Dashed boundary ellipse contains 50% more area than the bounded phase space area.

frequency or come up with a more compact version of the isopath solution, as will be shown later. A dotted line has been drawn which bounds the phase space in such a way that a new emittance ellipse and orientation can be discerned. It sets the maximum limit of the emittance growth under 3rd order conditions, which under these conditions the boundary has ~50% more area than the area bounded by the initial ellipse. Notice that the distortion on the ellipse makes the phase space seem as if it has a tilt much different than the expected first order results. A more objective way to go about determining the new ellipse characteristics for both the transverse and longitudinal phase spaces is to evaluate the rms emittance and Twiss parameters by the statistical methods suggested at the end of chapter 1. This requires a more realistic initial distribution, such as a Gaussian or water-bag model, and a distribution of particles at each q-state according to the q-state fractions described by the methods of the next section.

Based on these initial calculations it is certain that suppression of higher order chromatic aberrations will be necessary. It was shown in the previous section that there is sufficient dispersion at points 4 and 6 from Fig. 3.8 to separate the different charge states. Any of these two regions is ideal for inserting higher order multipole fields, such as hexapoles and octupoles, for suppressing the chromatic aberrations discussed above. It was shown in the previous chapter how COSY can be used to find the best location and field strengths necessary from the higher order multipoles to suppress geometrical aberrations. Since the mirror-symmetric dipoles in the mass separator could not separate the masses far enough in the multipole region, very little could be done about chromatic aberrations there. In the case of the multi-q system here, there seems to be a negligible amount of geometric aberrations in comparison with the chromatic aberrations. It is clear

that further studies with the *q*-filtering systems will be necessary to resolve such issues for the final RIA design.

3.2.2.3 Other isopath systems under consideration

The 180º isopath described above serves mainly as a proof of principle. Further studies have allowed us to find other practical solutions in terms of shortening the path length and reducing the number of necessary elements. A scheme that would replace the function of the 180º isopath described earlier is shown in Fig. 3.13. The system is essentially a hybrid between the mirror-symmetric 90º achromatic bend in Fig. 3.7(a1) and the four-dipole chicane of Fig. 3.7(a2). The inside dipole bends beyond what an ordinary chicane would in order to provide an overall bend by the entire system. With the appropriate tune, the switch in polarity of the dispersion function will lead to a vanishing of the integral in Eq. (3.20). Implementing this scheme into a 180º isopath results in the system shown in Fig. 3.14. The first dipole (B_1) bends the beam outward by 10º, while the next one (B_2) bends inward by 55º before the beam reaches the halfway

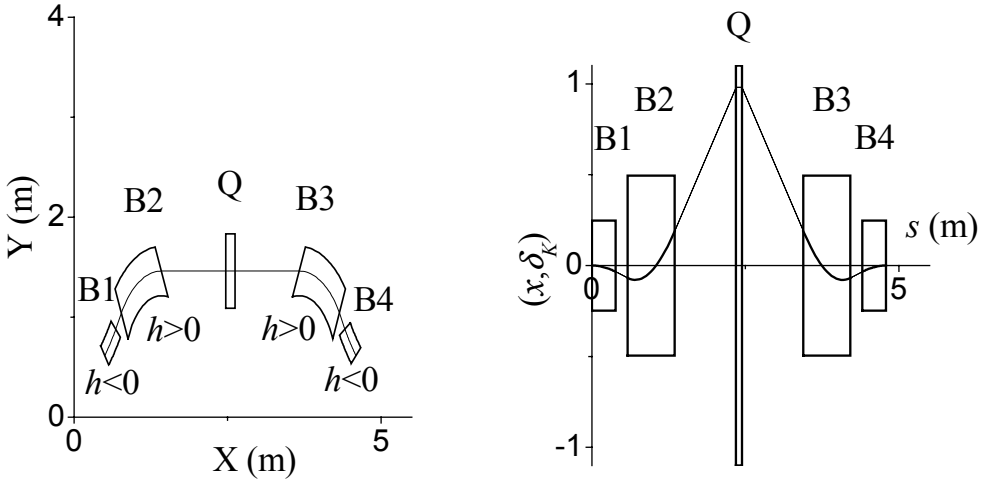

Figure 3.13 Diagram of an alternative scheme of obtaining an isopath system with four dipoles and without the use of a chicane as in the system in Fig. 3.8 does (left). Plot of the dispersion function along the optic axis (right).

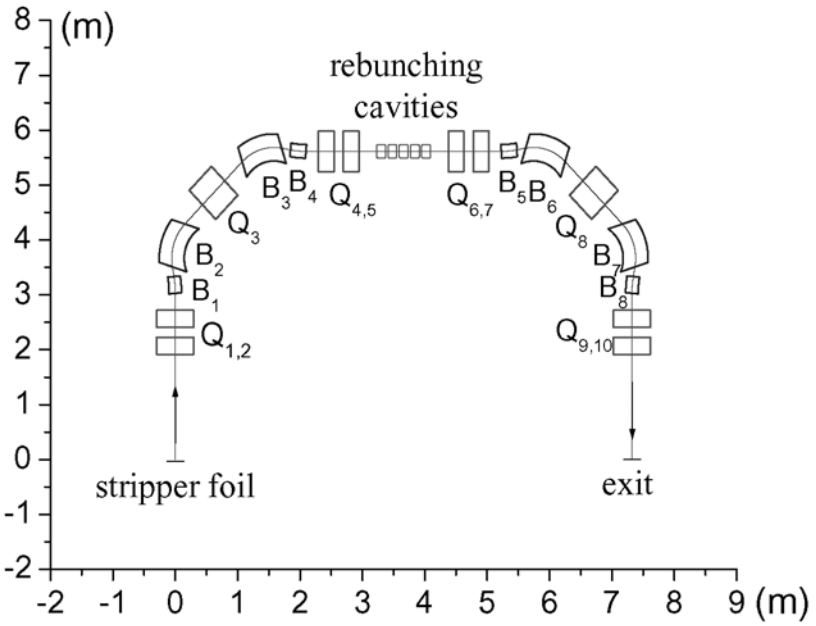

Figure 3.14 180º Bend scheme.

point of the achromat. The system is mirror symmetric about the midpoint of Q_3 only if the rebunching cavities are off. The entire system is mirror symmetric about the center point of the cavity array even with the fields from the RF cavity. We do not go into the full details of this system, but instead refer to the literature where the work has been reported [Portillo01].

Lastly, we mention two other systems that are being considered for the design of the RIA driver accelerator. The dog-leg system shown in Fig. 3.15 will be the rebunching *q*-state filter following the first stripping stage of uranium at 9.43 MeV/u. It bends outward at B_1 then back inward at B_2 and takes on an anti-symmetric geometry at the center point of the expected superconducting RF (labeled as SRF) cavities. This system is unique in that it is not truly a full achromat at the center point since (a,δ_K) does not vanish. Since the region of the cavity array is expected to be short (~1 m), then the horizontal dispersion at positions away from the center should be negligible.

The advantage of the dog-leg scheme is that it leaves room for a branching out beam line that makes use of beam that would otherwise be diverted to a dump. Instead it can be diverted to a medium energy experimental area. It is expected that ~70% of the beam would be accepted as a five charge state beam with reference charge $q_0 \approx 70$. Since the q-state fractional distribution is very symmetric, then about 15% of the unaccepted beam can be diverted to the experiments and the other half is diverted to a beam dump. Notice that we have not actually discussed how the unwanted multi-q states will be diverted away from the accepted q-states. Future studies will need to incorporate septum magnets for this purpose.

The last scheme, which is depicted in Fig. 3.16 is an option that had originally been considered in an alternative design. It assumes that there are three stripping stages with this one being the first one. It would strip a uranium beam of ~4 MeV/u at initial mean charge state of $\overline{q} \approx 28.5$ up to $\overline{q} \approx 54$. This system is actually not an isopath or full achromat at the center and is designed such that there are minimal effects from the time of arrival differences of each different q-bunch. It functions much like a chicane but with rebunching at the center position. At present, this option has been ruled out due to consideration of the extra beam losses in a relatively small cost section of the linac.

There are still issues that need to be resolved with the q-state filters. The higher order effects for all these systems are still expected to be a problem if not corrected. Studies are ongoing in this matter to finalize the designs. At this point, however, it has been shown that the principles of the isopath transport can allow us to determine design solutions that are practical for the RIA facility.

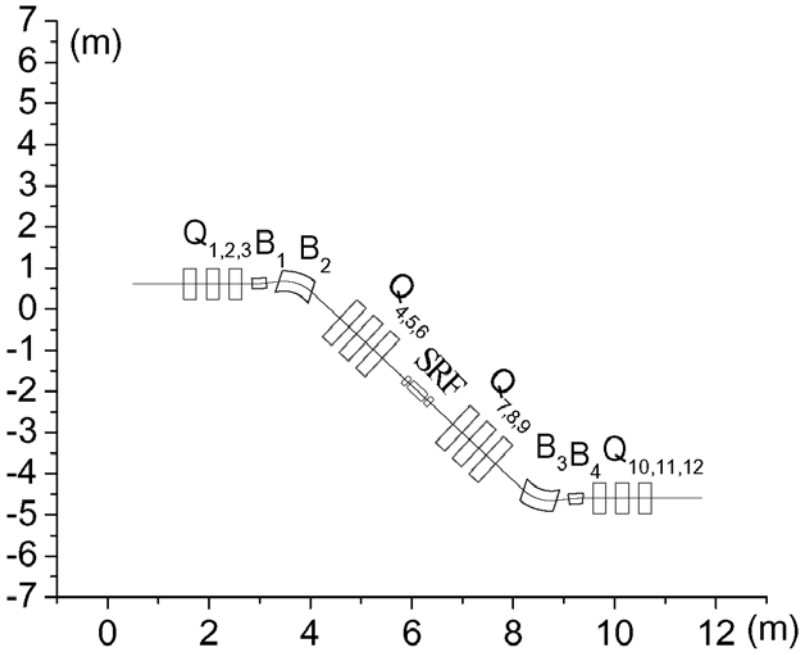

Figure 3.15 Dog-leg scheme. The SRF stands location for superconducting RF cavities.

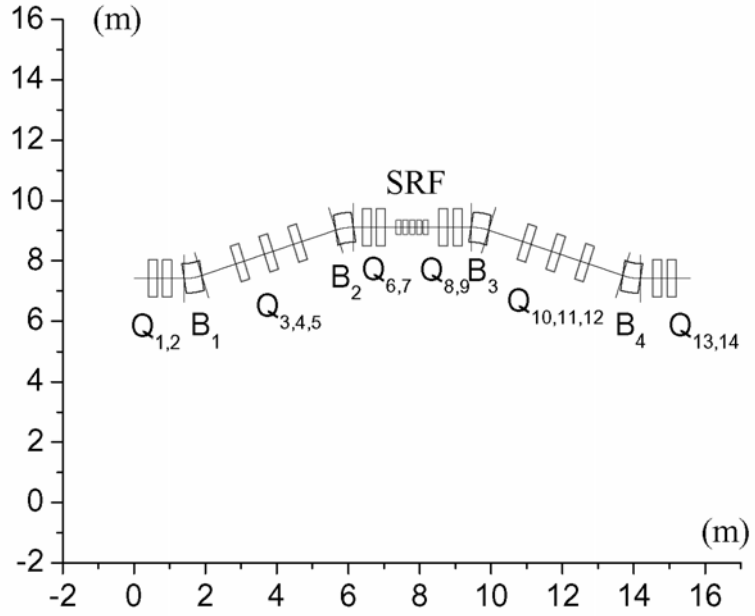

Figure 3.16 Chicane scheme.

3.3 Determining the distribution of *q*-states

3.3.1 Importance of maximizing q

Maximizing the charge state of heavy ions in an accelerator system plays a critical role in the design. One advantage of going to higher q is that lower field strengths for bending and focusing of the beam are necessary. Note that the maximum energy that may be bent by a magnet of rigidity, χ_m, is given by the equation,

$$K / A = \frac{c^2 \times 10^{-12}}{2u} \chi_m{}^2 \left(\frac{q}{A} \right)^2 , \tag{3.21}$$

where the units are in MeV/u if the atomic mass unit, u=931.5 MeV/c^2, and rigidity is in Tesla-meter. K/A depends on the square of the charge of the particle. For example, at q/A=90/238 and χ_m= 5 Tesla×0.72 meter the maximum beam energy is 90 MeV/u. This factor is especially important for cyclotrons, where χ_m is already set at the technological limit of the magnet(s) and the only gain may come from increasing q.

Going to higher q will require fewer accelerating structures for attaining the final energy of interest. In this case, the effect of increasing energy gain is linear with q/A. This can be readily understood by expressing the energy gain per accelerating structure in the form [Ostroumov00b],

$$\Delta K = \frac{q}{A} e\overline{E}_s(\beta_G) \cdot T(\beta, \beta_G) \cdot L_c(\beta_G) \cdot \cos\varphi_s \tag{3.22}$$

Here, $\overline{E}_s(\beta_G)$ is taken to be the average electric field over the effective gap length, $L_G(\beta_G)$, that is experienced by some particle traveling at a constant velocity, $c\beta_G$. The length $L_G(\beta_G)$ is approximated to be the length of region in which the magnitude of the field is above ~95% of maximum. In determining $\overline{E}_s(\beta_G)$ it is assumed that the center point between each gap is separated by some integral distance of the RF wavelength,

$\beta_G \lambda(n+1/2)$ (see derivation of Eq. (3.11)), and also that the cavity phase is set to the phase angle, φ_m, where the β_G particle gains maximum ΔK. The cosine term in the equation accounts for the use of sinusoidal fields in the cavity at phase angle, φ_s, relative to φ_m. φ_s is often referred to as the synchronous phase, since it usually is chosen such that there is optimum stability in the oscillations of the bunch. Finally, the term, $T(\beta,\beta_G)$, is called the transit time factor and accounts for the fact that particles of velocity differing from $c\beta_G$ will obtain less than optimal acceleration. Thus, it will always be less than unity, except when $\beta=\beta_G$. Notice that, except for $T(\beta,\beta_G)$ and φ_s, all terms may be determined directly from the on-axis field, $E_s(s)$. The transit time factor may be determined by evaluating ΔK at $\varphi_s=0$ for every β. Although not demonstrated here, this is an ideal application for the new COSY elements described in section 3.1.

Modeling arrays of structures in the form of Eq. (3.22) is the method used in evaluating the final energy of the full driver linac. Accurate results will depend on how well the process of stripping of electrons at foils is understood. As we shall demonstrate below, the distribution of charge states depends on the incident energy of the particle. As a result, there are many combinations of locations along the linac at which the beam can be stripped, and each one will yield different charge distribution and final mean charge state, $\overline{q}$. Knowing the q-state distribution is also necessary to determine the requirements for handling of the q-states to be accepted or dumped at q-filter systems of the type described in the previous section.

The most challenging species of ions to strip and accelerate are those of 238U. At any energy, it will yield the lowest q/A of any other stable ion and require energies above ~500 MeV/u to approach the fully stripped state (q/A=92/238=0.387). For the RIA

design it was necessary optimize for lowest cost by strategically determining the best places along the linac to strip. As shown in Fig. 3.5 the two strippers are at ~10 and 85 MeV/u for the uranium beam. As we shall demonstrate below, the two energy regimes are quite different and require their own respective analysis. A brief survey of the available methods for determining q-states at each energy regime is given below.

3.3.2 The charge state evolution process

Before describing the techniques for evaluating q-states, it is instructive to look at the underlying process. Consider that the particle may be at some charge state, q, and additionally, in some electronic excited state. Neglecting nuclear excitation effects, the collisions that the particle undergoes while traveling through some dense region of material cause the following types of processes:

- *Excitation* of the most loosely bound electron, or active electron, of a q-state ion to higher excited states. In the energy level diagrams shown in Fig 3.17, this would mean a jump to any state above the ground state within the left diagram.
- *Ionization* from charge state q to q+1. The simplest case being that in which the electron receives enough momentum from the collision to overcome the ground state ionization potential, $V_{i,N=0}(q)$ and go to the ground state of the q+1 ion. The arrow that goes from left to right between the diagrams illustrates this. The ion can also undergo multiple excitations through multiple collisions before climbing above the full $V_{i,N=0}(q)$ potential.
- If a more tightly bound electron is extracted from an ion at q, then the q+1 will be left in an excited state (levels above ground on the right diagram). If there is enough potential energy remaining, then the q+1 ion may then de-excite by

emitting another electron (Auger process) and/or photon(s). This type of *de-excitation* processes is associated with some lifetime and can occur even after passing the material.

- The q-state ion can also *capture* an electron from the atoms/ions in the material that it collides with. As such, the captured electron will go into either the ground state of q-1 or into one of its excited states. Radiative electron capture (REC) occurs whenever there is an ejection of a photon as the electron is captured, which is the inverse of the photoelectric effect. A non-radiative capture (NRC) occurs when the electron is transferred from a bound state of a target electron to the bound state of the active electron of the projectile.

Note that N is some integer that has been treated as a quantum number to represent the state of the ion. Although a more detailed set of quantum numbers may be used, we adopt this notation for simplification in which the ground state is at N=0 and all N>0 are excited states.

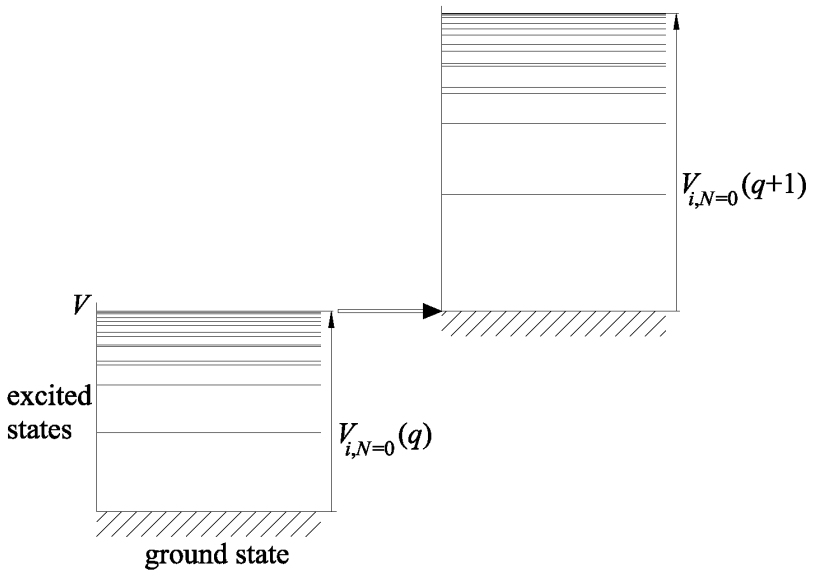

Figure 3.17 Hypothetical quantum state level diagrams showing a simplified transition from a q to q+1 ionization state.

Every possible process should be associated with some cross section that specifies the probability of occurrence with respect to the independent variable. Instead of using time for the independent variable, it is usually more convenient to use the displacement, z, of the particle along the direction of impact. The elapsed time may be extracted from the average instantaneous velocity of the particles. Here, we shall interpret $\sigma(q,N;q',N')$ as the probability per unit depth of some ion at charge and quantum states, q and N, respectively, going to states q' and N' through either a collision event or spontaneous process. We call $Y_{q,N}$ the fraction of particles in the (q,N) state, such that the sum of the fractions over all possible states are conserved through

$$\sum_{q}\sum_{N} Y_{q,N} = 1. \tag{3.23}$$

The derivative with respect to z of all the fractions form a system of linear coupled differential equations in the form of [Betz72],

$$\frac{dY_{q,N}}{dz} = \sum_{q\neq q'}\sum_{N\neq N'}\left[Y_{q,N}\cdot\sigma(q,N;q',N') - Y_{q',N'}\cdot\sigma(q',N';q,N)\right]. \tag{3.24}$$

As long as all the particles have the same mass then it is possible to separate them with respect to their beam rigidity and measure the total yield at some q-state,

$$Y_q = \sum_{N} Y_{q,N} = \frac{J_q}{J}. \tag{3.23}$$

The rigidity spectrometer cannot resolve excited states with a given q; thus, all N are lumped together in flux, J_q. Here, J is the total flux of all possible q-states. This equation establishes the relationship between measurable and evaluated quantities.

In order to model the evolution of charge states, stopping powers, and kinematic momentum transfer one must determine the cross sections for the most dominant interactions. The cross sections will vary along the depth of the gas or solid as the

velocity of the projectile, v_p, drops and the population of excited and ionization states evolve. Due to the effect from screening of the nuclear charge many of these cross sections tend to depend strongly on the velocity of the most loosely bound electron, or the active electron, of the projectile. This velocity is approximately given by [Betz72],

$$v_e = v_0 q Z_p^{-1/3}, \tag{3.24}$$

for an ion of charge state, q, that is in the ground state. Here, Z_p is the atomic number of the projectile, Z_t is the atomic number of target atoms, and $v_0=e^2/\hbar=2.188\times x10^6$ m/s is taken to be 1 a.u. (velocity in atomic units). This approximation is valid as long as $(Z_p-q)\geq 3$ and $Z_p\geq 36$. In terms of the screening effect there are three distinct velocity regimes described as follows:

- In the low velocity regime ($Z_p \cdot v_p << v_e \cdot Z_t$) the electron capture cross section dominates and a few interacting molecular states can be used to determine the state of the ion.
- In the high velocity regime ($Z_p \cdot v_p >> v_e \cdot Z_t$) the excitation and ionization cross sections dominate such that perturbative two-atomic state models determine the state with sufficient accuracy.
- In the intermediate velocity regime ($Z_p \cdot v_p \sim v_e \cdot Z_t$) the capture cross sections are comparable in magnitude to the excitation and ionization cross sections. Thus, developing models that reproduce experimental results is especially crucial in this regime [Vernhet96].

Since there are a large number of possible excited states within each q-state, there are necessarily quite a large number of cross sections to reference or evaluate. The number of differential equations may also become so large that it becomes almost impossible to

achieve good accuracy and consistency. Thus, it is necessary to make as many simplifications by grouping together any states that are similar and applying any available scaling laws to reduce the amount of cross section data that needs to be stored and referenced. We shall describe some codes that have been developed under this principle and demonstrate some of the results that they yield.

Before going into details about the models, we should mention the concept of the equilibrium charge state distribution. In order to demonstrate this concept results taken from the ETACHA [Rozet96] code system and illustrated in Fig. 3.18. The plots are of Y_q in units of percent versus the depth into the target material, which we label as thickness. The calculation assumes an ion beam of 238U incident at 24.1 MeV/u on aluminum ($Z_p \cdot v_p / v_e \cdot Z_t = 0.09$) at 2.7 g/cm^3. The details of the calculations will be given later, but for now we should like to point out the effects that occur after a sufficient amount of interaction with the target has occurred. Notice that the fractions tend to level off after a thickness of about 1 mg/cm^2 as if to reach some equilibrium. The plot on the top accounts for the average energy loss as the particle goes through the material. In this particular case, the ion will lose about 1.4% of energy at 1 mg/cm^2, and over 10 times that amount by the time it gets to 10 mg/cm^2. The energy loss has been evaluated through numerical integration of the stopping powers, $S(K)=dK/dz$, which may be obtained from the SRIM code system [SRIM98]. The plot at the bottom is for the yields in which the cross sections are not corrected for the energy loss in the target. If the plot were not logarithmic along the horizontal axis, then the two plots would look almost identical.

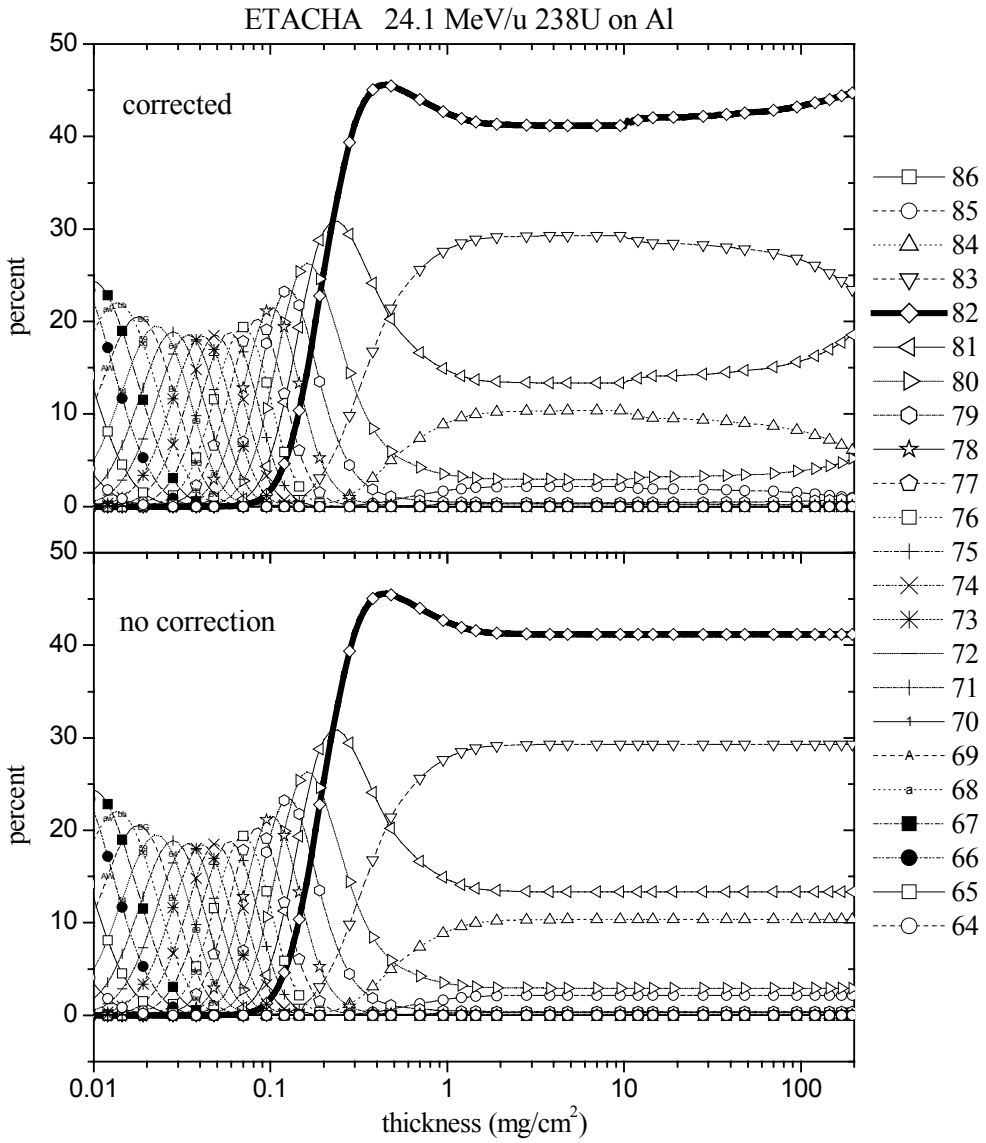

Figure 3.18 Charge state evolution of 238U on Al foil according to ETACHA. A comparison is made between a calculation using cross sections that are corrected for energy loss (top) and one without corrections (bottom).

Realistically, the corrected values will not completely reach some equilibrium because the velocity of the particle is constantly being reduced by interactions with the target material. The uncorrected plot, is merely a hypothetical process that is assumed to occur in many measurements of equilibrium charge state distributions. For many practical situations, such as this one, it is a reasonable approximation since for all $Y_{q,N}$,

$$\frac{dY_{q,N}}{dz} \rightarrow 0\,, \tag{3.24}$$

after some depth. Whenever this type of equilibrium of fractions exist, or may be assumed to exist, we shall refer to the equilibrium distribution of the fractions, Y_q, as $F(q)$. We shall first discuss some methods used to determine the equilibrium charge state distribution through empirical parameterizations and then discuss other methods that numerically integrate the set of ODEs in Eq. (3.24).

3.3.3 Empirical methods for determining F(q)

Target and particle systems in which q-state equilibrium regions have been observed have been extensively studied and documented in the past [Reynolds55] [Baron88] [Shima92] [Baron93] [Leon98]. With experimental data it has been possible to develop methods of calculating equilibrium charge state distributions using semi-empirical formulations. We shall provide the formulations prescribed by both [Baron93] and [Leon98], since they are complementary to each other in terms of the range of species that they cover. The following is a summary of the conditions upon which the formulations are based on:

- The formulation in [Baron93] is based on extrapolations from experimental results for ions species within $18 \leq Z_p \leq 92$ and energy range of $0.2 \leq K/A \leq 10.6$ MeV/u.
- The formulation in [Leon98] is an extension of the work in [Baron93] with additional data for species within $36 \leq Z_p \leq 92$ and energy range of $18 \leq K/A \leq 44$ MeV/u.

The formulations are based on the assumption that the equilibrium q-state distribution is symmetric about some value, $\overline{q}_e$, as long as the distribution does not extend to the region

of (Z_p-q)<3. Although shell effects are observable in some studies [Shima92], they are generally negligible for these approximations. For systems in which very few electrons are left, the distribution is non-symmetric and the shell effects become pronounced enough so that they may no longer be neglected, especially for helium like ions. The form of the symmetric distribution is represented best by a Gaussian that is of the form,

$$F(q) = \frac{1}{d\sqrt{2\pi}} \exp[-(q - \bar{q}_e)^2 / 2d^2)], \tag{3.25}$$

where by definition of $F(q)$ we should have that the mean is given by,

$$\bar{q}_e = \sum_q q \times F(q). \tag{3.26}$$

and square of the deviation by,

$$d^2 = \sum_q (q - \bar{q}_e)^2 \times F(q). \tag{3.27}$$

The mean equilibrium charge is evaluated from the semi-empirical formulation given by,

$$\bar{q}_e = Z_p \cdot f(Z_p, \beta) \cdot h(Z_t, \mathrm{v}_p, Z_p) \cdot g(Z_p), \tag{3.28}$$

where the first of the three function carries the dependence on the projectile velocity, $\mathrm{v}_p = \beta c$, by

$$f(Z_p, \beta) = \begin{cases} 1 - \chi \exp\left(\dfrac{-83.275 \times \beta}{Z_P^{0.447}}\right) & \text{[Baron93]} \\ 1 - \exp\left(\dfrac{-83.275 \times \beta}{Z_P^{0.477}}\right) & \text{[Leon98]} \end{cases}. \tag{3.29}$$

The formulation of Baron requires that

$$\chi = \begin{cases} 0.9 + 0.0769 \times (K / A) & K/A > 1.3 \text{ MeV/u} \\ 1 & K/A \le 1.3 \text{ MeV/u} \end{cases} \tag{3.30}$$

for best results. The target Z_t dependence is embedded in the function,

$$h = \begin{cases} [1 - 5.21\times10^{-3}(Z_t - 6) + 9.56\times10^{-5}(Z_t - 6)^2 - 5.9\times10^{-7}(Z_t - 6)^3] & \text{[Baron93]} \\ [(0.929 + 0.269\exp(-0.160Z_t)) + (0.022 - 0.249\exp(-0.322Z_t))\frac{v_p}{Z_p^{0.477}}] & \text{[Leon98]} \end{cases} \quad (3.31)$$

Leon adopts the same form of the function, *g*, as given by Baron in the form,

$$g(Z_P) = [1 - \exp(-12.905 + 0.2124(Z_P) - 0.00122(Z_P)^2)] \quad (3.32)$$

The form of the standard deviation is evaluated by the functions,

$$d = \begin{cases} 0.5\sqrt{\bar{q}_e\left(1 - (\bar{q}_e / Z_p)^{1.67}\right)} & \text{[Baron93]} \\ 1.1432\sqrt{\bar{q}_e[0.07535 + 0.19(\bar{q}_e / Z_P) - 0.2654(\bar{q}_e / Z_P)^2]} & \text{[Leon98]} \end{cases} . \quad (3.33)$$

The two models give about the same deviation within a few percent; however, they differ in $\bar{q}_e$. The Baron model tends to give a higher $\bar{q}_e$ by up to 10% at the low energy limit for Z_p~90. The difference diminishes with Z_p until it is ~1% higher for Z_p~30. The difference becomes less at the higher energies until is only a fraction of a percent at ~40 MeV/u. At the high energy end, both models overestimate the mean charge state compared to the available data in [Leon98] and agree with the data best at ~30 MeV/u.

The results given by the semi-empirical formulae are useful for approximating the equilibrium charge state; however, they offer no information about the variation of the distribution or of the thickness required for equilibrium. The studies done in [Leon98] do not attempt to characterize the thickness, but merely mentions that for all their measurements the thickness of the foils varied from 1 μg/cm^2 to several mg/cm^2. On the other hand, Baron offers the following formula for determining the equilibrium thickness in μg/cm^2 given that *K/A* is in units of MeV/u [Baron79]:

$$D_m[\mu g / cm^2] = 5.9 + 22.4(K / A) - 1.13(K / A)^2 \quad (3.34)$$

In his equation, there is no attempt to put any Z_t or Z_p dependence. Much of the reason for the lack of characterization with target thickness has to do with the erratic uniformity found in most available thin foils. This applies especially for carbon foils, which are the most commonly used. Measurements usually only provide an average value of the thickness in the region of the beam; however, the actual thickness is very non-uniform and it is not uncommon for it to deviate by as much as a by a factor of two from the average value. This makes it difficult to correlate the thickness with the charge distribution, and consequently, with the atomic numbers of projectile and target as well. To obtain data that is associated with less uncertainty more stringent requirements will be needed of the foil uniformity. The other alternative is to rely on accurately known cross sections to extrapolate the thickness as explained below.

The work of Dmitriev focused on determining the equilibrium target thickness from capture and stripping cross sections [Dmitriev82]. He takes the cross section of losing the final electron before obtaining a fully stripped ion, $\sigma_l(Z_p\text{-}1,Z_p)$, and the capture, $\sigma_c(Z_p, Z_p\text{-}1)$, to the hydrogen-like ground state and applies it to the equation,

$$\varepsilon\,\bar{q}_e = \left|Y_q(0) - Y_q(\infty)\right| \exp\left[-D(\bar{q})\rho(\sigma_l + \sigma_c)\right]. \qquad (3.35)$$

Here, the factor $\rho=A_t/N_A$ converts D into units of atoms/cm^2, where A_t is the atomic mass of the target and N_A is Avogadro's number. $Y_q(0)$ and $Y_q(\infty)$ are the initial and equilibrium fractional yields for $q=\bar{q}$. Solving for $D(\bar{q})$ will, therefore, yield the thickness necessary to obtain mean charge state $\bar{q}$ at equilibrium. The factor ε is a scaling factor that he determines should be about 0.01 to fit the data from empirically determined cross sections at energies below 100 MeV/u [Dmitriev79]. For energies above this limit he adopts the cross sections from a Born approximation for electron loss

[Senashenko70]. The results for stripping of uranium are shown in the plot of Fig. 3.19, along with those of the linear formula from Baron in (3.34).

Also plotted are some values that have either been reported as a measured quantity or have been determined by charge evolution codes. The following explains the data points labeled 1 to 3:

1. Experimentally measured equilibrium thickness values from [Scheidenberger98].
2. Experimentally measured equilibrium thickness values from [Leon98].
3. Evaluated using the codes GLOBAL and ETACHA.

There is little experimental work available in the literature about the stripping of uranium at the region between ~40 and 100 MeV/u, thus we have resorted to the results of some available codes that will be described later. The point at 45 MeV/u is at 21 mg/cm^2 as deduced from the results shown in Fig. 3.20 for an ETACHA calculation of U ions on a C

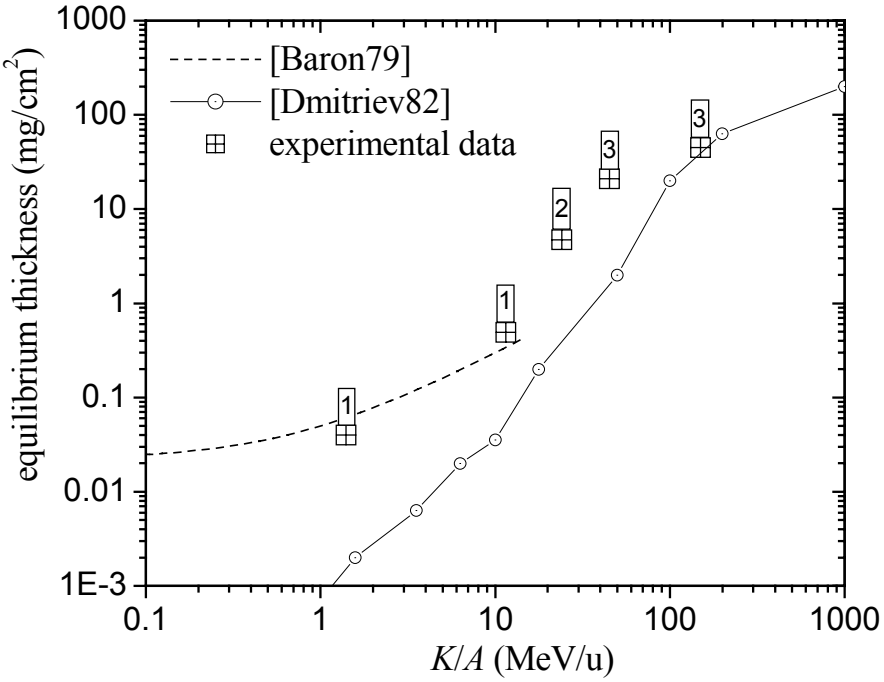

Figure 3.19 Equilibrium thickness for uranium beams according to formulation by Baron and Dmitriev as explained in the text. Also shown are values determined as explained in the text.

foil. The point at 150 MeV/u is taken from a calculation from the code GLOBAL, which indicates that equilibrium sets in at about 45 mg/cm^2.

The formulation of Baron gets within 10% of the experimental value at 1.4 MeV/u and within 30% for the data at 11.5 MeV/u. Beyond this point the approximation seems to be no longer valid. The thickness evaluated by the model of Dmitriev seems to be in agreement with the available codes for high energy, where the ions are fully stripped, but fails to agree with the experimentally determined values at the lower energies. Neither of the two models seems to predict the experimentally determined value at 24.1 MeV/u. There is, however, some agreement at this point between the calculations shown in Fig. 3.18 (corrected) from ETACHA for stripping with aluminum foils. The point at which the fraction for charge state 83 is a maximum occurs at ~4 mg/cm^2 and it is also the point at which there is maximum mean charge state. If this were to be interpreted as being the point of equilibrium then there is good agreement with the experimentally determined

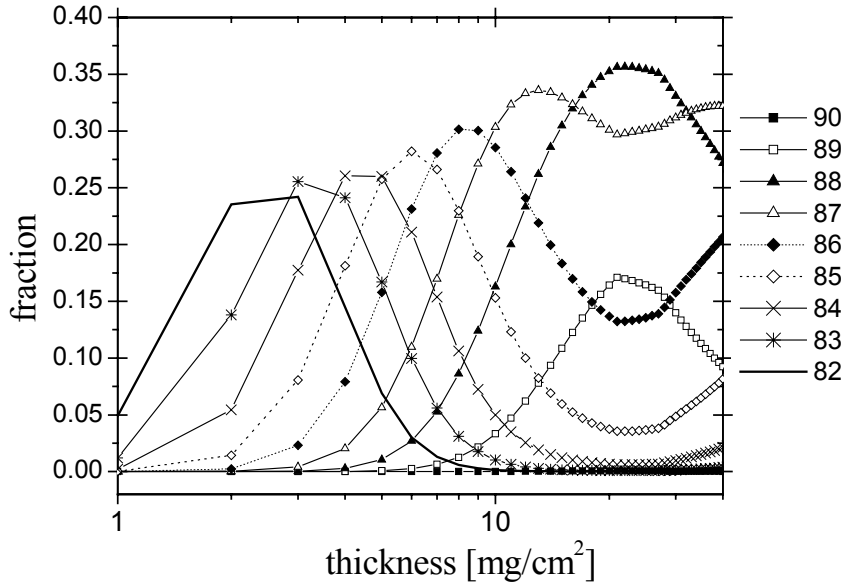

Figure 3.20 Evolution of charge states for *K/A*=45 MeV/u ions of U according to the ETACHA code. The maximum mean charge occurs at ~21 mg/cm^2 at which point $\bar{q}$ =52.5 and $\tilde{q}$ =0.69.

value of 4.7 mg/cm^2 at point 2 in Fig. 3.19. For this measured value, [Leon98] provides tabulated data of charge state distributions versus the thickness of the foil. Unfortunately, this is not true of the values taken from [Scheidenberger98]; however, the author assures the reader that the results are obtained from measurements taken at equilibrium.

3.3.4 Codes available for determining charge state evolution

Up to this point we have not described codes that take the approach of solving the form of Eq. (3.24) numerically. In principle, it is possible to apply this type of solution to particles having energies within the range of the empirical formulations; however, the number of electrons and excited states that the code must account for becomes too large to be practical for heavy ions, such as uranium. Fortunately, the charge screening effects cause most of the shell effects to be small enough that the empirical formulas can be scaled with the available data to provide a reasonable prediction of the charge state distribution.

At energies where the ions become almost fully stripped scaling laws tend to be less reliable and it becomes necessary to account for quantum shell effects. Typically, the excitation, ionization, NRC and REC capture cross sections need to be specified for each Z_p and Z_t combination as a function of v_p and the physical characteristics of the target, such as the density. We provide a brief summary of two codes that can be used for evaluating the evolution of charge states as a function of thickness.

3.3.4.1 ETACHA

The ETACHA code system has been tailored around experiments from the GANIL cyclotron facility for ion energies ranging from 10 to 80 MeV/u for Ar, Ca, Fe, and Kr ($18 \geq Z_p \leq 36$) on targets that range from Z_t=1 to 54 [Rozet96]. The code solves the system of first order differential equations through numerical methods by accounting for

up to 28 electrons (minimum charge state of $q=Z_p$-28) distributed over the n=1, 2, and 3 subshells. It assumes that the first Born approximation, or plane-wave Born approximation (PWBA) is valid as long as the ratio $(v_e/v_p)(Z_t/Z_p)<0.35$; i.e. $K_{\text{proton}}>200$ keV for p→H collisions. As such, it evaluates excitation and ionization cross sections from the PWBA using screened hydrogenic wave functions. For excitation and de-excitation the code also allows interaction with the n=4 subshell by applying a $1/n^3$ scaling law in evaluating the cross sections. In evaluating partial and total radiative Auger decays, the code uses a method prescribed by [Larkins81].

For electron capture the code applies the Bethe-Salpeter formula [Bethe57], which derives from an Eikonal approximation for evaluating NRC cross sections [Meyerhof85]. These approximations are best suited for the energy region in which $(v_e/v_p)(Z_t/Z_p)$ stays below ~1. Beyond this limit, the code allows the user to apply a more accurate method in which NRC cross sections are evaluated through the continuum distorted wave (CDW) approximation at the expense of more computing time [Belkié84]. The code also allows a similar CDW approximation to be applied for evaluating the ionization cross sections when $(v_e/v_p)(Z_t/Z_p)$ is above unity.

In order to minimize the number of differential equations the calculation neglects any spin orbital coupling effects. This allows the code to treat each electron within each of the 1s, 2s, 2p, 3s, 3p, and 3d shells as being the same, and a scaling law is used to average over the transition rates between the n=1 to 4 subshells and the orbital states within each them.

To test the results from the ETACHA model we have compared the mean charge states with those of tabulated experimental results for 24.1 MeV/u [Leon98]. The foils

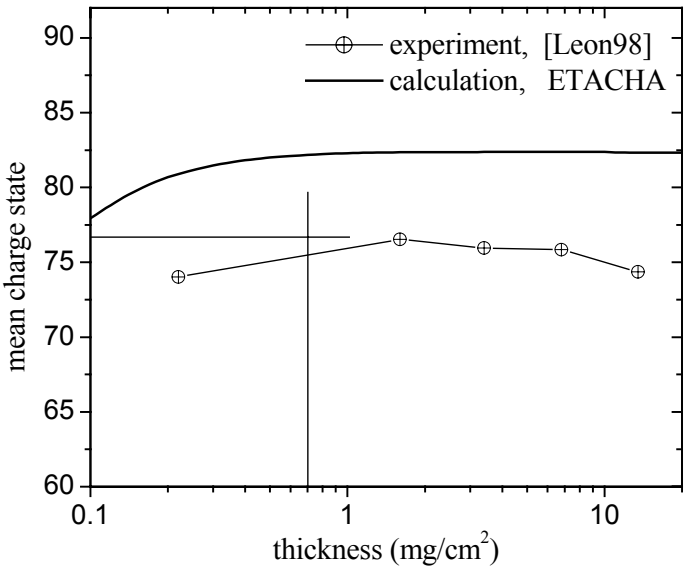

Figure 3.21 Mean charge states evaluated from charge state evolutions of 24.1 MeV/u 238U from experimentally measured values [Leon98] and from the code ETACHA. The lines that intersect mark equilibrium thickness (0.7 mg/cm^2) and mean charge ($\bar{q}$ =76.6) according to the analytical models.

are of aluminum and vary in thickness from 0.2 to 13.5 mg/cm^2. The results are plotted in Fig. 3.21. The mean charge appears to be at a maximum at $\bar{q}$ =76.5 for 1.5 mg/cm^2. According to the results from the ETACHA calculation, at this same thickness $\bar{q}$ levels off to a maximum of 82.3 (8% higher). The crossing lines indicate the thickness given by Eq. (3.32) and the value of $\bar{q}_e$ predicted by the empirical model of ref. [Leon98]. The values are 0.7 mg/cm^2 for the thickness and $\bar{q}_e$=77.3. It seems that the ETACHA calculations agree reasonably well with the data in terms of the onset of equilibrium but not for the resulting mean charge state.

3.3.4.2 GLOBAL

Another code that evaluates the evolution of charge states is called GLOBAL [Scheidenberger98]. It was developed after the ETACHA code and also takes into account up to 28 electrons for the n=1 to 3 subshells. The scale factors that it uses are based on

data obtained for ions of energies ranging from 80 to 1000 MeV/u at the BEVALAC accelerator at Lawrence Berkeley Laboratory [Alonso82] and the SIS synchrotron at GSI in Darmstadt. The cross sections used for excitation and ionization are similar to the PWBA used in the ETACHA code but has in addition a relativistic factor included. The code is recommended for use with projectiles of Xe to U ($54 \geq Z_p \leq 92$) impinging on solid or gaseous targets of Be to U ($4 \geq Z_t \leq 92$). The work of Sheidenberger and others makes comparisons between compiled experimental results and the predictions of the ETACHA code and finds that there is reasonable agreement up to ~30 MeV/u. They concede that the results of GLOBAL are not very accurate below ~100 MeV/u and that there is no technique available to make good predictions in the range of 30 MeV/u to 100 MeV/u. Unfortunately, this is in the regime at which the second stripper for the RIA driver linac intends to strip. We shall discuss some of the results predicted by the codes at both the first and second stripper and how they apply to RIA.

3.3.5 Estimating q-state distributions for the RIA driver

Some of the results from the ETACHA and GLOBAL codes that are used as examples in the discussions leading up to here are actually results relevant to the RIA driver linac. In particular, the results plotted in Figs. 3.18 and 3.20 (corrected) deserve further discussion. Notice in going from 24.1 MeV/u to 45 MeV/u that the region that could be considered equilibrium becomes narrower. In other words, the flat region that appeared before is no longer there, and it is not obvious that any such equilibrium condition even exists. It seems that right at the point at which the ion begins to approach equilibrium it begins to slow down considerably to the point where a reverse process begins to take effect, as shown by the drop in charge state. Clearly, the models indicate

that the stopping powers become a very important factor as the ion approaches the H- and He-like states. For the 45 MeV/u case, the highest mean charge, $\overline{q}_m$, and lowest standard deviation in charge occur at about 21 mg/cm^2. In arriving at the equilibrium thickness values plotted in Fig. 3.19 and labeled as 3, we assumed that $\overline{q}_e \approx \overline{q}_m$. Furthermore, calculations from GLOBAL at 45 MeV/u yield a similar thickness and mean charge within a fraction of a percent of those of ETACHA. This should not be surprising, since the cross sections of GLOBAL are similar to those of ETACHA when relativistic effects become negligible.

At the high energy end of the spectrum, GLOBAL seems to indicate that the equilibrium-type behavior becomes pronounced once again. This can be seen from the plot shown in Fig. 3.22, where the evolution has been plotted for 150 MeV/u 238U ions on carbon. This result had been used for choosing the other equilibrium thickness labeled as 3 in the plot of Fig. 3.19. Evidently, the equilibrium behavior seems to be less prominent after an energy of ~40 MeV/u and reappears gradually after ~100 MeV/u. The

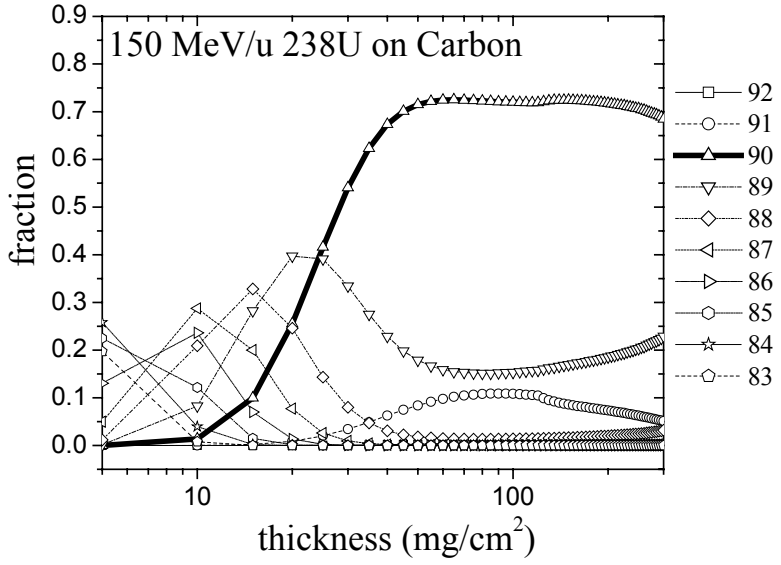

Figure 3.22 Evolution of charge states at the high energy range of uranium on carbon as calculated by GLOBAL.

work of Gould and others [Gould84] at the Bevalac reports the equilibrium at the higher energy regime for stripping of uranium. There they have stripped at energies as high as 962 MeV/u where they obtained 85% of the beam stripped to q=92 starting from q=68. The minimum foil thickness needed to reach the plateau region of equilibrium was 150 mg/cm^2 with Cu and 85 mg/cm^2 with Ta. At 437 MeV/u they needed 90 mg/cm^2 Cu to obtain 50% of the beam in the q=92 state. The same group later reported the results from 200 MeV/u uranium ions on foils of Mylar (Z_t≈6.6), aluminum, copper, and silver [Gould85]. Equilibriums are observed there as well, unfortunately, they do not report the minimum thickness needed from each material. The authors make some attempt to characterize the highest mean charge, $\overline{q}_m$, possible using different Z_t from scaling done with capture and ionization cross sections. They claim that higher $\overline{q}_m$ are obtained with high Z_t at the high energies, and that there is a gradual trend so that at the lower energies lower Z_t give higher $\overline{q}_m$. Their lower energies imply <200 MeV/u, which would apply more to our studies at >80 MeV/u. From stripping at energies of ~500 MeV/u they find that some intermediate Z_t gives the higher $\overline{q}_m$.

Clearly, there is experimental evidence of an extended plateau that indicates there is some equilibrium condition reached at the lower and higher energies. The plateau region is convenient for selecting a minimum thickness for the foil. Unfortunately, the codes have not shown this type of plateau region to exist for the intermediate energy region, and in some cases even the low energy region. The latest design of the RIA driver linac requires that there be stripping and filtering of charge states at a low and intermediate energy. We recall from Fig. 3.5 that that the current values are at 9.43 MeV/u and 85.3 MeV/u for low and intermediate energy, respectively. We have been forced to chose the

thickness needed at the point where $\bar{q}_m$ occurs, as for the 45 MeV/u example discussed above. One problem with this is that there is quite a large amount of energy loss for the corresponding thickness. In the case of 45 MeV/u uranium, we expect to lose ~15% of the energy compared to only a ~1.5% loss for the predictions of $\bar{q}_e$ at 24.1 MeV/u. For the 150 MeV/u case of GLOBAL, there is about a 5% energy loss expected for a $\bar{q}_e$ =89.8 at 45 mg/cm^2. When the energy loss in the stripper foils is so large, the trade-offs of the loss versus the increased energy gain from the higher charge states has to be carefully evaluated. The effects on the beam emittance due to additional energy spread and angular divergence must also be taken into consideration. For a high particle flux, one also needs to consider the power density resulting from higher losses and the effects on the lifetime of the stripper foils, as will be demonstrated later.

A number of results have been generated from the ETACHA and GLOBAL codes to make some analysis on the effects of stripping by different Z_t for varying thickness. Foils of Li, Be, C, and Al have been considered for the case of 9.43 MeV/u 238U as shown by the plots in Fig. 3.23 generated from the results of ETACHA. At this point we will assume that the codes are reliable and make some analysis based on the results that they yield. The thickest line in the plot is for q=81 and we choose the thickness of the foil to be at the point where this curve takes on a maximum. For the case of Al we take the thickness where the curve slopes off to a plateau. We do this only to establish some consistency as to where to select the foil thickness, since there is no plateau region observed for the cases of Li, Be, and C as there is for Al. A listing of average q values obtained at the equilibrium thickness for the ETACHA code and empirical calculations is given in Table 3.4. The empirical calculations predict $\bar{q}$ ~70, whereas the ETACHA

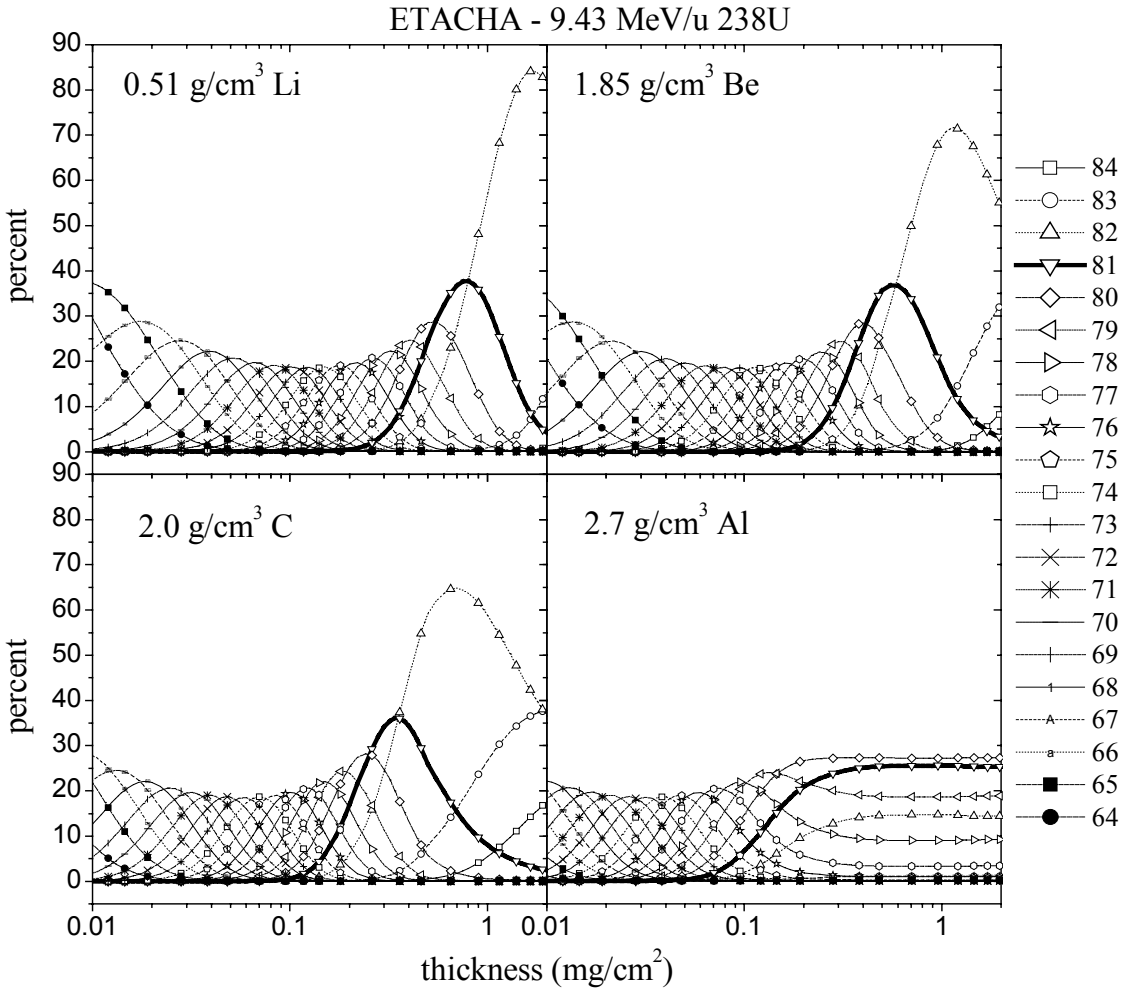

Figure 3.23 Charge state evolution according to ETACHA for 238U going through various types of foils. Cross sections corrected for energy loss.

Table 3.4 List of values that compare the results from the ETACHA code and analytical codes for stripping at 9.43 MeV/u. Thickness, *D*, is in mg/cm^2.

[Leon98]				ETACHA			
Z_t	D	$\bar{q}$	$\tilde{q}$	Z_t	D	$\bar{q}$	$\tilde{q}$
3	0.12	70.6	2.45	3	0.78	81.1	0.95
4	0.12	69.8	2.45	4	0.57	80.9	1.03
6	0.12	68.3	2.50	6	0.35	81.0	1.05
13	0.12	64.7	2.56	13	0.30	80.0	1.43

values are ~81 and even larger at a higher thickness. It is seems quite possible that at least one or more of the cross sections scales away from realistic values, such that higher q-states are predicted. The fact that the ETACHA code overestimates the mean charge by 10 to 15 charge units for Z_t =3 to 13 supports this argument. If we believe the empirical models, then either the cross sections from the code must have the electron loss too high or the capture too small. Clearly, it would be very useful to investigate the details of the cross sections and other assumptions in ETACHA to improve its accuracy for uranium in this energy regime.

Only foils of Li and C are considered for stripping at 85.3 MeV/u as shown by the plots in Fig. 3.24 evaluated by both ETACHA and GLOBAL. Unfortunately, the ETACHA stopping powers are only scaled up to 40 MeV/u in the version available, thus the ETACHA results in Fig. 3.24 have not been corrected for any energy loss in the target. Despite this fact, the results of ETACHA and GLOBAL agree well up to about the point where the q=89 fraction starts to level off at a maximum. Any discussion will be based on the region below this point.

The empirical formulations of both [Leon98] and [Baron93] both predict that lower Z_t materials will yield higher equilibrium charge states at all energies within their applicable range. This effect is also evident from the ETACHA calculations at 9.43 MeV/u. Notice, however, that at 85.3 MeV/u it is the higher Z_t that yields the higher charge states. This may imply that for the fully stripped states it is the higher Z_t material that gives the highest charge states, and vice-a-versa at the lower q-state region. The other factor that will play a part in choosing Z_t is the foil thickness needed and the amount of energy loss. The results from Gould seem to indicate that there are no clearly defined trends and that

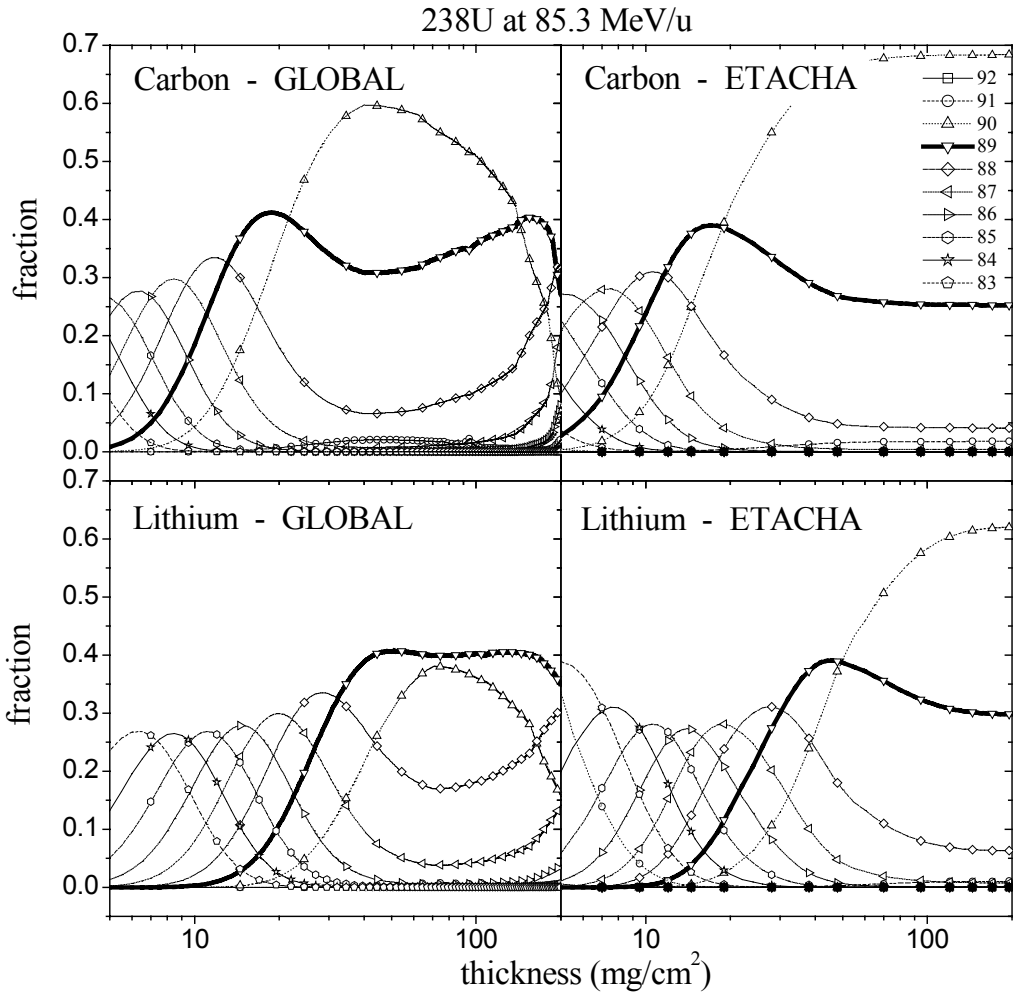

Figure 3.24 Charge state evolutions according to ETACHA and GLOBAL calculations of uranium under Li and C foils. No corrections for energy loss done for the ETACHA results.

ultimately, experimental tests with different Z_t materials may be necessary to make the best selection.

Using low Z_t materials may be advantageous if the liquid Li films being developed for RIA [Nolen02b] can be made to be thin enough to use as strippers. On the other hand, being able to use high Z_t materials such as Ta may be advantageous since it is refractory metal that can be machined into a very uniform thickness. Any solid target

would likely need to be set up on a device such at a rotating target wheel to extend the life of the target [Roa96].

At this point it would probably be pointless to dig at the results given by the empirical formulas and the codes. There is very little if any data to make any conclusions about them. It is clear, however, that further experimental and theoretical studies would be beneficial for these types of studies and the design of future heavy ion accelerators.

3.3.6 A final word about target survival and beam quality

Since the beam can affect the physical properties of the foil and the foil can have an effect on the phase space properties of the beam, it is necessary to look for some method of making reasonable estimates. Some discussion is offered here regarding available tools that have been found in the literature along with some useful estimates.

One beam parameter that must be kept to a minimum is the spread in energy of the bunch, δ_{Km}. One way to determine growth in this variable is to take a semi-empirical formulation suggested by Baron and Ricaud [Baron88]. The results are based on experimental results for beams on carbon foils at energies ranging from 3.2 to 6.5 MeV/u for heavy ions up to Ta. Taking δ_{Km} to be the half-width fractional energy spread, then the following formula may be applied:

$$\delta_{Km} = \frac{10^{-3}}{2(K/A)}\left[1.866 + 1.57\log(K/A)\right]\frac{Z_p}{A}\sqrt{\frac{Z_t}{A_t}D} \tag{3.36}$$

The thickness of the foil, D, must be given in units of μg/cm^2. For comparison the Monte Carlo code, SRIM, was applied. If we assume an upper limit on the foil thickness at 85.3 MeV/u to be 20 mg/cm2, we find that δ_{Km}=0.018 according to (3.36) and δ_{Km}=0.0008 according to SRIM. The results from Eq. (3.36) seem to overestimate the value from

SRIM by a factor of ~23. Note that the empirical values include effects such as non-uniformities of practical foil, while the SRIM calculations assume a uniform foil.

Some values of the transverse emittance growth were also estimated with the SRIM code. It is found that the base-to-base full width of the divergence imposed by scattering of the projectile ions through the target will vary between 0.5 to 1 mr depending on the projectile. In the case of 238U at 85.3 MeV/u, a half width of 0.6 mr at the boundary containing 95% of the total beam must be superimposed on the incoming transverse emittance of the beam. Focusing the beam to a small spot size at the stripper can minimize the effect that this multi-scattering has on the emittance. This is also true of the longitudinal emittance, where it is best to minimize the bunch width in time.

Another factor that should be taken into account is the lifetime of the carbon foil. The maximum temperature of the foil can be modeled by considering a Gaussian spatial beam distribution in the transverse plane as described by [Catalan96]. The form of the peak temperature may then be evaluated approximately by the formula,

$$T_{\max} = \left(\frac{\Delta K \cdot I}{4\pi\varepsilon_T \sigma_{SB} \tilde{x}\tilde{y}} \right)^{1/4}, \tag{3.37}$$

where $\Delta K \cdot I$ is the total power dissipated in the target determined by the energy loss and beam current. The dimensions of the beam are expressed by the rms width values, $\tilde{x}$ and $\tilde{y}$, while the two constants, ε_T and σ_{SB}, are the total emissivity of the foil and the Stephan-Boltzmann constant, respectively. Typical values of the emissivity for amorphous carbon are found in the tables to be about 0.81 at 1500 K. Taking, for example, the case of a circular beam with a 3mm rms radius and a beam current of 0.6 pμA for the 238U beam, we get a maximum temperature of about 3000°C. Although this

is still well below the sublimation temperature of carbon (~4100 K), care must be taken to ensure that the beam radius does not go much lower. Furthermore, about 20% of the power is dissipated through conduction considering that the radius of the holder is about three times larger that of the foil. Good thermal conductivity to the target holder may be a factor in keeping the temperature as low as possible. Since small beam spots are desired, a dynamic target may be necessary to keep the peak temperature low. This type of analysis has been done in the past from foils rotating on a wheel [Roa96]. Flowing liquids that form thin regions have also been studied and are found to be much more immune to these types of problems [Nolen02b].

For rotating and still targets Baron was also able to characterize the lifetime of the stripper in terms of the displacement of atoms within the foil [Baron79]. SRIM calculations suggest that over 800 vacancies may be generated per 238U ion on a 20 mg/cm^2 carbon foil. On average, about 6 of these atoms will escape the foil. The elevated temperature of the foil should re-order much of the lattice of the foil. With these assumptions, the theory of Seitz [Seitz56] predicts that the lifetime of the foil may be estimated by,

$$\tau_d = C \frac{(K/A)}{Z_p^{\,2} \cdot \bar{d} \cdot j} \tag{3.38}$$

Here, $\bar{d}$ is the average number of atoms displaced from the bulk, j is the beam current density within the rms boundaries of the beam, and C is a constant determined from experimentally observed lifetimes. Baron finds that a value of

$$C = 3.6\times10^4 \text{ h-p}\mu\text{A-cm}^{-2}(\text{MeV/u})^{-1} \tag{3.39}$$

fits his observed results best. We adopt a value of $\bar{d} \approx 6$ here from estimates with the SRIM code. We obtain from Eq. (3.38) that for 0.6 pμA of uranium of 3 mm diameter

beam spot, the foil should last about 28 hours. For a rotating target we simply need to multiply by the circumference traced by the beam on the target and divide by the diameter of the beam spot.

Chapter 4

PRODUCTION OF NEUTRON-RICH ISOTOPES BY A TWO-STEP PROCESS

The development of devices that can provide sufficient quantities of rare isotopes will be an on-going task for any rare isotope production system. The chemical properties and decay lifetimes vary considerably throughout the spectrum of nuclei away from stability. Although a particular device may turn out to be best for some group of species, it will not necessarily be competitive for others. We look at an example here in which even the way the primary beam is directed at the target system makes a difference in the performance in production.

Some of the most important properties to be studied for any target system are the efficiency of production, release, and ionization. An experiment was conducted at the Petersburg Nuclear Institute of Physics (PNPI) to evaluate these properties for the production of Rb and Cs isotopes within a UC*x* filled target. Also, we evaluate the two-step process in an ISOL configuration as a possible alternative for the production of neutron-rich nuclei.

4.1 Motivation and applied approach

Of the many species of rare isotopes that can be made available at a facility like the proposed Rare Isotope Accelerator system, neutron-rich species are presently a very high priority for the nuclear physics community. In general, neutron-rich nuclei are less understood than their neutron-deficient partners at the same distance from the valley of stability. Moreover, there are more neutron-rich nuclei that are expected to be bound

than are neutron-deficient ones. At large neutron excess, a variety of phenomena are predicted, such as the existence of neutron halos, or skins, and vanishing of standard magic numbers. Searching for methods that would make neutron-rich nuclei available in sufficient amounts for acceleration is essential. Two methods of production will be studied here to assess some of the possible target configurations by a direct comparison.

It will be shown that the two-step reaction process for the production of rare isotopes in thick targets for ISOL offers some advantages over the one-step configuration. In the one-step, a primary beam of high energy particles, such as protons, directly impinges on the target. Most, if not all, of the power is then dissipated directly in the target. Estimates on the amount of production necessary for intense beams of rare isotopes require that that at least 100 μA of protons at energies ranging from 0.5 to 1 GeV be directed on target. [ISL92]. Studies in the past have predicted that most conventional targets will not be able to sustain the type of power densities imposed under these conditions. Issues pertaining to target lifetime and reliability require that alternative methods of production be considered since it has been found that the power density in the target may cause temperatures to become too extreme [Talbert97] [Eaton79].

The Monte Carlo models that have been utilized here suggest that isotopes lying at the neutron rich side of the valley of stability are most readily produced via neutron induced fission of heavy elements. In the case of 238U, the region of the neutron spectrum that contributes the most lies between 1 to 5 MeV, and is commonly referred to as the "fast neutron" region [Gomes98] [Nolen93].

Facilities that produce isotopes for on-line research very often use high energy protons, which generate fast neutrons. There is a tendency to associate most of the

production with the direct interaction of the protons with the target nuclei. This study will show that the secondary neutrons induced by the protons actually contribute to the production and tend to be the dominant process for very neutron-rich production. We shall demonstrate the use of a technique that gives direct evidence of this. This requires that some efficient production of fast neutrons at some separate primary target be used to produce a sufficient amount of neutron flux. Since the neutrons are generated at a separate target, we call this the two-step method of production. With an optimized secondary target arrangement this technique can be used as alternative method for future ISOL targets. The one-step, or direct, method refers to the technique in which protons impinge on the production target directly. The two competing methods are compared using the measured and calculated yields of isotopes with mass at the Rb and Cs region.

The experiment was conducted at the IRIS facility [Novikov98] at the Petersburg Nuclear Physics Institute. The apparatus used there allows an immediate switch over between a one-step and two-step configuration. The Monte Carlo calculations were conducted at Argonne National Laboratory and are compared with the experimental results. To arrive at the production yields the simulation relies on a wide array of nuclear cascade events. Release curves are measured in order to characterize the efficiency of the particular IRIS target/ion source used [Barzakh00]. The efficiencies are used to unfold the data and obtain absolute yields with a UC*x* target [Panteleev00]. Other factors that affect the efficiency of transport throughout the mass separator system are also accounted for as discussed in the sections that follow.

4.2 Applying isotope production models

Modeling of reaction processes is a useful tool in the optimization of production and release of present and future ISOL targets. The production mechanism has to be considered along with several other factors, such as the expected beam power, temperature, and release times for various elements. Optimum diffusion and release is dictated by the physical and chemical properties of the target and modeling is necessary to gain a concise understanding of a particular configuration. We construct a model of the production via the primary beam to simulate the production in the experiment.

The scheme used for simulating the reaction processes requires two separate codes to handle the "low" and "high" particle energy regimes. The Monte Carlo code, LAHET, tracks all charged particles and neutrons above 20 MeV [Prael89]. Below this threshold limit LAHET will cease to track a particle, but will save the space and momentum coordinates to be used by another application. The MCNP code is then applied to continue the tracking of neutrons below 20 MeV until they either escape the target or induce a fission reaction [Briesmeister86]. A code by Gomes then applies the fission branches for neutrons of <20 MeV to obtain the final yields [Gomes98]. It is evident that neutrons of energy lying in the range of 2 to 10 MeV generate a significant portion of the fission events leading to neutron rich isotopes from 238U.

In this experiment, the objective was to verify that the results of the simulations agree with those of the measurements. Furthermore, we have tested the performance of the target material and will show some of the results. The experiment took place with a conventional ISOL setup constructed by the IRIS group at the PNPI facility. We measure the yield and release-time of rubidium and cesium isotopes diffusing out of the target and ionizing on a hot surface. A porous form of a refractory uranium carbide (UC*x*) material

is taken up to a temperature of 2500ºC to obtain fast release. In this experiment, the target endured more than 3 days under such conditions. A 0.1 μA beam of 1 GeV protons from the synchrocyclotron was directed at either of two side-by-side targets using magnetic steering upstream from the target region.

4.3 Target and extraction system

The IRIS facility is ideal for these measurements. First of all, the production rate via protons tends to level off to little growth after ~1 GeV and the protons from the synchrocyclotron are at this energy. Also, the beam line allows steering between targets that are 3 to 5 cm apart and eliminates having to reconfigure the target. This is important considering that many of the conditions of the ion source and mass separator are not easily reproducible after any tampering of the set up. A joint collaborative effort within the facility made it possible to produce the necessary target material as well as the refractory parts necessary to construct the target/source. Some details of the process used to make the carbide material are mentioned below.

4.3.1 Production of UCx materials

A variety of refractory carbide materials have been studied in the past for properties of release and lifetime under extreme temperature conditions. Preliminary studies on these materials primarily focused on producing solid rods with large grain structures for use in reactors─the goal usually being to obtain a high density carbide with low diffusion rates to minimize the amount of activity released into the atmosphere. For ISOL targets, one strives for the opposite effect since optimizing for fast release is necessary. In both applications, however, it is desirable to retain the refractory properties inherent from the carbide while retaining the highest possible concentration of uranium.

An extensive review has been detailed about the properties of the carbides formed under various conditions with uranium by Frost [Frost63]. For $0<x<2$ the carbide tends to exhibit the refractory properties of graphite. As x approaches unity, the material exhibits more of the properties of UC and tends to break down and evaporate at temperatures below 2500°C. The properties of graphite are best suited for fast release; hence, it is necessary to obtain $x>2$ at the end of the reaction. Exact details of the processes used in obtaining the different forms of the carbide are described further in the literature [Martin74] [Matthews94] [Gutierrez81].

For the particular sample used here we start with a mixture of powders, such that there is 10.7 g of U_3O_8 and 2.8 g of graphite powder. The temperature of the sample is ramped up slowly until there was about a 21% loss in mass, which implies that there is about a value of $x=3.4$. The resulting form is a mix of graphite powder and UCx, which in this case has grains with an average radius of 3 μm (1 to 5 μm). The resulting overall density of the sample is 3.1 g/cm^3 once inside the target. In the past, similar forms of highly porous carbides have exhibited fast release of noble gases, alkalis, and other elements [Carraz79].

4.3.2 Target layout

Fig. 4.1 illustrates a side view of the target/source configuration. The compressed UCx compressed powder is encased in a 1 mm thick graphite container to avoid any temperature induced corrosive interactions with the walls of the container. The inner diameter of the cylindrical container is about 6.5 mm and has a height of 36 mm. After packing the powder to a density of 3.1 g/cm^3, the total amount of uranium in the container is about 3.2 g. A tube was rolled from a 50 μm thick tungsten foil for encasing

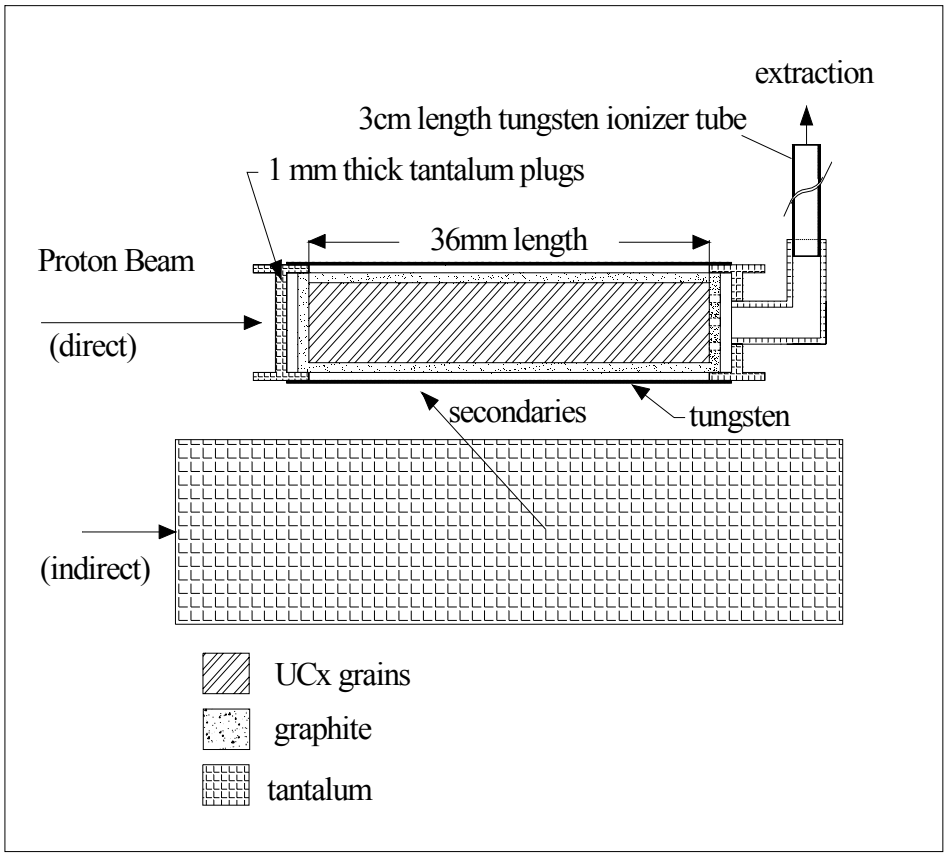

Figure 4.1. Cross sectional top view of the target/source used for rare isotope production. All objects are cylindrical except for the Ta block, which has a square cross section in the beam direction and rectangular as viewed from the top. Secondary neutrons produced by the 1 GeV proton beam on the Ta target react with the 238U in the target to produce the isotopes of interest.

the graphite container along with tantalum plugs, which are shown at each end. The tungsten wall had an effective thickness of 0.2 mm, while the walls of the tantalum plugs have a thickness of ~1 mm. A DC potential forces currents as high as 600 amperes through the sample for ohmic heating of the target material. The ionizer is heated independently with a separate DC power source. A combined power of about 2.1 kW is capable of taking the target and ionizer to temperatures exceeding 2500°C, as verified by optical pyrometer measurements. The target thickness in the direction of the incoming

beam is low enough such that only a fraction of the proton energy is dissipated at the target (~0.1 kW), thus having a negligible effect on the temperature.

The intensity distribution of the proton beam and the exact point of impact were measured at the beginning of the experiment. A photographic plate was placed at the front of the UC*x* and tantalum block targets to determining the beam positions. The images on the photographic plates verified the reproducibility of the beam positions and are used to make estimates of the parameters for a 2D Gaussian function to model the spatial distribution. The beam profile formed an upright ellipse with an rms width of 3 mm in the horizontal direction and 3.75 mm in the vertical. This was the case whether the beam was steered towards the UC*x* target or the Ta block.

The outer encapsulation layers of tungsten and tantalum confine the products as they migrate to the tube extraction region shown at the right side of the diagram. Direct production is induced by steering the proton beam towards the UC*x* target (one-step production). Indirect production yields were obtained by impinging the proton beam on the tantalum block to induce the neutron flux (two-step production). Both configurations are simulated by the Monte Carlo models used with Gaussian distributed beam distribution are used to determine the expected production.

Isotopes undergo diffusion out of the UC*x* powder then through the walls of the graphite container. Effusion occurs throughout the remaining vacuum regions of the target and ionizer tube. The transition between the regions of diffusion and effusion are not clearly distinguishable due to the porous nature of the target and the graphite casing. The usual convention is that effusion begins right after the particle leaves the individual grains. Even within the surface ionization tube, which has an inner diameter of ~1.5 mm,

there is not necessarily pure random effusion occurring since the potential drop across in the ionizer tends to drive the ions towards the extraction region. The combined effects of the transport processes will be characterized by the measured release curves as explained later.

Once extracted from the ionizer tube, the ions form the beam that is then focused through an electromagnetic mass separator. The magnetic rigidity is varied to be able to scan a mass range that spanned between the limits of 90 to 96 amu and 141 to 148 amu. Extracted yields at any mass could be measured for both the direct and indirect target configurations.

4.4 Isotope transport and detection

A brief introduction of the release analysis is given here to describe the transport from a target to the extraction region. The region of extraction is where isotopes can migrate out of the target container and either get ionized and extracted or lost as neutrals to the outside vacuum. The flux of particles leaving the target through this channel is denoted by $F(t)$ and can be in units of atoms per second. Inevitably, there will be losses to other traps surrounding the target, such as leaks in the container and diffusion through the container material itself. They would have to be accounted for with a separate term, say $F_i(t)$, since their release mechanism is not necessarily similar in form to $F(t)$. The containment of the target used here is secure enough to ensure that such losses are negligible.

For these experiments the release flux, F, was measured for a selected mass region of interest by using an electromagnetic isotope separator to purify the beam. The beam is extracted at 10 kV and then accelerated up to 30 kV through electrostatic tube apertures

that simultaneously focus the beam through the magnetic sector. Finally, the beam is steered and refocused through a beam line equipped with a Faraday cup, an ion counting system, and a tape transport system that allows detection of decay radiation at suppressed background levels.

4.4.1 Measuring the transported products

The actual measurable quantity is the accumulated rate, $R(t)$, at any of the detectors and is directly proportional to $F(t)$ by

$$R(t) = \varepsilon_i \varepsilon_T \varepsilon_D F(t) \tag{4.1}$$

The three leading constants of proportionality are the ionization efficiency, the transport efficiency, and the detection efficiency, respectively. The transport efficiency accounts for any losses that occur while the ions are accelerated and focused through the mass separator system. Most of the losses occur in front of the detection system, where vertical jaw slits at the image of the beam transport enhance the resolution of the mass separator. Based on the estimated production of 89Rb and ionization efficiency, it was determined that the transport efficiency is about $\varepsilon_T = 0.25$ when making comparisons with the measured current at the Faraday cup at mass 89.

The extracted ion detection efficiency, ε_D, varied depending on the detector being utilized. Fig. 4.2 illustrates the arrangement of the detection systems used. The Faraday cup and the electron multiplier were utilized when counting ion flux directly. The electron multiplier could tolerate no more than about 10^4 particles per second (pps), while the Faraday cup required at least 10^6 pps to register above the background of the picoammeter.

The solid-state detector of the tape transport system (labeled 2 in Fig. 4.2) offered a very low background environment and was used in measuring the ion flux after issuing a short pulse of proton beam. Particles accumulated on the tape could be transported within 1.3 seconds to a position near to the detector lying 5 mm away from the tape. In this geometry the detection efficiency is about ε_D =0.02 for β^- particles of >20 keV. Corrections for the dead time of the detector and background subtractions were applied for the data obtained from β^- detection.

The surface ionization probability, ε_{is}, can be estimated under thermal equilibrium using an equation given by the Langmuir-Saha model [Langmuir25],

$$\varepsilon_{is} = \frac{n_i}{n_i + n_o} = \left(1 + \frac{\xi_o}{\xi_i} e^{(V_i - V_s)/kT}\right)^{-1} \qquad (4.2),$$

with n_i and n_o the number of ions or atoms evaporated from the surface, ξ_i and ξ_0

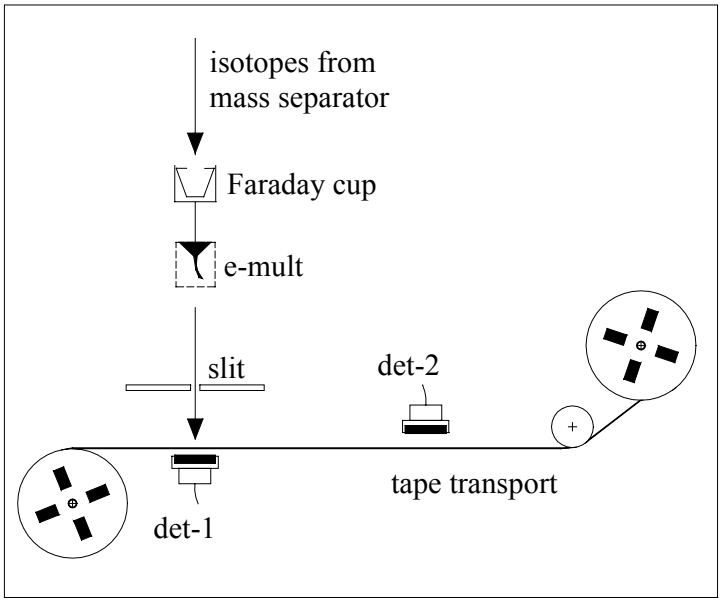

Figure 4.2. Diagram describing the tape transport system used for collection isotopes as ions focused through the slit at the image plane. Two solid-state detectors were used for detection of nuclear decay while a Faraday cup and electron multiplier setup is used to measure ions directly.

statistical weights for ions or atoms, V_i the ionization potential of the ion, and V_s the work function of the surface.

Some consideration has been given to the formation of a hot cavity plasma within the ionizer tube in accordance with a formalism introduced by Kirchner [Kirchner78]. The parameterization prescribed by Kirchner in reference [Kirchner81a] for determining the thermal ionization efficiency, ε_{iT}, is applied and the results are compared with the surface ionization efficiency in Fig. 4.3. The details of the formulation for arriving at the thermal ionization values are left to Appendix C.

In a later test we observed a strontium component in the beam, where the target temperature was similar but the ionizer tube temperature had gone beyond 3000°C. The mass lines, however, did not appear when the ionizer temperature was kept at 2500°C, which led us to conclude that the thermal plasma effect plays a negligible effect in the

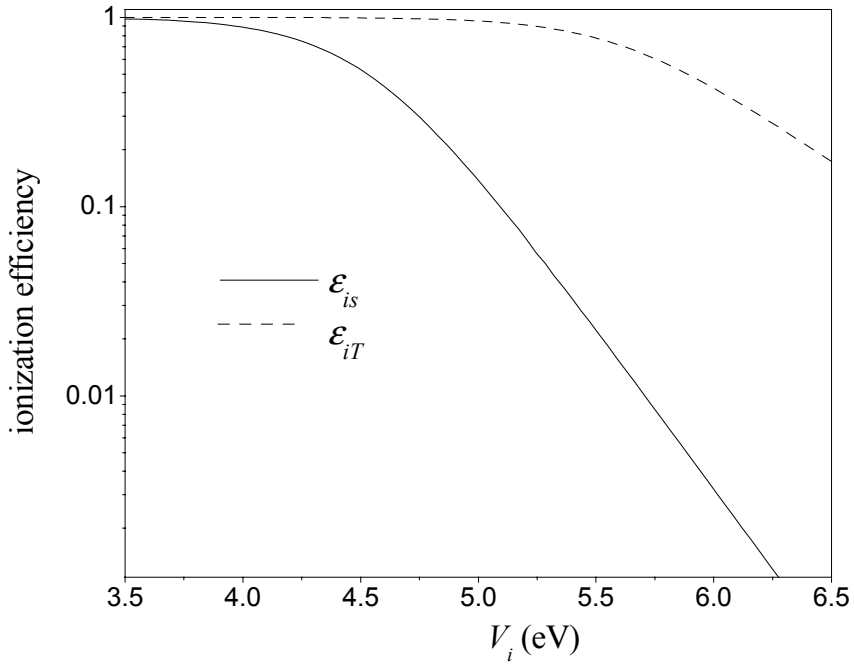

Figure 4.3. Ionization efficiencies for a tungsten tube at 2800 K according to the surface ionization (ε_{is}) and hot cavity thermal ionization (ε_{iT}) models.

ionization. This does not mean that there is no plasma formation, but merely that it is likely that its boundary cut off is too deep from the extraction region to have an effect on final extracted ionized species. Particles ionized by the plasma will likely collide with the hot tungsten walls at the exit side of the ionizer tube. Equation (4.2) is adopted in evaluating the ionization efficiency from equation (4.1), since it is most consistent with the observed results.

4.4.2 Product release from target

Of particular interest in this study is determining the production rate occurring inside the target. This rate is denoted as P and is the probability of producing an isotope, denoted by (Z,A), per incident proton. The Monte Carlo simulations provide these quantities and they may be compared with the values predicted by the experimental results after unfolding the relevant efficiency values from the measurements. The efficiencies for the ion transport and detection, along with those attributed to the time dependent processes such as decay, diffusion, and effusion are all taken into account for obtaining the flux out of the target, F, from the detected rates, R, as described below.

A set of first order differential equations could be constructed for balancing the production, decay, and extracted flux of an isotope. The production can be expressed as $J \times P$, where J is the incident flux of protons and F is the probability of yielding a particular isotope (Z,A). This is a simplified expression since there is actually a detailed spatial dependence affecting the production. The Monte Carlo models account for such geometrical effects. We let N be the total number of (Z,A) in the target. The time rate of change of its population should vary as

$$\dot{N} = J \times P - F - \lambda N + \lambda_n N_n \qquad (4.3).$$

The decay rate, λ, of (Z,A) must include all probable channels that lead to another distinct isotope—the most common being that of β-decay. The final term, $\lambda_n N_n$, represents the sum of all decay channels that feed the population of (Z,A) isotopes, such as the decay of the (Z-1,A) by β^-. Beta delayed neutron decay can also be significant, such as in the case of 147Cs, where 43% of its decay feeds into the 146Ba channel. In general, there will be a system of differential equations of the form (4.3) to account for all such possible cross terms in a system of equations and each isotope species will have its own corresponding extracted flux.

The form of the time release flux, F, is usually a complex function of the target geometry and depends on the diffusion and effusion coefficients. Especially for the target configuration used here, the transport of atoms through the target can be quite a complex system to model if one is to apply Fick's laws of mass transport [Crank75]. The form of the effusion coefficients by themselves can be a subject of much speculation since the electric fields induced by the resistive heating can affect the migration of isotopes that are easily ionized on surfaces.

The use of equation (4.3) can be simplified by selecting an isotope where the decay terms are negligible and the production takes place at a very small interval of time. In some studies, the target is moved to a counting station where the decay of (Z,A) is measured as a function of time [Carraz79]. This requires that the half-life of the isotope be relatively long compared with the diffusion. Furthermore, the ramping of the target temperature must be short compared with the diffusion time. In this study a set of isotopes with a wide range of half-lives must be measured, so that it is more proficient to

determine the form of F from on-line measurements. Most of the terms in the rate equations have some effect on the results obtained in the analysis, thus it is instructive to elaborate on their effects. Appendix D describes a simplified method of arriving at analytical solutions under common limit conditions. It also introduces the concept of the release curve, $p(t)$, and its relation to the release flux, $F(t)$. When feeding from decay is negligible (λ_n=0) the release coefficient is given by

$$\eta(\lambda) = \int_0^\infty \exp(-\lambda t)\, p(t)\, dt \ . \tag{4.4}$$

We can consider the quantity $\eta \times P$ as forming the figure of merit for a release target for some given (Z,A). Setting aside the production, the delay function carries much of the information that is useful when characterizing the performance of a given target. Essentially two distinct processes affect the form of the delay function. One is the diffusion of the particles out of the target matrix, while the other is the effusion of the particles throughout any remaining open spaces whereby the particle may migrate by hopping from surface to surface. The physical and chemical properties of the given isotope affect these processes, since the diffusion coefficients and surface sticking times should vary for different Z.

It is useful to select an isotope of a given element with negligible decay rates compared to the flux term in equation (4.3). Under such conditions, models of diffusion and effusion may be directly applied to measuring the rate of release. Such studies form the basis for selecting adequate target materials and optimizing target geometry. For this study it was sufficient to consider 88Rb and 139Cs, in which case the lifetimes are long enough to measure $p(t)$ with negligible effects from decay.

4.5 Models of the delay function

As explained in Section 4.3 above, the delay time is affected by the physical characteristics of the target. Models for the delay function at the limit where $\lambda_n N_n << \lambda N$ are introduced here and applied to the release curves of 88Rb ($T_{1/2}$=17.8 *min*) and 139Cs ($T_{1/2}$=9.27 *min*). Cases for which decay feeds into (*Z*,*A*) are more complex since they require knowledge of the diffusion of mother nuclei whose release properties are not necessarily similar. The half-lives of these two species are also ideal since they are long compared to the diffusion time.

The diffusion and effusion processes by themselves tend to exhibit unique delay time distributions, $p_D(t)$ and $p_E(t)$, respectively. We can combine the two different functions as a convolution in time by assuming that particles effuse after release from the bulk material and never diffuse back into the bulk after. The diffusion takes place between the time interval $[0,\tau]$ and effusion between $[\tau,t]$. Under these conditions the following integral equation applies [Kirchner92]:

$$p(t) = \int_0^t p_D(\tau) p_E(t-\tau) d\tau \tag{4.5}$$

Two different models are utilized here and applied for comparison with the measured delay curves and are discussed below.

4.5.1 Diffusion-Effusion based release model

For the diffusion of atoms from uniform spherical grains, Ravn and others [Carraz79] offer a form of the delay function given by

$$p_D(t) = \frac{6\gamma}{\pi^2}\sum_{n=1}^{\infty}\exp(-n^2\gamma t) \tag{4.6}$$

where γ is the diffusion parameter and is a function of the radius of the spheres, r. The diffusion coefficient, D, is determined by $\gamma=\pi^2 D/r^2$. The temperature affects the diffusion according to $D=D_o\exp(-V_a/kT)$, where D_o is the diffusion constant and V_a is the activation energy of inter lattice position exchange. The release efficiency that this delay function yields is obtained by integrating equation (4.4). The result is a form given by an infinite sum that converges rapidly,

$$\eta_D(\lambda) = \frac{6\gamma}{\pi^2}\sum_{n=1}^{\infty}\frac{\exp(-n^2\gamma t)}{n^2\gamma+\lambda} \tag{4.7}.$$

For effusion, we apply the same form of the release for the evacuation through an orifice from a container described in the appendix [Kirchner81b]. In the form,

$$p_E(t) = \nu\exp(-\nu t) \tag{4.8}$$

the factor ν is inversely proportional to the average number of surface sticking events, n_S, that a particle undergoes before exiting from the volume. It is common practice to express the mean delay time as $\tau_d=1/\nu= n_S(\tau_s+\tau_f)$, where τ_s and τ_f are the average sticking and flight times, respectively. Solving for the release coefficient gives that

$$\eta_E(\lambda) = \frac{\nu}{\nu+\lambda} \tag{4.9}.$$

The convolution of the two delay functions results in the final form,

$$p(t) = \frac{6\gamma\nu}{\pi^2}\sum_{n=1}^{\infty}\frac{\exp(-\nu t)-\exp(-n^2\gamma t)}{n^2\gamma+\nu} \tag{4.10}.$$

This time integral yielding η results in a similar summation that converges to a hyperbolic cotangent form expressed in final form as,

$$\eta(\lambda) = \frac{3\nu[W\coth(W) - 1}{(\nu + \lambda)W^2}, \quad W = \pi\sqrt{\lambda/\gamma} \tag{4.11}.$$

A chi-square minimization with respect to the measured delay curves is applied to the release curves of 88Rb and 139Cs to extract γ and ν. The normalized delay function is plotted as the dashed curves in Fig. 4.4(a) and (b) with the resulting values listed in Table 4.1. The diffusion parameter is estimated by taking the average radius of the grains to be 3 μm.

Table 4.1 Parameters that give the best fit to the delay release curves plotted in Fig. 4.4.

	γ[s^{-1}]	ν[s^{-1}]	D[cm^2/s]
88Rb	0.039	0.26	3.6×10^{-14}
139Cs	0.025	0.20	3.6×10^{-14}

The time scales indicate that overall Rb is released faster than Cs. The results of the best fit to the date indicate that the Rb effuses over 1.5 times faster than Cs from the UC*x* particles, while the diffusion coefficients turn out to be about the same for both species. The diffusion rates found here are about two orders of magnitude smaller than the diffusion rates measured for noble gases penetrating through similar bulk materials where a D of 4×10^{-12} cm^2/s for 133Xe and 85Kr is found [Frost63]. This discrepancy is probably due in part to the inert character of noble gases; however, the model applied for that other study does not account for effusion through the pores in the material. This would tend to make the diffusion through the true bulk material seem faster since the effusion is incorporated into the diffusion parameter. What is more important to point out here is that the two species have similar diffusion coefficients, and the significance of the overall magnitude is less relevant since the distribution of grain size can vary by more than a factor of two from the average value taken here.

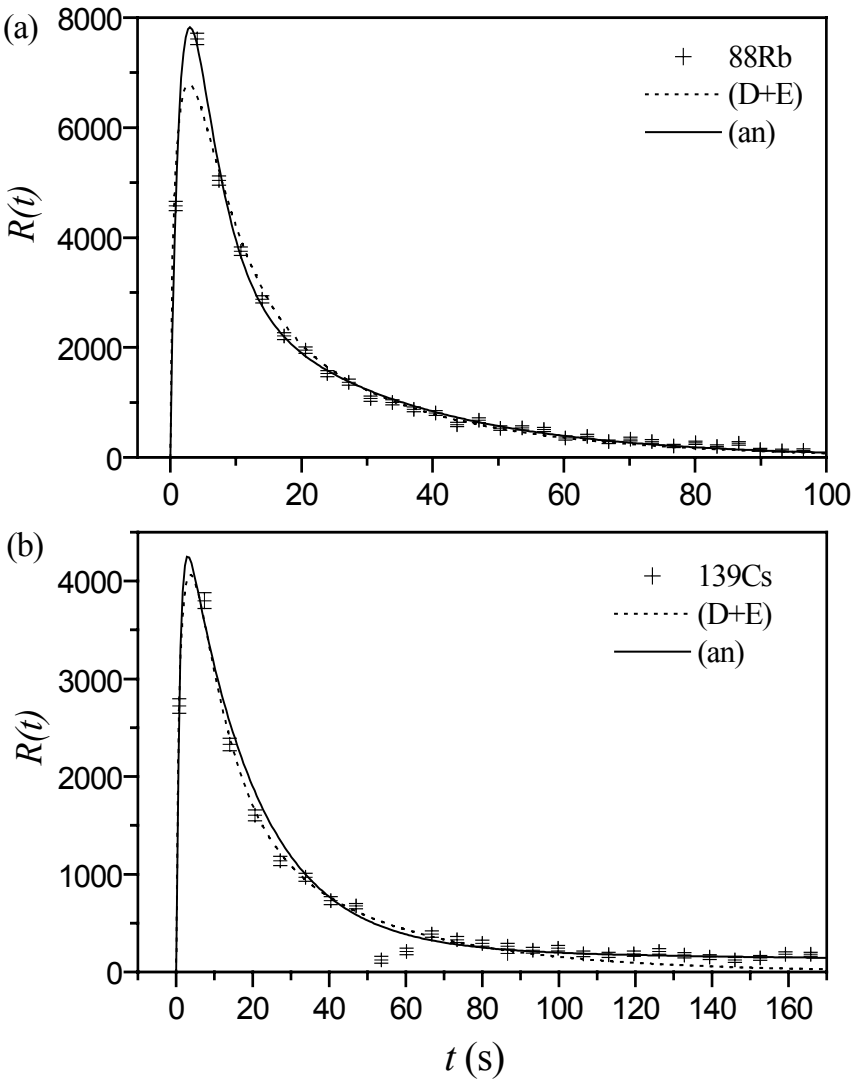

Figure 4.4. Time dependent release of (a) 88Rb and (b) 139Cs isotopes from the target/source after issuing a pulse to the target in direct production mode. The average temperature of the target is about 2500°C. Two models are applied for comparison by way of a chi-square minimization algorithm to arrive at the relevant parameters that yield the best fit. The curves are labeled for the diffusion/effusion model (D+E) and the analytical (an) equation model described in the text.

The difference in the effusion coefficients found by the fit may be interpreted by application of the model. If we assume that the sticking time is negligible with respect to the drift time then the system is very similar to a gas effusing through network of evacuated capillaries. Since the Cs and Rb atoms travel the same average length we can

make a relative comparison of the average time elapsed between wall collisions between the two elements. From the kinetic theory of gases the average energy is given by $\overline{E} = 3kT/2$, thus we expect the ratio between the hopping events to be given by $\nu_{Cs}/\nu_{Rb} = \sqrt{m_{Cs}/m_{Rb}}$. This relation holds to within 3% from the values listed in the table.

The physical interpretations seem reasonable; however, some difference remains between data and model. A poor fit is seen at about the 8 s mark of the release curve for the 88Rb curve, and also for the 139Cs a poor fit is seen for all t>100 s. In the case of Cs, it seems likely that contamination by the slower diffusing 139Ba ($T_{1/2}$=83 *min*) contributes to the extended tail for large t. In the case of Rb, the corresponding 88Kr ($T_{1/2}$=2.84 *h*) is long lived enough to rule out this effect. It appears that there should be a faster component of diffusion superimposed to obtain a better fit to the data. Typically, this target has been observed to have a 200 K temperature difference between the outlying plugs and the center, which would make the diffusion significantly slower at the colder regions. There are quite a number of uncertainties that could contribute to such small details, but for the most part it can be concluded that the model fits the data reasonably well to make some assessment about migration processes taking place in the target. Another model is adopted in the next section that gives a better fit to the data and allows us to interpret the data from a standpoint of the release efficiencies.

Other more elaborate codes have been developed recently for modeling of the diffusion and effusion model [Mustapha01]. We do not resort to them here since they involve Monte Carlo random walk simulation of the effusion, which are more difficult to arrive at a fit to the data. The models used here are easier to apply and are adequate for the analysis that is need on the measurements.

4.5.2 Simplified analytical model of release

In the interest of obtaining a release coefficient from curves that fit the observed data more closely, we adopt an analytical form of $p(t)$. This form is given by the equation,

$$p(t) = A\left(1 - e^{-\lambda_r t}\right)\left(Be^{-\lambda_f t} - (1-B)e^{-\lambda_s t}\right) \qquad (4.12),$$

where A is the normalization constant. The migration process is composed of a superposition of a fast and slow release components, where λ_f and λ_s characterize the fast and slow release rates, respectively. The parameter B weighs in the amount of each of these two components. The first term in parenthesis determines the rise time of the delay curve by the rate term, λ_r. We note that no distinction is made between diffusion and effusion by this model, and overall, these parameters have less direct physical meaning than those of the model described in the previous section. A previous study, however, does suggest that the rate parameters should scale as Arrhenius like relations with temperature and have offered some experimental evidence this is the case [Novikov98]. We do not attempt to make such arguments here for lack of temperature dependence data; however, the model is utilized since it offers a closer fit to the data, which is attributable to a higher number of parameters.

Solving for the release coefficient using this model is straightforward and gives that

$$\eta(\lambda) = A\left(\frac{B}{(\lambda+\lambda_f)} - \frac{(1-B)}{(\lambda+\lambda_f)} - \frac{B}{(\lambda+\lambda_r+\lambda_f)} + \frac{(1-B)}{(\lambda+\lambda_f+\lambda_s)}\right) \qquad (4.13).$$

Fitting this model to the measured release curves yields the resulting curves illustrated within Figs. 4.4(a) and (b), labeled as the simplified analytical model. The agreement between model curves and data show an improvement throughout most of the time spectrum compared to the previous model used.

Fig. 4.5 illustrates the resulting release coefficient curves for Rb and Cs as a function of $\tau=1/\lambda$. The curves approach unity for very long lived isotopes since we have assumed that $\lambda_n \approx 0$. The Rb curves from the both models overlap each other despite the fact that their respective release curves vary significantly at the region about the peak of the delay function. On the other hand, the release curves of Cs behave very similar in this same region, yet the two coefficient curves exhibit well-marked differences. The dominant effect seems to stem from the behavior of the delay curves at the region well beyond the point where the peak occurs. The diffusion/effusion release curve drops off more rapidly in this region than those of the simplified analytical model. The result is an enhancement

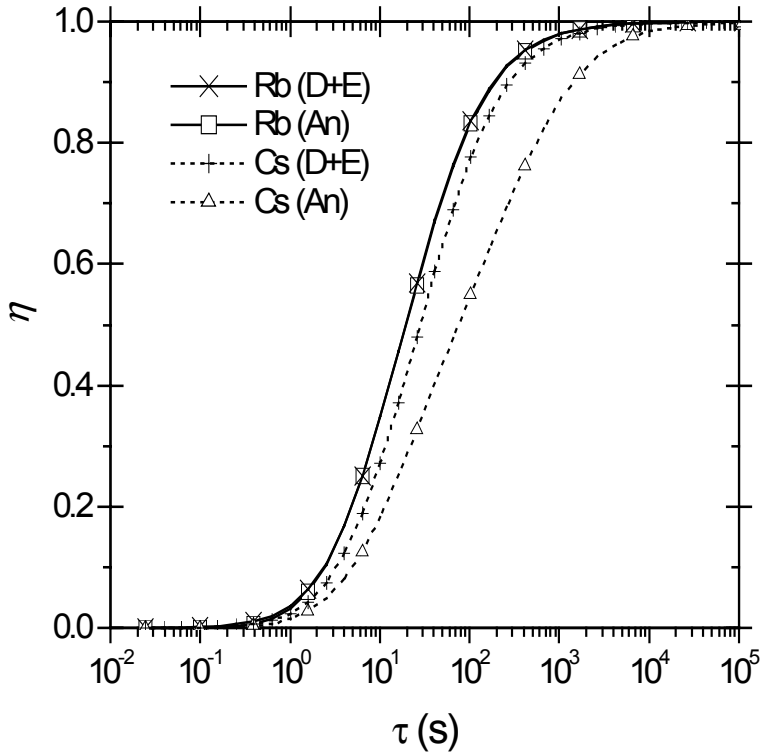

Figure 4.5. Release coefficients obtained from applying the diffusion/effusion model (D+E) and the simplified analytical (an) form of the release curves. The release curves of Rb exhibit a faster, more efficient release process than the curves of Cs. The Rb curves given by the two models overlap with each other, while the Cs curves have a well difference.

of the release coefficient curve of Cs exhibited for the diffusion/effusion model. This effect is rather a dramatic one, considering that the release curve has dropped by over a factor of 20 from its maximum value before the difference between the two becomes apparent. The rate at which the curve converges to zero at the far region of time will weigh a substantial effect on the probability of release due to the fact that an ample fraction of the total area lies beyond the region of the plots. It is easy to see how determining the exact background level can become a critical factor. This is task is rather non trivial since the mass separator can introduce high levels of background coming from transmitted isotopes of dissimilar (*Z*,*A*) [Menat42].

Another likely cause of this tail may be from feeding of 139Cs via the 139Xe ($T_{1/2}$=39.7 *s*), 139I ($T_{1/2}$=2.3 *s*), and 140I ($T_{1/2}$=0.86 *s*, β-*n* 9.3%). Isobaric contamination by 139Ba ($T_{1/2}$=83 *min*) and its respective feeding channels was pointed out earlier. If it is contamination at the mass separator level, then the presence of longer-lived background isotopes can also explain the discrepancy. Whatever the case may be, the discrepancies are significant enough to reconsider using the analytical model at all. Adopting the efficiency from the diffusion/effusion model as being the most accurate seems reasonable, despite the fact that the fits may be in less agreement with the observed results.

Before moving on to the next discussion we show the results of the production as calculated by the Monte Carlo models. The plots in Figs. 4.6(a) and (b) illustrate the mass distributions predicted by the simulation for Rb and Cs isotopes for both the direct and indirect setup. The contribution to the production by the high and low energy spectrum of particles has been plotted separately, along with their sums. The lower

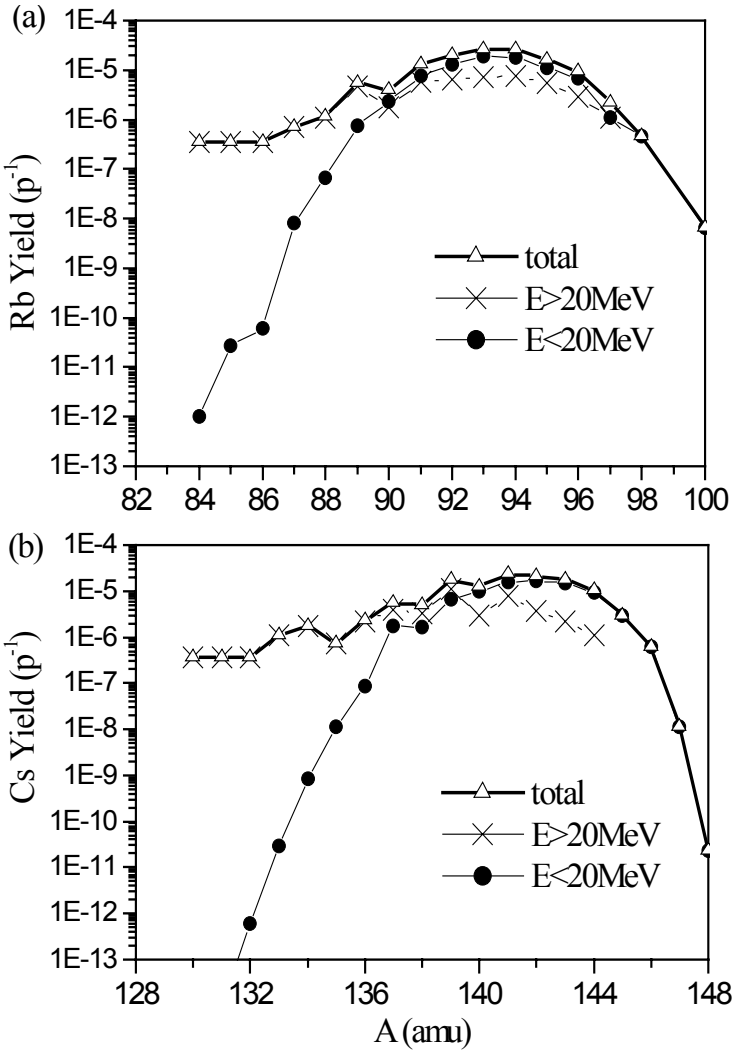

Figure 4.6. (a) Mass yield distribution of the Rb isotopes in the indirect target configuration when striking the neutron generator with 1 GeV protons. A curve is given for the yields given by the LAHET code for E>20 MeV particles as well as those resulting from the production by neutrons of E<20 MeV. (b) Similar mass distribution for the Cs isotopes.

energy neutrons cause a Gaussian like mass distribution and seem to be the dominant component at the neutron rich side of the mass spectrum. The characteristics of production by fast neutrons or high energy protons have been detailed previously [Crouch77]. The neutron production exhibits peak production of isotopes at about mass 100 and 135 forming an asymmetric distribution about mass 118. It is characteristic of 238U nuclei to fission into unequal parts under the excitation of fast neutrons. On the

other hand, collisions by high energy protons tend to cause a high level of excitation, which leads to spallation or the fission of highly excited nuclei. Consequently, for the production by fast particles yields a mass distribution that is predominantly symmetric about the mid region of the initial total mass of the target nucleus.

4.6 Comparison of the two production methods

The results of the Monte Carlo calculations are provided in the form of mass distributions. The code tracks the events initiated by 1 GeV protons striking the target and registers the creation of every possible isotope product. For protons directed at the UC*x* target, the simulation records the production for a total of 6×10^5 incident protons. In the case of protons striking the tantalum block, a factor of 10 more protons were used since only about 23% of the neutrons generated at the block actually penetrate the UC*x* target.

Measurements of the accumulated yields, *R*, are recorded for each isotope mass region to obtain the production rate in both the direct and indirect setup. Having subtracted out the background signal at the detector, we then take the ratio of the direct to indirect accumulation for each species of interest. The experimental conditions remain the same for both measurements, since only the position of the beam on target is varied. Thus, the ratio only carries the effects of the production, *P*, of each isotope observed. Past experience has shown that the diffusion rate can be enhanced by the vacancies that the proton beam leaves behind [HagebØ92]. Comparing the release curves between both configurations would be one way to measure any difference in diffusion times; however, the effect seems to be negligible according to the results obtained here.

The ratios are plotted in Fig. 4.7(a) and (b) for Rb and Cs, respectively, for the neutron-rich mass region. The measurements are obtained primarily from the tape transport and beta detection system. At the less neutron-rich side the production is sufficient to measure electrical current with the Faraday cup. When possible, a comparison between both methods of measurement serves to verifying that the results are

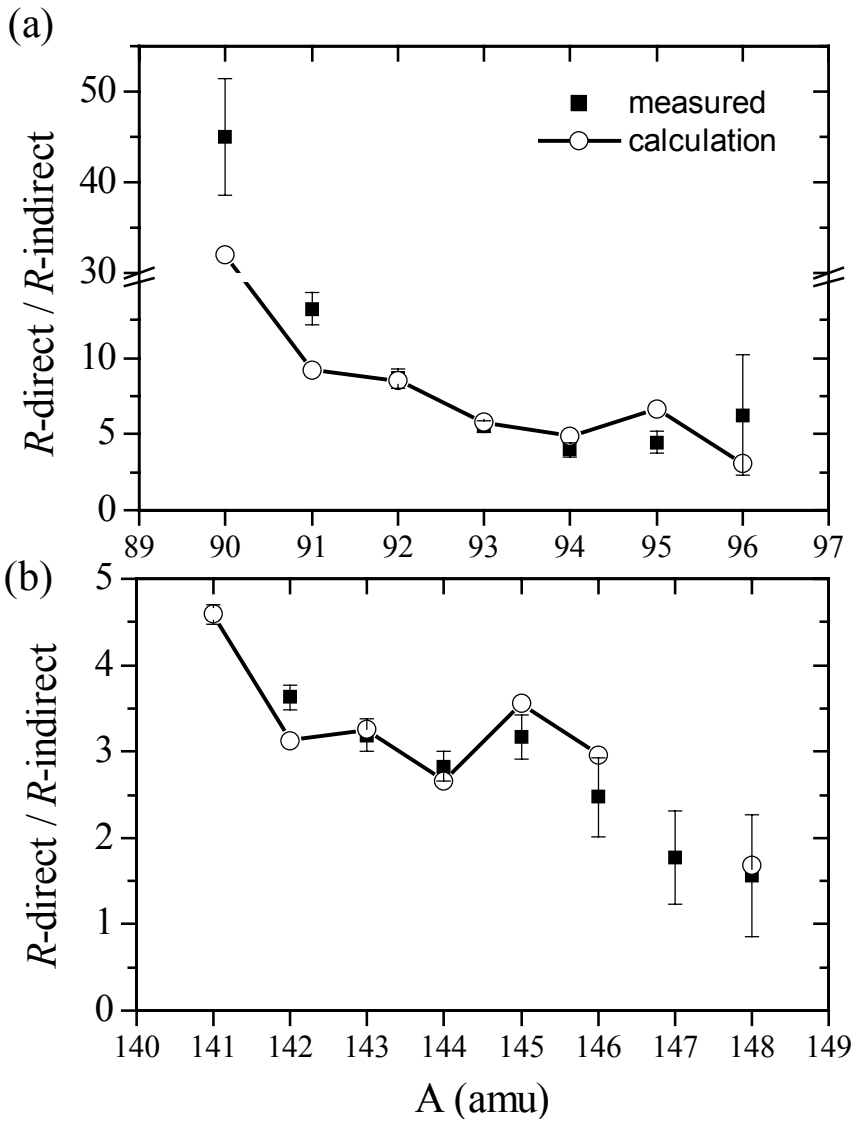

Figure 4.7. (a) Plot of the ratios for the measured yields in the direct and indirect configuration in the neutron rich Rb mass region. Plotted also are the predicted ratios given by the Monte Carlo calculations. (b) Similar plot for the neutron rich Cs mass region.

consistent with each other. For the case of mass 90 and 91, the error bars are associated with the systematic error in the picoammeter read out. The error bars in the rest of the data come directly from counting statistics. The ratios are in agreement with the trend predicted by the Monte Carlo calculations in both mass regions. The results of the comparison instill confidence in utilizing the models for simulating production yields.

4.7 Purity of beams

Up to this point, we have not taken full advantage of the measured release efficiencies calculated in Section 4.4. In this section we will use the efficiency values predicted by the analytical model, as well as any other relevant efficiencies, to obtain the absolute yields, *P*, from experimental measurements. The results can be compared to the absolute yield values predicted by the Monte Carlo calculations and an assessment can be made about the purity of the mass separated beams.

When making mass measurements in regions where adjacent mass peaks are at least an order of magnitude larger, there is always some amount of contamination that crosses over into the accepted window at the mass of interest. This effect generally occurs when other masses are scattered by residual gas atoms or chamber walls, such that they end up at the detection region. Another source of contamination stems from isobars, i.e. isotopes of the same mass number. Being that the mass separator system used has a resolving power $\leq$800, it is not possible to separate isobars, such as those of Ba or Sr. We depend a great deal on the chemical selectivity of the ionizer, and to some extent, of the diffusion process, to yield mostly Cs and Rb; however, it is almost inevitable to have some level of contamination. We attempt to look at the magnitude of this effect and how it may affect the final results.

4.7.1 Time dependent decay measurements

The mass separated beams are collected on tape right in front of the detector (det-1 Fig. 4.2) as the proton beam is directed at the UC*x* target. The Faraday cup is used to detain or release the ion products to record the decay activity versus time. The results obtained for the Cs mass region between A=144 and 148 are plotted in Fig. 4.8. The ions were collected throughout a series of one minute intervals as the activity from the chain of decay was recorded at 1 second intervals. The curves plotted with the data are calculated from the corresponding rate equations for decay of each respective Cs isotope. For example, in the case of A=147, we assume that the curve labeled "0" is that of only the 147Cs→147Ba decay channel. The next curve, labeled "0,1", sums the 147Ba→147La decay to the previous one by assuming equal probability of detection. Each consecutive decay in the scheme is added to the previous one in this manner until a stable isotope occurs, or one of negligible decay rate. In the case of 146Cs, 147Cs and 148Cs there is a beta-delayed neutron decay channel that is probable which must be accounted for. This was especially important in the case of 147Cs where 43% of them will decay through 146Ba→146La→146Ce→146Pr by β^- decay. The curve that includes this chain is labeled as "0,...,4,bn(43%)". The rate of isotope accumulation, R, is chosen such that final results minimize chi-squared relative to the measured count rate.

Quite a remarkable fit is obtained for the case of A=144 and 145 giving a reasonable amount of confidence that the collected isotopes are mostly of Cs. For higher mass the statistics become worse and the fit to the data becomes poor. The fact that we assume equal probability of detection for each daughter may have something to do with it, but it seems more likely that some amount of contamination might be causing the shape of the curve to deviate due to differing decay rates by contaminants.

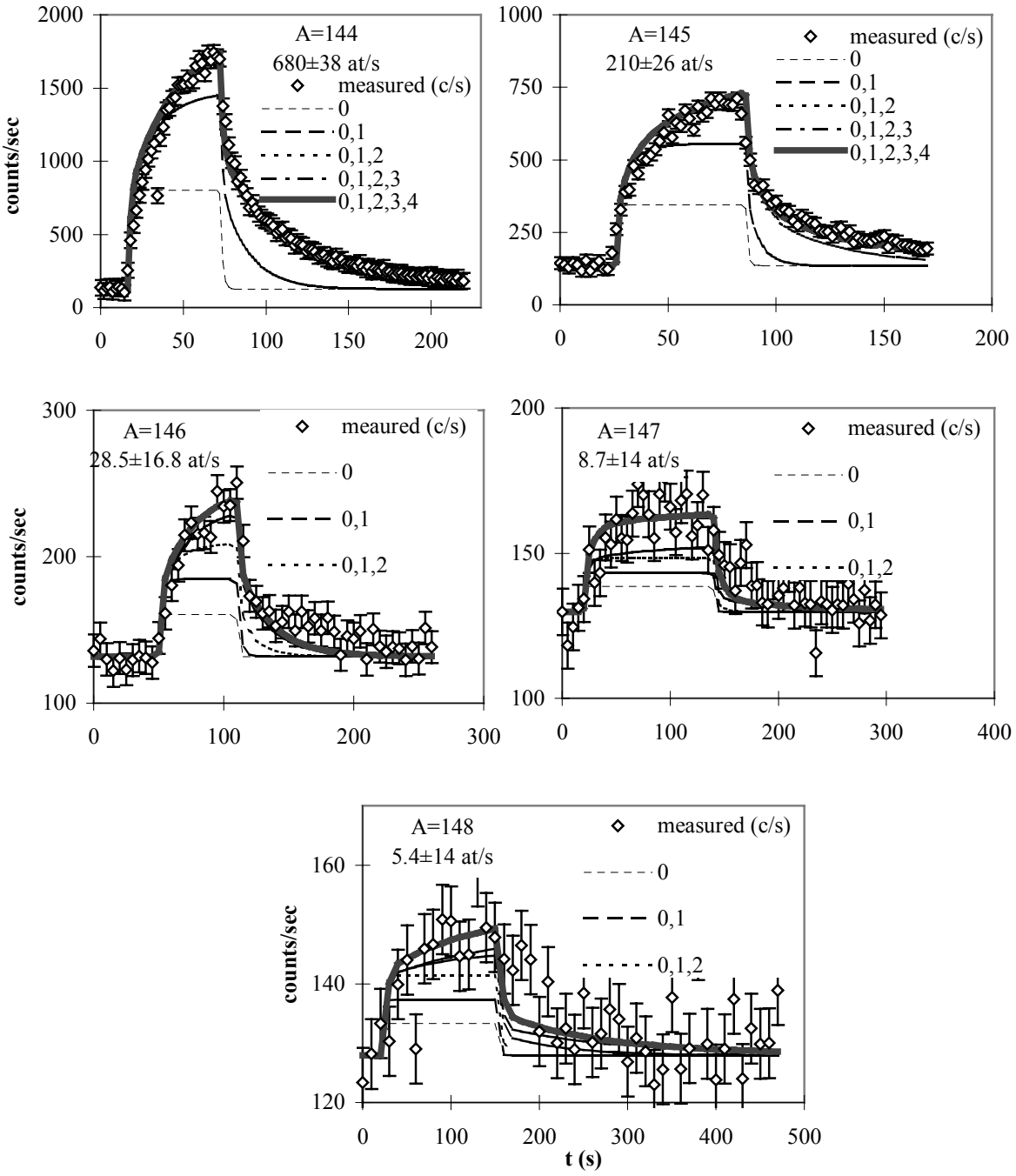

Figure 4.8. Measured activity as a function of time at the solid state detector (det-1 on Fig. 4.2) at various mass regions. The various line graphs result from simulation as described in the text.

4.7.2 Absolute yields

During the irradiation of the sample the production and release are approximately at equilibrium, thus the accumulation rate, R, is related to the absolute yield by

$$R \approx \varepsilon_i \varepsilon_T \varepsilon_D \eta (J \times P) \qquad (4.14).$$

Applying this relation to the data gives the values plotted in Fig. 4.9 along with their respective absolute yield values predicted by the Monte Carlo calculations. If we trust that the calculations are correct, then we should expect that the experimentally determined yields should drop more rapidly for increasing neutron number. Since this is not the case, then there is a possibility that contaminants are present that make the measured count rate higher than expected.

It is instructive to do some estimates based on the calculated production yields by

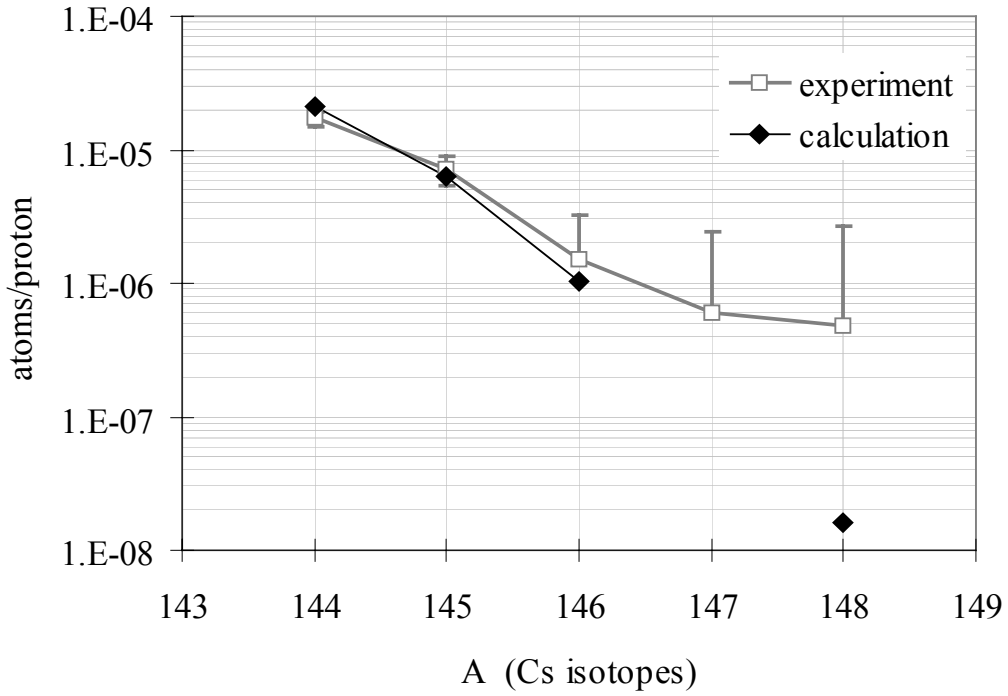

Figure 4.9. Experimentally measured values of the absolute yield at the target obtained by correcting the values of R for release, ionization, and transport efficiency. The production for Cs isotopes as given by the Monte Carlo models is shown for comparison.

applying the above equation to predict R for any isobars that are possible. Generally, we would need to determine the release efficiency of the isobars, since they generally have different chemical properties that vary the rate of diffusion. For the sake of simplicity, we just assume that the release coefficient of each element is the same. This assumption may be reasonable for the Rb/Sr and the Cs/Ba isobaric combinations; however, it is likely that La, Ce and Pr have significantly different chemical properties than Cs.

The factor that sets the elements apart the most is the ionization efficiency, where the values plotted for surface ionization from Fig. 4.3 have been adopted. Again, we treat the detection efficiencies for β^- decay as equal for each decay. The percentage of R expected from each isobar is evaluated at each isotope mass of Rb (a) and Cs (b) and has been listed in Table 4.2. Isobars whose contamination level falls below the 1% level are omitted.

The predictions suggest that only a small amount of contamination should be expected at the Rb, except for 96Rb where the 96Sr production is significant. This is consistent with the observed results of the Rb data. On the other hand, there is a significant amount of Ba and La isobaric contamination predicted for Cs isotopes. Thus, it is quite possible that the discrepancies in the decay data for the Cs are associated with isobaric contamination.

There are more direct methods of looking for contaminants, for example by using gamma ray detection. Such techniques may be useful in verifying some of the results. It is quite probable that cross contamination by beam scattering contributes, but the extent to which it does may require an enhanced detection system. Such information is useful in evaluating the performance of the ionization and mass separation technique and could

Table 4.2 Estimated fractional contamination for Rb(a) and Cs(b).

Mass	Components
92	95% Rb, 5% Sr
93	96% Rb, 4% Sr
94	99% Rb, 1% Sr
95	99% Rb, 1% Sr
96	83% Rb, 17% Sr

Mass	Components
143	90% Cs, 10% Ba
144	73% Cs, 27% Ba
145	54% Cs, 44% Ba, 2% La
146	18% Cs, 75% Ba, 6% La, 1% Ce
147	58% Ba, 24% La, 17% Ce
148	1% Cs, 26%, Ba, 16% La, 44% Ce, 2% Pr

lead to improvements by changing some of the experimental conditions, such as the surface ionizer temperature, or by modifications to the design of the separator.

Despite the lack of means for direct identification, there is still another level of comparison that gives value to the production ratios of Fig. 4.7. The plot in Fig. 4.10 shows the values calculated for the direct to indirect yield ratios for each possible isobar contaminant of Cs. The values for Cs are the same ones appearing in Fig. 4.7, where we compare with the experimentally measured values. The calculations show that one should expect the ratios of Cs and its corresponding Ba isobars to be very similar at A=143 to 148. The La isobars deviate by as much as a factor of two in this range, but not as much as expected for the Ce isobars. Superposing the Ce ratios according to the percentages evaluated for Table 4.2 would cause the data to look significantly different,

since the production of these isotopes by the direct setup is expected to be exceptionally high. There is little indication that the effect of a Ce contaminant is present, which may indicate that its release may be negligible compared to Cs and Ba. In fact, there is little evidence in the literature to suggest that La and Ce leave UC*x* targets rapidly compared to Cs and Ba [HagebØ92]. Carraz and others even claim to have used a carbide of Ce for fast release, which implies that Ce forms at least a semi-stable compound with carbon even at these high temperatures [Carraz79]. Evidently, if there is any contamination, it is very likely that most of it comes from Ba, and the agreement between the experimental

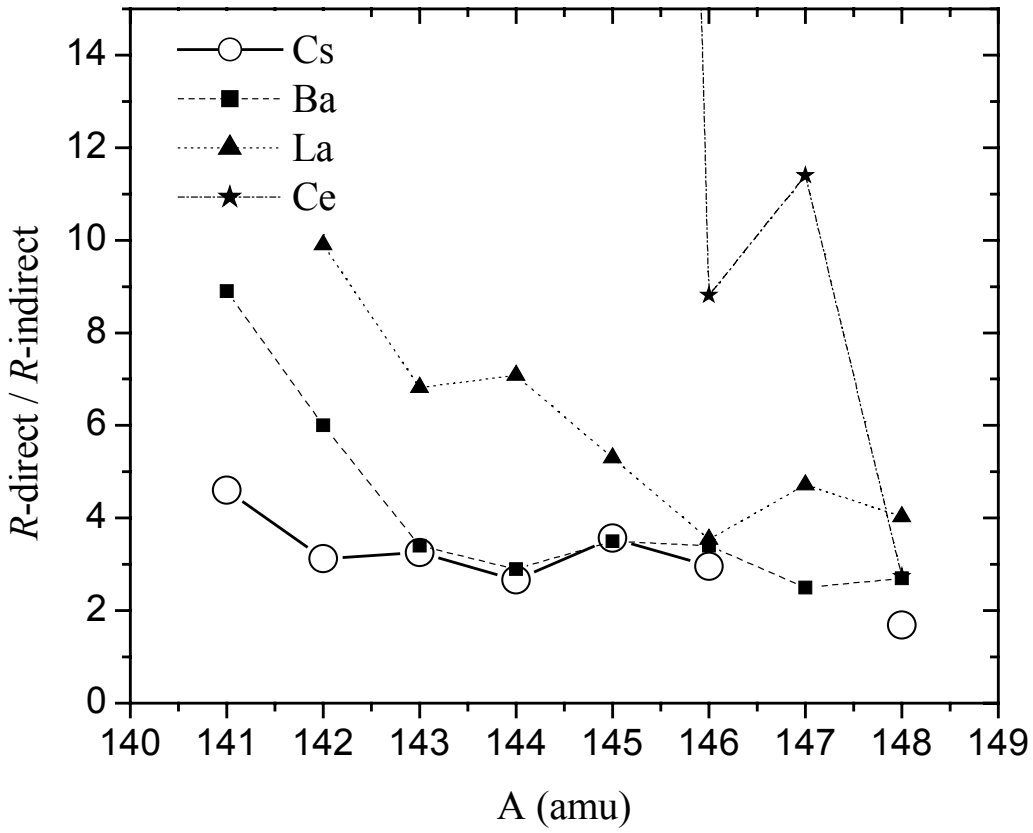

Figure 4.10. Direct to indirect production ratios as calculated by the Monte Carlo models for Cs, Ba, La, and Ce. Relative to Cs, the Ba ratios are very similar but a significant difference is observed; especially for Ce.

and calculated ratios arguably remain sound.

4.8 Mixture targets

From the mass yield distributions plotted in Fig. 4.6 (a) and (b) it is apparent that many of the neutron-rich isotopes are produced mainly by fission initiated from fast neutrons. Using the results given by the Monte Carlo production models an example of a mixture target is given here to determine if it is possible to enhance production by introducing a neutron generator, or material that produces more neutrons per occupied volume.

Consider a species of isotope whose yield results exclusively from neutron induced fission of the direct target nuclei, 238U, with all other interactions having a negligible contribution. We treat each UC*x* molecule as a direct target particle giving ς_d neutrons per incoming 1 GeV proton per molecule (n/p), while only one fission is allowed for each of the N_d molecules. Blended within the mixture are a total of N_g generator atoms, in which each yields ς_g neutrons per proton. The generator is assumed to be tungsten since it has a high density and provides a neutron energy spectrum that is similar to that of the UC*x* direct target. Using the geometry of the container of Fig. 4.1, the Monte Carlo calculations yield that for a pure tungsten mixture of 19.3 g/cm^3, $\varsigma_g = 4.3\times10^{-23}$ n/p. For a pure UC*x* target it gives that $\varsigma_d = 7.6\times10^{-23}$ n/p. The attenuation of the protons is stronger with the tungsten generator but the effect has a negligible effect on the neutron flux generated by each of the targets in the mixture, thus the materials behave essentially the same as a mixture.

The total volume occupied by the mixture is a constant and is given by,

$$V = V_d + V_g \tag{4.15},$$

where V_d is the volume occupied by the direct target and V_g for the generator. The total rate of neutron production is then

$$\zeta_n[n/p] = \zeta_d N_d + \zeta_g N_g \tag{4.16}.$$

If χ is the atomic density, then the number of target particles can be evaluated for each target by $N=V\chi$. The rate of neutron-induced fission can then be expressed as,

$$Y[p^{-1}] = \sigma_n \zeta_n N_d = \sigma_n V_d \chi_d (\zeta_d V_d \chi_d + \zeta_g V_g \chi_g) \tag{4.17},$$

where σ_n is the fission cross section. By applying equation (4.15) and taking the derivative with respect to V_d to find an extremum, it is found that a maximum occurs at

$$V_{dm} = \frac{V/2}{1 - \chi_d \zeta_d / \chi_g \zeta_g} \tag{4.18}$$

as long as

$$\chi_d \xi_d < \chi_g \xi_g \tag{4.19}.$$

For a mixture of UCx and tungsten, it is found that the optimum rate of fission can be obtained from a mixture in which V_d/V=0.62. The plot in Fig. 4.11 shows how the fission rate varies with the fractional volume of the direct target. Since it is assumed that only fission by uranium yields the product of interest, the rate vanishes as only tungsten occupies the entire target. Having pure UCx (V_d/V=1) gives almost 60% less fission yield than the maximum expected when using the mixture (V_d/V=0.62).

The tungsten generator was used here mainly to illustrate the effects of using a mixture where the generator material has no chance of contributing to the production of isotopes from fission. In principle, it is possible to use a high density form of UCx mixed in with the fast releasing powder form. In this approximation, the overall fission rate will rise as the square of the density of UCx. Although the release may be slower than from

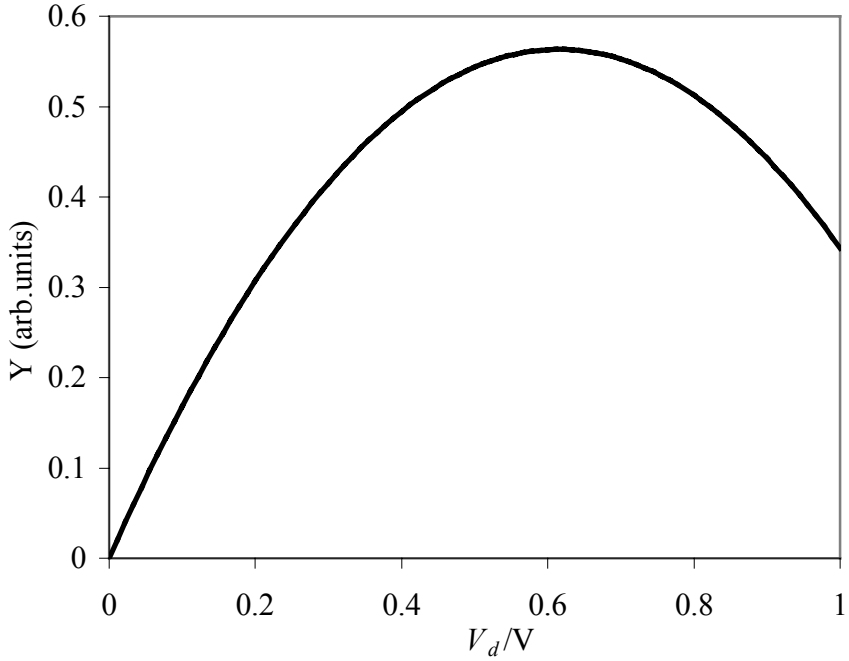

Figure 4.11. Fast neutron induce fission rate as a function of the occupied volume of the neutron generator. The neutron generator here is taken to be tungsten mixed with the UCx fission target of 3.1 g/cm3. Using a mixture with 62% UC*x* powder gives an enhanced fission rate by ~60% relative to the rate at pure UC*x* (V_d/V=1).

the powder material, some amount of enhancement to the production should still be expected, especially for the longer lived species.

4.9 Summary

The analysis of the experimental results indicates that the two-step production process is a useful mechanism for providing isotopes at the neutron rich side of the valley of stability. Since the power from the primary beam does not necessarily have to be dissipated directly onto the target, it has the potential to surpass production levels that are far from reach with direct targets when considering the extent of the damage and lifetime of the source. The Monte Carlo production models suggest that by setting up a geometry in which the UC*x* surrounds a secondary neutron production target, the production rate

for some isotopes will surpass that of the direct target geometries. Since the two-step process produces very few proton rich isotopes, this method is also useful in reducing isobaric contamination in studies of isotopes.

Comparisons of the data with results obtained from the Monte Carlo simulations have verified the vital role of fast neutron interactions for a target enriched with natural uranium. Before these experiments, there had been little direct experimental evidence of the importance of the two-step process. The models predict that for a wide variety of neutron-rich isotopes, the two-step process is solely responsible for their production even in direct proton irradiations.

Dense neutron generator materials, such as tungsten, are ideally suited for extreme primary target conditions and should be considered in the design of future two-step targets. The required beam energy for two-step targets need not be as high, since neutron containing particles, such as deuterons or alphas, can impinge at energies of about ~100 MeV/u to yield an adequate spectrum of neutron energies. For current targets in which high energy protons are utilized, it may also be possible to optimize released yield by either using more dense target material, or by mixing the fast releasing porous kinds with those that generate high neutron fluxes.

The production and release processes combined must form the figure of merit for ISOL targets. Measuring these properties while the target is exposed to extreme temperature and irradiation conditions is essential for developing target/source design for future rare isotope facilities

Chapter 5

DEVELOPMENTS IN BEAM DIAGNOSTICS

In this chapter we describe a number of beam diagnostic techniques that were developed and tested for future RIA beams. The main focus will be on a beam imaging monitor (BIM) that is intended for low beam intensities. Prior to the development of the BIM device there had also been a wire/slit emittance scanning device and a low background ion counting detector developed for other measurements. Since these other two devices were used in obtaining reference measurements for the BIM, we have incorporated them into this chapter and describe each of them.

5.1 Design features of the BIM

A layout of the BIM is illustrated in Fig. 5.1. The beam comes in from the left and passes through any necessary slits or apertures, such as a pepper pot plate (a pepper pot is a plate with an array of small holes). Particles strike a flat aluminum surface that is oriented at 45° relative to the beam direction. The plate serves as a dynode since the ion signal is converted to a burst of secondary electrons (SE). These secondaries are promptly accelerated by a 5-15 kV potential imposed by a grid lying parallel to and 5 mm from the surface. Motion feed-throughs are used to insert the aluminum foil dynode and a dual-slit plate upstream. A diagram illustrating a Simion 7 [Simion7] simulation of this process is shown in Fig. 5.2. We note that the beam cross section in the horizontal plane will appear $\sqrt{2}$ times large due to the 45º tilt relative to the beam coordinate system of the beam, which is also shown in the diagram.

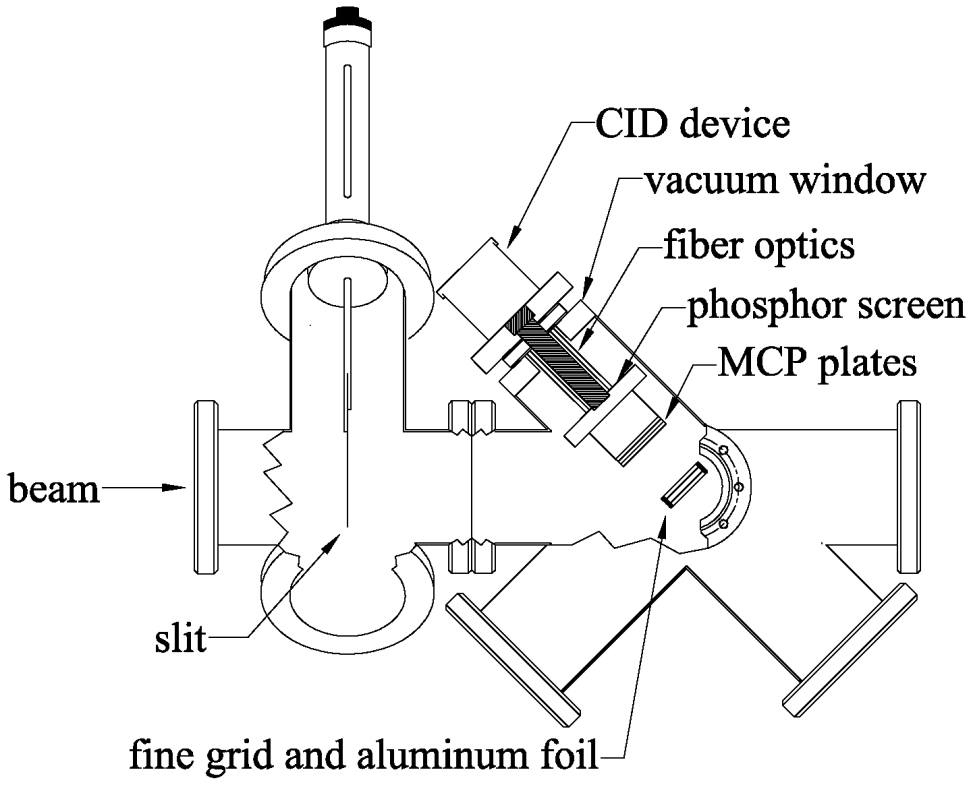

Figure 5.1 Diagram of the BIM.

A position sensitive microchannel plate (MCP) is excited by the SEs and further amplifies the signal induced by the secondaries. The MCP is parallel to the conversion surface as well and lies 47 mm after the grid. The accelerating potential is distributed evenly enough such that the electrons are accelerated perpendicular to the conversion surface; thus the system may be used to map the ion beam intensity along the transverse planes.

The actual detection of the signal is done with the combination of a phosphor screen and a light sensitive detector. A monochromatic CCD (charge coupled device) would be sufficient for detecting the light signal; however, we chose a CID (charge integrating device) since it has less cross sensor-induced noise as well as less thermal induced noise.

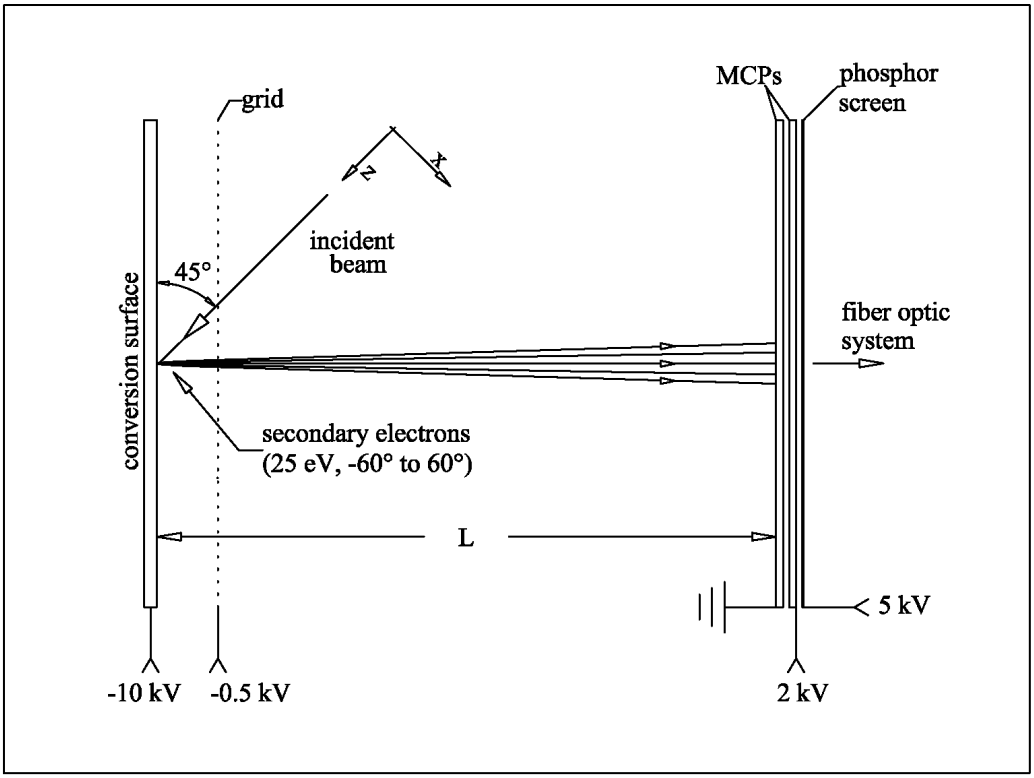

Figure 5.2 Diagram SE collection region of BIM. Trajectories of electrons exiting the surface at angles ranging from -60° to 60° with a kinetic energy of 25eV are simulated with Simon using a 330 μm spaced grid. Bias potential used for each element is shown along the bottom. The beam coordinate system is oriented such that the *z*-axis points in the direction that the beam travels.

A dual MCP detection system was actually used here to obtain high gain. The second MCP lies 0.5 mm behind the first, such that the channel holes align. Both MCPs are identical at 41 mm in diameter and can sustain a maximum bias of 1000 VDC each. A resistive circuit was constructed to allow both MCPs to have equal biases and run off of a single power supply. The dual MCP system has a combined maximum gain of 4×10^7.

About 0.5 mm behind the second MCP there is a type P-20 phosphor plate. It is biased at 3 kV relative to the MCP output to convert the accelerated electron's energy into photons of predominantly 560 nm wavelength. The quantum efficiency is estimated to be about 0.063 photons/eV/electron in this wavelength region [Forand90].

The image is demagnified by a factor of 3 and transmitted to the CID sensor via a fiber optic transport system. The demagnifying element is a fused, tapered fiber optic bundle that goes from 41 mm to 13.7 mm in diameter. Between the end of the tapered rod and the phosphor screen is a 13.7 mm diameter fiber optic rod in direct contact, such that loss of light is minimized. The fiber optic rods are both made of fused glass, optical fiber rods with polished faces. The combined optical system has about 15% total transmission efficiency for most of the visible spectrum of light. The spatial resolution for a single particle exciting the MCP surface directly is better than 0.15 mm according to the manufacturer's specifications [Colutron] and the reported results of Shapira and others [Shapira00].

The CID sensors accumulate a charge that is directly proportional to the total photon flux absorbed at each respective location. The charge is integrated over a 33 ms period and each sensor is discharged after each reading. The thermal noise of the CID sensor array limits the integration period and the amplification gain; however, cooling the sensor and electronics to about -10°C is expected to improve the performance over room temperature operation. We chose to test the performance of this system at room temperature in this study.

The electronics within the camera allow the CID sensors to be read out in the RS-170 image rastering standard. The signal is amplified and then fed into a PCI-1408 frame grabber circuit board. The board features its own amplification with programmable gain to processes the signal before it is delivered to an 8-bit flash ADC. This ADC is capable of sampling at up to 16.5 MHz; however, it only needs to function at 12.3 MHz in the RS-170 raster mode. The images may be digitally processed in real time with the use of

National Instruments IMAQ software [NI] and may be stored for later reference or processing. The signal from the image may also be split to be monitored simultaneously with a TV monitor. The beam imaging system including MCP, phosphor screen, fiber optic rod and CID camera was purchased commercially from the Colutron Research Corporation [Colutron].

The PC also has a stepper motor control board and encoder reference input. This allows us to control and monitor the position of the linear feed through devices that introduce the conversion surface and the upstream slit pattern. The conversion surface may be removed to allow the beam to pass when detection is no longer necessary. The position of the slit and conversion surface is monitored with differential encoders.

A group at the Leuven facility has reported the performance of a similar device [Krublov00]. The most notable feature of their set-up is the use of microsphere plates (MSP) instead of a dual MCP as used here. Although its known to sustain higher pressure conditions than the MCP, the MSP generally exhibits artificial structure resulting in poorer resolution. The Leuven device has a limited grid potential of 5 kV and little is referenced about the effects that the grid spacing has on the image resolution. In contrast, for the BIM device here we can apply up to a 15 kV potential with little thermionic emission and breakdown at pressures better than 10^{-6} Torr. Furthermore, the Leuven set up uses a CCD lens camera for detection from the phosphor screen as opposed to the CID sensor and fiber optics utilized here. Other systems based on SE emission imaging have been tested or are underway for the measurement of ion beam transverse and longitudinal profiles [Feschenko96].

In another study conducted by Shapira and others, a detection system similar to the one constructed here was used with thin foils of carbon or aluminized Mylar instead of a polished aluminum surface [Shapira00]. They utilized a similar MCP detection system to study fast timing and position resolution with the use of a Position-Sensitive Timing Detector. Their results support some of the conclusions found in this study.

5.2 Low-background ion counting system

Part of the interest with the BIM lies in knowing what minimum ion flux can be discernable when acquiring beam images. For this analysis an ion counting detection system that had been developed for some earlier studies is employed. The ion counting system is similar to the BIM system in that it relies on SEs from a conversion surface to amplify the signal from colliding ions. Instead of an MCP, however, this system uses a channeltron for amplification of the SE signals as shown in Fig. 5.3.

A number of features have been implemented for making this system ideal for counting of heavy ion beams. At the heart of the system is a channeltron with a gain about 10^6 and dark current of less than 10^{-12} amps at a 2 kV bias. The mouth of the detector is 25 mm in diameter with a copper mesh that sits 25 mm away to allow an even field distribution with the conversion surface. The mesh is made of thin copper wires spaced evenly in squares of 0.33 mm sides to give a transmission ~90%. The conversion surface is made of a thin coating of BeO with stainless steel backing. The surface normal is oriented at an angle of 70º relative to the direction of the incoming beam to maximize the SE yield [Dietz75]. Measurements show that an average of 8.7 electrons are released with low energy Cs^{1+} beams of 10 keV. The pulse width of the ion signal is about 2 ns at half width and is amplified with a fast timing amplifier. Using a constant fraction

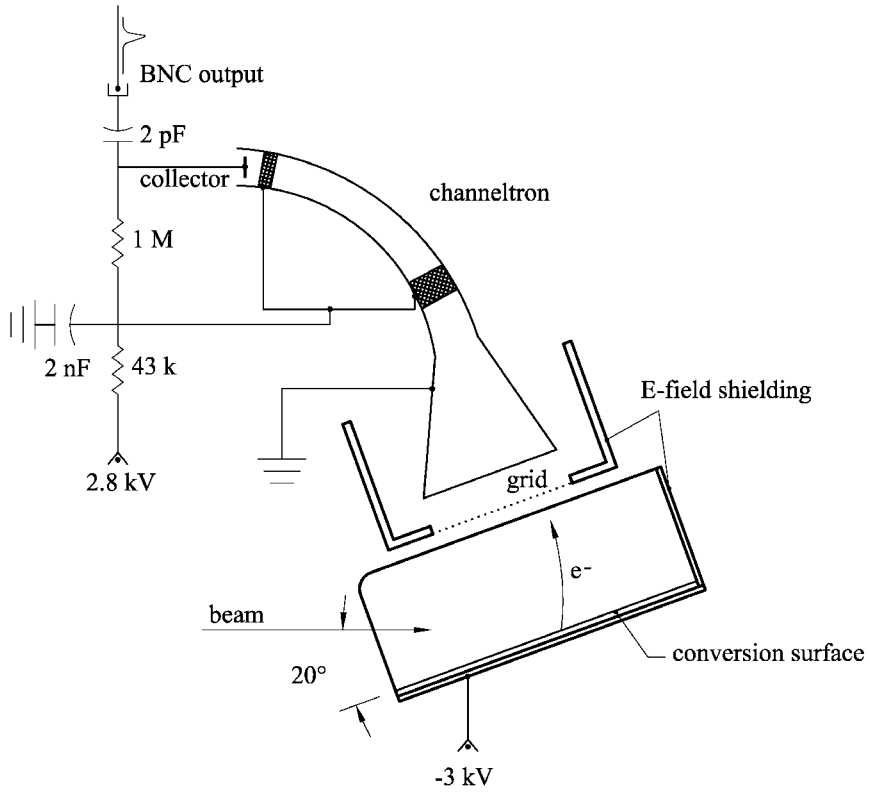

Figure 5.3 Ion counting detection system based on a channeltron electron multiplier and a BeO conversion surface. Resistance is in units of Ohms.

discriminator it was possible to obtain as little as 0.3 counts/s background without ions. The system has almost 100% detection efficiency at count rates of $<10^3$ and >50% for count rates as high as 6×10^6 counts/s as shown by the plot in Fig. 5.4.

The detector was installed 20 cm upstream from the slit of the BIM at the "8°+27° West" beam line at the Argonne Dynamitron accelerator facility. A focused DC beam of $^{84}Kr^{+1}$ with energies ranging from 300 keV to 1.5 MeV is used. Two dipoles bending in the same direction are used to select the isotope of interest over a 15 m long transport line and a quadrupole doublet refocuses the beam as it is delivered to the target region as shown by Fig. 5.5.

The plasma source of the accelerator typically delivers beams at the tens of microamperes for steady operation; thus, a beam attenuation system outside of the accelerator is needed. Two grid attenuators of know transmission are used for reducing the beam intensity down to the level of hundreds of ions per second. Both are located

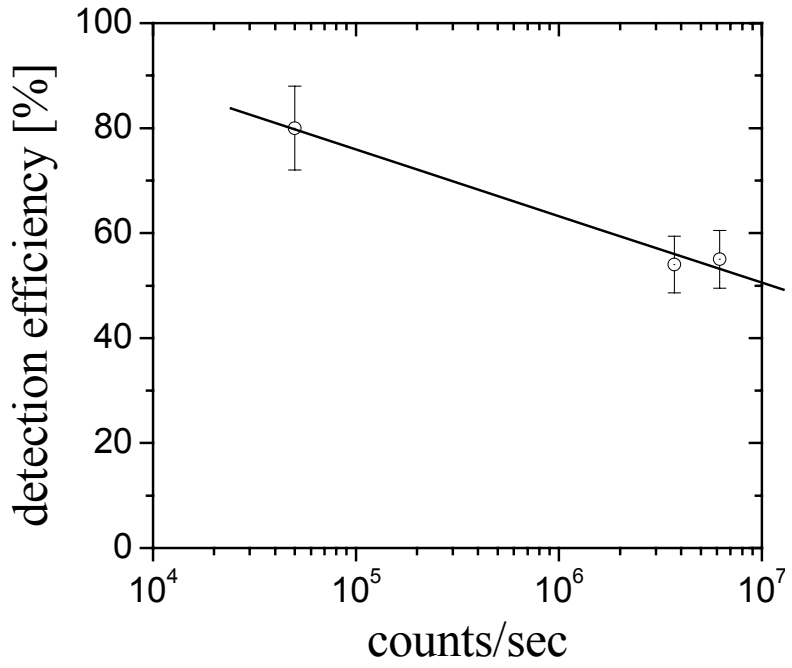

Figure 5.4 Detection efficiency for counting ions of $^{133}Cs^{+1}$.

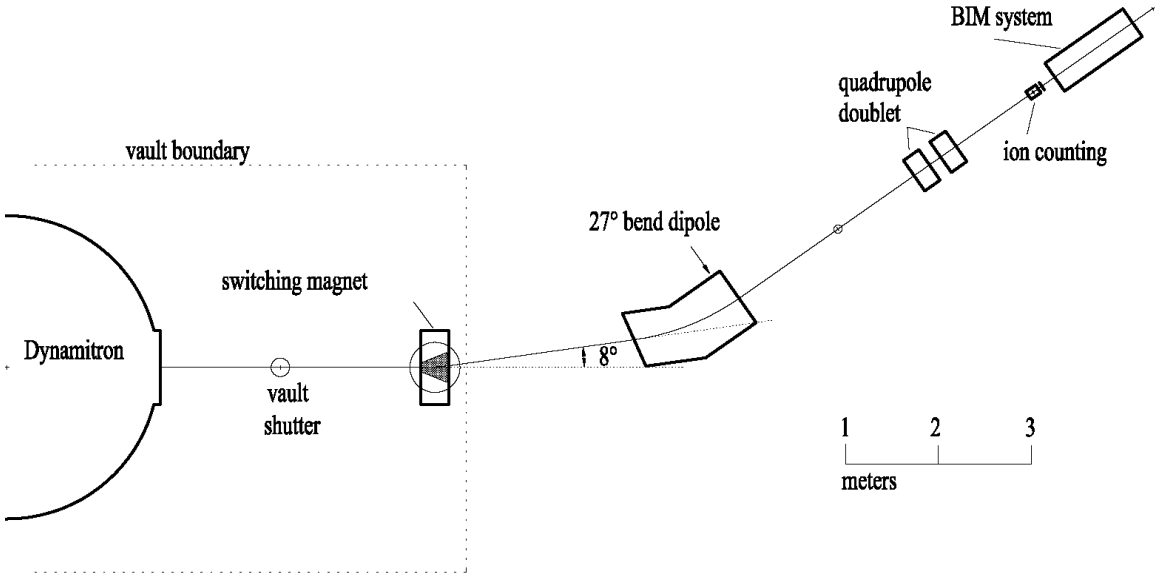

about 1.5 m apart with the 27° bend dipole between them. Four-jaw slits are used for lowering the intensity even further and can be used for locating the exact beam position before the BIM. We are able to suppressed beams down to the 10^2 pps level for an $84Kr^{+1}$ beam at 12 keV/u and still visibly detect the ions striking the conversion surface of the BIM within a 2 mm by 2 mm surface area.

5.3 Beam emittance measurements with wire scanner

Another measurement system developed for emittance scanning was incorporated with the BIM system during tests. It is designed to scan the emittance in only one plane and must be rotated after breaking vacuum to measure the other plane. In this case it scans the *y*-plane.

The main features of this device are best described by referring to the diagram in Fig. 5.6. Stepper motors are used to drive the linear feedthroughs, while the differential encoders are used to reference the exact position. The details about the slit plate are described in the later sections since it has been especially designed to function with the BIM. For now we just mention that slit that lies in the same direction as the wire that is used for the emittance scan in this system. The wire is made of tungsten and is 0.25 mm wide. The beam flux that hits the wire is measured at with a picoammeter in series with a battery that imposes a bias voltage of –45 V on the wire. The bias allows the SEs leaving the wire to amplify the current by ~3 and suppress any stray electrons generated elsewhere in the system, such as on the slit plate. With this emittance scanning system we are able to obtain very highly resolved scans of the emittance used to compare with those of the BIM described in Section 5.6.

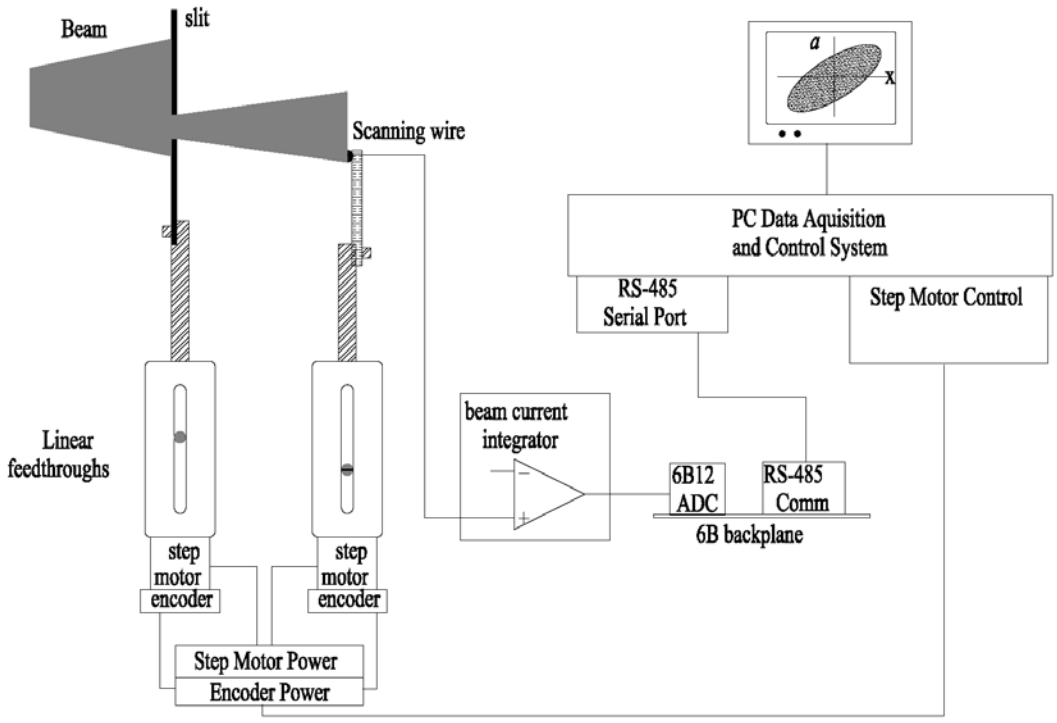

Figure 5.6 Diagram illustrating the slit/wire emittance scanning system.

5.4 Properties of secondary electrons and effects on detector

A significant amount of signal amplification of the BIM is attributable to the collision of the ion with the aluminum dynode. The excitations from the colliding projectile at the dynode result in the ejection of other ions, neutrals, photons, and electrons. The energy and angle distributions of ejected SEs have been studied by Rothard and others [Rothard90]. They find that the angular distribution of the ejected electrons tends to obey a $\mathbf{cos}\theta$ distribution, but indicate that there is no dependence on the angle of incidence of the projectile. When surface roughness is appreciable the intensity seems to drop off more rapidly when sampling away from the surface normal.

The energy distribution of secondaries tends to exhibit a feature that is predominantly independent of the combination of projectile and target used. The distributions tend to

exhibit a sharp peak at 2.1±0.3 eV that contains ~85% of the total distribution. The rest of the distribution lies along a decaying exponential like curve with some structure present as a result of Auger and kinematic effects [Rothard90]. The average number of SEs ejected per ion event, γ, depends on many characteristics of the projectile/surface combination. We provide some arguments that support the fact it is actually excitations very close to the surface that generate most of the SE flux.

The range even for 0.3 keV/u 84Kr is about 200 Å and most of the energy is deposited evenly along the path of the collision cascade. The mean free path of electrons with energies even at 20-100 eV is 3-5 Å [Bauer72]; therefore, it is conceivable that only the energy deposited within first few Å from the surface contribute to the SE flux. To support these arguments it has also been shown that the average number of ejected electrons is actually proportional to the electronic stopping power *dE/dx* of the projectile/target combination [Albert92]. As mention previously, the energy deposited close to the surface increases with the angle of incidence, and studies have shown that the distribution of SE flux along the angle relative to the surface normal, θ, varies in close proportionality with $\mathbf{sec}\theta$ [Dietz73].

The number of SEs ejected per ion event can be characterized by a Polya, or negative binomial, distribution as shown by Dietz and Shefield [Dietz73] [Dietz75]. Binary collisions between atoms are generally described best by a Poisson distribution; however, the effects of the bulk surface on the escaping electrons results in a broadening that depends much on the ion/target species as well as other surface properties. The result is an overall growth in the variance, σ, for the distribution. For example, it had been observed that a 30 keV Cs^{+1} beam impinging on an oxygen treated Cu-2%Be surface

gives ~10% larger σ than expected form a Poisson distribution at the measured γ [Dietz75]. The broadening affects the efficiency of detection and makes it impractical to apply any technique that would allow discriminating between particles, say of different mass, striking the surface.

In this study we measure the overall electron flux by applying a potential to the dynode to suppress the electrons and subtract the ion current. At an incident angle of 45° we obtain ~12 e-/ion for 1.5 MeV $84Kr^{+1}$ on the untreated aluminum surface. Building up an oxide layer at the surface and using materials such as Cu-2%Be can increase γ; however, we use an untreated surface since it is less susceptible to surface degradation over long exposures to heavy ions. We should note that similar measurements were used to measure γ for the low-background ion detector described in Section 5.2. There we obtain a lower γ since we were using Cs ions at 10 keV.

Trajectory simulations were carried out using Simion 7 to determine the broadening effects caused by the overall drift and microlensing at the grid. Monte Carlo techniques were applied to simulate the energy and angular distribution of the secondaries. The distribution of initial angles from the surface is taken to be proportional to $\mathbf{cos}\theta$. A combination of two Gaussians and a Maxwellian function is utilized to form a probability density that best fits the data of Rothard [Rothard90] for the energy distribution. The function is expressed by

$$p(x) = \frac{\alpha_1}{\sqrt{2\pi\sigma_1^2}}\exp[-(E-E_{C1})^2/2{\sigma_1}^2] + \frac{\alpha_2}{\sqrt{2\pi\sigma_2^2}}\exp[-(E-E_{C2})^2/2\sigma_2^2] + \frac{\alpha_3}{E_M}\exp(-E/E_M) \quad (5.1),$$

where the parameters used are listed in Fig. 5.7 along with a plot of the simulated distribution. The initial positions of all trajectories are distributed evenly along the grid over 8 grid spaces. This was necessary since the focusing action of the grid depends on this initial position. The relative displacements were recorded for each trajectory to evaluate the rms displacement, σ_e. The results obtained when sampling σ_e, along with the rms transverse velocity, δv, are shown in the double axis plot of Fig. 5.8(a). The grid potential is V_g=13 kV.

We also consider the case where the perpendicular component of the velocity, $v_\perp$, is non-relativistic and the transverse component is small compared to $v_\perp$. Also, we assume that the acceleration takes place in a region that is negligibly short compared to the drift that follows. Under such conditions we can apply the relation,

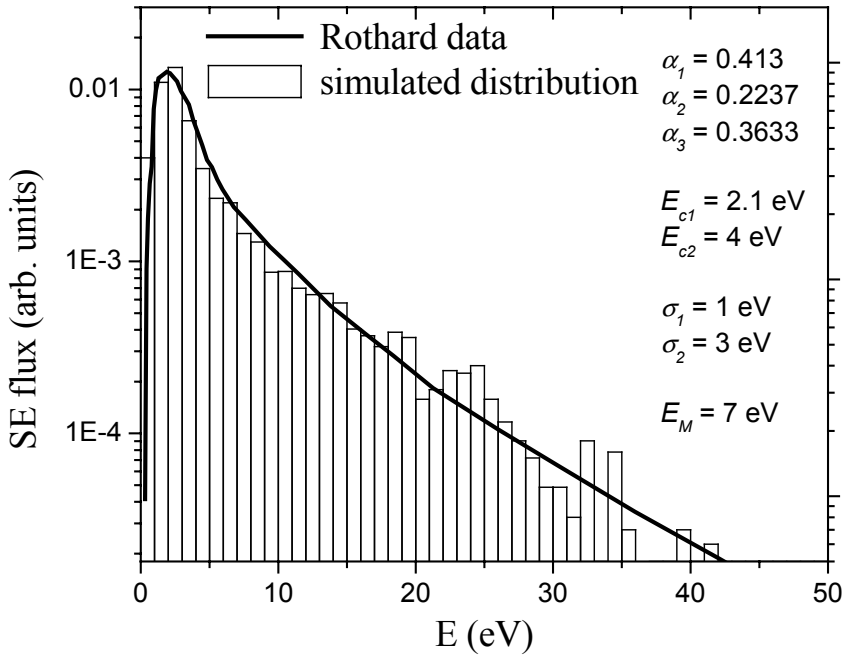

Fig. 5.7 Simulation of energy distribution (bar graph) compared to the experimental data of Rothard as explained in the text. The parameters used with the probability density function are listed.

$$\sigma_e \approx L \cdot \frac{\delta v}{v_\perp} \approx \delta v \sqrt{\frac{L^2 m_e}{2 \cdot V_g e}}, \tag{5.2}$$

where L is the distance between the dynode and MCP surface, m_e/e is the mass to charge ratio of the electron, and V_g is the acceleration potential. The term in the square root of Eq. (5.2) is approximately constant; hence σ_e scales very linearly with δv. The transverse velocities are amplified by the grid potentials as the grid spacing becomes larger—especially beyond 0.5 mm. A 0.33 mm spaced copper grid with ~90% transmission was used for this apparatus just as it was for the low-background ion detector.

We then turn our attention the broadening dependence on the grid accelerating potential. For a 0.33 mm grid spacing, V_g is varied over some range, and the broadening is better understood if we rewrite Eq. (5.2) as

$$\sigma_e \approx w \cdot \delta v \Big/ \sqrt{V_g} = w \cdot \xi(V_g), \tag{5.3}$$

where w is a constant obtained by comparing with Eq. (5.2) and the dependence on V_g is absorbed into the function, $\xi(V_g)$. A comparison is made between this equation and the results of the Simion simulation in the graph shown in Fig. 5.8(b). The σ_e (left axis) and δv (right axis) values are plotted for $0<V_g<20$ kV. The rms transverse velocity seems to increase linearly with accelerating potential, however, only by ~10% throughout this range. The solid line is obtained by Eq. (5.3) under similar conditions.

Since the rms velocity remains approximately constant, it is possible to decrease the divergence by increasing the grid potential. Going from 5 kV to 13 kV decreases σ_e by almost 40%. The rate at which σ_e decreases lessens appreciable for higher potentials and

will eventually shift to an increases with V_g as δv will eventually begin to dominate. The actual limit obtained with our detector seems to be at about 15 kV, at which point the thermionic emission produces considerable noise to the detector.

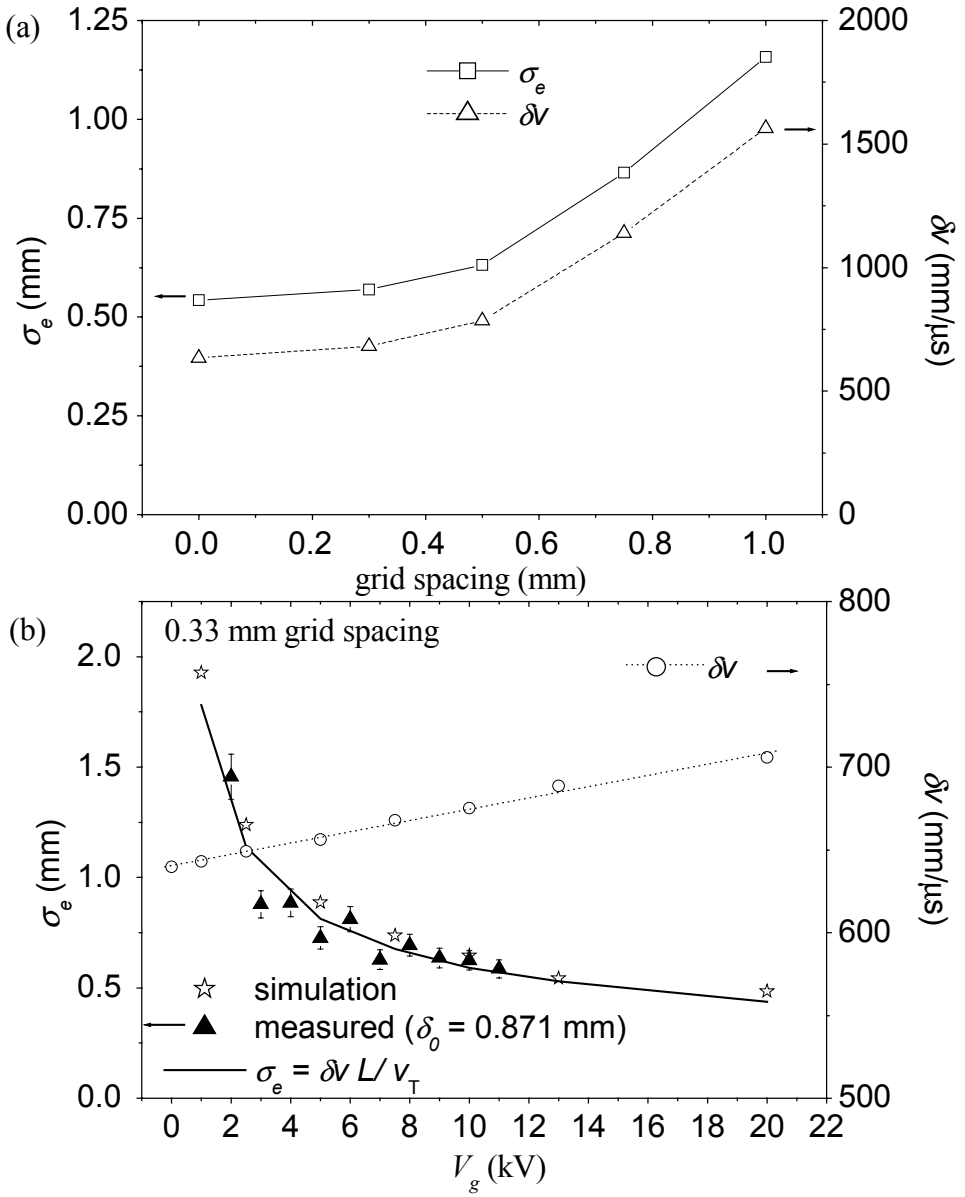

Figure 5.8 (a) Broadening of the secondaries as they are transported to the MCP for detection as calculated by Simion 7. The rms of the transverse velocity, δv, component increases with mesh size, which causes σ_e to increase almost proportionately. (b) Results of simulation showing the σ_e (left axis) and δv (right axis) dependence on grid potential for a 0.33 mm grid. The solid line is evaluated from an equation that explains what the physical significance of the process where δv is taken to be a linear function of the grid potential.

The dependence on V_g was measured experimentally with a beam spot centered on the dynode surface. The weighed rms moments along the horizontal axis, H_{rms}, were measured for a grid potential varying from 2 kV to 11 kV. A constant factor, δh_0, is summed in quadrature to σ_e to account for both the finite beam size and broadening due to the electron and photon optics at the MCP. This results is expressed as follows:

$$H_{rms}^2 = \sigma_e^2 + \delta h_0^2 \tag{5.4}$$

Fitting this equation with the measured H_{rms} values yields that δh_0=0.87 mm if σ_e is evaluated by Eq. (5.2) and δv values are taken from a linear fit of the simulation. We solve for σ_e and plot the values in Fig. 5.8(b). The effect of the grid potential on the broadening seems to be well understood by this result.

5.5 Measuring transverse density distributions

The tests with $^{84}Kr^{+1}$ ions at the Dynamitron showed that beam of 3.6 keV/u and 18 keV/u can be well imaged with an intensity as low as 4×10^2 pps. The maximum intensity that it could take may be higher than ~200 nA; however, of the grid and MCP detector lifetime will suffer. In this study there were no observable deleterious effects even when running up at up to 10^{12} pps at 1.5 MeV for several hours.

Bitmap images of snap shots taken of two different beams are illustrated in Fig. 5.9. Fig. 5.9(a) is that of 18 keV/u krypton ions at rate of 4×10^2 pps. Each resolvable spot represents at least one ion collision event. We point out that the voltage across the MCP system need only be high enough to obtain a detectable light intensity when keeping the phosphor system at peak sensitivity. This is necessary to extend the lifetime of the MCP.

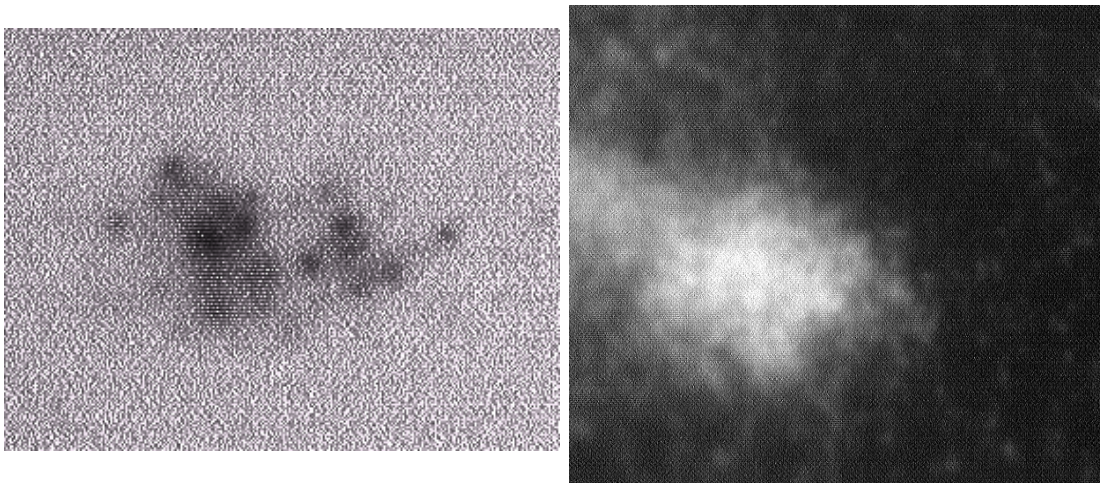

(a) (b)

Figure 5.9 Beam images of a) low intensity ~4×10^2 pps 18 keV/u krypton beam, area size is 5.1 mm × 6.5 mm; b) Total intensity of 2.5 ×10^5 pps of a radioactive beam line. Area covered in coordinate system of the beam is ~17.0 mm×18.2 mm.

Since the MCP plates are highly insensitive to gamma radiation (and to a lesser extent, beta radiation), this detection system is sufficiently immune to radioactive decay of a wide range of implanted particles. From a recent experiment we obtained the results illustrated in Fig. 5.9(b), where a momentum selected, mixed beam of $17F^{+9}$ (67 MeV), $16O^{+8}$ (56 MeV), and $16O^{+7}$ (43 MeV) is striking the conversion surface. The $17F^{+9}$ component constituted 68% of the 2.5×10^5 pps resulting from an inverse kinematics in-flight production technique used at the ATLAS to produce a variety of radioactive species at energies at or below the coulomb barrier [Pardo98].

At the high intensity limit, the vertical profile of 1 MeV Kr^{+1} beam with an intensity ~200 nA was measured with both the BIM/slit combination and a 0.25 mm scanned wire. The resulting beam profiles are shown in Fig. 5.10. The two scans coincide well, which demonstrates that the BIM system is useful for scanning profiles. This served as an initial test for the emittance measurements to be discussed next.

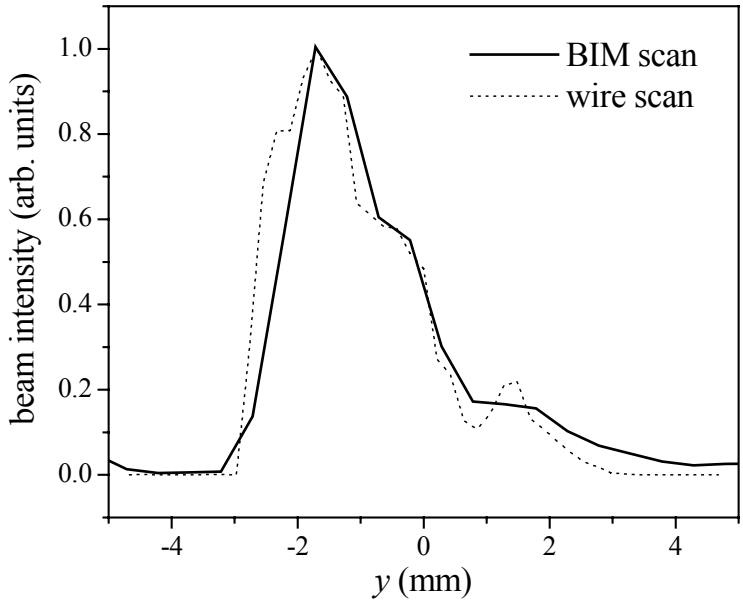

Figure 5.10 Beam profiles in the *y*-direction measured by both the wire scanner and BIM systems when the grid accelerating potential is 13 kV.

5.6 Emittance profile measurements with BIM

The previous section demonstrated that profiles in the transverse plane could be measured over a wide dynamic range. This section looks at the performance of such a device when used to measure the transverse phase space character of a beam. In Chapters 2 and 3 we discussed the importance of knowing the phase space properties of a beam. With enough spatial and angular resolution, emittance-scanning devices can even offer details about higher order aberration effects and the orientation of the ellipse. We test the performance of the BIM as an emittance-scanning device.

A schematic diagram of the dual slit plate used for these measurements is shown in Fig. 5.11. Each slit is 0.2 mm wide and about 45 mm in length. The beam is aligned and focused within a region bounded by a circle of ~30 mm diameter such that each of the two slits scans both the *x*– and *y*–profiles along separated intervals. The plate is located a distance L=30.5 cm upstream from the center of the dynode surface and a linear feed

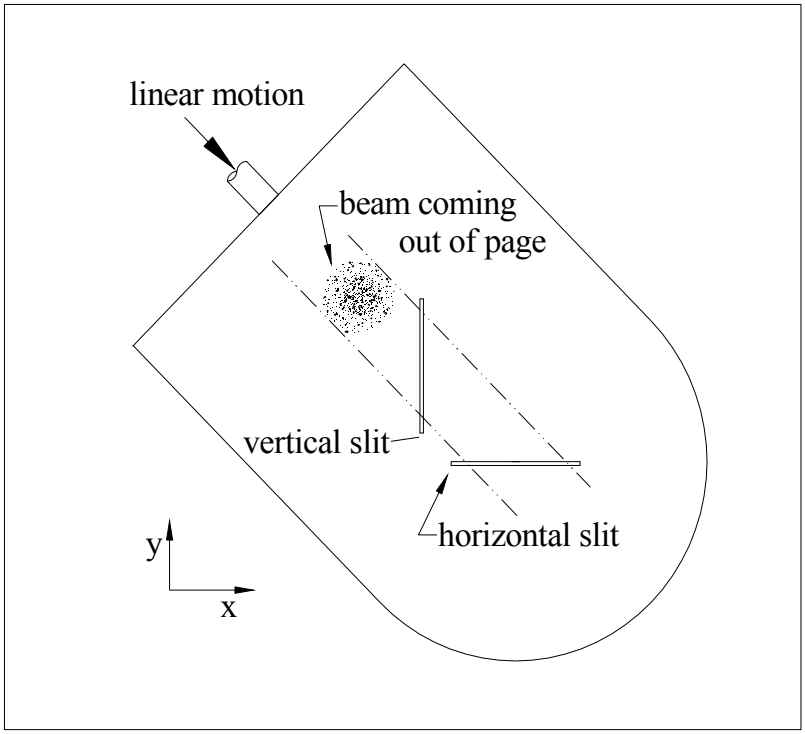

Figure 5.11 Double slit plate used to scan both the *x*- and *y*-profiles. The orientation is such that the beam is coming out of the page and the relative beam coordinate axes are labeled on the bottom left.

through that is driven by a step motor is used to scan the plate across the beam in the transverse plane.

At any position of the slit plate, a snap shot can be acquired of the image and recorded at the CID sensor array. An average from multiple snap shots may be processed in order to reduce white noise in cases where the noise to signal level is high. The image is then stored in memory as a 2D array of 8-bit integers whose intensity is denoted as M_{ij}. The subscripts i and j denote horizontal and vertical position, respectively, of each pixel along the plane of the sensor array. Each snap shot yields a distribution of the beam divergence along the length of the slit. For example, when the beam is in the vertical slit position (see Fig. 5.11), the intensity will be proportional to the distribution of divergence values, a, along the slit that runs along the y-axis of the beam coordinate system. Any

constants of proportionality derive from a transformation that converts the position values at the sensor array to those of the beam coordinate system (compare Figs. 5.2 and 5.11).

The emittance distribution in the x—a plane is obtained from a series of profiles, $M_{ij}(x)$, measured for all x-values with the vertical slit. Similarly, the y—b distribution is obtained from a series of profiles, $M_{ij}(y)$, in which the horizontal slit is in the region of the beam. Notice from Fig. 5.11 that if the linear feed moves by Δr in the direction shown, then there is a corresponding movement of $\Delta x=\Delta r/\sqrt{2}$ by the vertical slit and $\Delta y=-\Delta r/\sqrt{2}$ by the horizontal. Depending on which slit is in the beam region, a statistical average of the profile is taken by summing values along the orientation of the slit. For example, for every $M_{ij}(x)$ profile we take the sum over the index j,

$$H_i(x) = \sum_j M_{ij}(x), \tag{5.5}$$

to obtain the 1D array with values that represent the average beam intensity along the horizontal direction at the aluminum surface, which is tilted 45º relative to the beam coordinate system. Similarly, a profile along the vertical axis is obtained by

$$G_j(y) = \sum_i M_{ij}(y). \tag{5.6}$$

Of interest is the rate at which the beam disperses out as it drifts from the slit to the aluminum plate, i.e. the divergence of the beam.

To determine the divergence at a given position of the slit we must transform the units of position as referenced at the CID sensor to those of the beam coordinate system. The displacements must be evaluated relative to the slit position by applying the following transformations:

$$h_i = i \cdot k_x - x \cdot \sqrt{2} \qquad \text{(vertical slit)} \tag{5.7}$$

and $$g_j = j \cdot k_y - y \qquad \text{(horizontal slit)} \qquad (5.8).$$

Here, h_i represents the corresponding horizontal position at the aluminum plate at pixel row, i, and g_j represents the vertical at column, j. The constants k_x and k_y are the scale factors that account for the magnification of the tapered fiber optic rod and the distance between each pixel in the horizontal and vertical directions, respectively. Both are taken to be 40.5±0.3 μm per pixel in this setup. The √2 factor in Eq. (5.7) accounts for the 45° tilt of the aluminum plate along the horizontal plane

From these arrays we can then evaluate the first and second statistical moments at each position. In the horizontal plane, the second moment, h_{rms}, is evaluated about the first moment, h_m, at each x-position by taking the square root of

$$h_{rms}{}^2(x) = \frac{1}{H_0}\sum_i H_i (h_i - h_m)^2 \qquad (5.9)$$

where H_0 is the integrated profile intensity. Similarly, g_{rms} values are evaluated for each y─position. Furthermore, we assume that broadening due to the transport of electrons and photons through the detection system, h_d, can be accounted for by a deconvolution of Gaussian functions. The convolution theorem dictates that the final rms values of convoluted normal distributions yields another normal distribution with rms value equal to the quadrature sum of each rms component [Parzen60].

Suppose we are interested in rms broadening, h_b, caused solely by the divergence of the ion beam, then broadening contributed by any other factors, σ_d, must first be determined before a deconvolution may be applied in obtaining the true broadening caused from the divergence. The dominant component of σ_d here is the broadening of secondaries, σ_e; however, there is some contribution, σ_{OP}, gained due to the limited

resolution of the MCP and photon optics. For now, we make the assumption that σ_{OP} is negligible.

As long as it is valid to model the measured rms value of the data as a convolution of distributions with rms values of σ_e and h_b, then we must have that

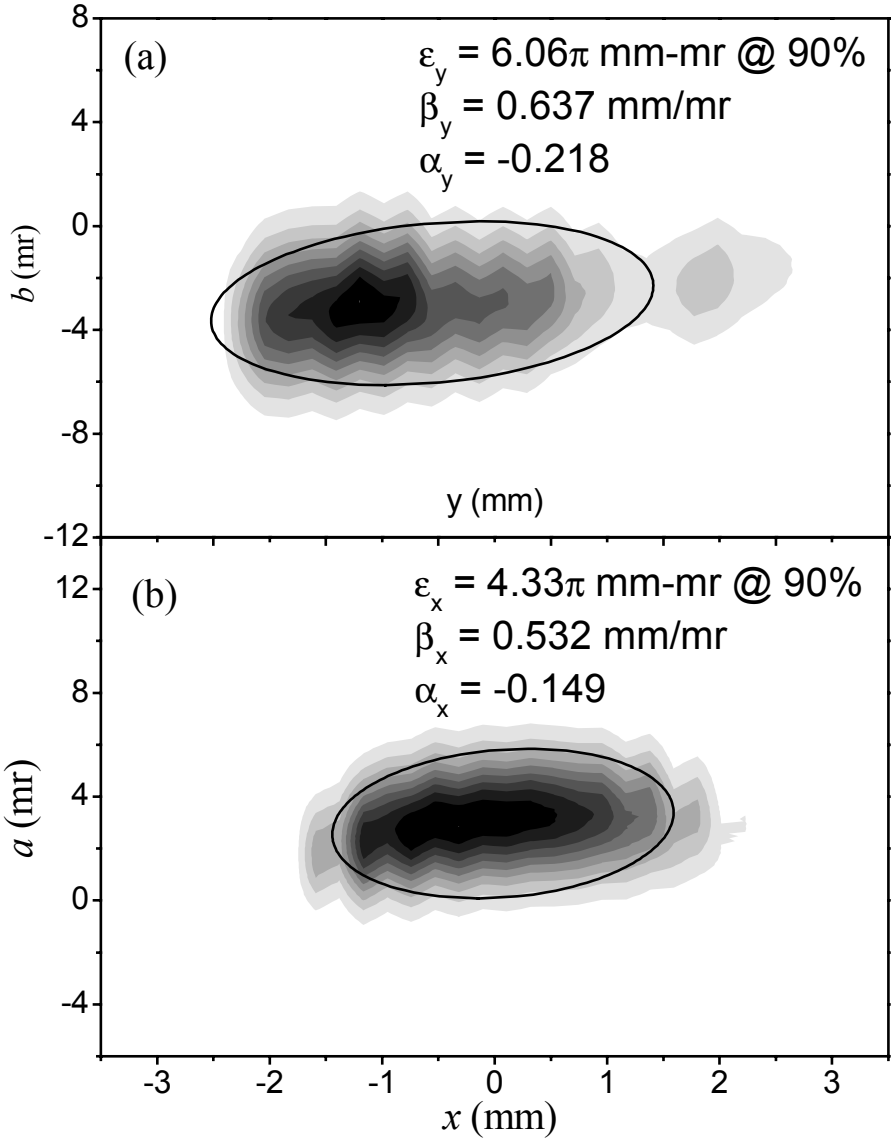

Figure 5.12 Emittance profiles extracted from the divergence profiles as described in the text. The ellipse drawn fits the phase space area given by ε_x and ε_y. If the distributions were truly Gaussian in form then 90% of the total beam intensity would lie within this boundary. The Twiss parameters and rms emittance were evaluated by a statistical analysis.

$$h_{rms}{}^2 = h_b{}^2 + \sigma_e{}^2 \qquad (5.10).$$

The corrected profile, H_i^c, can be extracted by applying the product of the function, $A_i(x)$, with H_i to deconvolute two Gaussian distributions at each x position. This function is obtained from

$$A_i(x) = \exp\left[-(h_i - h_m)/2h_0^2\right] \qquad (5.11),$$

where

$$h_0^2 = h_{rms}^2\left[(h_{rms}/\sigma_e)^2 - 1\right] \qquad (5.12).$$

The results along the y-axis are obtained in the same way. The resulting profiles, H_i^c and G_i^c ,should represent the distribution of ion current density in the coordinate system of the conversion surface. The b─axis coincides with the vertical axis directly but the a─axis does not because of the 45º tilt; therefore, the transformations for finding divergence along each respective axis must be given by

$$b_j \approx g_j / d_0 \qquad \text{and} \qquad a_i \approx h_i / \sqrt{2} d_0 \qquad (5.13),$$

expressed in units of radians, where d_0 is the distance from the slit to the midpoint of the conversion surface. The deconvoluted emittance profiles obtained by these transformations are shown in Figure 5.12(a) and (b) for the y─ and x─profiles, respectively. The method of statistical analysis described in Chapter 1 to extract the rms values of the phase space ellipse are applied here to obtain the Twiss parameters and the rms emittance, $\tilde{\varepsilon}_x$. The y─profile emittance seems to be over predicted largely due to an aberration that appears at the +y─side of the profile. The aberration seemed to be caused by a misalignment between the beam axis and the quadrupole doublet. The same structure also appears on the y─profile taken with the wire scanner described in Section 5.3. The profile from this device is shown in Fig. 5.13.

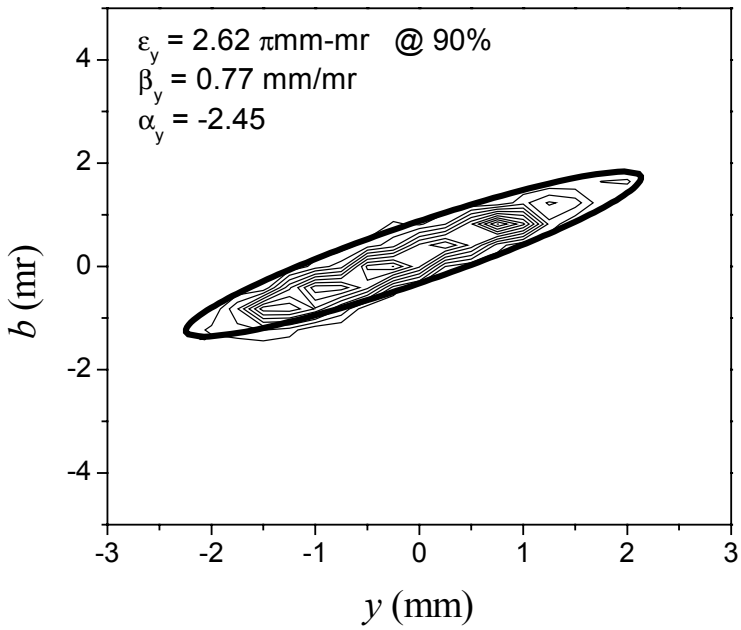

Figure 5.13 Phase space profile measured with wire system.

A comparison between the *y*─profiles taken with the BIM and wire scanner indicates that the measurements of the BIM overestimate the emittance by a factor of ~1.8. This is largely due to the fact that the divergence is very small for the allotted drift from the slit (L=30.5 cm). The scans already obtained, however, already give a good indication of the resolving limits of the BIM. From the wire emittance scan we estimate that the rms spatial width due to divergence was no greater than ~0.12 mm in these measurements. To obtain a resolvable emittance scan with measurable divergence, the optical set up should allow the rms width to be at least 0.5 mm. The present set-up made it to difficult to do this without having to make major modifications to the beam line used for these tests.

5.7 Summary

The current developments in beam diagnostic hardware provide useful information. The ion counting and wire scanning systems were very useful in providing reference

measurements to test the dynamic range and resolution of the device. From the analysis we have made some conclusions of the expected performance and how to make improvements where possible. Efforts are ongoing in the development of beam diagnostic devices for RIA accelerator systems.

Chapter 6

DEVELOPING EXPERIMENTAL TECHNIQUES FOR RIA

As pointed out in Chapter 4 the RIA facility will require advanced production target techniques that require research and development. Some work was done at the Dynamitron accelerator facility to address some of the issues related to the thick target ISOL technique and a brief summary of some of the activities is given in this chapter.

6.1 Adapting the Dynamitron accelerator facility for RIA developments

6.1.1 About the accelerator

The 4MV-Dynamitron-Tandem accelerator at Argonne National Laboratory is an RF power driven DC machine that has been operational since the mid 1970s. It accelerates positive ions of any species along a 3.7 meter long column of axially symmetric apertures. The last known modification to the accelerator column was documented in early 1983 as shown in the scanned diagram from the HV end, Fig. 6.1 (a), and the grounded extraction end, Fig. 6.1 (b) [Ruthenberg83]. A series of 1.5 inch (3.8 cm) diameter apertures (darkened in the diagram) were installed along the column in order to suppress the back streaming electrons. There are 11 of them in all and are 12 inches apart. The rest of the apertures remain at the original 3.3 inches (8.4 cm). The modification is intended for "higher quality" beams as well as to prevent electron collisions with beams of molecular species for the Coulomb explosion experiments described in the literature [Gemmell80] [Koenig85] [Zaifman92].

(a)

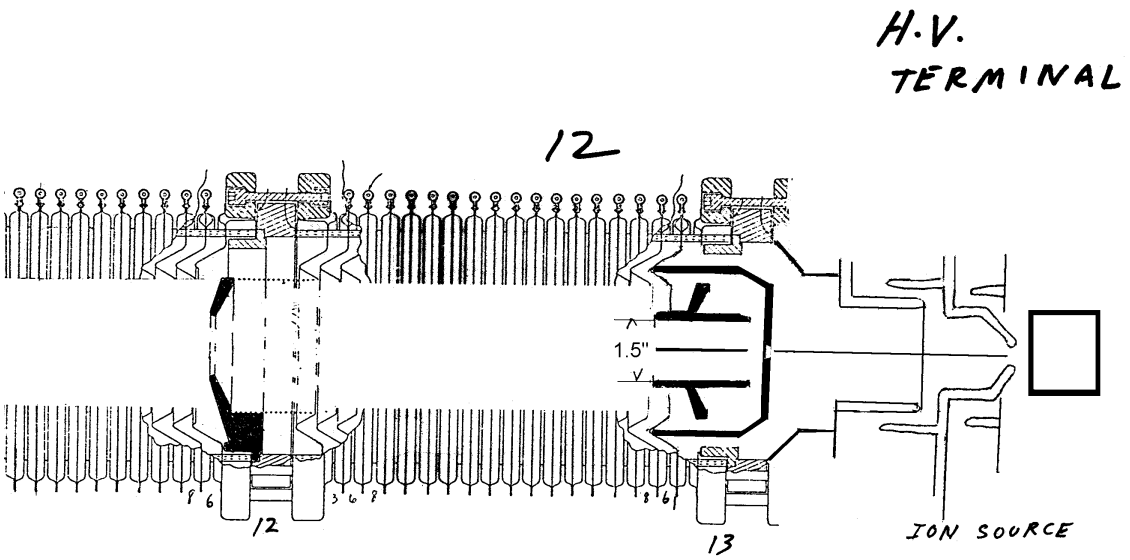

(b)

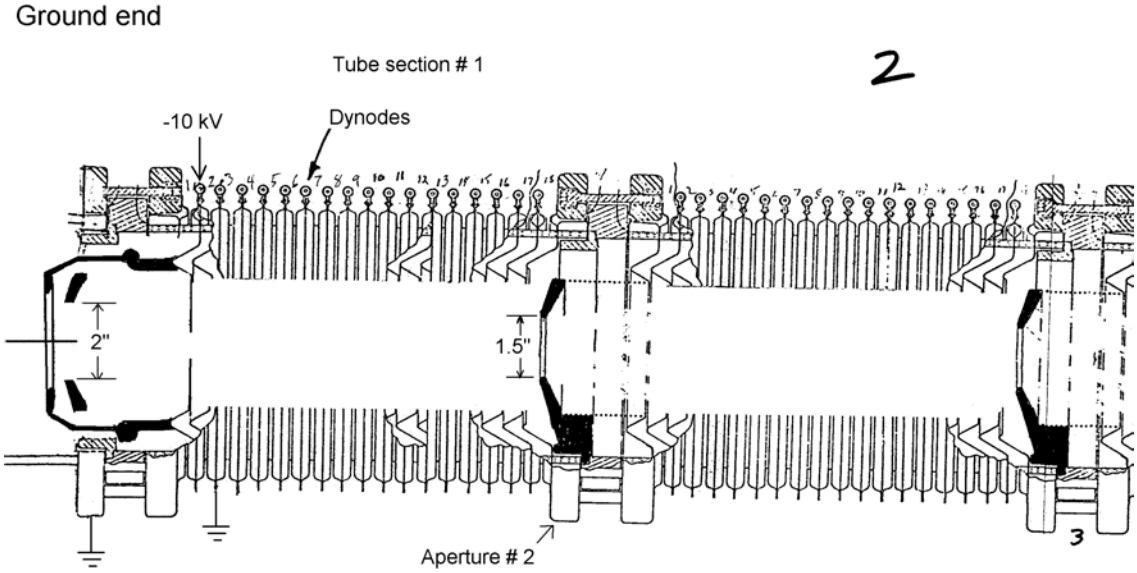

Figure 6.1 Scanned diagrams of original figures documented for the last modifications made to the column of the Dynamitron accelerator. (a) is at the HV end by the ion source and (b) is at the extraction end section. Notice the 1.5 inch apertures that had been installed.

A calculation is carried out to demonstrate the beam dynamics within the accelerating

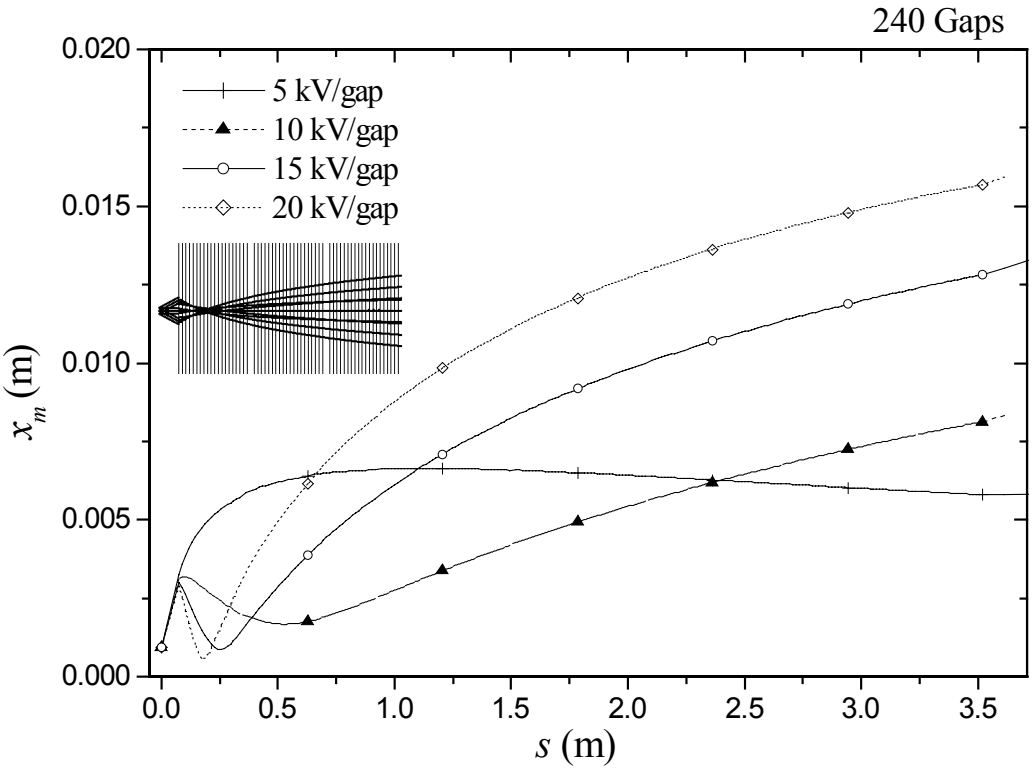

Figure 6.2 Simulated beam envelopes for an accelerating column under different accelerating gradients. The inset plot has the same horizontal scale and shows the rays calculated for the 20 kV/gap case.

column. We have used the accelerating gap structures described in Chapter 1 with gap dimensions that are very similar to the acceleration column of the Dynamitron. The beam envelopes are calculated to first order for a 5, 10, 15 and 20 kV potential between each gap and are plotted in Fig. 6.2. The inset plot shows the rays calculated for 20 kV/gap. For every calculation we have assumed a beam of m/q=2/1. The beam initially has a kinetic energy of 20 keV, a normalized emittance area of 0.01π mm-mr, and a 2.6 mm diameter with $\alpha_x=\alpha_y=0$ ellipse orientation.

The most notable feature is the oscillation that occurs at the first stages of the acceleration. The oscillation becomes sharper at higher accelerating gradients since the over-focusing effect is stronger. As the beam gains energy the focusing becomes weaker

and there are no further oscillations. The results indicate that the sharpness of the initial oscillation determines the maximum size of the beam envelope occurring at the remaining sections of the acceleration. In particular, for higher terminal voltages the beam will expand more and run the risk of striking the apertures in the column; however, it is possible to reduce the effect by extracting the beam from the source at higher energies and applying a focus to minimize the width of the beam at the entrance of the column. The Dynamitron allows the extraction potential to be as high as 60 kV and has a maximum allowable potential of 30 kV for the lens following the extractor.

The plasma ion source at the terminal is of the type described by [Witteveen79]. Beams of protons, deuterons, krypton, and xenon were readily available from the source through an automated manifold system. Beams from solid material can be produced by placing a sheet of the material against the probe next to the plasma.

The accelerating column is isolated in an SF_6 environment to suppress voltage breakdown. For these studies the pressure in the tank remained between 38 and 43 pounds per square inch (p.s.i.). A recycling system is used to move the gas to a reserve tank every time the accelerator needed to be opened for maintenance or modifications. Since small leaks in the recycler system cause the system to lose some gas every time the source had to be serviced, the gas pressure decays somewhat (~0.4 p.s.i. between servicing).

6.1.2 Experimental beam lines

There are two major beam lines at the Dynamitron that have been set up for RIA studies. Both are shown in Fig. 6.3, where we denote each line by the direction of bending at the switching magnet. The beam exits the accelerator in the direction north

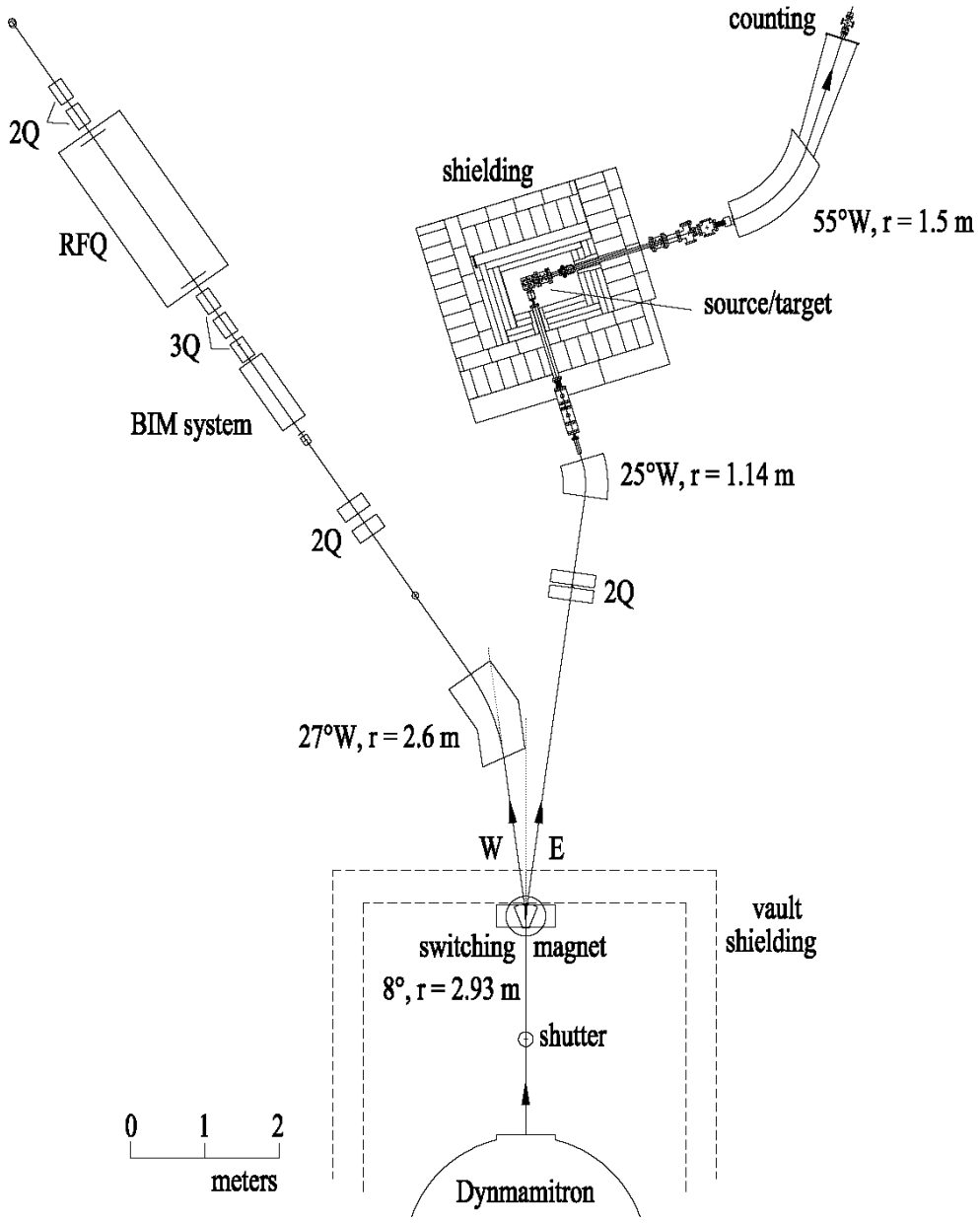

Figure 6.3 RFQ and target/source layout at the Dynamitron accelerator facility.

and is either bent to the 8ºW or 8ºE direction at a 2.93 m radius by a switching magnet. The bend yields a mass dispersion of about 0.05 cm/$_{\%m/q}$ in either direction, and at normal beam tuning conditions there is a mass resolving power of $m/\Delta m$~3. The second bend at each of the two lines (27ºW for the 8ºW beam and 25ºW for the 8ºE beam line)

provides an extra amount of resolving power to obtain a total of $m/\Delta m$~50 on target. A water-cooled copper block is positioned along the manifold of the switching magnet with 2.5 cm diameter apertures to let the selected beam through and stop beams outside the selected mass widow.

The two beam lines have different beam requirements. The 8ºW line is used to provide Xe beams to an RFQ accelerator test bench, as well as beam diagnostic systems, such as the beam-imaging monitor described in the previous chapter. The energies and intensities are generally very low (<<1 μA at <1 MeV). The 8ºE beam line is used for providing proton or deuteron beams for radioisotope production at the highest energy and currents possible (>5 μA at 3-5 MeV). The beam is steered into a heavily shielded 2×2×3 ft hollow region, or cave, with a minimum shield thickness of 13 inches of steel and ~2 feet of concrete. The shielding is designed to suppress neutron radiation, which is typically generated by deuterons on beryllium, by a factor of 10^4. Two sides of the walls are on a rolling cart in order to remove them to gain access into the cave.

Another beam line exits at 90ºE relative to the direction of the primary beam from the cave. An isolation transformer rated at 20 kV was installed close by to provide up to 5 kW of ion source power within the cave. The extracted beam could be mass separated with a commercially available sector magnet [DANFYSIK]. The dipole bends the beam by 55º at a 1.5 m radius and has a 35º exit edge angle for stigmatic-focus downstream. Similar dipoles have been described in the literature and have been rated with a mass resolving power of as high as ~1500 [Dumont78]. Since the resolving power depends on ion source and other optical settings, some measurements were carried out to characterize this particular system.

6.2 Source development

In order to address issues related to target production and release at Argonne some ion source and target developments were started. The design required that we consider efficient heating and heat shielding, a large target volume, efficient ionization, and isolating components for high voltage.

A diagram that illustrates the major components of the ion source is shown in Fig. 6.4. Starting from the bottom and going up we identify the following parts and characteristics:

- Three copper leads from high voltage isolated feedthroughs provide DC power to the ionizer and heating elements. They are all identical and rated for 20 kV isolation at <15 amps.
- A cylindrical BN block is used for support of the components. This insulator is well suited for high voltage isolation at high temperature.
- Molybdenum leads are used for directing the DC current to the ionizer and heating element.
- A tantalum cup that is supported from the BN block holds the target material. It has an inner diameter of 23 mm and overall length of 50 mm.
- An outer tube made of titanium supports the oven components and front part of the target. This material was chosen for its low thermal conductivity and minimizes heat losses to the BN support.
- A dimpled Ta sheet is rolled around at the outer diameter of the target and heating elements for heat shielding.
- A graphite filament was selected for the heating elements. It was machined from a single piece with up and down windings to increase the path length, and hence,

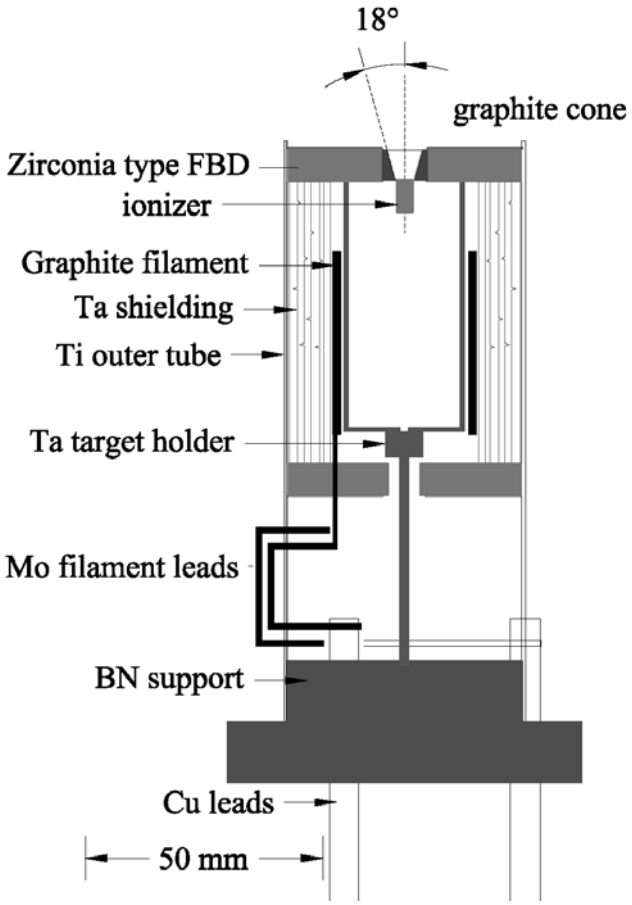

Figure 6.4 Diagram of surface ionization source for production target.

the resistance. Graphite is ideal since it has a high resistance and does not sag at high temperatures. Not shown in the diagram is an yttrium oxide (Y_2O_3) coating that covers the graphite filament and the tantalum surfaces that are close to it. The oxide has a melting point of 2415ºC and is highly inert. It was applied as a water-based paint mixture that was obtained from a commercial vendor [ZYP].

- The ionizer is placed at the extraction region. In doing these studies we went through a series of ionizer designs. The first one was a 3 mm tube made of platinum for its high work function (ϕ_W>7 eV) and relied on heating by the oven. This seemed to work well for the ionization of Cs, Rb, and K, but was very poor

for the ionization of Na. We eventually changed to a coiled filament that is made from a commercially available W26%Re alloy [OMEGA]. The ionization of Na is compared to that of K with a current versus filament temperature plot shown in Fig. 6.5. The temperature characteristics of the filament had been calibrated with an optical pyrometer. Notice that Na (V_i=5.14 eV) requires higher temperatures compared to K (V_i=4.34 eV) to ionize.

- The front and backside of the oven had been shielded with dimpled Ta sheets as well, but we conducted a study that found better insulation if using a porous form of a refractory oxide. The porous oxide is made of an yttria stabilized zirconia material, otherwise known as Zirconia type FBD by the commercial vendor [ZircarZ]. It has a very low thermal conductivity even at very high temperatures. We conducted a set of measurements in which only Ta shields were used. A thermocouple was placed in thermal contact with the bottom of the Ta target cup to measure the amount of power necessary to achieve a given equilibrium

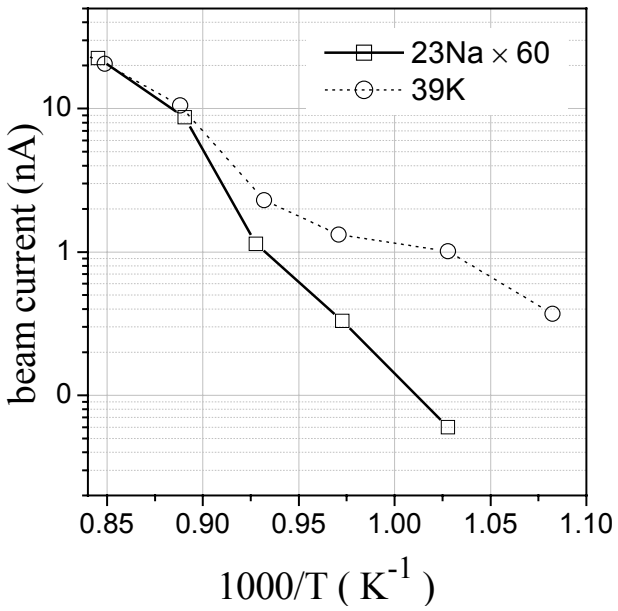

Figure 6.5 Beam current as a function of temperature for a Na and K from ionization at a W%26Re wire.

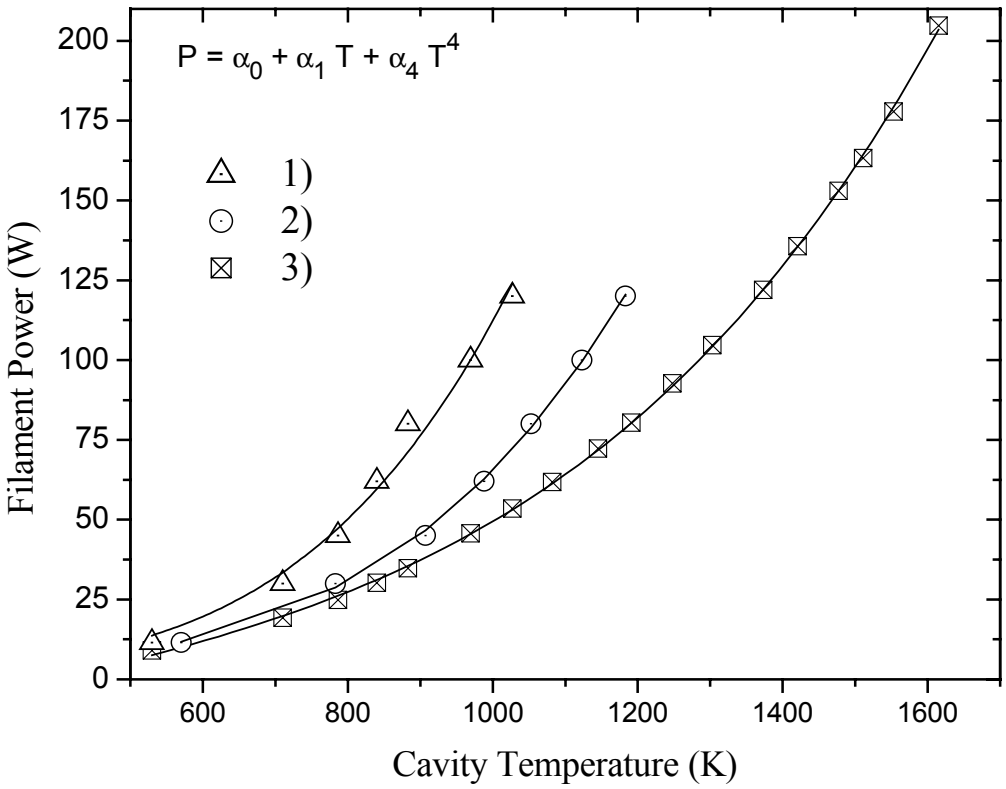

Figure 6.6 Filament power used to get cavity temperature under the following conditions: 1) Graphite at front, Ta shields in back 2) Zirconia type FBD at front, Ta shields at front 3) Zirconia type FBD at front and back.

temperature in the cavity. The results are plotted in Fig. 6.6 with a curve labeled as 1). We did a similar test with the front Ta shielding replaced with the oxide and did a similar measurement and found the results along curve 2). The back end was then replaced to yield curve 3). Both pieces were obtained in the form of a disk that is easy to machine. The measurements clearly show an improvement in the oven efficiency when using the porous oxide. The curve was fitted with the polynomial temperature dependence shown in the figure to predict the temperature when the oven is being used.

- An ion extraction channel made of graphite is positioned right in front of the ionizer and has a cone angle of 18º.

The overall performance of the oven and ionizer was found to be reasonable for experiments requiring temperatures below about 1500ºC. Above this temperature the rate of yttria reduction on the graphite filament destroys the layer of insulation and causes the filament to short out on the target or heat shields. We tried using a layer of hafnia, which is also a refractory oxide, but found that it reduced even faster than yttria under the same conditions.

From the resistivity curve of the graphite versus power it seems that the filament is reaching temperatures that may exceed ~2000ºC to obtain about 1500ºC at the target cup. This may be due to the fact that the electrical insulation is also a good heat insulator and does not allow the target cup to reach temperatures closer to that of the filament. With enough shielding this could be avoided, but the target supports tend to act as a heat sink, which lowers the temperature of the target cup. There is, however, an enhancement by the ionizer, since it introduces about 50 to 100 W of power right inside the target cup. It is not clear whether using some other material, such as a Ta or a W alloy, will alleviate the chemical breakdown problem with the oxide. Since the initial experiments would not require any higher temperature than ~1200ºC, we did not pursue such issues any further. Further studies with the refractory oxides, however, are still ongoing with high temperature ovens at the ECR ion sources of the ATLAS accelerator facility.

6.3 Mass separator and ion source performance

A number of diagnostics were carried out on the ion source and mass separator system in order to characterize their performance. The source was installed with no target material for these tests. It was never necessary to introduce any material into the ion source to produce beams of alkali elements, since there are always measurable

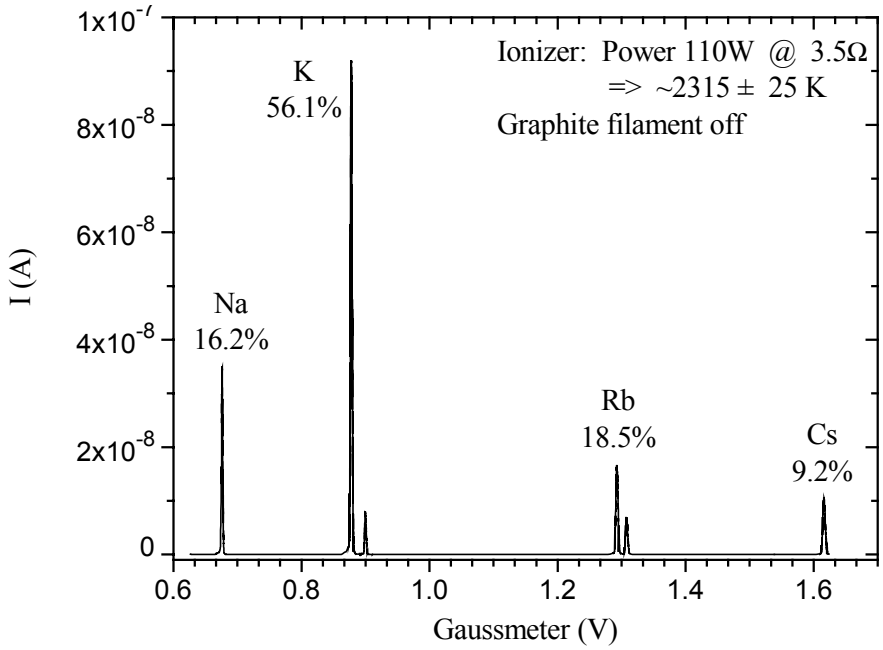

Figure 6.7 Total current at each mass obtained with only power at the W%26Re ionizer filament.

residual quantities present. A typical mass scan of the extracted beam is shown in Fig. 6.7, where the magnetic field is varied and measured with a Gaussmeter. The accelerating potential is always 10 kV unless otherwise noted.

The peaks that are easily discerned from the spectrum are from Na, K, Rb, and Cs. The beam current is measured with a picoammeter that is in series with a Faraday cup positioned behind a 1 mm slit at the focal plane. The percentage of current from each element is evaluated by numerical integration along the spectrum and is labeled next to each of them. The Gaussmeter was found to be linear to within 3% across the entire mass spectrum shown and could be calibrated with peaks from 23Na, 39K, 41K, 85Rb, 87Rb, and 133Cs. Notice that no heating from the graphite filament was necessary since the ionizer provided 110 W of heating power in this case. When there is power to the graphite filament the components vary slightly, with the Na and K peaks increasing more than those of Rb or Cs.

6.3.1 Emittance of source

The emittance of the beam was measured before the mass separator with the wire scanner and slit system. Two einzel lenses were used to focus the beam at the slit of the wire scanning device described in the previous chapter. The slit and wire are aligned vertically and move horizontally. The resulting profile from a typical scan is shown in Fig. 6.8 (bottom). The top plot is that of the emittance area within each contour level having a given percentage of the total beam current. At the 90% integrated intensity contour there is about an area of 11.9 π mm-mr area. The emittance varied slightly

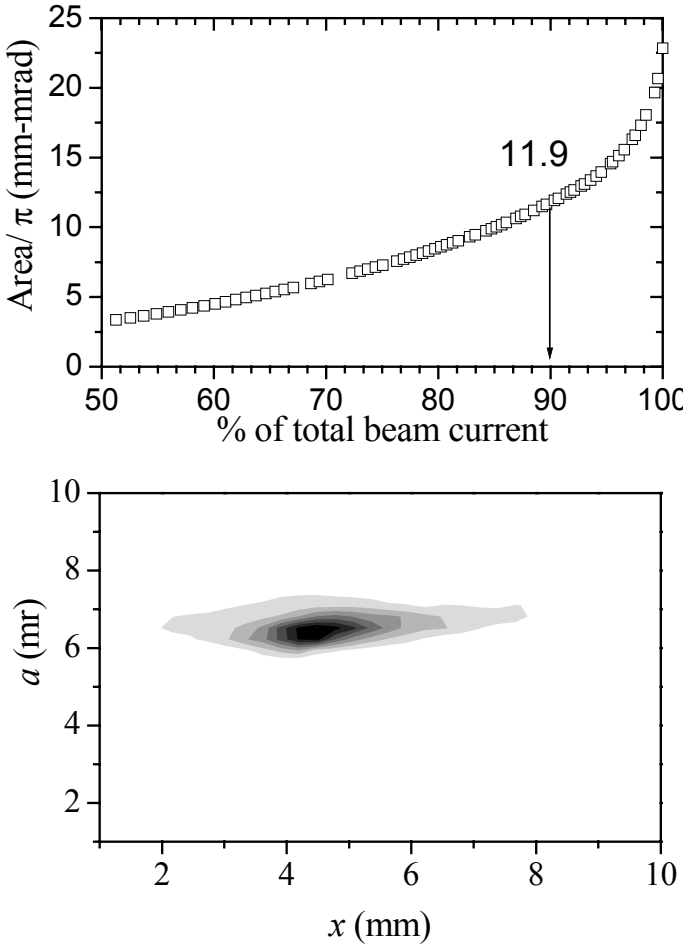

Figure 6.8 Emittance area (top) evaluated from the emittance profile (bottom) measured right before the entrance of the mass separator dipole.

according to the power on the ionizer filament and the one measured here represents one of the larger ones since the ionizer power is high (~110 W).

Depending on the power to the ionizer and oven we were able to go above a 10 kV accelerating potential. Raising the energy of the beam did not improve the emittance as would be expected from Eq. (1.35). This is due to the fact that the beam got its full accelerating potential from the extractor. Hence, raising the extraction potential will pull ions out that would otherwise have transverse velocity components that are too high to make it through the exit. To avoid this an accelerating column that is independent of the extraction potential would need to be used to vary the acceleration. The extraction potential could go as high as 15 kV at low source power, but would cause a significant amount of breakdown when running a the high temperatures. The source was very stable at 10 kV, which is the reason we stuck with this potential for most of our runs.

6.3.2 Mass separation characteristics

The performance of the mass separator is characterized in greater detail by observing the ion flux between mass peaks. The first measurements are obtained from measuring current at the Faraday cup behind the focal plane of the magnet. The vertically aligned jaw slits were opened up to 0.2 mm to obtain the spectrum shown in Fig. 6.9. The natural abundances have been labeled next to the corresponding isotope peaks of Na and K. Notice that each of the peaks has very similar structure at the tails. We observe very broad exponential drop offs at the sides that are mainly attributable to elastic scattering with residual gas atoms in the vacuum [Menat64] [Ruedenauer70] [Camplan81]. The vacuum in the region of the mass separator is about 10^{-7} Torr while in front of the ion source the vacuum would typically be as high as 4×10^{-5} Torr. The effect should reduce

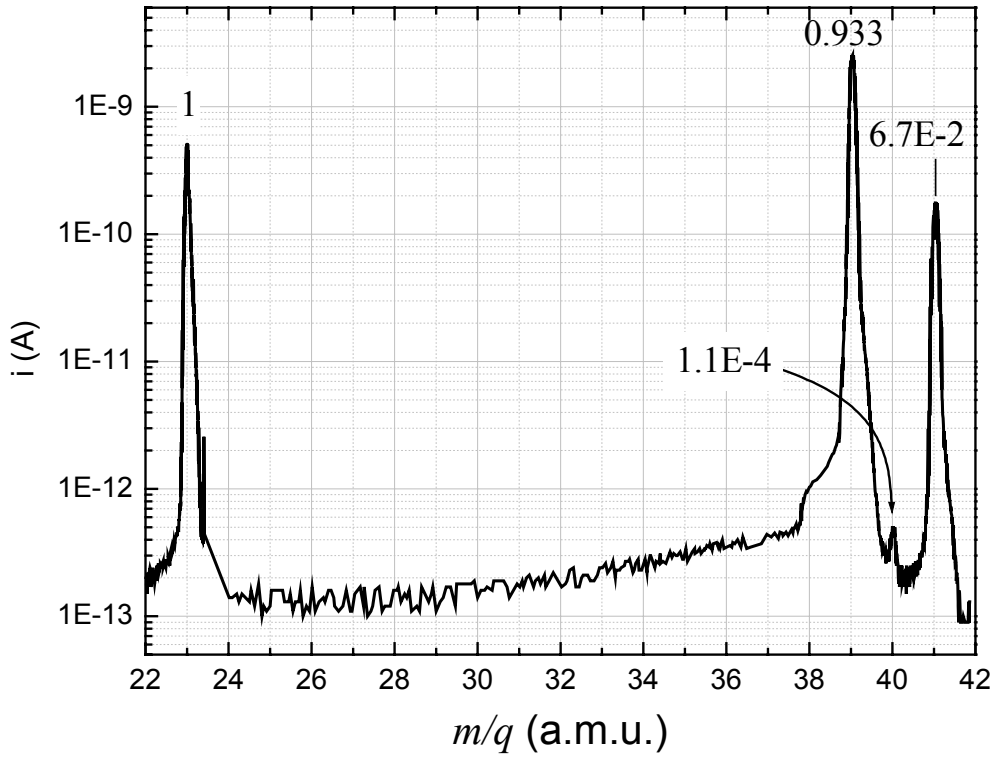

Figure 6.9 Detailed mass spectrum between mass 22 and 42. The natural abundances have been labeled next to the corresponding isotope peaks of Na and K.

proportionately with the vacuum; however, we did not have enough pumping speed to do this for these experiments. The hump to the left side of each peak may be caused by a second order aberration of the dipole, but may also be structure from the ionization region. For example, there may be some ionization that is occurring at the exit cone or walls of the target cup.

It is possible to do some analysis with the mass lines of potassium isotopes, since they are so close together. About 55 % of the intensity at m/q=40 is made up of 40K, while ~37% consists of 39K and ~8% 41K. From these estimates we are able to estimate the enhancement factor described in Section 2.4. For 90% transmission through the jaw slits at the focal plane we obtain that EF=1.1×x10^4.

We looked into the spectrum at an even deeper level by counting ions in the same mass region and found that there is some other structures that seemed to not be related to any known ion species. The peak structures seemed to move up and down along the spectrum slightly which seemed to indicate that a scattering process, such as with a chamber wall, may be occurring. In order to test for this we installed an energy suppressor that consists of a 2 cm tube that is gridded at the end. The tube is floated at a high potential to stop any ions having energy below a certain threshold. A diagram illustrating a Simion [Simion7] simulation of this device is shown in Fig. 6.10. Ions of q=1 come in from the left with an energy of 10 keV, while the grid is at 10.3 kV potential. The effective resolution in energy is not much better than about 3% if we consider the device to be a high pass filter, which sufficient for our purposes.

The ion detector was positioned after the exit aperture at the right side of the figure. A typical spectrum that is observed between mass 24 and 38 is shown in the top plot of Fig. 6.11. Although the beam is accelerated with an 8.5 kV potential here, a similar spectrum appears even for 10 kV acceleration. A broad structure appears that peaks at

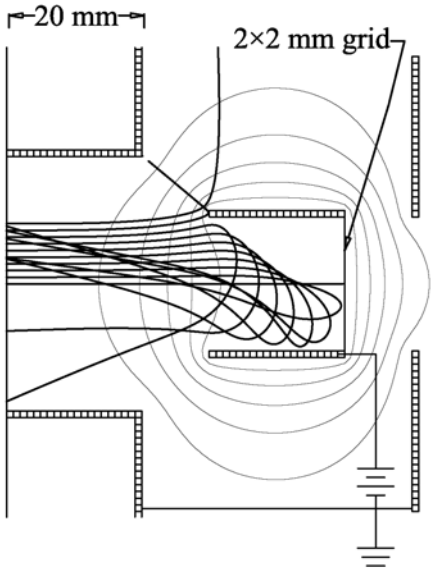

Figure 6.10 Simulation of beam energy suppressor. The 2 cm diameter tube is gridded at the end go provide a uniform potential for suppressing particles of energy below the applied potential.

about mass 32 that is ~10^{-4} times the size of the 39K beam. Most of the peak disappears when the suppression gets to at least 7.8 kV and disappears completely by 8 kV. The peak at m/q=27 remains unperturbed, and it is very likely that of 27Al, which has an ionization potential of V_i=5.99 eV. The broad peak was of more concern, however, since it would tend to broaden and cause background at other regions depending on what the tune of the system was.

Finally, we did some mass resolution studies by measuring the FWHM of the mass 23 peak. The mass resolving power varies with the tune of the lenses before the separator as shown by Fig. 6.12, where we vary the first lens and optimize the second lens to obtain the smallest waist at the focal plane. The trend agrees with a 1st order calculations

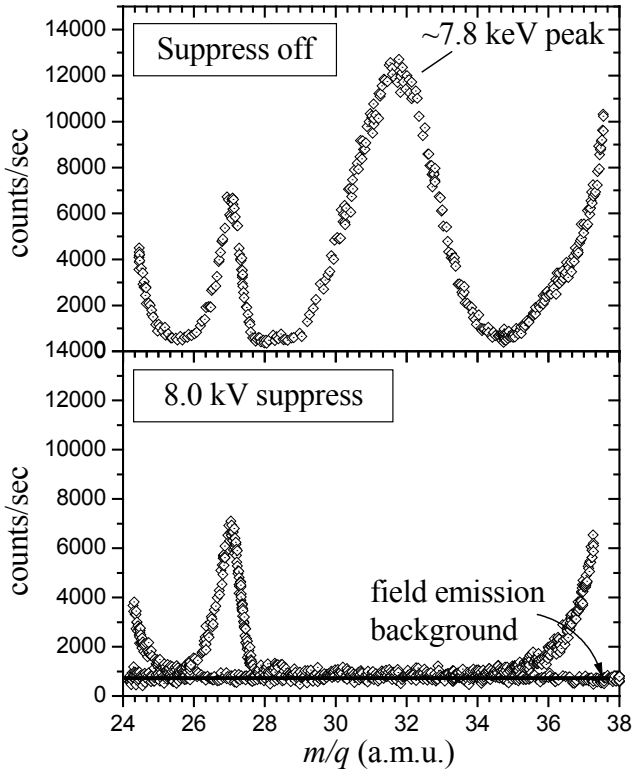

Figure 6.11 Mass region between Na and K detected with ion counting system for a beam accelerated with an 8.5 kV potential. Peak appearing at mass 27 is likely that of Al^{1+} (V_i=5.99 eV). The broad peak at about mass 32 totally disappears when the suppressor is above 8 kV.

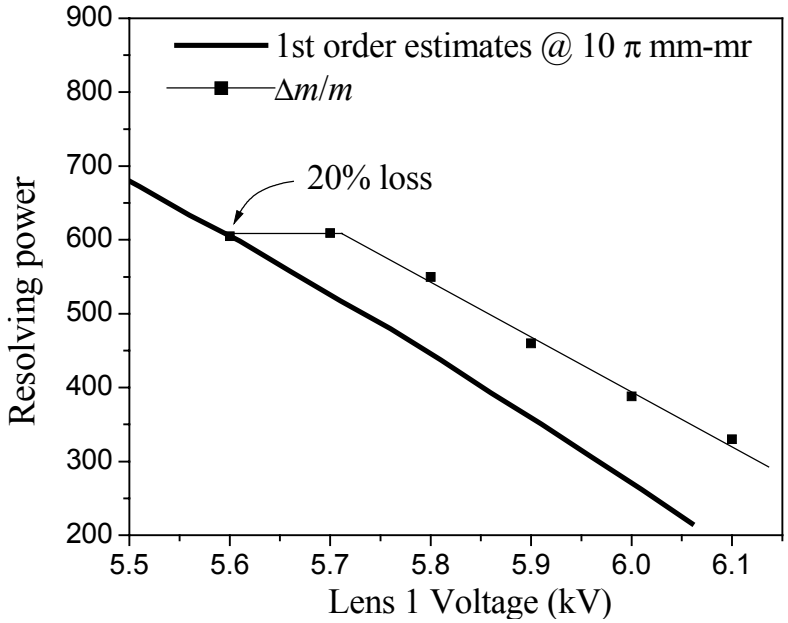

Figure 6.12 Calculated 1st order resolving power as a function of the potential at the first lens. A mass dispersion of 1.4 cm/%m/q is estimated. The actual measurements indicate a resolving power greater than the calculations by ~22%. The limit occurs at about $\Delta m/m$~600, at which point the acceptance begins to suffer.

carried out with COSY assuming a 10π mm-mr emittance area. The initial orientation of the ellipse was extracted from the emittance profile measurements depicted in Fig. 6.8.

The experimentally measured resolving power seems to level off below a certain lens voltage and the transmission through the magnet starts to drop off. This occurs because the size of the beam becomes too large to fit through the apertures before the magnet. The tune at about 5.7 kV at the first lens seems to be the most efficient for the highest obtainable mass resolving power of ~600. The calculation predicted a lower resolution by about 22% since the width had been selected at the 95.5% level instead of the 90% level that is taken for the experimental measurements.

6.4 Isotope production with neutrons

The primary mechanism for radioisotope production at the Dynamitron is that of neutron-induced reactions on a secondary target, i.e. a two-step mechanism. Instead of relying on spallation neutron production as in Chapter 4; however, these experiments rely on the reactions of deuterons on a primary target for the production of secondary neutrons. The low energies provided by the Dynamitron accelerator necessarily means that we should use light targets that are able to withstand high beam power.

6.4.1 Z dependence of neutron production

The fact that light targets can generate more neutrons was demonstrated by a simplified *n* detection experiment. A target ladder containing a variety of targets was situated 1 m away from a standard *n* detector that is filled with a Xylene scintillator liquid coupled to a photomultiplier tube. A diagram of the experimental set-up is shown in Fig. 6.13. The detector spans a surface area of 120 cm^2 in the plane perpendicular to the

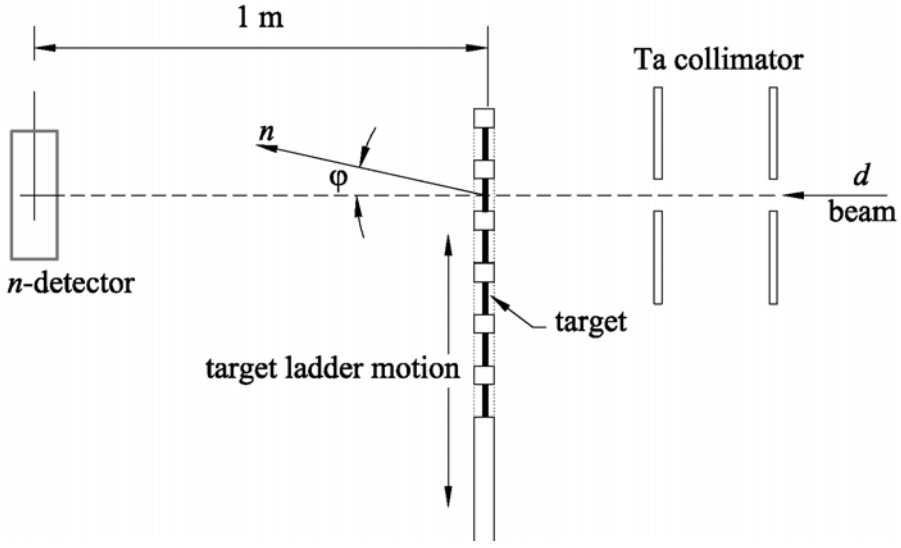

Figure 6.13 Diagram of target ladder set-up for neutron flux measurements of various targets.

target, which translates into a ~0.001 fraction of the surface of a sphere of 1 m radius. Since the neutron flux is very isotropic; i.e. has a weak dependence on the angle φ, this fraction is approximately the probability that *n* will cross the detector. The thickness of the detector is 10 cm in the direction parallel to the incoming *d*-beam. The components are situated inside the shielded cave and the deuteron is steered through a Ta beam collimator that is aligned with the target being irradiated.

These measurements were carried out in order to obtain relative detector sensitivities important to the commissioning of the accelerator for using high power deuteron beams. The *n* detector used here contains the same scintillator material used in the safety monitors around the area for detecting levels of neutrons [ES&H]. Knowing the neutron flux at the detector used here closely reflects the detected yields at the safety monitors. We are interested in the *n* yields emitted by materials that are used in many of the components in the beam line. Some of these components are beam measuring devices, apertures, beam stops, and accelerating column apertures.

Properties of the materials tested are listed in Table 6.1. Some of these materials are

Table 6.1 List of materials expected to be exposed to *d* beams.

Target	***Z***	**Range at 3.5 *MeV*** [μm]	**Target thickness** [μm]	V_C [MeV]
Be	4	80.5	500	2.3
C	6	63	2150	3.1
$C_{2.1}H_2$	1, 6	210	~1000	3.1, 1.2
Al	13	84	260	5.2
Cu	29	31	3420	8.7
S.S.*	24, 26, 28	31	850	7.7, 8.2, 8.6
Ta	73	28	3400	15.5

* Stainless steel comprised of a $Cr_8Fe_{74}Ni_{18}$ alloy.

compounds of differing Z elements, which are listed in the second column. The average range of the deuterons at the maximum beam energy is calculated with TRIM and listed in the third column, while the fourth column lists the actual thickness of the material used. The last column is an estimate of the Coulomb potential barrier for a deuteron colliding with a Z atom of mass number A, where we have taken the nuclear radius of the target to be approximately given by $1.2A^{1/3}$ fm [Wong90]. Notice that for hydrogen nuclei we have estimated V_C=2.3 MeV, and at the high Z extreme we have V_C=15.5 MeV for tantalum.

The results obtained from our measurements are plotted in Fig. 6.14. The detected neutron flux is normalized to the beam current and has been corrected for dead time and background count rate when the beam was not present. Notice that the Be target yields a detected flux that is anywhere from 5000 to 7000 times weaker than that from the Ta

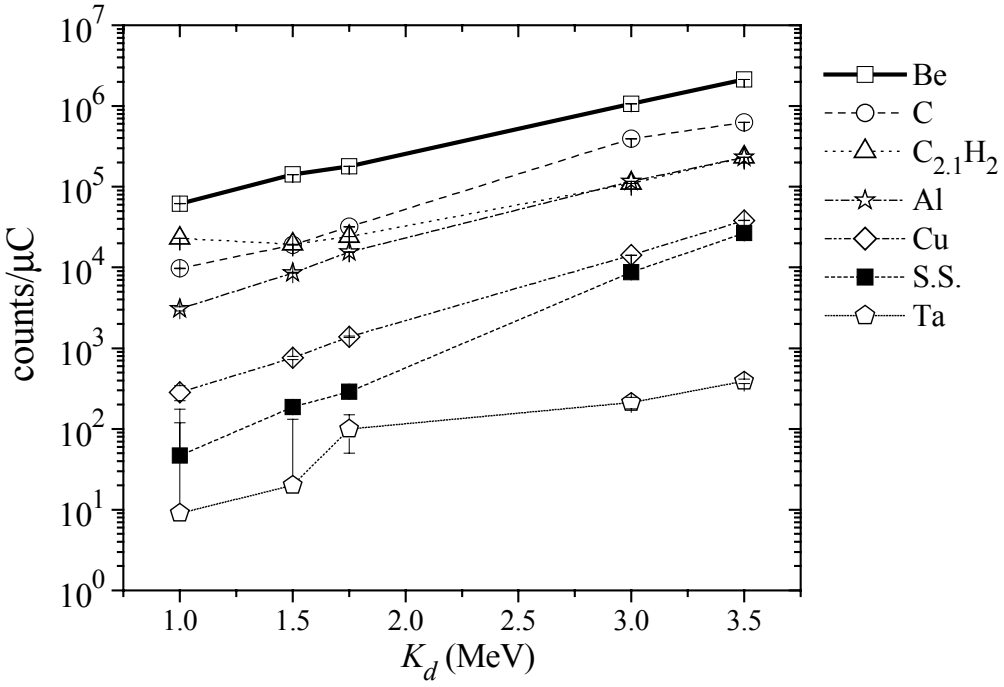

Figure 6.14 Count rate at neutron detector generated by deuteron beams colliding with various materials at kinetic energy, K_d.

target. The detected fluxes from the rest of the materials fall somewhere in between this range. Beryllium is one of the target materials used for *n* production and is chosen for this reason. Beryllium is not used anywhere else in the beam line.

Some of these materials of can be found along the beam line. Compounds of carbon are of special concern since vacuum pumps tend to introduce them into the vacuum and cause them to collect at surfaces that can be exposed to the beam. The other material that is of concern is Cu, since the beam dump at the manifold is made of this material. We find that the ion source provides beams of $d+$ and d_2+, where each d nucleus of the d_2+ molecule has half the energy of the $d+$ beam. We find that ~60% of the deuteron beam current is $d+$ and the rest is d_2+. Accounting for the two atoms in the molecule implies that ~43% of the deuterons are at 3.5 MeV and ~57% are striking the manifold beam dump at 1.75 MeV. Although, the neutron detector gives ~1500 times less count rate with 1.75 MeV deuterons on Be than with the 3.5 MeV, the manifold is very poorly shielded and causes a high count rate at the safety monitors.

To reduce the flux from the molecular component a Ta shield was introduced at the region of the Cu block where the molecular beam collides. Unfortunately, we actually only obtained a factor of eight times less flux with this modification, as apposed to a factor of ~14 expected from Fig. 6.14. Part of the reason was that some of the beam might have been hitting a steel mount for the Ta plate. Also, there is some flux generated by the halo component of the 3.5 MeV $d+$ beam striking the 2.5 cm Cu block aperture. Although, making more precise modifications to the Cu block could reduce these effects, there are technical difficulties involved in accessing the components. The decision was

made by the Dynamitron technical staff to manage with the neutron flux emitted at the manifold.

These measurements demonstrate the effect that Z has on the neutron production. The results are useful in making any modifications that may be necessary for obtaining higher beam performance and reducing neutron flux levels to avoid hazardous beam conditions.

6.4.2 Estimating the production by analytical models

In Chapter 4 we discussed the results of production calculations using elaborate Monte Carlo techniques. In this section we shall show how it is possible to make some approximations of the production based on analytical formulations. These calculations will be used to predict the production of isotopes with neutrons generated from low energy deuteron beams.

There are a number of properties of the system that make it possible to use analytical equations. First of all, the neutron flux is generated in a small region of the target surface as shown by Table 6.1 for a number of solid targets irradiated with 3.5 MeV deuterons. Also, the energy of the deuterons is low enough that cascading events may be neglected. Finally, there is a wealth of reported information on the neutron production, especially for deuterons on Be.

To calculate the production we must know the properties of the neutron yield at the primary target and the neutron reaction cross sections on the secondary target. Here, we have a target that is cylindrical with a 2.5 cm diameter and 3 cm height for a total volume of about 14.7 cm^3. The centroid of the secondary target lies about 27 mm in front of the primary target. The neutron yield actually does drop off slightly with the azimuthal

angle, φ (see Fig. 6.13), but only by about 20% for the region spanned by the target here. We adopt the values of the yield distribution, $Y_n(K_n,K_d)$, reported by [Meadows89] for measurements at φ =0º and assume that they remain the same up to the maximum extent of the target, φ ~25º. The yield distribution as a function of neutron energy, K_n, generated by deuterons of kinetic energy, K_d=3.4 MeV, is shown in Fig. 6.15 for the left axis of the plot. Notice that after K_n=2.5 MeV the distribution drops off significantly and becomes negligible after ~8 MeV. For the right axis we plot some examples of the reaction cross section, $d\sigma/dK_n$, for producing 27Al(n,α)24Na, 27Al(n,p)27Mg, and 9Be(n,α)6He reactions. From these types of cross section curves the rate of production can be evaluated in terms of the beam current from

$$\frac{dN_n}{dq} = \int_V \rho_A(\vec{r})dr^3 \int_0^\infty \frac{d\sigma}{dK_n} Y_n(K_n, K_d)dK_n \,, \tag{6.1}$$

where ρ_A is the atomic density of the target within the volume of the container, V. Since we assume no φ dependence in Y_n, the two integrals are decoupled and can be evaluated independently. We also make the assumption that ρ_A is uniform within the volume, V, so that the volume of the integral falls outside as a constant to obtain the form,

$$\frac{dN_n}{dq} = \rho_A \cdot V \cdot G \int_0^\infty \frac{d\sigma}{dK_n} Y_n(K_n, K_d)dK_n \,, \tag{6.2}$$

where G is a geometric factor determined from volume integral,

$$G = \int_V d\Omega r^2 dr \,. \tag{6.3}$$

For the geometry of the target here, we obtain that G=0.11 sr/cm^2.

There are quite a variety of targets that need to be assessed for use in rare isotope beam production. Some of the most important compounds are those of uranium, such as

the UC*x* refractory powders described in Chapter 4. We have avoided using these compounds, at least for the initial stages of the program, due to the complications that arise from uranium contamination in the vacuum system. Instead, we opted to use refractory oxides, such as magnesia (MgO) and alumina (Al_2O_3), which can be used for the production of Na isotopes. For example, the reaction cross sections for 27Al(n,α)24Na are plotted in Fig. 6.15. The reaction yields are comparable to those that result from fission of 238U, which makes them an ideal test case. A material that was of particular interest was a fiberous form of alumina with average fiber diameter of 3 μm [ZircarA]. The material was stable in the target within a graphite crucible up to ~1100ºC,

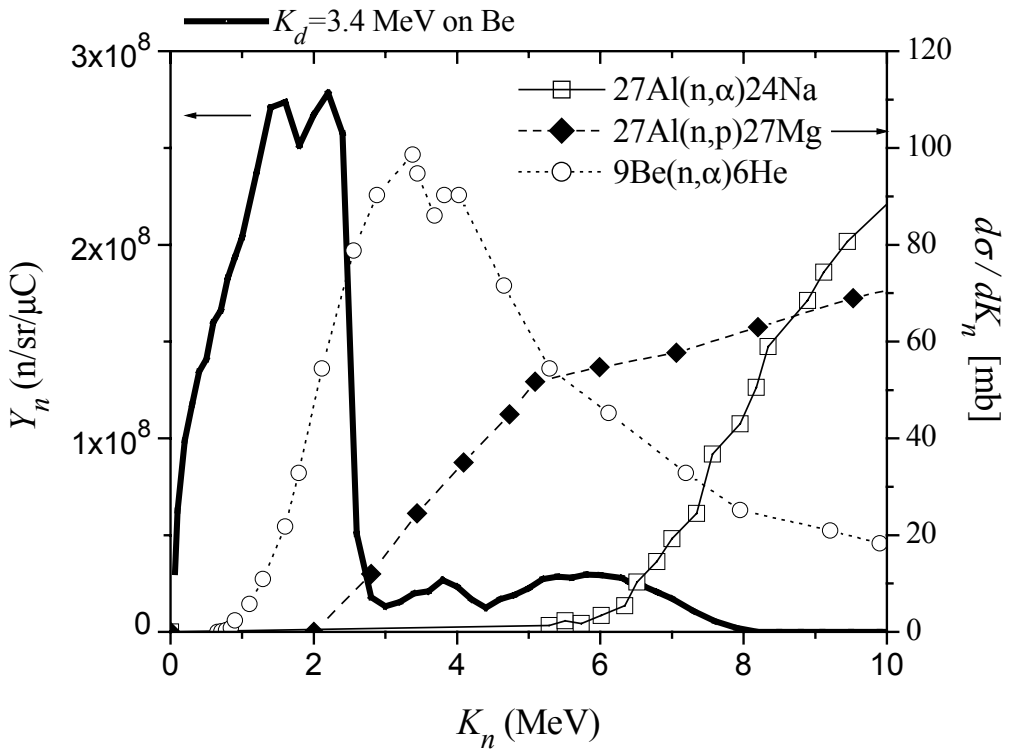

Figure 6.15 Neutron yield, Y_n, from 3.4 MeV deuterons on a Be target (left axis) and reaction cross sections by neutron of energy K_n for the reactions listed in the legend (right axis).

after which the vacuum pressure exceeded 10^{-4} Torr. Pure alumina actually able to withstand higher temperatures; however, a 3% SiO_2 component is used in fabricating the material and makes it less stable. We were able to pack about 1.6 g of the material into the target holder and calculate the production as a function of deuteron beam energy as plotted in Fig. 6.16. Also shown in the plot is the production of 24Na from a MgO powder target, 6He from a Be foil target, and 136Cs from a La_2O_3 powder. We include 6He in the estimates since it had been considered for effusion out of the target area into atom trap experiments.

We have made some off-line measurements of the production of 24Na from magnesia

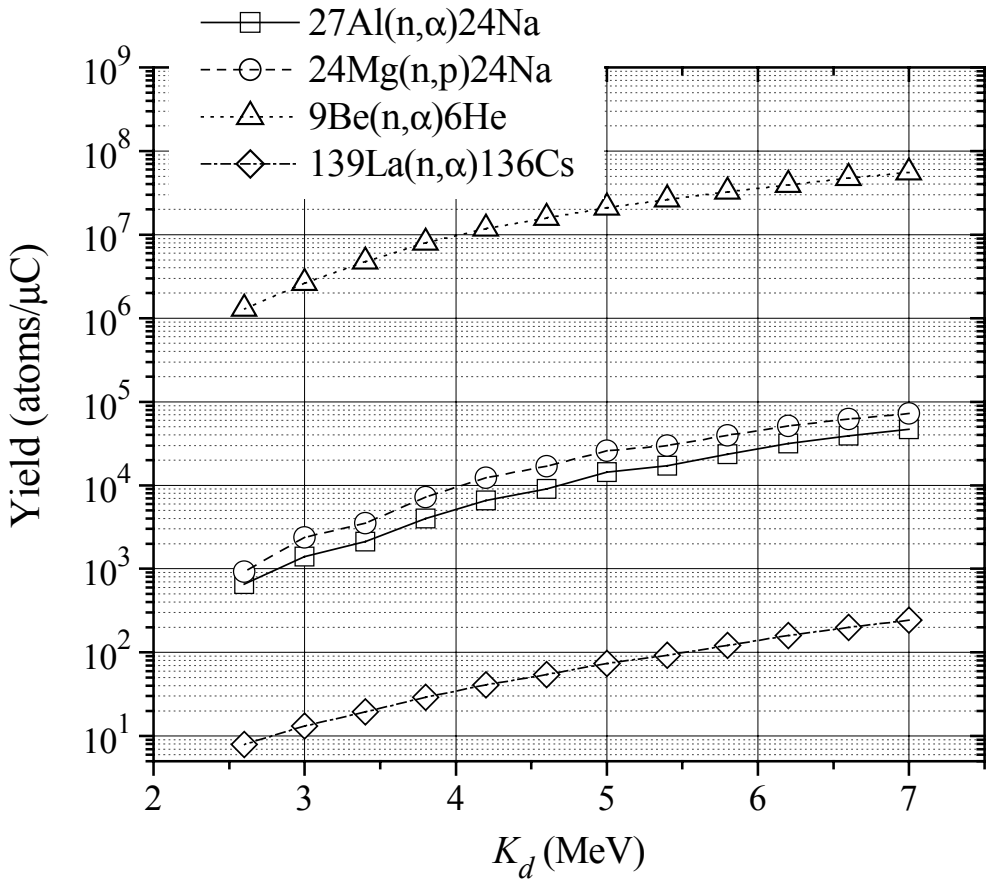

Figure 6.16 Production of certain isotopes versus the deuteron beam energy on a Be target.

and alumina samples with currents of up to 2.5 μA on the primary target for up to 3.5 MeV deuterons. The measured yields were found to be ~40% less than predicted. This may be due in part to the fall of in production with φ, as well as to the attenuation of neutrons by the material lying between the primary target and the oxide material. We measured a production of about 5×10^5 atoms/μC, which would be an excellent release candidate if it were not for its relatively high ionization potential (V_i=7.65 eV). We also used a 11B target as a primary target to test if there would be an enhancement to the production of 24Na. Notice from Fig. 6.15 that the cross sections require relatively high neutron energies to obtain significant production from 27Al. The 11B(*d*,*n*)12C reaction gives higher neutron energies since it has a reaction Q value of 13.2 MeV, compared to that of 9Be(*d*,*n*)10B, which is only about 3.84 MeV. We found that there was actually a factor of 30% less production of 24Na. This is due to a lower flux of neutrons from a heightened Coulomb barrier with boron nuclei.

Some attempts were made to try to measure ionized and extracted 24Na atoms from the material. At first we tried using the low-background ion counting system to detect the ions; however, the measurement was unsuccessful due to the high 23Na background signal that fall onto the mass 24 region. A typical mass spectrum is shown in Fig. 6.17, where a 4.5 μA deuteron beam of 3.5 MeV impinges on the 11B primary target. Even if the ionization and extraction efficiency were 100%, there would still be less than 800 atoms/s of 24Na on a background that is over 10^4 atoms/sec. Going to a 9Be target would have helped very little. We also tried using a 3% efficient plastic scintillator, but the neutron background from the primary beam was too high to measure the 15 hour half-life decay of 24Na. The same issue was true when using a germanium or NaI detector.

Clearly, there would have to be more elaborate methods of detection to measure above background, whether we are doing direct ion or decay counting.

Obviously, there is a lot to gain from going to higher deuteron energies and higher currents, but there were some technical difficulties with this as will be explained in the next section. At this point further experiments were halted to assess the operation for further enhancements that will improve the measurements to the point where release measurements could be done. Of course, any signal above background at all would have been useful for a measurement of the ionization and extraction efficiency of the source.

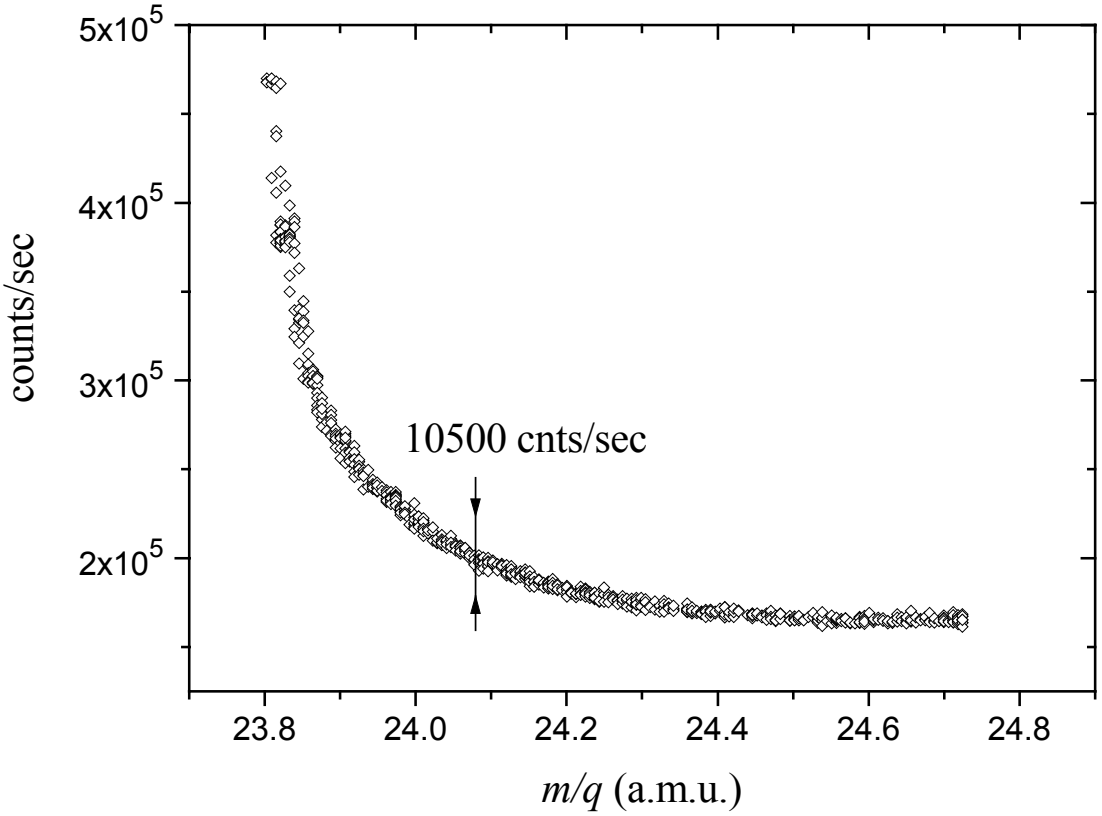

Figure 6.17 Mass spectrum at the mass 24 region with a 4.5 μA deuteron beam at 3.5 MeV on a 11B target.

6.5 Recommendations for future studies

6.5.1 Enhancements to the accelerator

The work done with Dynamitron production experiments have given us some experience with a number of issues related to RIA. In order to continue these studies, however, there will be a need to improve the accelerator performance and implement improved separator techniques.

The greatest improvement may come from an enhancement of the Dynamitron performance. During beam developments we found that the accelerator will not stabilize at higher terminal voltages with beams over ~4 μA. At one time a break down of the terminal voltage from 4 MeV caused serious damage to the plasma ion source RF supply. The minimum improvement that should be done here is to fill the SF_6 isolation tank to its nominal pressure of about 60 p.s.i. Throughout this development an improvement to the stability of the accelerator was observed in just going from 37 p.s.i. to 41 p.s.i.

Improvements could also be done at the plasma ion source. Since the accelerator break down is dependent on the amount of beam current in the column, it would be advisable to put a pre-mass separator at the terminal voltage side of the accelerator. This would eliminate a 30% beam component from deriving from H_20, N_2, CO_2, and other residual molecules. More importantly, it would eliminate the d_2+ component. It was found that this component hitting on the block of the manifold causes a significant amount of background radiation that it will eventually cause the allowed radiation safety limit to be exceeded. The radiation at the shielded cave performed exceptionally well, and does not seem to need any further improvements.

An issue of concern is also the apertures that were installed in the acceleration column as discussed in the first section. We found that break down was very sensitive to focusing beams at higher energy with the extraction and lens potentials at the terminal side. Typically, we would increase the focusing strength, which would in turn increase the transmission. The transmission would start to improve when increasing the focusing strength at the source focus before the accelerating column; however, this too would eventually lead to break down of the accelerator potential. The maximum achieved transmission during these test did not exceed 5% at ~4 μA and 3.5 MeV. This could be an effect of the over-focusing effect described in the first section and shown be Fig. 6.2. It may be beneficial to remove the apertures that were installed in the column to suppress back streaming electrons. Removing the apertures requires dismantling the entire acceleration column, which would be a time-consuming task.

Performance improvements to this type of accelerator are common. From previous studies with similar accelerator systems it seems that improvements can really enhance the performance. For example, in a late article by a group at Ruhr-Universitat Bochum, a 4 MV Dynamitron accelerator was enhanced to give up to 8 MeV acceleration of 100 μA of deuterons [Baumann86].

6.5.2 Enhancements to source and detection performance

The experience gained with the ion source, oven, and mass separator has also pointed out some possible enhancements that may improve the system. We shall discuss some of the difficulties encountered and the improvements that would help eliminate them. First of all, we expect stable residual beams to always be present from the source, and any production of alkali isotopes will necessarily mean that we would need to measure them

in the presence of the stable isotopes as shown in Fig. 6.17 for the Na mass range. This problem is more relevant in direct ion counting, which has the best detection efficiency.

The ideal thing to do to eliminate this is to bake out the source to reduce the amount of residual stable beams; however, after days of running at the highest temperatures (~1500ºC) we did not observe a reduction in any of the components, except for a very small amount for Rb and Cs. The estimated lifetime of the oxide insulation at the graphite filament is less than ~400 hours under these conditions, and there was no indication that any significant reduction would be achieved in this time. The slow decay of the residuals seems to be a result of having very well thermally insulated walls around the oven. The shielding acts as a reservoir of material that is being feed at an extremely small rate.

A way to eliminate this problem would be to introduce the components into a clean off-line oven in which to the unwanted material can be driven out. The components should be left exposed with as few obstructions as possible to speed up the rate of evaporation from the material. Unfortunately, this type of environment has not been constructed yet, but will be necessary for future RIA source developments.

Of course, detecting only the decay radiation as was done for the experiments described in Chapter 4 can easily eliminate the problem with the stable residues. Although, we have tried to make some radiation detection measurements here, they would require additional pulse discrimination to eliminate the background radiation from neutrons. Adding shielding around the detection region can eliminate this problem.

The best improvements will be to increase the production rates. Although increasing the deuteron beam current and energy on the target is necessary, it would also be helpful to

use as many of the neutrons as possible. To do this there will need to be a major redesign of the target geometry so that the target material can intercept more of the neutrons. We show an annular design scheme in the diagram of Fig. 6.18 that would be able to do this. A water-cooled probe would be inserted into the target and positioned so that maximum production efficiency is obtained.

The target is shifted slightly towards the beam since the stronger flux of neutrons is at the direction of the beam. One critical issue with this scheme will be the heating coil arrangement that surrounds the target. It actually may be better to go with an outside wall of Ta with a high current running directly through it to heat the target. Otherwise, it will be necessary to use the yttria insulations described earlier to isolate the target electrically from the target. Using fiberous oxides for heat insulation will play a key role in the design, since it will conserve the amount of power needed to heat the oven, and

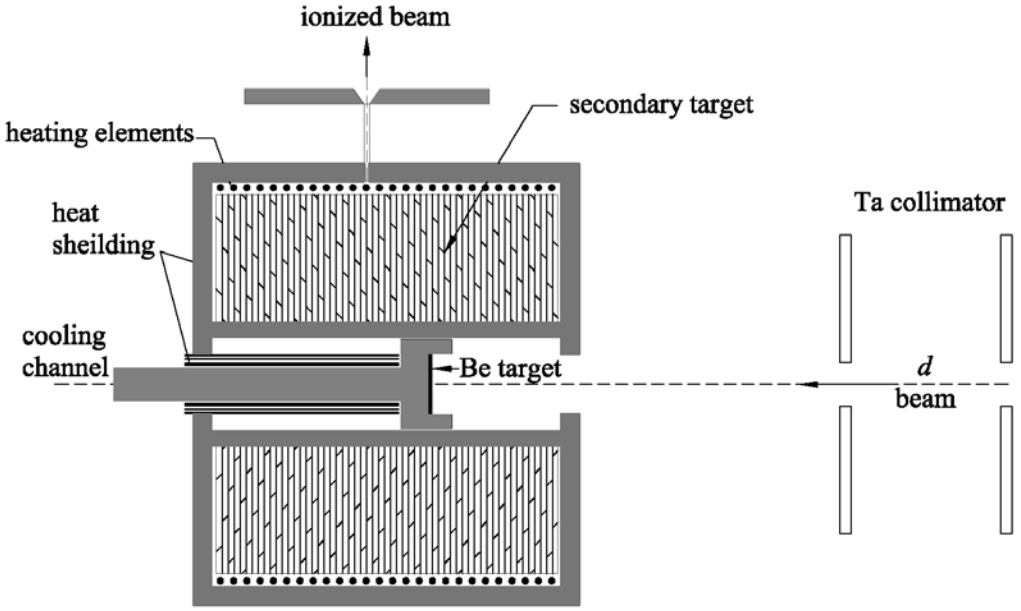

Figure 6.18 Annular target configuration for increasing production efficiency at Dynamitron.

therefore, conserve the lifetime of the heating elements. It is recommended that graphite be avoided if possible for the heating element unless it is supported so as to not touch any of the other components. There are other alloys, such as those of W and Re, which are more inert at extreme temperatures and may last longer in contact with refractory oxides.

The annular target geometry is being considered for the RIA target designs. There are prototypes being constructed that will be tested at the ISAC facility in TRIUMF in the near future. Designing and building prototypes that are durable under high temperature and beam power will be a critical part of the program. Measuring the release from the target region and testing different target materials will also be important. Also, it would be advantageous to conduct these types of tests at the Dynamitron accelerator facility, since it is available and close to commissioning as a ISOL facility.

Chapter 7

SUMMARY

A number of topics related to the RIA proposal have been covered. The facility will offer many new opportunities in nuclear physics and possibly other areas of science. The technological challenges that come with such a facility go well beyond the nuclear physics scope.

In Chapter 2 it was demonstrated how implementing DC acceleration into map-based optics can be used in the design of an isobar separator. The separator design that was discussed must be an integral part of the RIA facility, since it will need to purify beams at very high mass resolution. It was shown that axially symmetric accelerating devices could be used in making a dual-potential spectrometer fully achromatic to first order. The COSY INFINITY code system has been modified to allow this feature to be used with map methods. A fifth order analysis was carried out in order to determine the necessary multipole fields necessary to correct higher order geometric aberrations. The challenges ahead in sector magnet and multipole design were discussed.

The focus was then shifted to the driver accelerator in Chapter 3, where the problem of filtering and transporting of multiple charge state beams was addressed. Such optical systems require map-based methods as well; however, there was the need to implement axially symmetric time-dependent fields for rebunching the beam. It was demonstrated that this could be done with the COSY INFINITY code system by modifications to the equations of motion and implementing algorithms that evaluate RF field effects in the map. The properties of the beam phase space and charge state distribution are very

important to the design of these systems and the accelerator; hence, it was necessary to explore models and existing measurements that will aid in this area. A brief survey of the most recent studies on this topic is covered and the most relevant results are presented. The results indicate that there are critical issues that need to be studied further with actual measurements that pertain to the stripping of particles such as uranium.

In Chapter 4 there were some important issues in target design that are addressed. Since the heart of any rare isotope facility is the production target, target development will be an ongoing process during the operation of the machine. It was demonstrated by simulation and experiment that the two-step process is a technique that will need to be used to extend the lifetime of targets to a level that is essential for obtaining intense beams of neutron rich nuclei. The analysis of the ion source and ISOL system was necessary to unfold the absolute yields and compare with Monte Carlo calculations. This includes the measurement and modeling of the release curves, verifying the products from decay curves, and obtaining the efficiency of the transport system. The evidence found in the results supports the models that suggest that the two-step method is essential for very neutron rich nuclei production. Some suggestions for future target design were included.

Chapter 5 and 6 are mainly concerned with experimental techniques that must be developed for RIA applications. A number of devices for ion counting and beam imaging were constructed and tested at the Dynamitron facility. The results of the performance of each device are discussed as well as the application that it can serve in RIA. The techniques are used to test the performance of an ion source and mass separator system, as well as beams from the Dynamitron accelerator. Chapter 6 is

concluded with some recommendations that may help in enhancing the performance of the production of rare isotopes at the Dynamitron. The difficulties that were encountered reflect on the types of challenges that the RIA facility will offer. The final section offers a diagram of an ion source design based on an annular target surrounding a neutron generator. The Monte Carlo production models described in Chapter 4 verify that this type of design is the most efficient production mechanism.

The production of intense beams for acceleration offers a wide variety of problems in beam and target applications. This study offers some solutions to future and present designs and suggestions for future studies.

APPENDICES

APPENDIX A

CANONICAL TRANSFORMATIONS AND THE SYMPLECTIC CONDITION

This appendix demonstrates how to exploit the symmetries present in an optical system by applying a symplectic approach. The concept of a canonical transformation in the matrix approach is introduced in order to ultimately obtain some relations between first order elements of the map.

In order to obtain the differential equations of motion in terms of another independent variable requires that a transformation be applied that will preserve any symmetry present in the system. We will begin with the set of differential equation expressed in terms of the Hamiltonian of the system where time t is the independent variable. The time derivatives of the generalized coordinates and momenta are then simply given by the six-paired equations,

$$\begin{aligned} \dot{x} &= \partial H / \partial p_x & \dot{p}_x &= -\partial H / \partial x \\ \dot{y} &= \partial H / \partial p_y & \dot{p}_y &= -\partial H / \partial y \,, \\ \dot{s} &= \partial H / \partial p_s & \dot{p}_s &= -\partial H / \partial s \end{aligned} \tag{A1a}$$

where the dot signifies the time derivative, *d/dt*. If the Hamiltonian has an explicit time dependence, then the condition,

$$\dot{H} = dE / dt = \partial H / \partial t \,, \tag{A1b}$$

must also be accounted for, where E is the total energy in the system. Expressing the form of Eq. (A1a) in the form of a matrix that is acting on a vector, we get that

$$\frac{d\boldsymbol{r}}{dt} = \dot{\boldsymbol{r}} = \begin{bmatrix} \dot{x} \\ \dot{p}_x \\ \dot{y} \\ \dot{p}_y \\ \dot{s} \\ \dot{p}_s \end{bmatrix} = \mathbf{J}\left(\frac{\partial H}{\partial \boldsymbol{r}}\right) = \begin{bmatrix} 0 & 1 & 0 & 0 & 0 & 0 \\ -1 & 0 & 0 & 0 & 0 & 0 \\ 0 & 0 & 0 & 1 & 0 & 0 \\ 0 & 0 & -1 & 0 & 0 & 0 \\ 0 & 0 & 0 & 0 & 0 & 1 \\ 0 & 0 & 0 & 0 & -1 & 0 \end{bmatrix} \begin{bmatrix} \partial H/\partial x \\ \partial H/\partial p_x \\ \partial H/\partial y \\ \partial H/\partial p_y \\ \partial H/\partial s \\ \partial H/\partial p_s \end{bmatrix} \tag{A2}$$

where the vector $\boldsymbol{r}=(x, p_x, y, p_y, s, p_s)$ consists of the canonically conjugate coordinates and **J** represents the antisymmetric matrix. A similar form will be obtained for the system once it has been transformed for a relative comparison.

The equations will be transformed such that the position variable, *s*, which lies along the optic axis, becomes the independent variable instead of the variable *t*. The new coordinates to be used are listed as follows:

$$\begin{array}{ll} x & a = p_x / p_0 \\ y & b = p_y / p_0 \\ l = -(t - t_0)\mu_0 & \delta = (K - K_0)/K_0 \end{array} \tag{A3}$$

The variable δ is the fractional difference between the kinetic energy of an arbitrary particle, *K*, and that of the reference particle, K_0. Notice that a change in kinetic energy is equivalent to a change in the total energy of the system, thus *dE=dK*. The variable *l* is equal to the position along the optic axis of an arbitrary particle, relative to the reference particle in the lab frame of reference. It is proportional to the difference in time of flight between an arbitrary particle and the reference particle, where the constant of proportionality is $\mu_0 = \mathrm{v}_0\gamma/(\gamma+1)$.

The passage from one set of independent variables to another can be effected by means of a Legendre transformation [Landau76a]. The transformation is carried here by means of taking the total differential of two functions that describe the entire system but have slightly different variables,

$$E = H(x, p_x, y, p_y, s, p_s, t) \quad \text{and} \tag{A4}$$

$$p_s = -F(x, p_x, y, p_y, t, E, s), \tag{A5}$$

to obtain following two expanded equations,

$$dE = \left(\frac{\partial H}{\partial x}dx + \frac{\partial H}{\partial p_x}dp_x\right) + \left(\frac{\partial H}{\partial y}dy + \frac{\partial H}{\partial p_y}dp_y\right) + \left(\frac{\partial H}{\partial s}ds + \frac{\partial H}{\partial p_s}dp_s\right) + \frac{\partial H}{\partial t}dt \tag{A6}$$

and

$$-dp_s = \left(\frac{\partial F}{\partial x}dx + \frac{\partial F}{\partial p_x}dp_x\right) + \left(\frac{\partial F}{\partial y}dy + \frac{\partial F}{\partial p_y}dp_y\right) + \left(\frac{\partial F}{\partial t}dt + \frac{\partial F}{\partial E}dE\right) + \frac{\partial F}{\partial s}ds\,. \tag{A7}$$

Solving for dp_s in Eq. (A6) and comparing terms with Eq. (A7), we obtain the three resulting pairs of differential equations,

$$\begin{aligned} x' &= (1/p_0)\,\partial_a F & a' &= (-1/p_0)\,\partial_z F \\ y' &= (1/p_0)\,\partial_b F & b' &= (-1/p_0)\,\partial_y F \\ l' &= (\mu_0/K_0)\,\partial_\delta F & \delta' &= (-\mu_0/K_0)\,\partial_l F \end{aligned}, \tag{A6}$$

where the prime notation denotes the derivative with respect to the new independent variable, s. The switch to the s variable in the derivatives result from terms, such as $\dot{x}/\dot{s} = x'$, which appear after substituting the Eq. (A1) into Eq. (A6). Finally, the variables defined by Eq. (A3) are used to determine the constants outside of the differential.

Notice that the variables x, $a \cdot p_0$, y, $b \cdot p_0$, $-l/\mu$, and $\delta \cdot K_0$ are canonically conjugate, and F is the corresponding Hamiltonian with units of momentum. In a matrix notation, a new form of the matrix **J** is obtained such that we can write the equation,

$$\frac{d\boldsymbol{r}}{ds} = \boldsymbol{r}' = \begin{bmatrix} x' \\ a' \\ y' \\ b' \\ l' \\ \delta' \end{bmatrix} = \mathbf{J}\left(\frac{\partial F}{\partial \boldsymbol{r}}\right) = \begin{bmatrix} 0 & 1/p_0 & 0 & 0 & 0 & 0 \\ -1/p_0 & 0 & 0 & 0 & 0 & 0 \\ 0 & 0 & 0 & 1/p_0 & 0 & 0 \\ 0 & 0 & -1/p_0 & 0 & 0 & 0 \\ 0 & 0 & 0 & 0 & 0 & \mu_0/K_0 \\ 0 & 0 & 0 & 0 & -\mu_0/K_0 & 0 \end{bmatrix} \begin{bmatrix} \partial_x F \\ \partial_a F \\ \partial_y F \\ \partial_b F \\ \partial_l F \\ \partial_\delta F \end{bmatrix}. \tag{A7}$$

Now we consider the transformation of the coordinates by way of the transfer map of an optical system. Recall that the final coordinates are related to the coefficients of the map by,

$$r_{f,i} = \sum_{k=1}^{8} r_{0,k} \left\{ (r_i, r_k) + \frac{1}{2} \sum_{l=1}^{8} r_{0,l} \left\{ (r_i, r_k r_l) + \frac{1}{3} \sum_{m=1}^{8} r_{0,m} \{ (r_i, r_k r_l r_m) + \cdots \} \right\} \right\}, \tag{A8}$$

from position s_0 to s_f, along the optic axis. The general relation,

$$\frac{\partial r_{f,i}}{\partial s} = \sum_{k=1}^{6} \frac{\partial r_{f,i}}{\partial r_{0,k}} \frac{\partial r_{0,k}}{\partial s}, \tag{A9a}$$

for $i \in \{1,2,3,4,5,6\}$ can be written in matrix notation as

$$\frac{\partial \boldsymbol{r}_f}{\partial s} = \begin{bmatrix} \frac{\partial x_f}{\partial s} \\ \frac{\partial a_f}{\partial s} \\ \frac{\partial y_f}{\partial s} \\ \frac{\partial b_f}{\partial s} \\ \frac{\partial l_f}{\partial s} \\ \frac{\partial \delta_f}{\partial s} \end{bmatrix} = \mathbf{A}\left(\frac{\partial \boldsymbol{r}_0}{\partial s} \right) = \begin{bmatrix} \frac{\partial x_f}{\partial x_0} & \frac{\partial x_f}{\partial a_0} & \frac{\partial x_f}{\partial y_0} & \frac{\partial x_f}{\partial b_0} & \frac{\partial x_f}{\partial l_0} & \frac{\partial x_f}{\partial \delta_0} \\ \frac{\partial a_f}{\partial x_0} & \frac{\partial a_f}{\partial a_0} & \frac{\partial a_f}{\partial y_0} & \frac{\partial a_f}{\partial b_0} & \frac{\partial a_f}{\partial l_0} & \frac{\partial a_f}{\partial \delta_0} \\ \frac{\partial y_f}{\partial x_0} & \frac{\partial y_f}{\partial a_0} & \frac{\partial y_f}{\partial y_0} & \frac{\partial y_f}{\partial b_0} & \frac{\partial y_f}{\partial l_0} & \frac{\partial y_f}{\partial \delta_0} \\ \frac{\partial b_f}{\partial x_0} & \frac{\partial b_f}{\partial a_0} & \frac{\partial b_f}{\partial y_0} & \frac{\partial b_f}{\partial b_0} & \frac{\partial b_f}{\partial l_0} & \frac{\partial b_f}{\partial \delta_0} \\ \frac{\partial l_f}{\partial x_0} & \frac{\partial l_f}{\partial a_0} & \frac{\partial l_f}{\partial y_0} & \frac{\partial l_f}{\partial b_0} & \frac{\partial l_f}{\partial l_0} & \frac{\partial l_f}{\partial \delta_0} \\ \frac{\partial \delta_f}{\partial x_0} & \frac{\partial \delta_f}{\partial a_0} & \frac{\partial \delta_f}{\partial y_0} & \frac{\partial \delta_f}{\partial b_0} & \frac{\partial \delta_f}{\partial l_0} & \frac{\partial \delta_f}{\partial \delta_0} \end{bmatrix} \begin{bmatrix} \frac{\partial x_0}{\partial s} \\ \frac{\partial a_0}{\partial s} \\ \frac{\partial y_0}{\partial s} \\ \frac{\partial b_0}{\partial s} \\ \frac{\partial l_0}{\partial s} \\ \frac{\partial \delta_0}{\partial s} \end{bmatrix} \tag{A9b}$$

in which the matrix $\mathbf{A}$ is identified as the Jacobi matrix. The terms in the Jacobi matrix are the elements in the map as shown by the equation,

$$\frac{\partial r_{f,i}}{\partial r_{0,k}} = \sum_{k=1}^{6} \delta_{i,k} (r_i, r_k) = (r_i, r_k). \tag{A10}$$

Assuming that the optical system has midplane symmetry, no explicit time-dependent fields, and at most some constant energy gain, then the Jacobi should take the form of

$$\mathbf{A}=\begin{bmatrix} (x,x) & (x,a) & 0 & 0 & 0 & (x,\delta) \\ (a,x) & (a,a) & 0 & 0 & 0 & (a,\delta) \\ 0 & 0 & (y,y) & (y,b) & 0 & 0 \\ 0 & 0 & (b,y) & (b,b) & 0 & 0 \\ (l,x) & (l,a) & 0 & 0 & (l,l) & (l,\delta) \\ 0 & 0 & 0 & 0 & 0 & (\delta,\delta) \end{bmatrix}. \tag{A11}$$

Notice that when we speak of an overall energy gain, we assume that all particles in the beam have the same charge as the reference particle, ($q_0 e$). An example of such a system would be an accelerating column in which a potential drop between the entrance and exit changes the energy of every particle by $\Delta K = -q_0 e(V_f - V_0)$. A similar differential is taken on the Hamiltonian of the system, but with respect to the initial coordinates, to give the equation,

$$\frac{\partial F}{\partial r_{0,i}} = \sum_{k=1}^{6} \frac{\partial F}{\partial r_{f,k}} \frac{\partial r_{f,k}}{\partial r_{0,i}}, \tag{A12a}$$

which can then be expressed in the matrix form,

$$\frac{\partial F}{\partial \boldsymbol{r}_0} = \mathbf{A}^{\mathrm{T}} \left(\frac{\partial F}{\partial \boldsymbol{r}_f} \right), \tag{A12b}$$

where $\mathbf{A}^{\mathrm{T}}$ is the transpose of the Jacobi. We also write the differential in Eq. (A7) such that it is evaluated at $s=s_0$ to obtain

$$\left(\frac{\partial \boldsymbol{r}_0}{\partial s} \right)_{S=S_0} = \mathbf{J}_0 \left(\frac{\partial F}{\partial \boldsymbol{r}_0} \right), \tag{A13a}$$

and at $s=s_f$ to get

$$\left(\frac{\partial \boldsymbol{r}_f}{\partial s} \right)_{S=S_f} = \mathbf{J}_f \left(\frac{\partial F}{\partial \boldsymbol{r}_f} \right) \tag{A13b}$$

for $s=s_f$. The terms in the **J** matrices at s_0 and s_f would then take the forms,

$$\mathbf{J}_0 = \begin{bmatrix} 0 & 1/p_{0,0} & 0 & 0 & 0 & 0 \\ -1/p_{0,0} & 0 & 0 & 0 & 0 & 0 \\ 0 & 0 & 0 & 1/p_{0,0} & 0 & 0 \\ 0 & 0 & -1/p_{0,0} & 0 & 0 & 0 \\ 0 & 0 & 0 & 0 & 0 & \mu_{0,0}/K_{0,0} \\ 0 & 0 & 0 & 0 & -\mu_{0,0}/K_{0,0} & 0 \end{bmatrix}, \tag{A14a}$$

and

$$\mathbf{J}_f = \begin{bmatrix} 0 & 1/p_{0,f} & 0 & 0 & 0 & 0 \\ -1/p_{0,f} & 0 & 0 & 0 & 0 & 0 \\ 0 & 0 & 0 & 1/p_{0,f} & 0 & 0 \\ 0 & 0 & -1/p_{0,f} & 0 & 0 & 0 \\ 0 & 0 & 0 & 0 & 0 & \mu_{0,f}/K_{0,f} \\ 0 & 0 & 0 & 0 & -\mu_{0,f}/K_{0,0} & 0 \end{bmatrix}. \tag{A14b}$$

Substituting both Eq. (A12) and Eq. (A13) into Eq. (A9) we obtain that,

$$\frac{\partial \boldsymbol{r}_f}{\partial s} = \mathbf{A}\left(\frac{\partial \boldsymbol{r}_0}{\partial s}\right) = \mathbf{A}\mathbf{J}_0\left(\frac{\partial F}{\partial \boldsymbol{r}_0}\right) = \mathbf{A}\mathbf{J}_0\mathbf{A}^{\mathrm{T}}\left(\frac{\partial F}{\partial \boldsymbol{r}_f}\right) = \mathbf{J}_f\left(\frac{\partial F}{\partial \boldsymbol{r}_f}\right), \tag{A15}$$

which implies that

$$\mathbf{J}_f = \mathbf{A}\mathbf{J}_0\mathbf{A}^{\mathrm{T}}. \tag{A16}$$

This matrix equation expresses the condition of symplecticity and can be used to predict properties of the map [Berz85]. This is a particularly powerful technique to use in situations where special conditions, such as midplane symmetry, are present in the optical system. If we apply the Jacobi at Eq. (A11) to (A14a) and (A14b), we obtain the following relations:

$$(x,x)(a,a)-(x,a)(a,x)=p_{0,0}/p_{0,f} \tag{A17a}$$

$$(y,y)(b,b)-(y,b)(b,y)=p_{0,0}/p_{0,f} \tag{A17b}$$

$$(l,l)=\mu_{0,f}/\mu_{0,0} \tag{A17c}$$

$$(\delta,\delta)=K_{0,0}/K_{0,f} \tag{A17d}$$

$$(x,x)(l,a)-(x,a)(l,x)=\frac{p_{0,0}\mu_{0,0}}{K_{0,0}}(x,\delta) \tag{A17e}$$

$$(a,x)(l,a)-(a,a)(l,x)=\frac{p_{0,0}\mu_{0,0}}{K_{0,0}}(a,\delta) \tag{A17f}$$

$$(a,x)(x,\delta)-(x,x)(a,\delta)=\frac{K_{0,0}}{K_{0,f}}(l,x) \tag{A17g}$$

$$(a,a)(x,\delta)-(x,a)(a,\delta)=\frac{K_{0,0}}{K_{0,f}}(l,a) \tag{A17h}$$

When there is no change in energy of the particles from s_0 to s_f, Eqs. (A17a) through (A17d) will all go to unity. This is a direct effect of the invariance of phase space volume under canonical transformations, as stated by Liouville's theorem [Landau76b]. It implies that as long as the total energy of the system is a constant of the motion, then the map acts as a canonical transformation on the system.

APPENDIX B

SPECIAL VERSION OF COSY INFINITY 8

This appendix is intended as an addendum to the COSY INFINTY reference manual for the use of a modified version of the code system. Descriptions about the elements that have been implemented and instructions on how to apply them are provided. Calculating the maps of these elements change the reference particles energy, hence it is necessary to inform the user on how to handle certain variables in the code. Some of the terminology should be referenced from the COSY INFINITY manual [Berz97].

B.1 Changing reference particle energy

When using the procedures listed below or other elements that involve changing the reference particle energy, it is important to note that the reference particle energy is kept track of in the global COSY variable **CONS(E0)** in units of MeV. A map calculated for the transport of a reference particle energy K_0 cannot be used for the transport of another of different K_0. There may be some scaling methods used to extrapolate a map to different kinetic energies as described in the COSY manual, although we will not discuss that here. This is important in cases where one stores the map to a variable or a file. Restoring the map, such as with function **AM**, will not change CONS(E0), since this variable changes only as the ODE integrator is calculating the map. The function AM simply restores the elements of the map, which does not keep any record of the absolute energy of the reference particle or any changes thereof. The user must keep track of what the energy *should be* and apply the **RP** command when it is appropriate.

One should also note that the function **PM** writes elements of the map for $(x,\cdots)$, $(a,\cdots)$, $(y,\cdots)$, $(b,\cdots)$, and $(l,\cdots)$, but not for $(\delta_K,\cdots)$. For DC fields one needs to only be

concerned with the (δ_K,δ_K) and higher order terms such as (δ_K,δ_K^n), when n is some integer. When time varying fields are involved it is necessary to consider other (δ_K,$\cdots$) elements. One should take extra measures to view these elements as described in the original COSY INFINITY manual.

B.2 Particle optical elements

B2.1 Analytical function generated models

IMMCAV2 $< V> <D> < L> < C > < \omega > < \phi >$;

This procedure is for a two-gap RF cavity with the on-axis potential taken from procedure **CEL** but with added time dependence of the form $V(t) = V \cos(\omega t+\phi)$. V is the peak voltage on the middle tube, D is the tube radius, C is the gap distance, ω is the angular frequency in rad/s, and ϕ is the phase in radians. L is the length of the center tube as shown in Fig. B1. The numerical integration begins at position s=-L/2-C-5D and ends at a distance s=L/2+C+5D where s=0 at the center of the structure. This ensures that the fields fall-off sufficiently from the peak value. The map is calculated in such a way that the cavity takes up no space in s making it effectively a thin lens. The user must account for this length and avoid having any other optical elements overlapping the region that the lens should span. The time and phase are defined such that ϕ=0 and t=0 when the particle enters at position s=-L/2-C-5D.

IMMCAV1 $< V> <D> < C > < \omega > < \phi >$;

This procedure is for a one-gap RF cavity with the on-axis potential approximated by

$$V(s) = \frac{V}{2}\left[1 - \frac{d}{\kappa C}\log\frac{\left(\kappa(s + C/2)/d\right)}{\left(\kappa(s - C/2)/d\right)}\right] \qquad \text{(B1)},$$

where κ is a scaling constant and is 1.315 [Hsi-men86]. The time dependence is similarly $V(t) = V\cos(\omega t+\phi)$ as in the previous subroutine just described. V is the peak voltage on the middle tube, D is the tube radius, C is the gap distance, ω is the angular frequency in rad/s, and ϕ is the phase in radians. The position s=0 is taken to be the center of the gap and integration begins at position s=-C/2-5D and ends at s= C/2+5D. The thin lens treatment also applies for IMMCAV2. The time and phase are defined such that ϕ=0 and t=0 when the particle enters at position s=-C/2-5D. We note that when both ω and ϕ are set to zero the result is an immersion lens that can apply a static potential for DC acceleration or deceleration, depending on the sign. Note that it is not recommended to use this procedure for higher order calculations. This is because the derivatives of the approximate on-axis function gives errors that increase with order. It is, however, easy to use and reasonable to use to third order.

B2.2 Modeling structures with charged multi-rings

In the two preceding examples, an approximate form for the potential on axis was used for simulating electric structures. This approximation is valid as long as the particles remain far from the surface of the structure (typically no closer than 1/2 the radius of the tube). For situations where more accuracy is needed, a number of subroutines have been devised that calculate the potential from a set of charged rings that lie on the electrodes of the structure. The method is described in the literature and is more immune to the type of errors that are associated with the approximations of the on-axis functions [Geraci02]. Furthermore, there is more flexibility in being able to distribute the rings that emulate the geometry of the structure. The subroutines allow the

user to simulate more details than the analytical approximations, such as radii of curvatures and relative position of tubes.

The first such subroutine of this type is one that emulates a two-gap cavity geometry. A tube is positioned with a cavity that has an entrance and exit aperture for the beam to pass as shown in Figure B2. The subroutine that calculates the map of this structure,

TWOGAP *<SS1> <SS2> <SCL> < ω> < ϕ> < RIEST >*;

has six parameters to be specified. Notice that when the frequency and phase are set to zero, this structure simulates an electrostatic lens. The coordinate system is devised such that s=0 at the center of the cavity. The parameters ω and ϕ are in units of radians/s and radians, respectively. The electric potential if the tube is determined by, $V(t)$= *SCL**cos($\omega t+\phi$), where *SCL* is the magnitude of the electric potential in kV. The parameters *SS1* and *SS2* are the start and endpoints of along the optic axis. The parameter *RIEST* is a user-supplied estimate of the radius of the cavity that is used to set the scale for range of integration step-size. It will define the nominal step size for the numerical ODE integration along s, and should usually be set to the inner tube radius. For more accuracy it may be set as small as desired, but it should generally not exceed a value of twice the radius. Care should be taken so that the start and endpoint of integration lie far enough to give the fields space to drop off sufficiently. Depending on the amount of accuracy needed, a length equivalent to about one radius is minimum, but applying about two or three radii is nominal. Before calculating the map with TWOGAP, it is necessary to execute a procedure that specifies the geometrical layout of the cavity. The procedure

GAPSTR1 *<RI> <RO> <RE> <RD> <RLRES> <RRES> <RLDT1> <ZDT1>*;

sets the parameters in units of meters for the parameters as depicted in Fig. B2. The charge on each ring is determined for a positive potential on tube. This procedure will save the charge, Q, and (r,s) coordinates of each ring to the following *structure* files:

KEN I.dat (calculated charge of the ring)

KEN II.dat (z coordinate value of the ring)

KEN III.dat (r coordinate value of the ring)

It will use unit 11 in the process, so it is important to avoid using this unit number during execution of this subroutine. The data stored in these files serves as later input when TWOGAP is called. The files are in ASCII character format and may be used to make scatter plots, such as one that shows the location of each ring in (r,s) space, by using any graphical software of choice. Note that the number of entries in any of the files is the total number of rings used. There is only one set of line feed deliminated values in each file and there is no index on the ring number; however, the ordering is the same in each file.

The data stored in the files is used to determine the on-axis potential via a sum of the analytic expressions for rings. DA is then used to determine the fields off-axis. GAPSTR does not have to be repeated for successive runs of TWOGAP as long as the geometrical parameters remain constant. When using the TWOGAP procedure, it is recommended that the local Cartesian coordinates be set such that time $t = 0$ when the particle starts its motion at *SS1*. This is done by the following command sequence,

LOCSET <0> <*SS1*> <0> <*SS1*> <0> <0> <0> ;

TWOGAP <*SS1*> <*SS2*> <*SCL*> < ω > < ϕ > < *RIEST* > ;

where the LOCSET command resets the local coordinates of the reference particle at the entrance point of the cavity as described further in the reference [Berz97]. By doing this the time and phase are defined such that ϕ=0 and t=0 when the particle enters at position s=*SS1*.

B2.3 Other procedures with and without time varying fields

There two other procedures that have been added to the COSY code system that work similar to the TWOGAP subroutine for determining maps of a two- and three-tube structures. These are, respectively, the **THREEGAP** and **FOURGAP** procedures (see Fig. B3 and B4, respectively). A parameter allows one to set even or odd parity between the two tubes in the THREGAP structure, as described in the diagram in Fig. B3. Under even parity both tubes have the same potential at any time, while in the case of odd parity the potential on each is off by 180º with respect to time. For the four gap structure the two outer tubes are 180º out of phase, while the middle tube is grounded. If unsure about the phase on each tube, the user can observe the sign of the charge on the rings of each corresponding tube. The values are listed in the same KEN I.dat file, which had been discussed for the TWOGAP subroutine. The subroutines that evaluate the charge on each ring are described in the figures containing their respective diagrams.

There is also a one-gap accelerating gap that can be used with RF, for example as a buncher. The procedure is

GAP1 <RA> <GAP> <RI> <RRES> ;

Here <RA> is the aperture radius, <GAP> is the gap length, <RI> is the radius of curvature, and <RRES> is the depth of the gap. The parameter <RRES> can be set to be

several radii to simulate an isolated accelerating gap. Typically, one should set this parameter to at least 5 times <RA> to minimize the effects at the boundary.

In order to calculate the map, the procedure

ONEGAP <SS1> <SS2> <SCL> <W> <PHI> <RIEST> ;

needs to be called, where these variables are described above in TWOGAP. Setting the frequency and phase to zero simulates a DC accelerating gap.

It is recommended that the user select a reasonable set of values for the parameters and plot the (*r*,*s*) positions in the structure files to be sure that the geometry makes physical sense. Be sure to issue the LOCSET command before calculating the map and keep track of CONS(E0) whenever these types of maps are calculated more than once during execution.

B2.4 Accelerating columns

STDCOL1 <RA> <RI> <RE> <RLRES> <RRES> <RO> <RAO><RLDT1>

<GAPP> <NRNG> <OFF> ;

This procedure describes an accelerating column, with the voltage varying linearly with ring number *k* as shown in Fig. B5. The parameter <NRNG> specifies the number of tubes. <RLRES> is the total length between the entrance and exit apertures. <RLDT1> is the length of each tube, which is set the same for all. The gap spacing between tubes is given by <GAPP>. <RA> is inner radius of the tubes and <RAO> is the radius of the entrance and exit apertures. <RI> and <RE> are the radii of curvatures as shown in the figure. <RO> is the outer tube radius, while <RRES> is the radius of the outer enclosure. <OFF> allows for a shift along the s-axis of the entire array of tubes with respect to the center position as shown in Fig. B5. The potential of tube *k* is determined by,

$V_k=k/(NRNG+1)$, where the potential of the entrance aperture is $V_i=0$ and that of the exit aperture will be normalized to 1. The potential of the system is then scalable within the procedure ACCELCOL1. The user should take care so that the parameters for <RLRES>, <NRNG>, <GAPP> and <RLDT1> correspond to a physical structure and that boundaries do not overlap. Also, note that along with the other procedures that generate the geometry of a structure, calling this procedure does *NOT* make the element act within a particle optical system. The ACCELCOL1 routine must be used in succession to allow the element to act.

CUSCOL1 <RA> <RI> <RE> <RLRES> <RRES> <RO> <RAO>

<RLDT1> <ZARR> <NRNG> <VARR> ;

This procedure produces a similar structure to STDCOL1, but allows for a more general distribution of the array of tubes within the housing. Fig. B6 illustrates the geometrical parameters for user input. The array <ZARR> should have NRNG elements, specifying the z-coordinate of the center of each tube. The outer housing is centered at z=0 by default. Also, it allows one to specify each individual tube potential. The array <VARR> must have <NRNG>+1 elements such that element VARR(N+1) specifies the potential of the exit aperture. The potential on tube *k* is specified by element VARR(*k*) for *k*=1,...,N, and the potentials on the tubes and exit aperture should be normalized so that the highest voltage is 1. The potential of the system is then scalable within the procedure ACCELCOL1**.**

ACCELCOL1 <SS1> <SS2><SCL> <RIEST> <NRNG> ;

This procedure will calculate the map of either the STDCOL1 or CUSCOL1 structures. The start and endpoints of integration are <SS1> and <SS2>. *Caution*: In order to ensure

consistent boundary conditions, it is not recommended to let the start and endpoints of integration exceed about 3 radii beyond the endpoints of the exterior housing at ±RLRES/2. At this point the electric field on axis should return to zero within a fraction of a percent, and the potential on axis thus becomes flat. Going below 3 radii will result in unphysical electric fields due to the boundary conditions employed for the field solver. <RIEST> should be set to <RA> or smaller, depending on the accuracy of the integration step that is desired. <NRNG> must be specified again here and must be the same value as that used in STDCOL1 or CUSCOL1.

The LOCSET command should be issued before ACCELCOL1 is executed to reset the local coordinates. In order to use the accelerating columns, first the geometry must be specified by using STDCOL1 or CUSCOL1 The geometry and charge density profile for each cavity is then stored in data files KEN_I.dat, KEN_II.dat, and KEN_III.dat, which are the same files used for the TWOGAP, THREEGAP, and FOURGAP routines. These files are overwritten each time one of these geometry producing procedures is called. To save some computing time it may be useful to store these files in another directory in case they need to be recalled for a common structure.

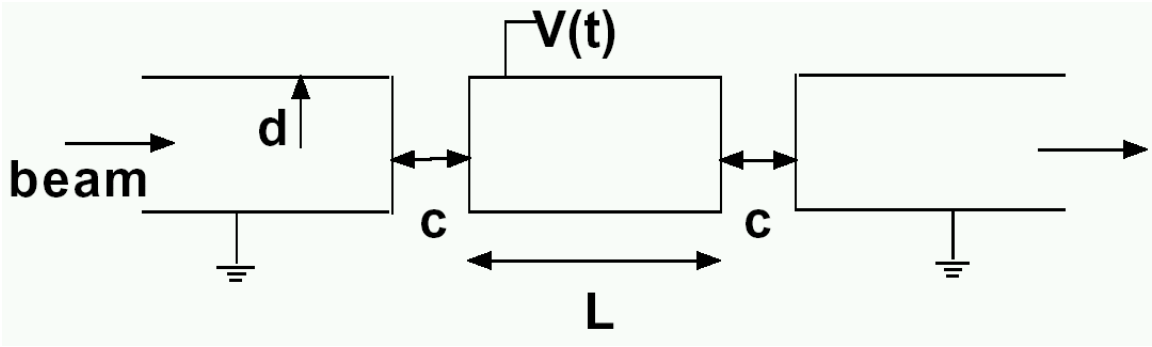

Figure B1. Diagram illustrating the parameters used in IMMCAV2.

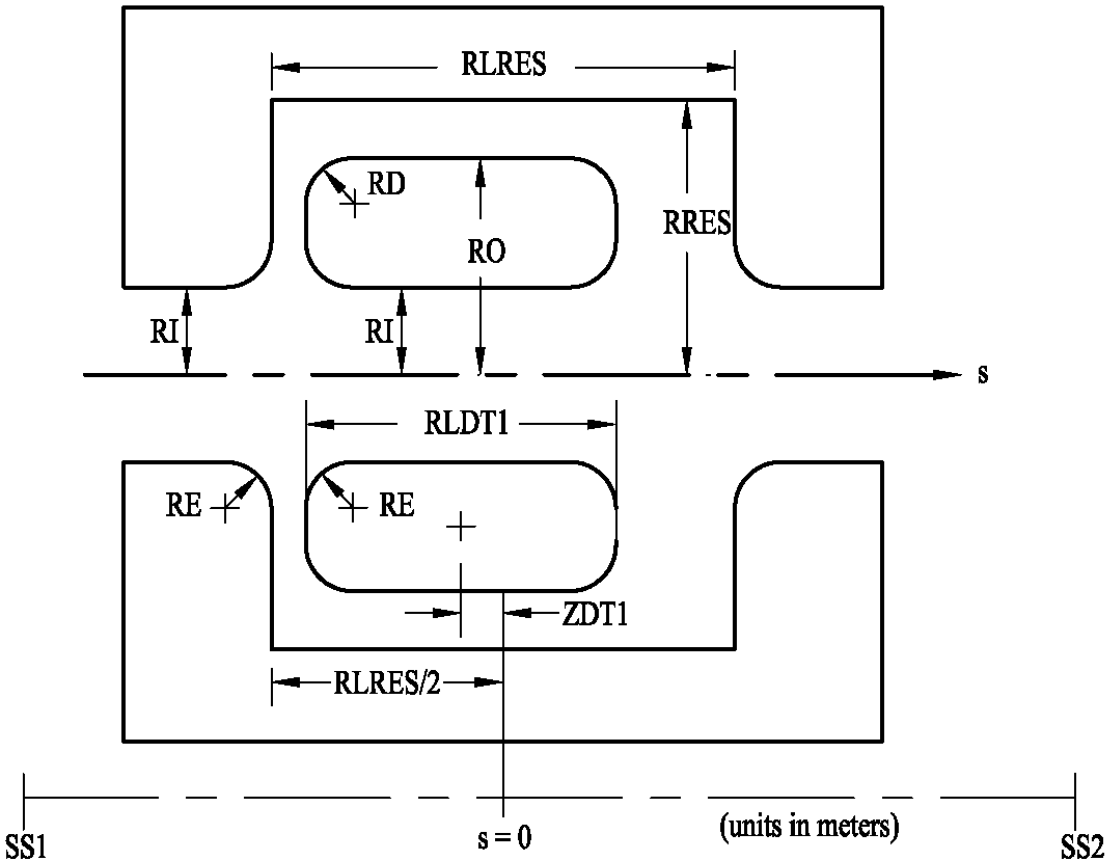

GAPSTR1 RI RO RE RD RLRES RRES RLDT1 ZDT1 ; (generates structure file)
TWOGAP SS1 SS2 SCL W PHI RIEST; (calculates map)

Cavity voltage, V = SCL*cos(W*t + PHI)

SCL = max voltage (kV)
W = angular frequency (rad/s)
PHI = relative cavity phase (rad)
RIEST = integration step (set the same or smaller than RI)
ZDT1 = shift in meters of tube relative to s = 0.

Figure B2. Diagram illustrating the parameters of subroutine TWOGAP.

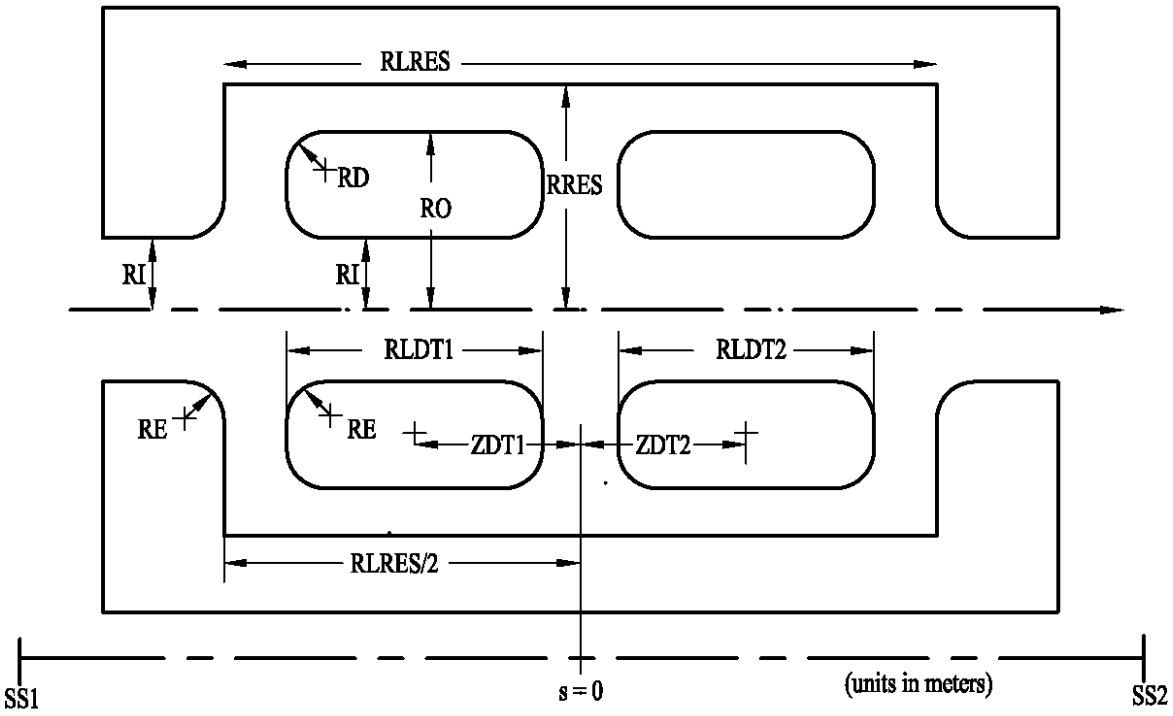

GAPIII1 RI RO RE RD RLRES RRES RLDT1 RLDT2 ZDT1 ZDT2 PAR ; (generates structure file)
THREEGAP SS1 SS2 SCL W PHI RIEST; (calculates map)

Cavity voltage, V = SCL*cos(W*t + PHI)

SCL = max voltage (kV)
W = angular frequency (rad/s)
PHI = relative cavity phase (rad)
RIEST = RI (set the same or smaller)
ZDT1 = center position of tube 1 relative to s = 0.
ZDT2 = center position of tube 2 relative to s = 0.
PAR = +1 for even, -1 for odd voltage symmetry between tubes

Figure B3. Diagram illustrating the parameters of subroutine THREEGAP.

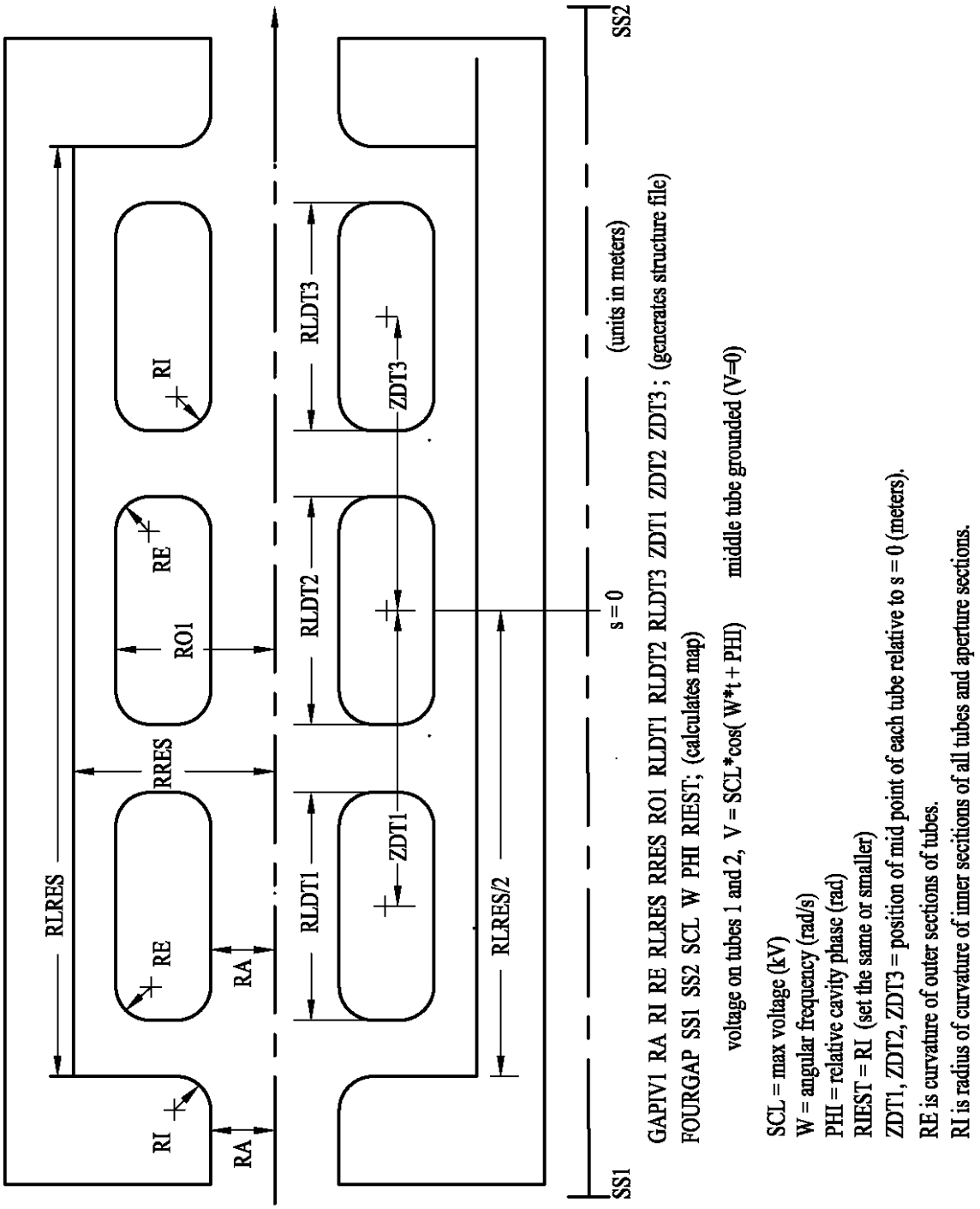

Figure B4. Diagram illustrating the parameters of subroutine FOURGAP.

Figure B5. Diagram illustrating the parameters of subroutines ACCELCOL1 and STDCOL1.

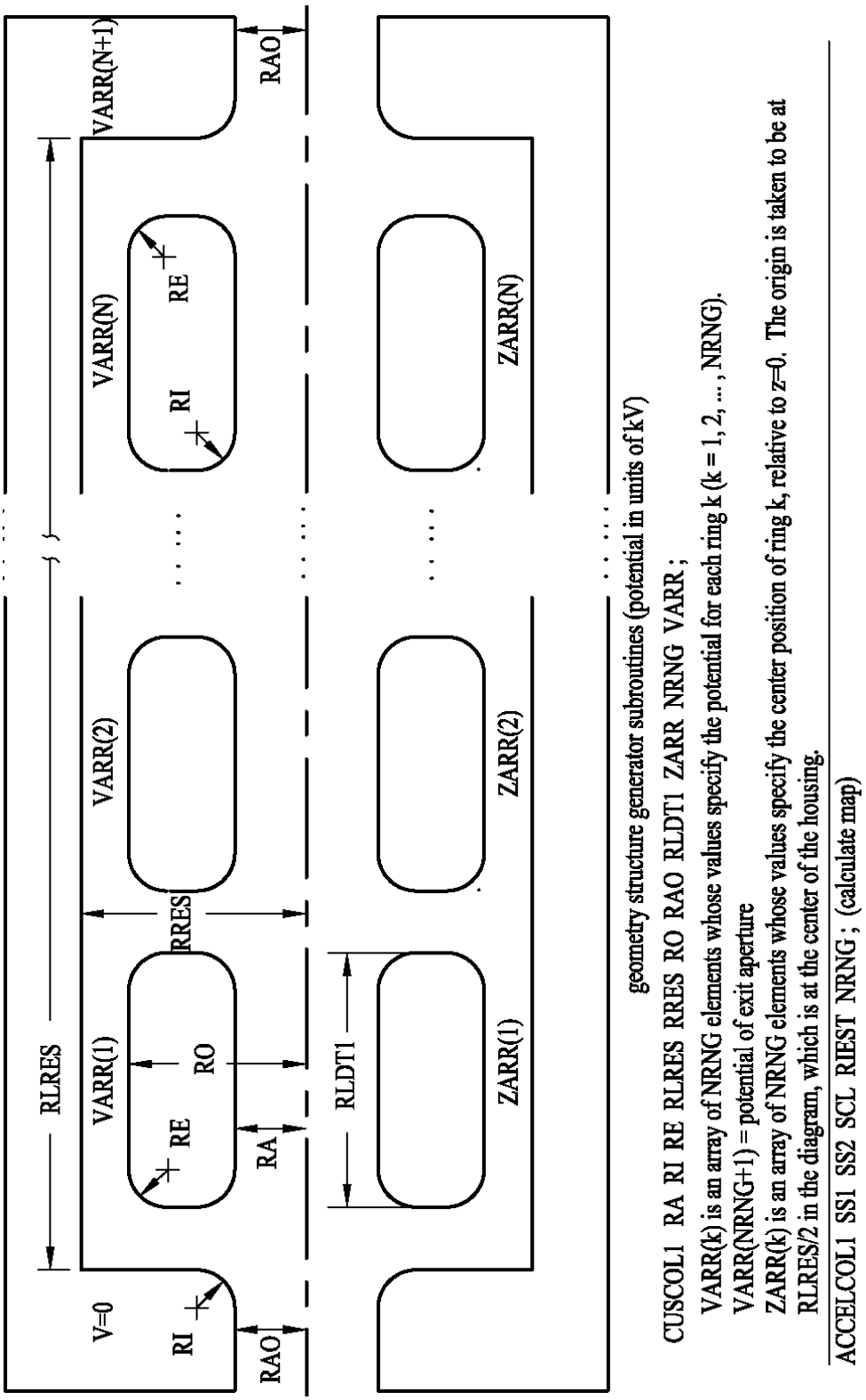

Figure B6. Diagram illustrating the parameters of subroutines ACCELCOL1 and CUSCOL1.

APPENDIX C

OBTAINING VALUES FOR THERMAL IONIZATION EFFICIENCY

Some consideration is given to the formation of a hot cavity plasma within a 1.5 mm diameter ionizer tube in accordance with a formalism introduced by Kirchner [Kirchner78]. For such an enclosure of tungsten walls at 3000 K we should expect the formation of an electron plasma whose density may be determined by Richardson's law. It states that

$$n_e = 2\left(2\pi kT / h^2\right)^{3/2} \exp(-V_s / kT) \tag{C1}$$

where the temperature of the electron plasma is determined by the potential drop across the resistive ionizer tube and may be approximately taken as kT_e=10 eV. At this temperature the Debye-length is less than 0.01mm, ensuring the existence of quasi-neutrality within the volume of the tube. Under such conditions it is expected that the electron density must be about $n_e = 2 \times 10^{13}\text{cm}^{-3}$.

Considering that the vapor pressure of tungsten at such a temperature is $n_{op} = 2 \times 10^{9}\text{cm}^{-3}$ and adopting Kirchner's assumption that about 1% of these atoms are ionized, then we obtain that the plasma sheath has a potential of about -2.3 V where the walls are taken to be at ground potential. Kirchner expects that such a thermal plasma should enhance ionization to a degree determined by the ionization potential from ground the state. The thermal ionization efficiency is expressed by the formula,

$$\varepsilon_{iT} = [\gamma_T / (1 + \gamma_T)] \tag{C2}$$

where the term,

$$\gamma_T = (2\xi_i / \xi_0)(2\pi m / h^2)^{3/2} P^{-1} (kT)^{5/2} \exp(-V_i / kT) \qquad \text{(C3)}.$$

The pressure is given by $P=(n_{op}+ n_i + n_e)kT$ where $n_i = 2 \times 10^{12}\text{cm}^{-3}$ is taken as the density of ionized atoms in the plasma. Note that this model applies to an infinitely long tube and does not account for losses at ends.

APPENDIX D

FORM OF SOLUTION OF THE TIME RELEASE RATE EQUATION

The rate equation for the population of a given isotope within the target is given by,

$$\dot{N} = J \times P - F - \lambda N + \lambda_n N_n \qquad \text{(D1)},$$

The rate constant rate, λ, must include all probable decay channels that lead to another distinct isotope. The final term, $\lambda_n N_n$, represents the sum of all decay channels that feed the population of (Z,A) isotopes. In general, there will be a system of differential equations of the form (D1) to account for all such possible cross terms in the equations.

The release flux term, F, will generally follow closely to the number of isotopes in the target. Thus, it is possible to express this term as

$$F(t) = g(t) \times N(t) \qquad \text{(D2)}$$

where g is a function that is imposed for characterizing the deviation of the function F away from N. Under steady state conditions we can expect g to be a constant.

Substituting Eq. (D2) into (D1) and solving for the instantaneous number of (Z,A) isotopes yields the integral equation,

$$N(t) = e^{-\lambda t - \mu(t)} \left[k + \int_0^t e^{-\lambda \tau - \mu(\tau)} \left(J \times P + \lambda_n N_n \right) d\tau \right] \qquad \text{(D3)}$$

where k is a constant determined by the initial conditions and

$$\mu(t) = \int_0^t g(\tau) d\tau \qquad \text{(D4)}.$$

We consider the special case in which a very short pulse of protons is delivered to the target. The flux term may be approximated by the use of a delta function, $J(t) \approx J_o \, \Delta t \, \delta(t)$, so that

$$J \times P = N_o \delta(t) \tag{D5}$$

where N_o gives the total number of atoms produced during the pulse. The condition $N(0)= N_o$ requires that k=0 and results in the general solution

$$N(t) = e^{-\lambda t - \mu(t)} \left(N_o + \lambda_n \int_0^t e^{\lambda\tau + \mu(\tau)} N_n d\tau \right) \tag{D6}$$

The quantity of interest is the fraction of N_o, which gets released from the target. This fraction of released product is denoted by the release efficiency

$$\eta(\lambda, \lambda_n) = \frac{1}{N_o} \int_0^\infty F(t) dt \tag{D7}$$

which gives the ratio of the extracted amount of (Z,A) isotopes to the total amount produced at the time of the pulse. It is useful to express Eq. (D7) as

$$\eta(\lambda, \lambda_n) = \int_0^\infty e^{-\lambda t} p(t) dt \tag{D8}$$

where the function $p(t)$ is defined by

$$p(t, \lambda, \lambda_n) \equiv \frac{F(t)}{N_o e^{-\lambda t}} = g(t) e^{-\mu(t)} \left(1 + \frac{\lambda_n}{N_o} \int_0^t e^{\lambda\tau + \mu(\tau)} N_n d\tau \right) \tag{D9},$$

and is commonly referred to as the delay function, or release probability; i.e. the probability that particle (Z,A) created at time t=0 will be released at time t from the target. The second term inside parentheses in Eq. (D9) carries the effect of the feeding term and allows for the possibility of having a release efficiency greater than unity. For this reason, η is referred to as the release coefficient rather than a value of the efficiency. Eq. (D9) is usually expressed in the literature for the special case where λ_n=0, in whereby the λ dependence drops out as well. The exponential term outside of the parentheses follows only due to the assumption made in Eq. (D2).

If we let λ_n=0 and treat g as constant, it follows that $p(t)=g\ exp(-gt)$. This is simply the solution to the delay function for the evacuation of a gas through an orifice from a container and $1/g$ is the time constant [Kirchner81a]. Solving for the release coefficient, $\eta=g/(g+\lambda)$, yields unity for vanishing λ.

For the case of $\lambda_n>0$ and $\lambda>0$, $\eta>1$ since the integral in the second term inside parentheses in Eq. (D9) is always positive. Generally, obtaining a form for $g(t)$ in Eq. (D9) is not trivial, since it forms a transcendental relation. The form of g must be assumed initially then tested against the measured delay curves. The emphasis of the exercise, however, is mostly to illustrate the effect of having $\lambda>0$ on the release efficiency.

BIBLIOGRAPHY

Bibliography

[Albert92] A. Albert, K. Kroneberger, O. Heil, K.O. Groeneveld, Nucl. Instrum. Methods Phys. Res. A **317**, (1992) 397.

[Alkhazov89] G.D. Alkhazov, E.Yu. Berlovich and V.N. Panteleev, Nucl. Instr. Meth. **A 280**, p. 141 (1989).

[Alonso82] J.R. Alonso *et. al.*, Science **217**, p. 1135 (1982).

[Baron79] E. Baron, IEEE Transactions on Nuclear Science **NS-26.2**, p. 2411 (1979).

[Baron88] E. Baron and Ch. Ricaud, "Beam foil interaction studies for the future stripper of GANIL" in *Proceedings of the 1st Eoropean Particle Accelerator Conference (EPAC),* (GANIL, Caen, France, 1988), GANIL-A88-02.

[Baron92] E. Baron, M. Bajard and Ch. Ricaud in *6th Conference on Electrostatic Accelerators and Associated Boosters*, June 1-5, 1992, Montegrotto Terme (Padova).

[Baron93] E. Baron, M. Bajard and Ch. Ricaud, Nucl. Instr. Meth. Phys. Res. A **328**, p. 177 (1993).

[Barzakh00] A.E. Barzakh, I.Ya. Chubukov, D.V. Fedorov, V.N. Panteleev, M.D. Seliverstov and Yu.M. Volkov, Phys. Rev. C **61**, p. 034404 (2000).

[Bauer72] E. Bauer, Vacuum **22**, (1972) 539.

[Baumann86] F.M. Baumann, G. Domogala, H. Freiesleben, H.J. Paul, S. Puhlvers and H. Sohlback, Nucl. Instr. Meth. Phys. Res. **A 247**, p. 359 (1986).

[Belkié84] Dž. Belkié, R. Gayet and A. Salin, Comput. Phys. Commun. **32**, p. 385 (1984).

[Berz85] H. Wollnik and M. Berz, Nucl. Instrum. Methods Phys. Res. A **238**, 127 (1985).

[Berz87a] M. Berz, H. C. Hoffmann, and H. Wollnik, Nucl. Instrum. Methods Phys. Res. **A258**, 402 (1987).

[Berz87b] M. Berz and H. Wollnik, Nucl. Instrum. Methods Phys. Res. A **258**, 364 (1987).

[Berz90a] M. Berz, Nucl. Instrum. Methods Phys. Res. **A298**, 473 (1990).

[Berz90b] M. Berz, Nucl. Instrum. Methods Phys. Res. A **298**, 426 (1990).

[Berz97] M. Berz, National Cyclotron Laboratory, MSU, East Lansing, Tech. Rep. MSUCL-1088 (1997). http://www.beamtheory.nscl.msu.edu/cosy.

[Berz99a] M. Berz, *Modern Map Methods in Particle Beam Physics*, **1**st edition (Academic Press, New York, 1999), Chap. 2, p.81.

[Berz99b] M. Berz, *Modern Map Methods in Particle Beam Physics*, **1**st edition (Academic Press, New York, 1999), Chap. 5, p.167.

[Berz99c] M. Berz, *Modern Map Methods in Particle Beam Physics*, **1**st edition (Academic Press, New York, 1999), Chap. 5, p.195.

[Berz99d] M. Berz, *Modern Map Methods in Particle Beam Physics*, **1**st edition (Academic Press, New York, 1999), Chap. 5, p.190.

[Bethe57] H.A. Bethe and E.E. Salpeter, in *Quantum Mechanics of One- and Two-Electron Atoms* (Academic Press, Springer, New York, 1957).

[Betz72] H. Betz, Rev. Mod. Phys. **44**, p. 465 (1972).

[Birdsall85] C. K. Birdsall, *Plasma Physics via Computer Simulation*, (McGraw-Hill, New York, 1985).

[Box58] G. Box and N. Muller, Ann. Math. Statis. **28**, p. 610 (1958).

[Brown64] K. L. Brown, R. Belbeoch, and P. Bounin, Rev. Sci. Instrum. **35**, 481 (1964).

[Brown81] K. L. Brown and J. E. Spencer, IEEE Transactions on Nuclear Science **NS-28**,3:2568 (1981).

[Briesmeister86] J.F. Briesmeister, " MCNP : A general monte carlo code for neutron and photon transport", LANL, LA-7396-M REV 2 (1986).

[Camplan81] J. Camplan, Nucl. Instr. Meth. **187**, p. 157 (1981).

[Carey92] D. C. Carey, *The Optics of Charged Particle Beams*, **2**nd edition (Harwood Academic Press, New York, 1992).

[Carraz79] L.C. Carraz, S. Sundell and H.L. Ravn, Nucl. Instr. Meth. **158**, p. 69 (1979).

[Catalan96] N. Catalan-Lasheras, M. Crescenti and M. Vretenar, (CERN, Geneva, Switzerland, 1996), CERN-PS-32-DI-363.

[Chartier97] M. Chartier et. al., Nucl. Instr. Meth. **B 126**, p. 334 (1997).

[Ciavola97] G.Ciavola, D. Rifuggiato, H. Weick, M. Winkler and H. Wollnik, Nucl. Instr. Meth. **B 126**, p. 17 (1997).

[Colutron] Colutron Research Corporation, 2321 Yarmouth Ave., Boulder, CO 80301, USA. http://www.colutron.com/

[Crank75] J. Crank, in *The Mathematics of Diffusion* (Clarendon Press, Oxford, 1975), 2nd, **Vol.** , p. 2.

[Crouch77] E. Crouch, Atomic Data and Nuclear Data Tables **19**, p. 417 (1977).

[DANFYSIK] Magent and vacuum box constructed by DANFYSIK, Jyllinge, Denmark.

[Davids94] C.N. Davids, *"Concept for an advanced EXOTIC BEAM FACILITY based on ATLAS"* (A working paper), http://www.phy.anl.gov/ria/index.html

[Davids89] C.N. Davids and J.D. Larson, Nucl. Instr. Meth. **B 40/41**, p. 1224 (1989).

[Davids92] C.N. Davids, *et. al.*, Nucl. Instr. Meth. **B 70**, p. 358 (1992).

[Dietz73] L. A. Dietz and J.C. Sheffield, Rev. Sci. Instrum. **44**, (1973) 183.

[Dietz75] L. A. Dietz and J.C. Sheffield, J. of App. Phys Vol. **46** No. 10, (1975) 4361.

[Dmitriev79] I.S. Dmitriev, V.P. Zaikov and Yu.A. Tashaev, Nucl. Instr. Meth. **164**, p. 329 (1979).

[Dmitriev82] I.S. Dmitriev, V.P. Zaikov, E.A. Kralkina, V.S. Nikolaev and Ya.A. Teplova in *Proceedings of the 9th International Conference on Cyclotrons and their Applications,* (Editions de Physique, Les Ulis, France, 1982), p. 299.

[Dragt85] A.J. Dragt, Nucl. Instr. Meth. Phys. Res. A **258**, 259 (1987).

[Dumont78] G. Dumont *et al.*, Nucl. Instr. Meth. **153**, 81 (1978).

[Eaton79] T.W. Eaton, H.L. Ravn and ISOLDE Collaboration, Nucl. Instr. Meth. B **26**, p. 190 (1979). (1979) p.190.

[ES&H] ES&H office, Bldg. 201, US Departement of Energy, 9800 S. Cass Ave., Argonne, IL 60439-4899.

[Feschenko96] A. V. Feschenko, P. N. Ostroumov et. al., Proc. of the 1996 Linac Conf., Chicago, 193, (1996).

[Forand90] J. L. Forand and and others, Rev. Sci. Instrum. **61**, 3372 (1990).

[Frost63] B.R.T. Frost, Journal of Nuclear Materials **10,4**, p. 265 (1963).

[Gemmell80] D.S. Gemmell, Chem. Rev. **80**, 301 (1980).

[Geraci02] A.A. Geraci, T.A. Barlow, M. Portillo, J. Nolen, K.W. Shepard, K. Makino and M. Berz, "High-order maps with acceleration for optimization of electrostatic and radio-frequency ion-optical elements", Rev. Sci. Instr. (2002). (In publication)

[Gomes98] I.C. Gomes and J. Nolen, "Influence of the incident particle energy on the fission product mass distribution" in *Topical Meeting on Nuclear Applications of Accelerator Technology,* (Gatlinburg, TN, Sep. 20-23, 1998), Argonne Rep. No. ANL/TD-FPP/CP-97197.

[Gould84] H. Gould, D.G. Greinger, P. Lindstrom, T.J.M. Symons and H. Crawford, Phys. Rev. Lett. **52**, p. 180 (1984).

[Gould85] H. Gould, D.G. Greinger, P. Lindstrom, T.J.M. Symons H. Crawford, P. Thieberger and H. Wegner, Nucl. Instr. Meth. Phys. Res. B **10/11**, p. 32 (1985).

[Gutierrez81] R.L. Gutierrez, R.J. Herbst and K.W.R. Johnson, Los Alamos, Apr. 14, U.S. Pat. 4261935 (1981).

[HagebØ92] E. HagebØ, P. Hoff, O.C. Jonsson, E. Kugler, J.P. Omtvedt, H.L. Ravn and K. Steffensen, Nucl. Instr. and Meth. B **70**, p. 165 (1992).

[Höffstatter96] G. H. Höffstatter and M. Berz, Phys. Rev. E **54, 5**, p. 5664 (1996).

[Hübner70] H. Hübner and H. Wollnik, Nucl. Instr. Meth. **86**, p. 141 (1970).

[Huyse95] M. Huyse et. al., Nucl. Phys. **A 588**, p. 313c (1995).

[Hsi-men86] C. Hsi-men, in *Aberration Theory in Electron and Ion Optics* (Academic Press, Orlando, 1986).

[ISL92] IsoSpin Laboratory Noth American Steering Committe, "The IsoSpin Laboratory (ISL): Reasearch opportunities with radioactive nuclear beams", Los Alamos, LALP-91-51 (1992).

[Jiang02] C.L. Jiang, B.B. Back, I. Gomes, A.M. Heinz, J. Nolen, K.E. Rehm, G. Savard and J.P. Schiffer, "Yield Calculations for an Advanced Facility for Short-Lived Nuclear Beams", (submitted to Nucl. Instr. Meth. B for publication, 2002).

[Kirchner78] R. Kirchner and A. Piotrowski, Nucl. Instr. and Meth. **153**, p. 291 (1978).

[Kirchner78] R. Kirchner and A. Piotrowski, Nucl. Instr. and Meth. **153**, p. 291 (1978).

[Kirchner81a] R. Kirchner, Nucl. Instr. and Meth. **186**, p. 275 (1981).

[Kirchner81b] R. Kirchner, K. Burkard, W. Hüller and O. Klepper, Nucl. Instr. and Meth. **186**, p. 295 (1981).

[Kirchner92] R. Kirchner, Nucl. Instr. Meth. B **70**, p. 186 (1992).

[Koenig85] W. Koenig, A. Faibis, E.P. Kanter, Z. Vager and B.J. Zabransky, Nucl. Instr. Meth. Phys. Res. B **10/11**, 259 (1985).

[Koester02] U. Koester *et al.*, "Resonant ionization laser ion sources", *Fifth International Conference on Radioactive Nuclear Beams, Divonne, France, April 3-8*, 2000. To be published in Nuclear Physics A.

[Kruglov00] K. Kruglov and others, Nucl. Instrum. Methods Phys. Res. A **441**, 595 (2000).

[Landau76a] L. D. Landau and E. M. Lifshitz, *Mechanics*, **3**rd edition (Pergamon Press, Oxford, 1976), Vol. **1**, Chap. 7, p.131.

[Landau76b] L. D. Landau and E. M. Lifshitz, *Mechanics*, **3**rd edition (Pergamon Press, Oxford, 1976), Vol. **1**, Chap. 7, p.146.

[Langmuir25] I. Langmuir and K.H. Kingdon, Proc. R. Soc. London **A107**, p. 61 (1925).

[Larkins81] F.P. Larkins, J. Phys. B **14**, p. 73 (1981).

[Leon98] A. Leon, S. Melki, D. Lisfi, J.P. Grandin, P. Jardin, M.G. Suraud and A. Cassimi, Atomic Data and Nuclear Data Tables **69**, p. 217 (1998).

[Lewis75] T.G. Lewis, *Distribution Sampling for Computer Simulation* (D.C. Heath and Co., Lexington, Massachusetts, 1975), Chap. 5, p.70.

[Lyneis98] C.M. Lyneis, Z.Q. Xie and C.E. Taylor, Rev. Sci. Instr. **69**, p. 682 (1998).

[Lyneis02] C.M. Lyneis, Rev. Sci. Instr. **73**, p. 508 (2002).

[Makino98] K. Makino, *Rigorous Analysis of Nonlinear Motion in Particle Accelerators*, Ph.D. thesis, (Michigan State University, East Lansing, MI) Rep. No. MSUCL-1093 (1998).

[Makino99] K. Makino and M. Berz, Nucl. Instr. Meth A **427**, p. 338 (1999).

[Matsuda77] H. Matsuda, T. Matsuo and N. Takahashi, Int. J. Mass Spectr. Ion Phys. **25**, p. 229 (1977).

[Matsuo76] T. Matsuo, H. Matsuda, Y. Fujita, and H. Wollnik, Mass Spectrosc. Jpn. **24**, 19 (1976).

[Meadows89] J.W. Meadows, Nucl. Instr. Meth. **A 324**, p. 239 (1989).

[Menat42] M. Menat, Can. J. Phys. **42**, p. 164 (1942).

[Martin74] W.W. Martin, D.H. Schell and J.M. Taub, Los Alamos, May 14, U.S. Pat. 3810962 (1974).

[Matthews94] R.B. Matthews, F.C. Church, K.M. Chidester and H.G. Moore, Los Alamos, Jun. 14, U.S. Pat. 5320786 (1994).

[Meyerhof85] W.E. Meyerhof, R. Anholt, J. Eichler, H. Gould, Ch. Munger, J. Alonso, P. Thieberger and H.E. Wegner, Phys. Rev. A **32**, p. 3291 (1985).

[Muller59] M.E. Muller, Comm. ACM **2,4**, p. 14 (1959).

[Muller59] M.E. Muller, Comm. ACM **2,4**, p. 14 (1959).

[Mustapha01] B. Mustapha and J.A. Nolen, "Optimization of ISOL targets based on Monte-Carlo simulations of ion release curves" in *Meeting of the American Physical Society,* (Washington, DC, Apr. 28-May 1, 2001), Argonne Pub. No. 38460.

[Menat64] M. Menat, Can. J. Phys. **42**, 164 (1964).

[NI] National Instuments Corporation, 11500 N. Mopac Expwy, Austin, TX 78759-3504. http://www.ni.com/

[Nolen84] J. A. Nolen, Proceedings of the International Conference on Instrumentation for Heavy Ion Nuclear Research, ORNL, Oak Ridge, TN, 171, (1984), edited by Dan Shapira Harwood Academic Publishers, London, (1985).

[Nolen87] J.A. Nolen, S. Tanaka, A. Zeller and N. Bhattacharya, "Optics of a 90º Analyzing Magnet", International Conference on ECR Ion Sources and their Applications, ed. J. Parker, East Lansing, MI, MSU-NSCL Rep. No. MSUCP-47 p. 454 (1987).

[Nolen93] J. Nolen in *Proceedings of the Third International Conference on Radioactive Nuclear Beams,* 1993, edited by D.J. Morrissey, (Editions Frontieres, 1993), p. 111.

[Nolen02a] J.A. Nolen, "Prospects for exotic beam facilities in North America",Eur. Phys. J. A **13**, (2002). (In publication)

[Nolen02b] J.A. Nolen *et al.*," Liquid lithium cooling for 100 kW ISOL and fragmentation targets", *Fifth International Conference on Radioactive Nuclear Beams, Divonne, France, April 3-8*, 2000. To be published in Nuclear Physics A.

[Novikov98] Yu. N. Novikov, V.N. Panteleev and V.I. Tikhonov, PNPI, “The IRIS facility and nuclear spectroscopic investigations of nuclides far from beta-stability region”, *PNPI Main Scientific Activities 1971-1996, High Energy Physics Division, PNPI, Gatchina*, (1998). OR http://www.pnpi.spb.ru/publishing/pnpi_25_content_hep_en.html

[OMEGA] OMEGA Engineering, Inc., P.O. Box 2284, Stamford, CT 06906-0284. http://www.omega.com.

[Ostroumov99] P.N. Ostroumov, K.W. Shepard, J.A. Nolen and R.C. Pardo, ICFA Beam Dynamics Newsletter **20**, p. 60 (1999).

[Ostroumov00a] P.N. Ostroumov, K.W. Shepard, V.N. Aseev and A.A. Kolomiets, "Heavy-Ion Beam Acceleration of Two-Charge States from an ECR Ion Source" in *Proceedings of the 20th Intl. Linac Conference (LINAC 2000),* 2000, edited by Alexander W. Chao, (USPIRES-SLAC, 2000), eConf C000821:MOD01,2000.

[Ostroumov00b] P. N. Ostroumov and K. W. Shepard, Phys. Rev. ST Accel. Beams **3**, p. 030101 (2000).

[Ostroumov01] P. N. Ostroumov and K. W. Shepard, Phys. Rev. ST Accel. Beams **4**, p. 110101 (2001).

[Panteleev00] V.N. Panteleev, A.E. Barzakh, D.V. Fedorov, F.V. Moroz, S.Yu. Orlov, A.G. Poljakov, M.D. Seliverstov, and Yu.M. Volkov, "Development of High Temperature Targets at Iris Facility", Proc. of RNB2000, Divonne, France, April, 2000.

[Pardo98] R. Pardo, B. Harss, K.E. Rehm, J. Greene, D. Henderson, C.L. Jiang, J.P. Shiffer, J. R. Specht, B.J. Zabransky, 15th International Conference on the Application of Accelerators in Research and Industry, Denton, Texas, (1998), edited by J. L. Duggan and I. L. Morgan, American Institute of Physics, Woodbury, New York, (Nov. 1998).

[Parzen60] E. Parzen, *Modern Probability Theory and Its Applications* (Wiley, New York, 1960) p. 317.

[Portillo01a] M. Portillo, J. A. Nolen, T. A. Barlow, " Design Layout of an Isobar Separator Based on 5th Order Calculation", Proc. 2001 IEEE Part. Accel. Conf., Chicago (2001) p. 3015. http://accelconf.web.cern.ch/AccelConf/p01/PAPERS/RPAH073.PDF

[Portillo01b] M. Portillo, V. N. Aseev, J. A. Nolen, P. N. Ostroumov, " Design of a Magnetic Optical System for Transport and Matching of Multiple-Charge-State Heavy-Ion Beams", Proc. 2001 IEEE Part. Accel. Conf., Chicago (2001) p. 3012. http://accelconf.web.cern.ch/AccelConf/p01/PAPERS/RPAH072.PDF

[Prael89] R.E. Prael and H. Lichtenstein, "User Guide: The LAHET Code System", Los Alamos, LA-UR-89-3014 (1989).

[Press92] W. H. Press, S. A. Teukolsky, W. T. Vetterling, and B. P. Flannery, *Numerical Recipes in C*, **2**nd edition (Cambridge University Press, Cambridge, 1992), Chap. 16.2, p.714.

[Purcell55] N.E. Purcell, U.S. Pat. 5 436 876 (1955).

[Reiser94a] M. Reiser, in *Theory and Design of Charged Particle Beams*, edited by Mel Month (John Wiley & Sons, Inc., New York, 1994), Chap. 2, p.16.

[Reiser94ab] M. Reiser, in *Theory and Design of Charged Particle Beams*, edited by Mel Month (John Wiley & Sons, Inc., New York, 1994), Chap. 3, p. 64.

[Reiser94b] M. Reiser, in *Theory and Design of Charged Particle Beams*, edited by Mel Month (John Wiley & Sons, Inc., New York, 1994), Chap. 3, p.66.

[Reiser94c] M. Reiser, in *Theory and Design of Charged Particle Beams*, edited by Mel Month (John Wiley & Sons, Inc., New York, 1994), Chap. 3, p.80.

[Reynolds55] H.L. Reynolds, L.D. Wyly and A. Zucker, Phy. Rev. **98**, p. 474 (1955).

[Roa96] D.E. Roa, L. Wright, J.D. Fox, J.P. Greene, B.B. Back and B.G. Nardi, Nucl. Instr. Meth. Phys. Res. A **368**, p. 307 (1996).

[Rothard90] H. Rothard and others, Nucl. Instrum. Methods Phys. Res. B **48**, (1990) 616.

[Rozet96] J.P. Rozet, C. Stephan and D. Vernhet, Nucl. Instr. Meth. Phys. Res. B **107**, p. 67 (1996).

[Ruedenauer70] F.G. Ruedenauer, Rev. Sci. Instr. **41**, 1487 (1970).

[Ruthenberg83] Arthur E. Ruthenberg, private communications.

[Savard99] G. Savard *et. al.*, Nuclear Physics A **654**, p. 961c (1999).

[Savard01] G. Savard, "The U.S. Rare Isotope Accelerator Project ", Proc. 2001 IEEE Part. Accel. Conf., Chicago (2001) 495.

[Savard02] G. Savard, J. Schwartz, J. Caggiano, J.P. Greene, A. Heinz, M. Maier, D. Seweryniak, B.J. Zabransky, Nuclear Physics A (1999) (in press).

[Scheidenberger98] C. Scheidenberger, Th. Stohlder, W.E. Meyerhof, H. Geissel, P.H. Mokler and B. Blank, Nucl. Instr. Meth. Phys. Res. B **142**, p. 441 (1998).

[Schmor99] P.W. Schmor, "Initial Commissioning of the ISAC RIB Facility" in *Proceedings of the 1999 Particle Accelerator Conference,* 1999, p. 508.

[Seitz56] F. Seitz and J. Koehler, Solid State Phys. **2**, p. 305 (1956).

[Senashenko70] V.S. Senashenko, V.S. Nikolaev, V.Yu. Shafer and I.S. Dmitriev, Vestnik MGU, Ser. Fiz. Astron. **2**, p. 1970 (136).

[Shapira00] D. Shapira, T.A. Lewis, L.D. Hulett Jr., Z. Ciao Nucl. Instrum. Methods Phys. Res. A **449**, 396 (2000).

[Shepard99] K.W. Shepard *et al.* in *Proceedings of the 9th International Workshop on RF Superconductivity, Nov. 1-5, 1999*, LA-13782-C, paper WEA003.

[Sherrill92] B.M. Sherrill et. al., Nucl. Instrum. Methods Phys. B **70**, p. 298 (1992).

[Shima92] K. Shima, N. Kuno, M. Yamanouchi and H. Tawara, Atomic Data and Nuclear Data Tables **51**, p. 173 (1992).

[Simion7] Simion 7, Scientific Instrument Services, 1027 Old York Rd, Ringoes, NJ 08551.

[Smythe34] W.R. Smythe, L.H. Rumbaugh and S.S. West, Phys. Rev. **45**, p. 724 (1934).

[SRIM98] J.F. Ziegler, SRIM, Copyright by International Business Machines, 1998.

[Takebe95] M. Takebe and S. Kumashiro, Nucl. Instr. Meth. **A 363**, p. 441 (1995).

[Talber97] W.L. Talbert, T.A. Hodges, H.-H. Hsu and M.M. Fikani, Rev. Sci. Instr. **68**, p. 3019 (1997).

[Vernhet96] D. Vernhet, J.P. Rozet, K. Wohrer, L. Adoui, C. Stéphan, A. Cassimi and J.M. Ramillon, Nucl. Instr. Meth. Phys. Res. B **107**, p. 71 (1996).

[Vorobiev01] L. Vorobiev, X. Wu and R. York, "Space Charge Beam Dynamic Studies of the Injection Line and the Main Ring for the University of Maryland Electron Ring Project", Proc. 2001 IEEE Part. Accel. Conf., Chicago (2001) 2954. http://pacwebserver.fnal.gov/papers/Thursday/AM_Poster/RPAH099.pdf

[Warren87] J.L. Warren, "Reference Manual for the POISSON/SUPERFISH Group of Codes", LANL, LA-UR-87-126 (1987).

[Witteveen79] G.J. Witteveen, Nucl. Instr. Meth. Phys. Res. **158**, 51 (1979).

[Wollnik71] H. Wollnik, Nucl. Instr. and Meth **95**, p. 1971 (453).

[Wollnik72] H. Wollnik, Nucl. Instr. Meth. **B 103**, p. 479 (1972).

[Wollnik87] H. Wollnik, J. Brezina, and M. Berz, Nucl. Instrum. Methods Phys. Res. A **258**, 408 (1987).

[Wollnik87a] H. Wollnik, *Optics of Charged Particles* (Academic Press, Inc., London, 1987), p. 189.

[Wollnik87b] H. Wollnik, *Optics of Charged Particles* (Academic Press, Inc., London, 1987), p. 236.

[Wollnik87d] H. Wollnik, *Optics of Charged Particles* (Academic Press, Inc., London, 1987), p. 215.

[Wollnik87e] H. Wollnik, J.M. Wouters and D.J. Vieira, Nucl. Instr. and Meth. Phys. Res. **A258**, p. 331 (1987).

[Wollnik87f] H. Wollnik, *Optics of Charged Particles* (Academic Press, Inc., London, 1987), p. 236.

[Wollnik91] H. Wollnik, Nucl. Instr. Meth. **B 56/57**, p. 1096 (1991).

[Wollnik95] H. Wollnik, Nucl. Instr. Meth. **A 363**, p. 393 (1995).

[Wong90] S.S.M. Wong, *Introductory nuclear physics* (Prentice Hall, Inc., Englewood Cliffs, NJ, 1990), p. 17.

[Yavor97a] M.I. Yavor, Nucl. Instr. Meth. **B 126**, p. 266 (1997).

[Yavor97b] M.I. Yavor and A.S. Berdnikov, Int. J. Mass. Spectr. Ion Proc. **128**, p. 149 (1993).

[Yoshinari95] K. Yoshinari, Y. Ose and F. Nakajima, Nucl. Instr. Meth. **A 363**, p. 429 (1995).

[Zaifman92] D. Zaifman, E.P. Kanter, T. Graber, Z. Vager and R. Naanam, Nucl. Instr. Meth. Phys. Res. B **67**, 22 (1992).

[ZircarA] Alumina Type ALBF-3, from Zircar Products, Inc., P.O. Box 458, Florida, NY 10921.

[ZircarZ] Zirconia Type FBD from Zircar Products, Inc., P.O. Box 458, Florida, NY 10921. http://www.zircar.com.

[ZYP] ZYP Coatings, Inc., 120 Valley Court, Oak Ridge, TN 37830.